Graduate thesis

NTNU
Norwegian University of Science and Technology
Faculty of Natural Sciences
Department of Physics

Sarah Nyeki

Optical Characterization of Intermediate Band Material

Graduate thesis in Master of Science in Physics (MSPHYS)
Supervisor: Turid Reenaas
Co-supervisor: Morten Kildemo

May 2023

NTNU
Norwegian University of
Science and Technology

Sarah Nyeki

Optical Characterization of Intermediate Band Material

Graduate thesis in Master of Science in Physics (MSPHYS)
Supervisor: Turid Reenaas
Co-supervisor: Morten Kildemo
May 2023

Norwegian University of Science and Technology
Faculty of Natural Sciences
Department of Physics

NTNU
Norwegian University of
Science and Technology

Abstract

In the coming years, due to global climate change, the demand for renewable energies will continue to increase. Developing solar cell technologies with higher efficiency could help address this challenge. In the Solar Cell Physics group at NTNU, research is focused on intermediate-band solar cell technology. Density functional theory (DFT) calculations from the literature showed that (Cr, N) co-doped TiO_2 can be an intermediate band material. In order to subsequently analyze the (Cr, N) co-doped TiO_2 samples, the undoped TiO_2 samples must first be characterized. Therefore, in this thesis, an optical characterization of TiO_2 is performed via spectroscopic ellipsometry (SE) and photoluminescence spectroscopy (PL). In SE, the data of TiO_2 anatase and rutile single crystals were analyzed only, as the samples were measured previously by a PhD student of the group, Thomas Brakstad. In PL, three TiO_2 single crystal samples with different crystal orientations were studied: anatase (110), rutile (110) and (001), and three undoped TiO_2 thin films grown on $SrTiO_3$ (STO), made in the research group via PLD.

From the SE data, two optical models of the dielectric functions were built for the extraordinary and ordinary axis of the two polymorphs of TiO_2: first a simple B-spline model and then, a general oscillator model where the classical picture of the absorption is used to deconvolute the dielectric functions. From the general oscillator model, the experimental bandgaps of the ordinary and extraordinary axis were determined to be 2.94 eV and 3.13 eV respectively for rutile, and 3.25 eV and 3.63 eV for anatase. The bandgaps for the ordinary axis correspond to the experimental bandgap from the literature. The ellipsometry analysis was next pursued by an attempt to connect the dielectric functions of TiO_2 to its band structure via a critical point (CP) analysis. The dielectric functions extracted from DFT calculation by another master's student Rasmus Hoholm were studied first. Then, the same analysis was performed on the B-spline model of rutile ordinary axis. The DFT dielectric functions were best fitted with seven excitonic CPs, while the SE dielectric functions were best fitted with four excitonic CPs.

PL spectroscopy of TiO_2 was a new subject for the group and only an initial analysis is performed in this thesis. The anatase (110) PL spectrum consisted of a single broad band, from approx. 2 to 4 eV. The sub-bandgap part (i.e. below 3.20 eV) was attributed to mainly self-trapped exciton (STE) emission and defect related emissions, in the literature and this thesis. Both rutile (001) and (110) PL spectra exhibit two bands: one broad band around bandgap of rutile (i.e. 3.00 eV) and a second centered at 1.52 eV. The first band is attributed to band-to-band radiative recombination and defect emissions, like for anatase. The band at 1.52 eV demonstrates the characteristics of the PL of a color center (most likely an oxygen vacancy in this work). A previous XRD analysis of the undoped TiO_2 thin films grown on STO showed that the samples are mostly textured anatase (001). The PL of the TiO_2 thin films is indeed similar to anatase. Due to the presence of the photoluminescence of STO in the spectra, which has a bandgap of 3.25 eV, the contribution of the TiO_2 thin films could not be determined. However, regardless of the PL origin, the emission seems to be mainly due to oxygen defects and excitonic states. There are some indications that the PL does come from the film.

In conclusion, from the PL and SE analysis, the optical properties of TiO_2 seem dominated by excitons. The PL results complement nicely the SE analysis, by showing the importance of the sub-bandgap state, whereas in SE only the above bandgap states were present in the spectra.

Sammendrag

I de kommende årene vil etterspørselen etter fornybar energi fortsette å øke, på grunn av de globale klimaendringene. Utvikling av solcelleteknologier med høyere effektivitet kan hjelpe til å takle denne utfordringen. I Solcellefysikkgruppen ved NTNU fokuseres forskningen på høyeffektive mellombåndssolceller. Tetthetsfunksjonal-teori (engelsk: *density functional theory, DFT*) beregninger fra litteratur viser at (Cr, N) ko-dopet TiO_2 kan være et mellombåndsmateriale. For å kunne analysere (Cr, N) ko-dopede TiO_2-prøver, må udopede TiO_2-prøver karakteriseres først. I denne oppgaven uttøres det derfor optisk karakterisering av TiO_2 ved bruk av spektroskopisk ellipsometri (SE) og fotoluminescensspektroskopi (PL). For SE delen av oppgaven er dataene til tre TiO_2 en-krystaller kun analysert, da prøvene ble målt tidligere av en doktorgradsstudent i gruppen, Thomas Brakstad. De tre en-krystallene har ulik orientering og/eller fase: anatase (110), og rutil (110) og (001). For PL delen ble de samme tre TiO_2 en-krystallprøvene og tre udopede TiO_2 tynnfilmer, deponert på SrTiO3 (STO) substrater, både målt og analysert. Filmene er laget i forskningsgruppen ved bruk av pulset laser deponering (PLD).

Fra SE-dataene ble to optiske modeller av de dielektriske funksjonene laget, for både ekstraordinær og ordinær akse for de to polymorfene til TiO_2 (anatase og rutil): Først en enkel B-spline modell og deretter, en generell oscillatormodell hvor det klassiske bildet av absorpsjon brukes til å de-konvulere de dielektriske funksjonene. Fra den generelle oscillatormodellen, ble de eksperimentelle båndgapene til ordinære og ekstraordinær akse bestemt til å være henholdsvis 2,94 eV og 3,13 eV for rutil, og 3,25 eV og 3,63 eV for anatase. Båndgapene for den ordinære aksen stemmer overens med det eksperimentelle båndgapet fra litteraturen. Ellipsometrianalysen ble tatt videre i et forsøk på å koble de dielektriske funksjonene til TiO_2 til båndstrukturen til TiO_2 via såkalt kritisk punkt (CP) analyse. De dielektriske funksjonene hentet fra DFT-beregning av en annen masterstudent, Rasmus Hoholm, ble studert først. Etterpå ble samme analyse gjort for B-spline-modellen for rutil, ordinær akse. For dielektrisitetsfunksjonen fra DFT beregningene, ble best tilpasning oppnådd med sju, eksitoniske kritiske punkter, mens B-spline dielektriskfunksjonen (målt med SE) ble best tilpasset med fire eksitoniske kritiske punkter.

PL-spektroskopi av TiO_2 var et nytt tema for forskningsgruppen, og bare en innledende analyse er utført i denne oppgaven. For anatase (110) bestod PL-spekteret av en enkelt (bred) topp. PL under båndgapet (dvs. under 3,20 eV) ble hovedsakelig tilskrevet såkalte ”self-trapped excitons” (STE) og oksygen-defekter, både i litteraturen og i denne oppgaven. PL spektrene for både rutil (001) og (110) viste to brede topper: en rundt båndgapet til rutil (dvs. 3,00 eV) og en annen sentrert ved 1,52 eV. Den første toppen tilskrives bånd-til-bånd strålingsrekombinering og strålingsrekombinering via defekttilstander. Toppen ved 1,52 eV stemmer overens med det man forventer av PL for et fargesenter (en urenhet eller defekt). Tidligere XRD-analyse av de udopede TiO_2 tynnfilmene (deponert på STO) viste at filmene for det meste består av teksturert (100) anatase. PL spektrene av TiO_2 filmene likner PL fra anatase en-krystallen. Men fordi STO har et båndgap på 3,25 eV, så er det vanskelig å skille PL fra substratet fra PL fra filmen. Uansett om PL signalet kommer fra filmen eller substartet, så skyldes den i hovedsak oksygen-vakanser og ”self trapped” eksitoner. Det er imidlertid indikasjoner som tyder på at PL signalet kommer fra filmen.

Avslutningsvis kan man konkludere fra både PL- og SE-analysen at de optiske egenskapene til alle TiO_2 prøvene er dominert av eksitoner. PL-resultatene kompletterer SE-analysen fint, ved å tydelig vise bidrag fra tilstander i båndgapet, mens man i SE i hovedsak ser bidrag fra tilstandene over båndgapet.

Acknowledgements

First, I would like to thank my supervisor Professor Turid Reenaas for her guidance and wise advices along my master's thesis. She made it easy for me to talk about the thesis and other topics, and I appreciate her openness of speech, accessibility, and humility. Finally, I would like to thank her for occasionally taking the time to explain to me the history and culture of Norway.

I also want to express my gratitude my co-supervisor Professor Morten Kildemo for its help in understanding the difficult topic of the critical point analysis. Having a second point of view on my work and the subject was enlightening. I valued your physics expertise very highly.

I am grateful to Thomas Brakstad, an ex-PhD student of the Solar Cell Physics group, for his encouragement and support during my master's thesis, as well as for taking the time to help me better understand the ellipsometry analysis.

I would like also to thank Rasmus Hoholm for having collaborated with me on the critical point analysis. It was motivating to achieve together this challenging analysis.

Finally, I want to say thanks to Joseba, Jacob, Andrés, Harry, and Ahmad for our weekly kanelboller gathering on Wednesdays. Spending my last year of master's degree with all of you was very pleasant. I am glad I met you. I have a special thanks for Joseba. I enjoyed working together at the beginning of the autumn semester on PL spectroscopy.

Acronyms

AFM atomic force microscopy

AR assessment report

BZ Brillouin zone

CP critical point

DFT Density functional theory

EMA effective mass approximation

FWHM full width half maximum

GIXRD grazing incidence X-ray diffraction

IB intermediate band

IBSC intermediate band solar cell

IPPC intergovernmental panel on climate change

JDOS joint density of states

KK Kramer-Kronig relations

MSE mean square error

PL photoluminescence spectroscopy

PLD pulsed laser deposition

PLE photoluminescence emission

SE spectroscopic ellipsometry

SEM scanning electron microscopy

SQ Shockley-Queiser limit

SSP shared socioeconomic pathways

STE self-trapped exciton

STE self-trapped exciton

TEM transmission electron microscopy

TMO transition metal oxide

VASE variable angle spectroscopic ellipsometry

XRD X-ray diffraction

ZPL zero phonon line

Contents

1 Introduction

The impact of human activities on climate change has been highlighted since 1965. The high consumption of and dependence on fossil fuels, mainly linked to the lifestyles of developed countries, are endangering biodiversity and the future of humanity. To reduce the impact of humans on their environment, it is necessary to change our way of life. Developing new technologies that consume less, and producing new energies that are more renewable is one of the human challenges that our generations face. It is in this context that the development of renewable energy with low impact on the environment, such as wind, solar, or thermal became essential.

Human-induced climate change has irreversible consequences, but also consequences that we can still limit. Since the intergovernmental panel on climate change (IPPC) was created in 1988, six assessment report (AR) have been published to take stock of the situation. Figure 1 traces the evolution of the publications of the IPCC. In the last IPCC report, they expose a direct link between CO_2, methane, and other greenhouse gas emissions (GHG emission) to global warming.[1] The objective is also to predict the possible evolution of climate change depending on the human reduction of emission of CO_2. The IPPC envisages in its reports the future temperature evolution according to 5 different shared socioeconomic pathways (SSP). In all emission scenarios, the global warming threshold of +1.5°C will be exceeded in the near future (between 2021 and 2040) and the average temperature on earth will remain above +1.5°C until the end of the century.[2] However, the current tendency heads more towards +3 °C by the end of the century.[3] If humanity stops now its activities, global warming would stop as a result. As this situation is not realistic to apply on a global scale, alternatives to produce energy must be found.

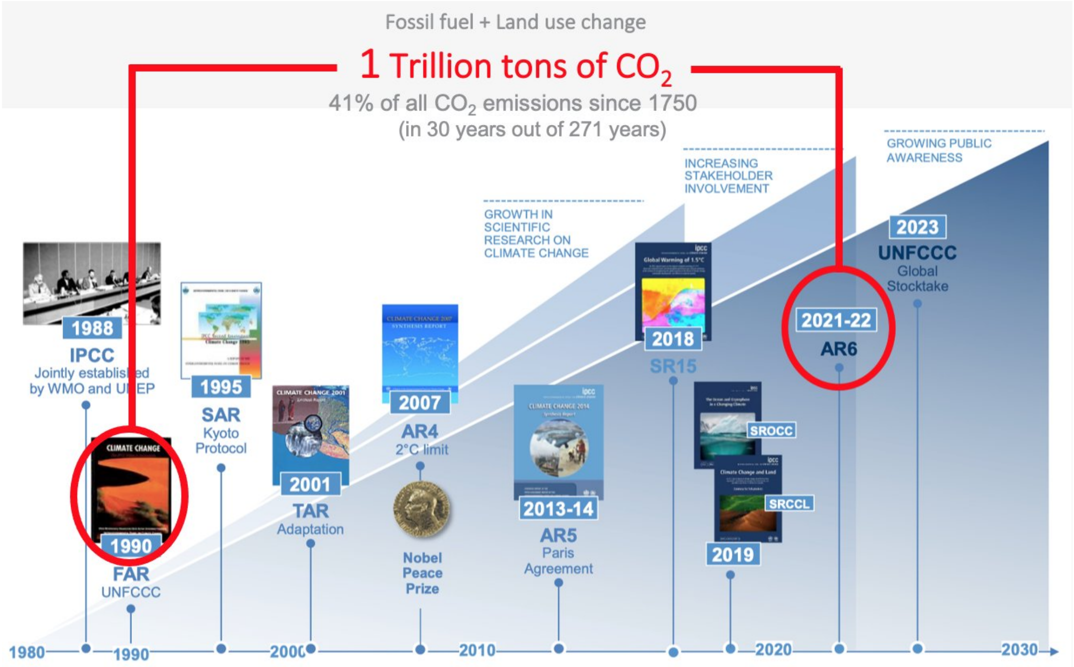

Figure 1: IPPC reports timeline. Taken from [3].

To reach the current goal of limiting global warming to +1.5°C, one of the solutions is to massively develop sustainable energies. As a result, the proportion of energy from renewable sources is expected to increase over the next 20 years and take a share of the energy production that currently relies on fossil fuels and gas.[4, 5] As solar energy is abundant on Earth, solar cells are major candidates to effectuate this transition to renewable energy sources. [6] One of the current challenges is the development and large-scale integration of solar panels in cities and on buildings, which involves increasing their efficiency. To this end, new devices must be designed to meet these specifications. It is in this context that third-generation solar cells are developed.

The rate of conversion into electric current in a solar cell is limited in absolute by a theoretical efficiency limit, the Shockley-Queiser limit (SQ). For single band gap solar cells, this limit is 40.7 % under fully concentrated light (32.33% under 1 sun illumination).[7, 8, 9]. To overcome this limit, new concepts have been developed and gathered under the name of third-generation solar cells. Such technologies are aiming to improve efficiency by increasing the proportion of solar energy utilized by the cells. The multi-junction solar cells or tandem solar cells, based on the use of materials with different bandgaps, are the most developed at the moment. The Solar Cell Physics group at the department of Physics at NTNU has dedicated its research on another promising technology: intermediate band solar cell (IBSC). The IBCSs are based on the simple concept of adding one additional layer to a material to increase the efficiency. Their theoretical efficiency limit is 63.2% under fully concentrated light.[10] The intermediate band (IB) material is characterized by having a narrow energy band in the forbidden bandgap of the semiconductor. Three ranges of photons can be absorbed, each related to one of the bandgaps, E_G, E_H or E_L, as illustrated in figure 2.

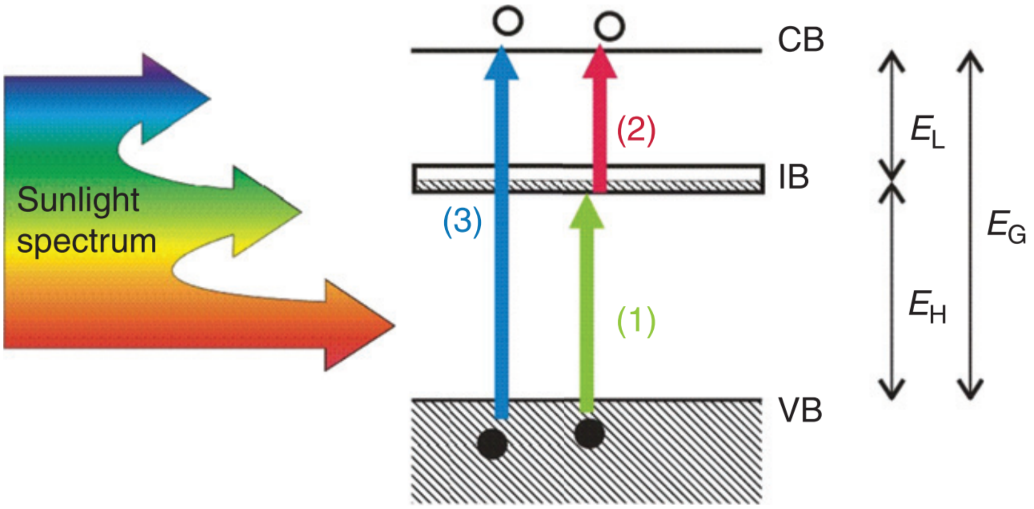

Figure 2: Schematic band diagram of an intermediate band material with its three bandgaps E_G, E_H and E_L. Taken from Ref.[11].

The additional band (IB) can be achieved by adding impurities that will introduce energy levels in the bandgap. In the Solar Cell Physics group, TiO_2 is studied as a possible host material for the intermediate band. DFT calculations in the literature show that (Cr, N) co-doped TiO_2 can be an intermediate band material.[12]

Thin film IBSCs are one way to address both the material reduction and the enhanced theoretical efficiency. The group specializes in the realization of such films via pulsed laser deposition (PLD). In the last years, master and PhD students of the Solar Cell Physics group made a large number of samples, trying to optimize the deposition technique as well as the doping of TiO_2. Now, to better understand the optical and electrical properties of these samples, it is necessary to characterize them. This starts by having a detailed understanding of the properties of the matrix material, TiO_2. It is in this context that this thesis project is inscribed. This thesis focuses on the optical characterization of the undoped TiO_2. This characterization is divided into two sub-studies: spectroscopic ellipsometry (SE) and photoluminescence spectroscopy (PL). The spectroscopic ellipsometry gives an insight into the dielectric functions (i.e. the refraction index and extinction coefficient) of the samples. Following this analysis, a line-shape analysis of the critical point (CP) of the dielectric functions has been carried out. The photoluminescence spectroscopy provides information about the optical behavior of the samples through their emission spectra. A curve-fitting of the PL is attempted to explain the origin of the PL peaks. The characterization focuses mainly on TiO_2 single crystal polymorphs, but also undoped TiO_2 thin films deposited on STO substrates have also been characterized.

2 Theory

In this section, a review of the concepts involved in the thesis is presented. The principle of the two main techniques, photoluminescence and ellipsometry, in addition to the theory of the critical point analysis are described.

2.1 Titania, TiO_2

TiO_2 is a transition metal oxide (TMO) composed of oxygen and titanium atoms. Its elements are present abundantly on the earth and are non-toxic, making TiO_2 an easily accessible and environmentally friendly material. In addition, its good optical and electronic properties designate it as an interesting material for a wide range of applications, from food pigments to semiconductors. It is well-known for its photo-catalyst ability to photo-induce the splitting of water molecules. TiO_2 mainly exists in three crystalline forms: anatase, rutile, and brookite. However, only anatase and rutile are polymorphs studied in the research, as brookite is unstable. Rutile is the most stable of them due to its lowest free Gibbs energy and thus the most present in nature. Anatase is also present in nature but less commonly. Usually, natural crystals have different purity leading to different appearances and colors (due to color centers). Figure 3 shows the crystal lattice of anatase and rutile. Both have a tetragonal unit cell with an octahedral structure of oxygen atoms around the titanium atom. Their respective lattices constants are $c = 2.9587$ Å and $a = 4.5936$ Å for rutile, $c = 3.784$ Å and $a = 9.515$ Å for anatase.[13]

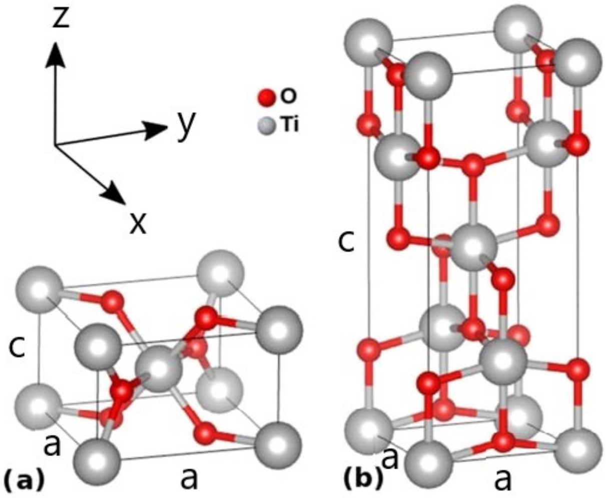

Figure 3: Representation of the tetragonal primitive unit cell of rutile and the body-centered tetragonal conventional cell of anatase TiO_2. Adapted from Ref. [14].

The difference in length of the unit cell along the z-axis, and the x- and y-axes leads to the optical anisotropic behavior of TiO_2, resulting in different optical properties for different directions in the crystal. Having a different lattice constant for the z-axis leads to a special case of anisotropy, where the material is said to be uniaxial. In this case, the material has two refractive indexes n_e and n_o in the extraordinary axis and ordinary axes directions. The axis can be easily identified as it is linked to the lattice constant, the axis with the c lattice constant is assimilated to the extraordinary axis, here z, while the other axes are ordinary.

TiO_2 is studied in the Solar Cell Physics group as a potential candidate for hosting an intermediate band. In addition to its optical and electronic properties, it has the important characteristic of having a wide bandgap (which sometimes leads to calling TiO_2 a dielectric). Bandgaps of rutile and anatase are reported in literature respectively at $E_g^R = 3.00$ eV and $E_g^A = 3.20$ eV (the values are based on experimental research). TiO_2 absorbs mostly in the UV region, however by inserting an IB, its absorption could be extended to the VIS and IR. The literature agrees on an indirect bandgap for anatase, while the nature of rutile bandgap is a matter of debate. A direct bandgap is often reported.[15] However, DFT calculation have shown that its indirect bandgap and direct one have close values.[16, 17] According to the thesis of Maria Jorge, a previous PhD student of the Solar Cell Physics group, sub-stochiometric TiO_{2-x} already shows states in the bandgap, due to oxygen vacancies. However, the energy of the oxygen vacancy states is too close to the VB and thus they are not eligible as an intermediate band. TiO_2 co-doped with chromium and nitrogen has been suggested as an interesting candidate for intermediate band solar cells by Zhu et al.[12] In their article, they demonstrated that co-doping could enhance the photo-activity of TiO_2 by increasing the dopant solubility compared to mono-doping, as high doping density is necessary to create an intermediate band. Moreover, another article from Wu et al. calculated a theoretical efficiency for an IBSC with such co-doping of 52.7%.[18] This is why, the group of IBSC at NTNU is currently focusing its research on (Cr, N)-codoped TiO_2 samples.

2.2 Spectroscopic Ellipsometry

Spectroscopic ellipsometry (SE) is an experimental technique based on the modification of the polarization state of an electromagnetic field upon specular reflection on a material (i.e. sample to be studied). This change is measured via a modification of the amplitude ratio ψ and phase difference Δ between the p- and s-polarization of the electromagnetic field of the light, whose origins will be explained in the following.

The SE is used to investigate the optical properties of materials by comparing experimental data to a mathematical model. In most cases, thickness and refractive index estimates are the main quantity explored with this technique. However, the optical response can also contain information about the composition, crystallinity, roughness, doping concentration, and other properties of the material.

The SE combined with other experimental methods is highly powerful. Various useful characteristics of the material are accessible from these other techniques, such as its crystallinity with transmission electron microscopy (TEM) images, its roughness with atomic force microscopy (AFM) imaging, its crystal phase thanks to X-ray diffraction (XRD) spectra, and more. Comparisons allow the scientist to improve the mathematical model, as well as verify its physical plausibility.

2.2.1 Variable Angle Spectroscopic Ellipsometry (VASE)

The variable angle spectroscopic ellipsometry (VASE) is a special case of ellipsometry where the instrument allows measurements at different angles of incidence of the incoming light beam. Then, in addition to the study of different angles of rotation of the sample over 360°(i.e. azimuth), the optical response of the sample is probed in function of the interaction of the wave-vector of the light with the electric dipoles of the crystal. Indeed, in function of the angle of incidence the scalar product of the vector changes.

The azimuth angles are also very convenient, especially when anisotropic materials are studied because of their anisotropic optical index. For example, the direction of the extraordinary and ordinary axis can be determined through ellipsometry.

2.2.2 Polarization of light

General polarization representation

Any polarization of an incoming electromagnetic field E_0 on an interface can be decomposed into two components: one in the plane of incidence, called p-polarization $E_p\vec{e_p}$, and one perpendicular to the incidence plane, s-polarization $E_s\vec{e_s}$. The direction of the propagation is defined by the wave vector $\vec{k}$ and is always orthogonal to the direction of the oscillating electric and magnetic field. Thus, $\{O, \vec{e_s}, \vec{e_p}, \vec{k}\}$ forms an orthogonal frame. Upon reflection the interaction between light and the material transforms the ratio of p and s components of the electric field, giving rise to a new elliptical polarization.

In the most general case, the s and p components travel at different speeds in a material (i.e. they may experience different refractive indexes) and their amplitudes evolve separately, which results in a generally elliptic polarization state. From this follows two specific and useful cases: when the two components are in phase, the polarization state is said to be linear, but, when they are 90°out-of-phase and equal in amplitude, the polarization becomes circular.

The orientation of the ellipse is described by the ellipticity ε which is the ratio of the minor axis over the major axis a. The corresponding ellipticity angle is $\chi = \tan(\frac{b}{a})$. The orientation of the ellipse is defined by the azimuth ψ, the angle between the s-axis (or p-axis depending on the definition chosen by the authors in the books) and the major axis of the ellipse (ψ is counterclockwise) as illustrated in figure 4.

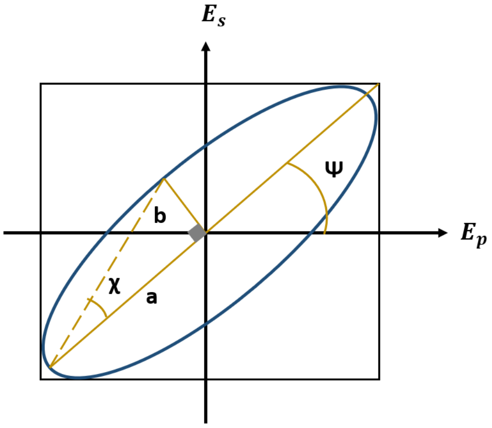

Figure 4: Ellipse of polarization, with the ellipticity angle $\chi = \tan(\frac{a}{b})$, the azimuth ψ, the minor axis b and the major axis a.

Stokes vector and Mueller matrix

The Stokes vector and Mueller calculus are a way of describing the polarization of an electromagnetic wave passing through an optical system. Other representation exists such as the

Jones matrix, with the difference that Jones vectors can only describe fully polarized light whereas Stokes vectors can also be used in the case of partially polarized light. The Stokes vectors can be written as:

$$\vec{J}\begin{pmatrix}S_0\\S_1\\S_2\\S_3\end{pmatrix} = \begin{pmatrix}I\\Ip\cos(2\psi)\cos(2\chi)\\Ip\sin(2\psi)\cos(2\chi)\\Ip\sin(2\chi)\end{pmatrix} \tag{1}$$

The four parameters depend on the total intensity $I = E_p^2 + E_s^2$ of the wave, the degree of polarization $p = \sqrt{S_1^2 + S_2^2 + S_3^2}/S_0$ and the shape of the ellipse of polarization (i.e. the ellipticity χ and the azimuth ψ). The degree of polarization defined to which extent the light is partially polarized, $0 < p < 1$, for $p = 1$ the light is fully polarized, and for $p = 0$ reciprocally unpolarized. Ip, 2χ and 2ψ are the spherical coordinates of $\begin{pmatrix}S_1\\S_2\\S_3\end{pmatrix}$ on the Pointcarré sphere as illustrated in figure 5.

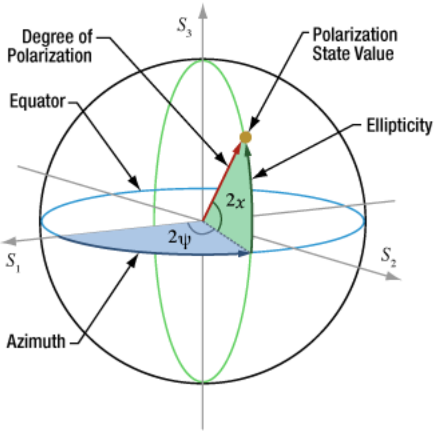

Figure 5: Pointcarré sphere showing the Jones vector polarization representation in 3D. Taken from Ref.[19].

The Stokes parameters S_2 and S_3 can also be expressed in terms of right/left circular polarization and of the ±45° linear polarization: $S_2 = I_r - I_l$ and $S_3 = I_{+45^\circ} - I_{-45^\circ}$.

In the same way as the Stokes vector is used for the incident light polarization state, the Mueller matrix describes the optical system (e.g. lenses) through a 4x4 matrix.

A Mueller matrix can be assigned to each element M_i of the system, in the way that the total system can be expressed as $S = M_n M_{n-1} ... M_i ... M_0$. In the case of an isotropic material M can be written as:

$$M_{isotropic} = \begin{pmatrix}1 & -N & 0 & 0\\-N & 1 & 0 & 0\\0 & 0 & C & S\\0 & 0 & -S & C\end{pmatrix} \tag{2}$$

where $N = \cos(2\psi)$, $C = \sin(2\psi)\cos(\Delta)$ and $S = \sin(2\psi)\sin(\Delta)$. For an anisotropic material the Mueller matrix is much more complex and can not be deduced directly from the data (i.e. ψ and Δ).

Finally, the new polarization states after the optical system can be find by computing $J_f = SJ_i$, where the subscripts $_f$ and $_i$ denote the final and initial states.

2.2.3 Electrodynamic theory

Macroscopic polarization of a medium

The averaging of the orientation of the microscopic electric dipoles in a material creates a macroscopic physical quantity called polarization. The polarization can be developed in Taylor series in the dielectric dipole approximation:

$$P = \varepsilon_0[\chi^{(1)}E + 1/2\chi^{(2)}E^2 + 1/6\chi^{(3)}E^3 + ... + o(E^3)] \tag{3}$$

where $\chi^{(i)}$ is the dielectric susceptibility tensor of rank i of the medium, ε_0 the dielectric permittivity of the air, and $\vec{E}$ the total electric field of the medium (the medium could have a permanent polarization and thus an internal $\vec{E_{in}}$ and undergo as well an external $\vec{E_{ext}}$). For a dielectric, isotropic, homogeneous, and linear material, the susceptibility becomes a constant and the polarization is $\vec{P} = \varepsilon_0\chi\vec{E}$.

Through the Maxwell equations describing the propagation of an electromagnetic wave in the matter, the polarization $\vec{P}$ can be linked to the displacement vector $\vec{D}$:

$$\vec{D} = \varepsilon_0\vec{E} + \vec{P} = \varepsilon_0(1+\chi)\vec{E}. \tag{4}$$

The term $1 + \chi$ is referred to as the relative permittivity ε_r. Finally, the relation:

$$\vec{D} = \varepsilon_0\varepsilon_r\vec{E} = \varepsilon\vec{E}. \tag{5}$$

gives the definition of the dielectric function ε. In the dynamic case where the physical quantities are frequency dependent, if the electric field oscillates too fast, a delay is introduced between the polarization $\vec{P}$ and $\vec{E}$. The modulus and argument of $|\chi(\omega)| = |\chi_1(\omega) + i\chi_2(\omega)|$ will give the amplitude and the phase shift of $\vec{P}$. It follows that all the physical quantities become complex, especially the dielectric function (now depending on ω) which describes the response of the matter to the electric field E_{ext}: $\varepsilon(\omega) = \varepsilon_1(\omega) + i\varepsilon_2(\omega)$, where ε_2 stands for the absorption of the material.

As the dielectric constant is related to the optical index via the relation $\varepsilon = N^2$, then the optical constant becomes also complex: $N(\omega) = n(\omega) + ik(\omega)$, where k is the extinction coefficient and n the optical or refractive index. Thus, the extraction of the imaginary and real parts of ε from Δ and ψ is of main importance in ellipsometry to retrieve the optical characteristics of the material.

$$\begin{cases} n = \varepsilon_1^2 + \varepsilon_2^2 \\ k = 2i\varepsilon_1\varepsilon_2 \end{cases} \tag{6}$$

As the dielectric function must be calculated from a model in SE, it is primordial to ensure their physical plausibility. To do this, the Kramers-Kronig (KK) relation can be used to connect the imaginary and real parts of an analytic function, which gives for the dielectric functions the following relations:

$$\varepsilon_1(\omega) = 1 + \frac{2}{\pi}P\int_0^\infty \frac{\omega'\varepsilon_2(\omega')}{\omega'^2 - \omega^2}d\omega' \tag{7}$$

and

$$\varepsilon_2(\omega) = -\frac{2}{\pi} P \int_0^\infty \frac{\varepsilon_1(\omega') - 1}{\omega'^2 - \omega^2} d\omega'. \tag{8}$$

The integrand blows up when ω' goes to ω, which is in concordance with the resonant response shape of ε_1. In practice, the Kramers-Kronig consistency derives from the extraction of ε_1 from ε_2.

It should be noted that Kramers-Kronig expressions integrate all over the spectrum whereas the measurements are performed only in an energy range. One way to calculate the integral is then to set ε_2 to zero when ω goes to 0 and to $+\infty$. However, the behavior of ε_1 and ε_2 outside the spectral range remains unknown and could affect the value of the dielectric constant. Therefore, in some cases, some absorption tails or peaks (i.e. poles) must be added outside the measurement range in the mathematical model used to find the dielectric functions from the SE data.

2.2.4 Physical quantities measured in ellipsometry

To detect a change in the polarization of the reflected beam, the polarization state of the incoming beam needs first to be controlled. The specific state can be selected via a polarizer, which induces a linear polarized state, a linear combination of the p and s components: $E_i = E_{ip} + E_{is}$. At the interface with the sample, a fraction dependent on the material characteristic (defined by the Fresnel reflection coefficients) is reflected with the same angle as the incident angle (i.e. specular reflection). The reflected beam can also be expressed as a linear combination: $E_r = E_{rp} + E_{rs}$. Because of the complex material properties, the linear polarized state is more likely to become elliptic after reflection as illustrated in figure 6. However, the light beam can also undergo some depolarization (i.e. no preferential oscillation axis, unpolarized light).

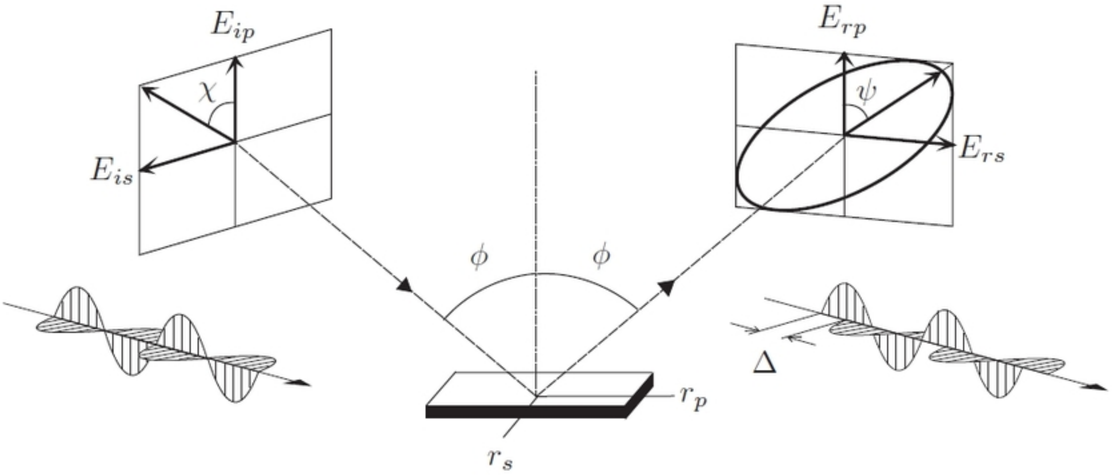

Figure 6: Schematic representation of the principle of ellipsometry. The incoming light beam with an incident angle ϕ is polarized in a known linear state. After the specular reflection, the beam is in an elliptical unknown polarized state described by an amplitude ratio (also called azimuth) ψ and a phase difference Δ. r_s and r_p are the Fresnel coefficients in the direction of the two components of the electric field. Remark: here χ is not the ellipticity, which is zero for a linear polarized light, it represents only the direction of the electric field oscillations. Taken from Ref.[20].

As an electromagnetic field can be described in function of a frequency ω and wave vector $\vec{k}$ thus one can write the incoming electromagnetic field for respectively for each polarization:

$$\vec{E_{ip}}(\vec{r},t) = E_{ip}e^{-i(\omega t - \vec{k_i}.\vec{r} + \delta_{ip})} \tag{9}$$

$$\vec{E_{is}}(\vec{r},t) = E_{is}e^{-i(\omega t - \vec{k_i}.\vec{r} + \delta_{is})} \tag{10}$$

after reflection, the electric fields become

$$\vec{E_{rp}}(\vec{r},t) = E_{rp}e^{-i(\omega t - \vec{k_r}.\vec{r} + \delta_{rp})} \tag{11}$$

$$\vec{E_{rs}}(\vec{r},t) = E_{rs}e^{-i(\omega t - \vec{k_r}.\vec{r} + \delta_{rs})} \tag{12}$$

where k is the wave vector and δ the phase accumulated related to the paths the ray takes, the p and s subscripts designate the p- and s-polarization. When the reflection occurs, the p-polarization and s-polarization interact with the electric polarization of the material (stemmed by the electric dipole moments). This interaction results in a change in the amplitude ratio of the p and s components before and after reflection, mathematically as:

$$tan(\psi) = \frac{E_{rp}}{E_{ip}}\frac{E_{rs}}{E_{is}} \tag{13}$$

In addition, if the material is anisotropic, the p and s components will ”see” different optical indexes. Thus, the propagation of one compared to the other will be delayed and will induce a phase shift $\Delta = (\delta_{rp} - \delta_{rs}) - (\delta_{ip} - \delta_{is})$. It follows that the physical quantity measured is:

$$\boxed{\rho = \frac{r_p}{r_s} = tan(\psi)e^{i\Delta}} \tag{14}$$

where r_p and r_s are the complex Fresnel reflection coefficients respectively in the p and s directions defined as:

$$r_p = \frac{E_{rp}}{E_{ip}} e^{i(\delta_{rp}-\delta_{ip})} \tag{15}$$

$$r_s = \frac{E_{rs}}{E_{is}} e^{i(\delta_{rs}-\delta_{is})} \tag{16}$$

If the incident light is linearly polarized, then the phase difference of the incident electric field is zero and their amplitudes are equal. Thus ρ becomes:

$$\rho = \frac{E_{rp}}{E_{rs}} e^{i(\delta_{rp}-\delta_{rs})}. \tag{17}$$

For a simple sample structure, Δ is linked to the imaginary optical index k and so the phase shift is related to the absorption process, while ψ is affected by the real optical index n.

In the case where the material can be considered as isotropic, the Mueller matrix can be extracted from ψ and Δ.

In a first approximation of the material constants, the raw data ψ and Δ can be converted into "pseudo" dielectric functions. To do so, the substrate surface is considered flat and its thickness semi-infinite:

$$\langle \varepsilon \rangle = < N >^2 = sin^2\phi \left(1 + tan^2\phi \left(\frac{1-\rho}{1+\rho}\right)^2\right) \tag{18}$$

where ϕ is the incident angle. Although the pseudo dielectric functions are not completely physical (denoted by the bra and ket notation) because they correspond to an ideal case, their shapes give a good estimate of the material properties, especially the energy ranges where the material is transparent and absorbing. In the transparent range, $< \varepsilon_1 >$ and $< \varepsilon_2 >$ oscillate as ψ and Δ do, while in the absorbing range, the interference not predominating anymore, the pseudo dielectric functions show a similar shape with different incidence angles. The peaks in the absorbing region of $< \varepsilon_2 >$ correspond to interband transitions. This change of character of the pseudo dielectric functions occurs at the bandgap of the semiconductor.[21]

Fresnel coefficients

For an ideal material (i.e. without defects, roughness, pores, anisotropy, etc...) the optical response could be deduced from the Maxwell equations and the boundary conditions. These equations govern the response of a material in terms of polarization (macroscopic averaging of microscopic electric dipole moments) and magnetization (macroscopic averaging of microscopic magnetic dipole moments). The Fresnel coefficients r_s and r_p, which derive from these equations, describe the ratio of the electric field before and after reflection. A Fresnel coefficient in transmission also exists but is not addressed in this thesis.

The simplest problem in ellipsometry is the reflection from a single ideal interface between a semi-infinite medium 0 with N_0 (most likely vacuum or air) and a semi-infinite isotropic, homogeneous, and uniform medium 1 with a complex optical index N_1 which is unknown. This corresponds to the first reflection in figure 7. After the computation of the Maxwell equations and introduction of the boundary conditions, this leads to the expression of the Fresnel coefficients:

$$r_p = \frac{N_1 \cos(\theta_i) - N_0 \cos(\theta_t)}{N_1 \cos(\theta_i) + N_0 \cos(\theta_t}) \tag{19}$$

$$r_s = \frac{N_0 \cos(\theta_i) - N_1 \cos(\theta_t)}{N_0 \cos(\theta_i) + N_1 \cos(\theta_t)} \tag{20}$$

The total reflection coefficient is defined as $R = R_s + R_p = |r_p|^2 + |r_s|^2$, and the total transmission coefficient is $T = 1 - R$. Then, the optical index $N_1 = n_1 + ik_1$ can be extracted from these expressions, where n_1 is the real optical index and k_1 is the extinction coefficient of the medium 1. Using Snell-Descartes law to express the Fresnel coefficients only in function of θ_i, N_0, and N_1. Then, using the relationship between the dielectric functions and the optical index and the expression of ρ, one can find an analytic expression for ε_1, the dielectric function of the medium:

$$\varepsilon_1 = \varepsilon_0 \sin^2(\theta_i) \left(1 + \tan^2(\theta_i) \left(\frac{1-\rho}{1+\rho} \right)^2 \right) \tag{21}$$

Equation 21 is the expression of the pseudo dielectric functions used to calculate the properties of a material in a first approximation.

However, in an advanced case where medium 1 has several transparent layers with different indexes N_i (for example a thin film and a substrate), the reflections at the interface between the layers should be considered. This will lead to several numbers of reflections, as illustrated in figure 7. At each crossing of the layer by the optical ray, the electric field accumulates a phase shift $\beta = \frac{4\pi d_1}{\lambda} N_1 \cos(\theta_1)$. As a result of the higher orders of reflection, the waves will modulate ψ and Δ with an interference pattern of frequency β depending on the thickness d_1 of the layer and its optical index N_1. Afterward, the thickness of the layer can be extracted from the distance between the interference fringes.

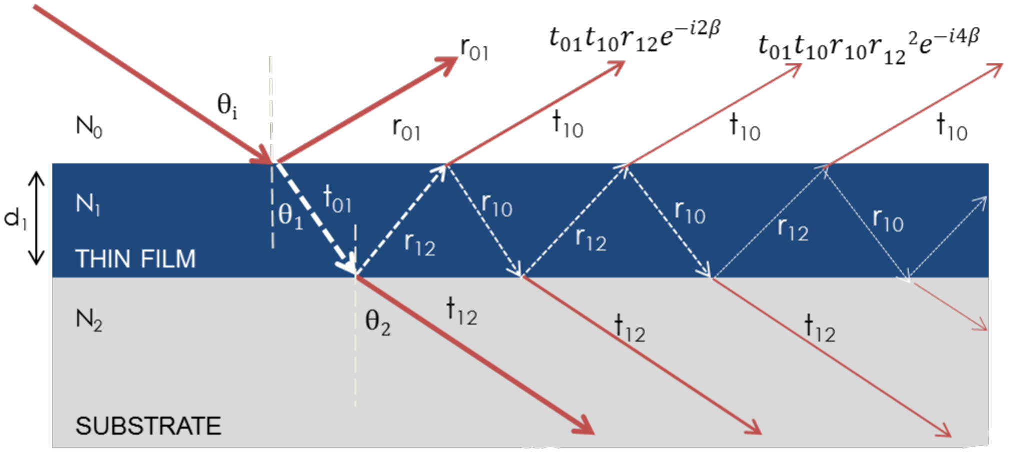

Figure 7: Schematic representation of optical interference at a sample surface-thin film and thin film-substrate interfaces, r corresponds to the reflection Fresnel coefficients while t to the transmission Fresnel coefficients. The subscripts denote the layers involved in the reflection. As the beam penetrates the material and reflects at the interface, it loses intensity and accumulates a phase shift of $e^{-i2\beta}$ at each reflection. The values d_1, N_1, N_2, and θ_1 correspond respectively to the thickness and refractive index of the first layer, the refractive index of the second layer, and the incident angle. Adapted from Ref. [22].

If one of the layers is anisotropic (e.g. birefringent), most of the assumptions in the calculation are no longer valid. [23]

In practice, the samples having complex structures and properties (such as anisotropy) as well as defaults (i.e. defects and impurities), require a model-based analysis to retrieve useful data. It stems from this that ellipsometry is a model-dependent technique. Later in this report (see section 4.1, the commonly used models will be presented with a particular emphasis on the models used in the context of this thesis.

2.3 Critical points (CP) theory

In this section, first, the origin of the dielectric functions is addressed, and then the critical point line-shape analysis of the dielectric functions.

2.3.1 Quantum theory of band-to-band transition

This section is based on ***Electronic States and Optical Transition in Solids*** *by Bassani, Parravicini and Ballinger.[24]*

The purpose of this section is to expose the connection between the quantum theory description of the crystal to its dielectric functions.

Here, only band-to-band transitions are considered. In the quantum theory framework, the energy of atoms in the crystal is defined by a many-body Hamiltonian. To facilitate the calculation, two approximations are often required. The Born-Oppenheimer approximation consists in considering that the electron cloud rearranges itself adiabatically around the nucleus. This approximation is based on the fact that nuclei mass is much heavier than electrons mass, thus the nuclei positions can be considered fixed compared to the electron motion. Additionally, the Hartree-Fock-Slater approximation can be applied to reduce the many-body Hamiltonian to a one-electron Hamiltonian in a crystal potential.

From the above approximations, a Hamiltonian H_0 can be built. Then, the action of the light on the crystal consists in adding a perturbation term $W(t)$ to the Hamiltonian $H = H_0 + W$. The perturbation, the electromagnetic field of a photon, interacts with the momentum $\vec{p}$ of the electron, and thus its kinetics and its spin, conducting to the Eq.(22):

$$\hat{W(t)} = \frac{e}{m}\hat{\vec{p}}.\hat{\vec{A}} + \frac{e}{m}\hat{\vec{S}}.\hat{\vec{B}} + \frac{e^2}{2m}\hat{\vec{A}}^2. \tag{22}$$

where m and e the mass and the charge of the electron, $\hat{\vec{A}}$ is the vector potential operator of electromagnetic field, $\hat{\vec{S}}$ the spin operator, $\hat{\vec{B}}$ the magnetic field operator. The potential vector describes the light emission and absorption of the crystal. Thus, $\vec{A}$ is divided into an absorption term and an emission term. In the following only the absorption is considered, the vector potential expression is then: $\vec{A} = A_0\vec{u}e^{i(\vec{q}.\vec{r}-\omega t)}$ for an electromagnetic field oscillating in the $\vec{u}$ direction and propagating in the $\vec{q}$ direction.

The electric dipole approximation can be applied when the wavelength at the origin of an electronic transition between two energy levels is much larger than the typical size of an atom. For UV-VIS light, λ is about 10^4 larger than the Bohr radius a_0, so the electric dipole approximation can be used here. Using the electric dipole approximation, the second and third terms in Eq.(22) can be neglected, and A reduces to the first term of its Taylor expansion. Thus, the perturbation reduces to:

$$\hat{W(t)} = \frac{e}{m}\hat{\vec{p}}.\hat{\vec{A}}. \tag{23}$$

Now, a transition between $|i\rangle$ an initial state in the full Valence band, and $|f\rangle$ a final state in the empty conduction band (i.e. a semiconductor at T = 0 K) is considered. Using the first order of the time-dependent perturbation theory, the probability of this transition is:

$$P_{if} = \frac{2\pi}{\hbar}|\left\langle f\middle|\hat{W(t)}\middle|i\right\rangle|^2 \tag{24}$$

Associating a spin s and a wave vector k to the electrons in each state (i.e. $|i\rangle = \psi^V_{k_i}\chi_{s_i}$ and $|f\rangle = \psi^C_{k_f}\chi_{s_f}$), and introducing Eq.(23) and $\vec{A}$ in the previous expression, the probability can be written as:

$$P_{if} = \frac{2\pi}{\hbar}\frac{eA_0}{mc}^2\delta_{s_i,s_f}|\left\langle\psi^C_{k_f}\middle|e^{i\vec{q}.\vec{r}}\vec{u}.\vec{p}\middle|\psi^V_{k_i}\right\rangle|^2\delta(E_f - E_i \pm \hbar\omega) \tag{25}$$

The first Dirac function states that the transition happens only if the electron has the same spin in the final and initial states. The second Dirac function embodies the fact that the absorption of a photon of frequency ω occurs only when the energy of the photon matches the energy difference between $|i\rangle$ and $|f\rangle$. In this term, $-\hbar\omega$ corresponds to an absorption and $+\hbar\omega$ to an emission.

The momentum operator is $\hat{\vec{p}} = -i\hbar\hat{\vec{\nabla}}$, which gives for the u-component $p_u = -i\hbar\frac{d}{du}$. To find the transition probability, one needs to diagonalize the matrix $\left\langle\psi^C_{k_f}\middle|e^{i\vec{q}.\vec{r}}\vec{u}.\vec{p}\middle|\psi^V_{k_i}\right\rangle$, which means that the determinant must be non-zero. This condition results in the conservation of momentum: $\vec{k_f} = \vec{k_i} + \vec{q} + \vec{g}$ where $\vec{g}$ is the reciprocal space lattice vector. As k_f and k_i are of the magnitude of $\frac{2\pi}{a_0}$, they are much larger than $q = \frac{2\pi}{\lambda}$, thus the electric dipole approximation can be applied. Considering, the first Brillouin zone (i.e. $g = 0$), the transition can be considered vertical:

$$\vec{k_f} = \vec{k_i} = \vec{k} \tag{26}$$

Then, the probability becomes:

$$P_{i\to f} = \frac{2\pi}{\hbar}\frac{eA_0}{mc}^2|M_{C,V}|^2\delta(E_C(k) - E_V(k) - \hbar\omega) \tag{27}$$

To find the transition rate $\mathcal{W}$, the probability must be integrated over all possible states in the 1st Brillouin zone (BZ) and sum over all bands, which gives:

$$\mathcal{W}(\omega) = \sum_{C,V}\int_{BZ}\frac{2dk}{(2\pi)^3}P_{if}(\omega) \tag{28}$$

In Eq.(28), the factor two in the integral accounts for the two spins of the electron (i.e. up and down). The transition rate corresponds to the number of transitions induced by the absorption of light oscillating at ω per second per unit volume in the reciprocal space. The final step is to make the link between the transition rate and the dielectric functions. The absorption coefficient formula is:

$$\alpha = \frac{2\kappa\omega}{c} = \frac{\omega}{nc}\varepsilon_2 \tag{29}$$

with n and κ the refraction index and the extinction coefficient of the crystal, which must not be mistaken with k the electron wave vector. The absorption coefficient is in essence the energy absorbed/s/unit volume over the energy flux:

$$\alpha(\omega) = \frac{\hbar\omega\mathcal{W}(\omega)}{uc/n} \tag{30}$$

with $u = \frac{n^2 A_0^2 \omega^2}{2\pi c}$ is the average energy density. Therefore, it is possible to connect the imaginary part of the dielectric function to the transition rate:

$$\varepsilon_2(\omega) = \frac{n^2\hbar\mathcal{W}(\omega)}{u} \tag{31}$$

Finally, the relation to the energy states of the transition is:

$$\varepsilon_2(\omega) = \frac{e^2 4\pi^2}{m^2\omega^2}\sum_{C,V}\int_{BZ}\frac{2dk}{(2\pi)^3}|M_{C,V}|^2\delta(E_C(k) - E_V(k) - \hbar\omega) \tag{32}$$

$\varepsilon_1(\omega)$ is then calculated via the Kramers-Kronig relations.

To go further, $\varepsilon_2(\omega)$ is proportional to the joint density of states (JDOS) as an electron-hole pair is considered. The JDOS between an empty state in CB and an occupied state in VB is:

$$J_{C,V} = \int_{BZ}\frac{2dk}{(2\pi)^3}\delta(E_C(k) - E_V(k) - \hbar\omega) \tag{33}$$

when considering $|M_{C,V}|^2$ is constant and setting it to 1. Using that:

$$\int_a^b g(x)\delta(f(x))dx = \sum_{x_0} g(x_0)(\frac{df}{dx})^{-1}|_{(x=x_0)} \tag{34}$$

with $f(x_0) = 0$. Then, Eq. (33) becomes:

$$J_{C,V} = \frac{2}{(2\pi)^3}\int_{E_C(k)-E_V(k)=E}\frac{dS}{\nabla[E_C(k) - E_V(k)]} \tag{35}$$

Where dS is an infinitesimal surface element of the curve $E_C(k) - E_V(k) = E$. From this expression, the JDOS presents interesting behavior when $\nabla[E_C(k) - E_V(k)] \to 0$. Each of these points is a singularity and makes the integral blows up. As explained in the next section, these points, called Van Hove singularities or critical points, correspond to positions of electronic transitions in k-space.

2.3.2 Critical points origin

Electronic interband transitions occur only for specific positions k (i.e. wave vector) in reciprocal space and coincide to critical points (CP) in the dielectric functions. The band structure of a material can be connected to the dielectric functions through the computation of the Schrodinger equation for a many-body system as seen previously. Those critical points correspond in the band structure to positions k where the valence band and the conduction band have parallel tangents. From the quantum mechanic point of view, the dielectric function is proportional to the joint density of states (JDOS):

$$\varepsilon(\omega) \propto J_{CV} = \frac{2}{(2\pi)^3} \int_{E_c(k)-E_v(k)=\hbar\omega} \frac{dS}{\nabla_k(E_c(k) - E_v(k))}. \tag{36}$$

For k where the energy difference is constant (i.e. derivative equal to zero), the denominator vanishes while the joint density of states blows up, thus increasing abruptly ε_2. Indeed, a high JDOS means that there are a large number of available states in the conduction band to promote electrons from the valence band to the conduction band, and the absorption coefficient increases. To find the critical points, the denominator of the JDOS is expanded in a Taylor series for $k << 1$ as follows:

$$E_c(k) - E_v(k) = E_g + \frac{\hbar^2}{2} \sum \frac{(k_i - k_{0,i})^2}{\mu_i} \tag{37}$$

where $i = x, y, z$ for each direction of the crystal and μ_i is the reduced inverse effective mass component in the i-direction and describes the curvature of the band in this direction. For an anisotropic material, k_i is different depending on the axis of the crystal, for a uniaxial material usually k_z is attributed to the c-axis (i.e. extraordinary) while k_x and k_y are attributed to the a axis (i.e. extraordinary). Thus, the surface of constant energy is an ellipsoid, whereas for an isotropic material, it is spherical. By inserting equation Eq.(37) in Eq.(36), the contribution of each axis of the crystal to the critical points is accessible. The number of non-zero μ_i gives the dimensionality d of the CP, while the sign of the μ_i gives the curvature. Four dimensionalities are accessible 3D, 2D, 1D, 0D. For 3D critical points, four kinds of critical points exist. If all μ_i are positive, then the critical point corresponds to a minimum and is denoted M_0. In the opposite case, the critical point is a maximum. When one or two μ_i are negative (respectively positive) the critical point is a saddle point (M_1,M_2).

A 0D critical point corresponds to the case where the conduction band and the valence band an almost flat, and describes the line-shape of an excitonic absorption. By computing the JDOS integral over the first Brillouin zone near the critical point, the following expression of the dielectric function is found for $d = 3, 1, 0$:

$$\varepsilon(\omega) = C - Ae^{i\phi}(\hbar\omega - E_0 + i\gamma)^n \tag{38}$$

where $n = d/2 - 1$, ϕ is a multiple of π and accounts for the different kinds of CP giving its symmetry [25], A the amplitude, E_0 the energy of the transition at the CP, γ the lifetime broadening and C a constant background.
For $d = 2$, $n = 0$, the expression Eq.(38) becomes:

$$\varepsilon(\omega) = C - Ae^{i\phi} ln(\hbar\omega - E_g + i\gamma) \tag{39}$$

The parameter that dominates the shape of the CP is phi. For 3D critical point, $\phi = 0, \frac{\pi}{2}, \frac{3\pi}{2}, \pi$ correspond respectively to M_1, M_2, M_0 and M_3 CP (when $A > 0$).[26] The energy gap always lies in between the two extrema of the second derivative but is nearly independent of l.

While around 20% of Γ depends on the dimensionality d. Indeed, the line-shapes are wider as the dimensionality increases.[27]. Figures 8, 9 and 10 show examples of the line-shape of respectively 3D, 2D and 0D critical points for various ϕ.

As Eq.(38) only considers the most resonant critical point, usually the derivative of the $\varepsilon(\omega)$ is calculated up to a certain order to reveal secondary CPs, and allows a more complete and relevant analysis of the dielectric functions. In the specific case of spectroscopic ellipsometry, the signal-to-noise ratio allows the derivation $\varepsilon(\omega)$ up to the second or third order. In practice, the expression Eq.(38) is used to fit the second-order numerical derivative, thus permitting the identification of the energy and type of the CPs. As differentiation often enhances noise, this method necessities to apply smoothing before fitting the second derivative. Usually, this is achieved with a linear filtering algorithm such as the Savitzky-Golay filter and then the parameters for each critical point are fitted by a least-squares regression. Another filtering method consists to calculate the Fourier Transform of the second derivative and remove the high-frequency contribution, which is most likely only noise. [28] In the present work, the CP analysis was performed thanks to a Matlab code written by a previous master's student of the group, Benjamin Roaldsson Hope.

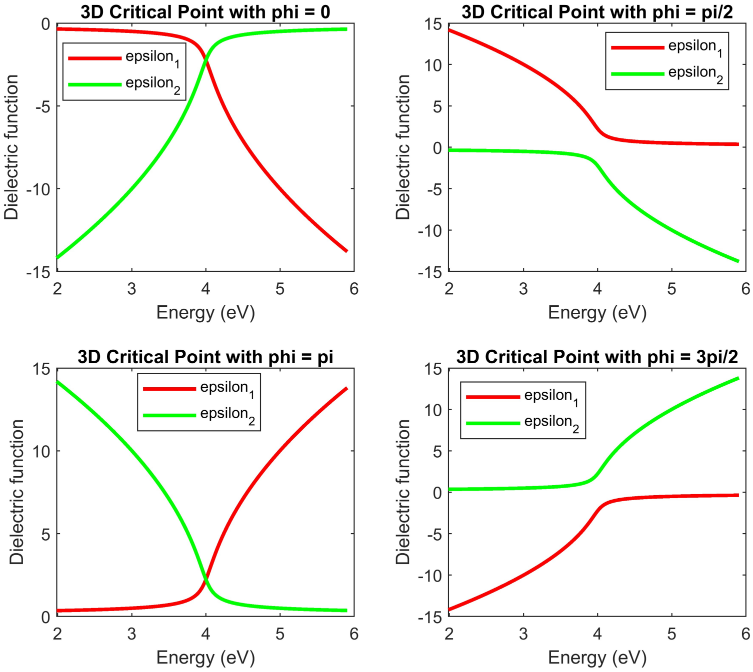

Figure 8: Shape of the 3D critical points ($n = 1/2$) for $\phi = 0, \pi, \frac{\pi}{2}, \frac{3\pi}{2}$, with the following parameters: A=10, $\Gamma = 0.1$, C=0 and $E_0 = 4eV$.

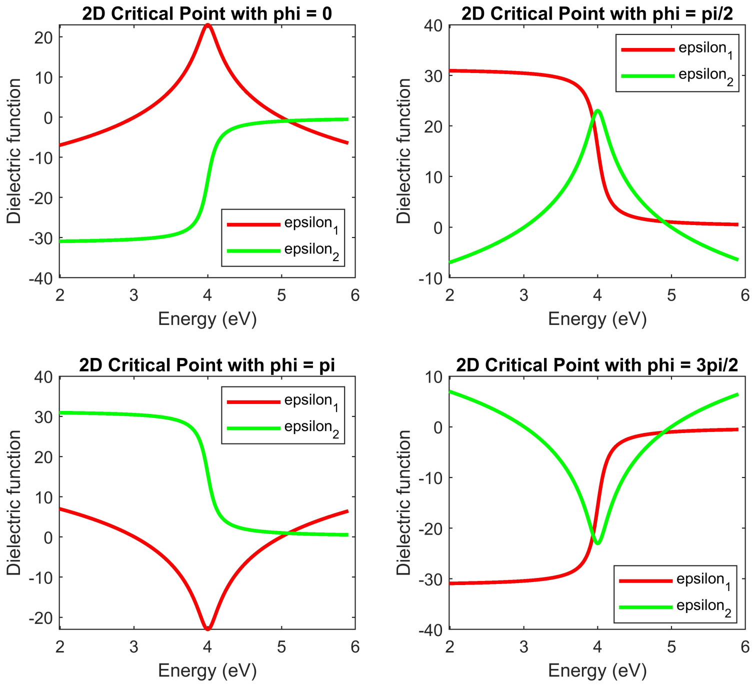

Figure 9: Shape of the 2D critical points ($n = 0$) for $\phi = 0, \pi, \frac{\pi}{2}, \frac{3\pi}{2}$ with the following parameters: A=10, $\Gamma = 0.1$, C=0 and $E_0 = 4eV$.

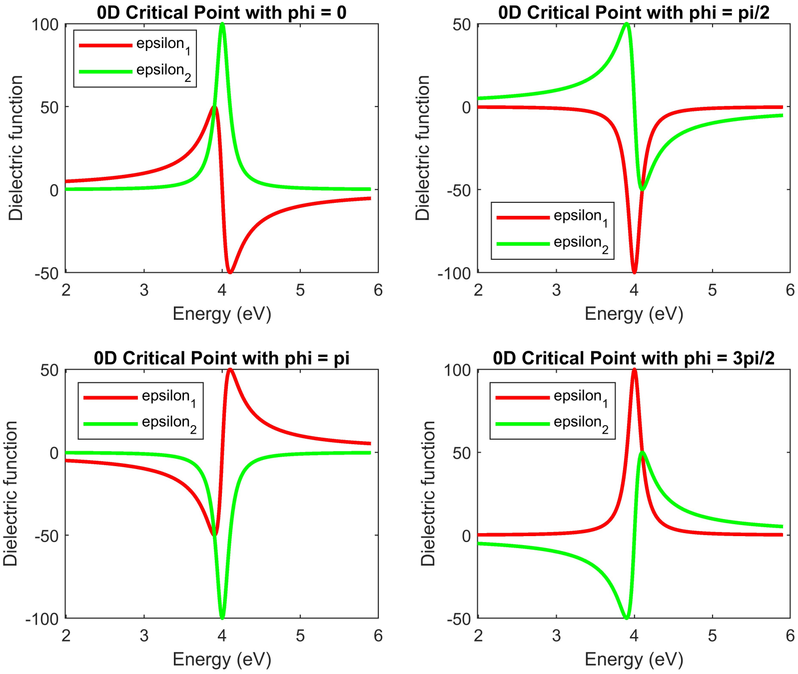

Figure 10: Shape of the 0D critical points ($n = -1$) for $\phi = 0, \pi, \frac{\pi}{2}, \frac{3\pi}{2}$ with the following parameters: A=10, $\Gamma = 0.1$, C=0 and $E_0 = 4eV$.

2.4 Photoluminescence spectroscopy (PL)

2.4.1 PL principle

Photoluminescence spectroscopy (PL) records the emission spectra of a material under optical excitation. Figure 11 shows the principle of PL. For semiconductor materials, upon an excitation, an electron-hole pair is formed. For the electron to be excited to the conduction band, the energy of the photon must be equal or larger than the bandgap. If the photon energy exceeds the bandgap, the electron usually relaxes to the conduction band edge. This intraband relaxation (also called thermalization) of electrons in the conduction band is on the picosecond scale. Next, if the electron and hole recombine radiatively, a photon of frequency associated with the energy of the transition between the initial and final state is emitted. Thus, PL spectroscopy is a useful measurement technique of energy gaps E_g of semiconductors. However, in practice defects or impurities in the semiconductor with energy levels inside the bandgap, will contribute to the spectra and must be considered during the analysis.

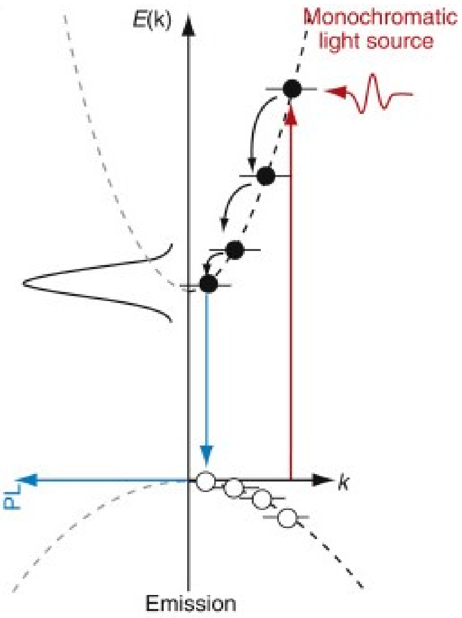

Figure 11: Schematic drawing of the emission process: under a monochromatic light beam, an exciton from the valence band is excited to the conduction band if the energy of the incoming photon is $\geq E_g$ (red arrow). The exciton loses its excess energy by relaxing first to the bottom of the conduction band (black arrows) and then by emitting a photon of energy $\sim E_g$ (blue arrow). The PL principle is based on the collection of this emission. Adapted from Ref. [29].

the emission of photons with energy below the band gap could show the existence of energy levels between the valence and conduction band and could open give insight into real-life intermediate band material, which is one of the goals of the Solar Cell Physics group. Nevertheless, a range of radiative phenomena can explain PL at lower energy than the bandgap and will be presented later in this report.

2.4.2 Mechanisms contributing to the PL spectrum

This section is essentially based on chapter 4, entitled "Mechanisms contributing to the PL spectrum" of the book "Spectroscopic Analysis for optoelectronic semiconductors" from Jimenez et al.[30]

For completeness, many processes are mentioned in this chapter. Not all are relevant for the samples studied.

Band-to-band transition

Depending on the thermalization in the conduction band, and the presence of impurities and/or defects in the sample, the excited electron can recombine radiatively through different pathways. After the thermalization, the most usual pathway is the PL emission from the bottom of the conduction band to the top of the valence band, so, at energies $\sim E_g$.

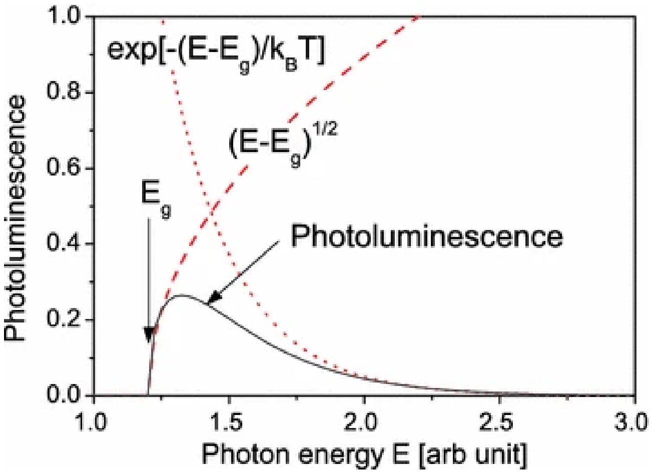

Figure 12: Characteristic shape of band-to-band PL of a semiconductor (black line). The red dashed line represents the electron density of states and the red dot line the occupation probability of he conduction band state. Taken from Ref.[31].

The shape of the PL spectra is defined by the density of states together with the occupation probability of those states, as illustrated in figure 12 in the most simple case. However, it is possible that emission processes, involving a different state not belonging to the conduction band or the valence band, add features to the spectra. On the other hand, if defects or impurities are present, the emission can occur at lower energy than E_g. These particular recombination mechanisms are described in the following, from the emission with the highest photon energy to the lowest.

Excitonic transitions

Excitons are electrons and holes bound together via Colomb interaction that lowers the energy of the pair. Thus, excitons are energetically more stable than free electrons and holes. Their energy levels have a similar structure to the hydrogen atoms:

$$E(n) = E_g - \frac{1}{n^2} E_{ex} \tag{40}$$

where E_{ex} is the binding energy of the electron with the hole. The first state is located at $E_g - E_{ex}$ and then the other states are in between this limit and E_g.

Different types of excitons are described in the literature:

- Wannier-Mott exciton: correspond to weakly bound excitons, whose energy levels are described by the Wannier-Mott equation. This type of exciton usually occurs in materials with a high dielectric constant which screens the Coulomb interaction inside the exciton. Thus, the electron and hole in the Wannier-Mott excitons have delocalized wave-functions, which leads them to be designated also by the terms "large radii excitons" or "free excitons". Indeed, they can move apart from each other over several lattice constants. [32]. When these excitons are excited in one of their energy levels $n > 1$ from the expression Eq.(40), they can later deexcite radiatively. As their energy levels are below the conduction band edge, because of their binding energy, the emission occurs at photon energies lower than E_g. This process is called free exciton emission and is usually denoted with an X.

- Frenkel exciton: are forming in material with low dielectric constant, where the Coulomb interaction between the electron and hole is strong. Due to the strong attraction between the electron and hole, their respective wave-functions are localized and the Frenkel exciton radii is small. Because of their higher binding energy, their energy levels are lower than the Wannier-Mott exciton, and thus they emit at longer wavelengths.
- Self-trapped exciton (STE): A polaron is a quasi-particle consisting of a conduction electron or a valence hole (i.e. a free carrier) together with its self-induced polarization of the crystal lattice. Like polarons, excitons can induce a distortion of the lattice around them. Then, when the coupling between electrons (respectively holes) and the crystal lattice is strong, the exciton can be self-trapped by the induced distortion. These excitons have states deeper in the bandgap than the free excitons because of their strong attractive interaction with the lattice, thus leading to emissions far below E_g. [33]

Defects and impurities related transitions

Similar to excitons, free electrons and holes can also be trapped by defects in the lattice, which results in a type of "ionization". Then, the energy of the transition corresponds to the band-gap energy minus the ionization energy (in a similar way to the binding energy of the excitons). From this phenomenon, we differentiate two types of defects:

- Shallow defects: are small perturbations (usually substitutional atoms) that affect the lattice potential by a weak Coulomb interaction similar to the Hydrogen atom model. Due to the screening of the potential by the other electrons of the lattice, the electron is loosely bound to the defect-ion and its wave-function extends over several lattice constants. The electron sees the periodic potential of the lattice and then its motion can be described by the effective mass approximation in a similar way to the Wannier-Mott excitons. Thus, to describe the energy potential felt by a weakly bound electron around the shallow defect, the Coulomb potential can be used by substituting the electron mass with an effective mass μ.[34]

- Deep level defects: can be compared to ”localized defects” in a similar way to the Frenkel excitons. In this case, the perturbation induced by the defect ion is much larger and the resulting Coulomb interaction is more localized than for shallow defects. This type of potential is usually created by interstitial atoms or vacancies coupled with some lattice distortion. Thus, both the lattice relaxation (i.e. the energy needed for the rearrangement of the atoms in the lattice) and the Coulomb interaction affect the potential of the trapped electron. Unlike their name could suggest, deep levels defects are not necessarily located in the middle of the bandgap. Nevertheless, when they are near the middle, they can trap either an electron or a hole and act as recombination centers (i.e. Shockley-Reed-Hall recombination).
- Acceptors and donors: correspond to the case where the semiconductors are doped (N or P type).

2.4.3 Color centers

Color centers, also called luminescence centers, are optically active defects or impurities in the lattice of the host crystal. When these defects are oxygen vacancies with one or two unpaired electrons, they are called F centers. The F comes from Farber, the German word for color. As they have their own energy levels, they act as a single atom or molecule inside the lattice, it is the reason why the Franck-Condon principle, described below, can be applied to them. Thus, the coupling between the phonon modes of the crystal with the electronic states of impurity or defect, instead of the coupling of the vibrational states of the molecule and its electronic states. If the color centers are present in the lattice in high density, they can cause substantial absorption and emission of light at photon energies below the bandgap. The effect of the color centers can be described as introducing additional levels in the energy level diagram, which lie between the conduction and valence band. Thus, photons with sub-bandgap energies can participate in processes. As a result of these additional states, some naturally transparent crystals, such as TiO_2, can exhibit pronounced colors.

The Franck-Condon principle states that the optical transition is vertical, because of the slower motion of the nucleus of an atom compared to its electrons, which are much lighter. The electron-phonon interaction couples phonon states with the excited and ground states of the defect, allowing a series of absorption and emission transitions. The green wave-functions in figure 13 represent the phonon energy levels of the color centers, the parabolas represent the electronic states of the defect, which can be considered as a single atom.

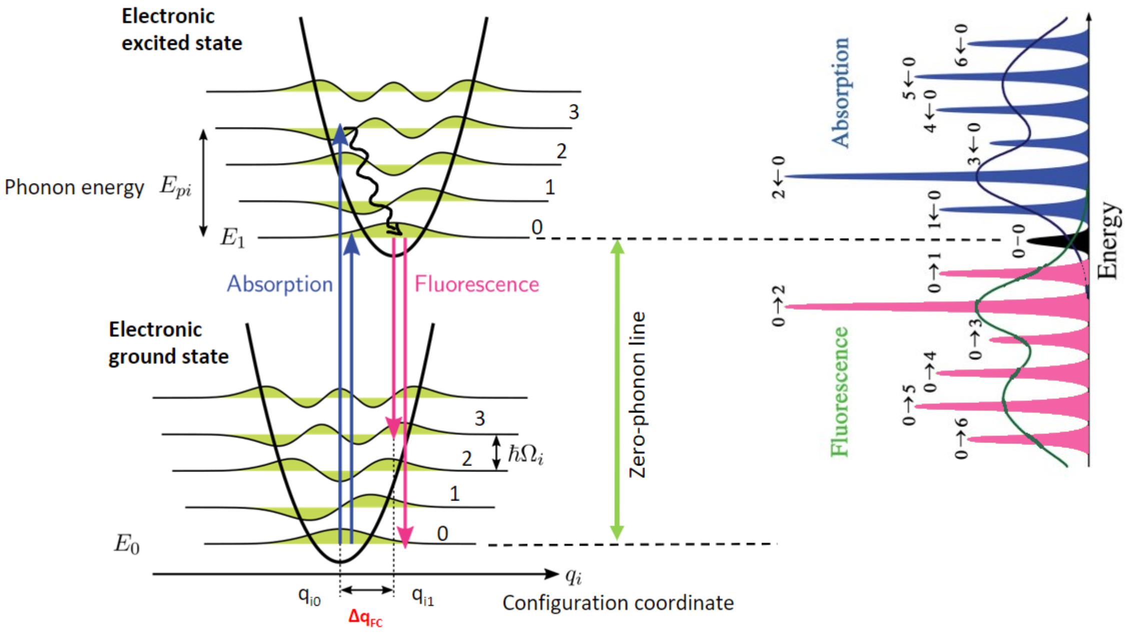

Figure 13: (Left) Schematic drawing of the Franck-Condon absorption and emission processes in the case of an electron-phonon coupling due to the presence of color centers in the crystal lattice. (Right) Line-shape of the absorption and emission spectra, which are mirror images of each other. The zero-phonon line in black has a Lorentzian shape with a width determined by the excited state lifetime. Adapted from Ref.[35].

As the Frank-Condon principle considers instantaneous transitions, when a photon is absorbed the transition must be compatible with the new average position of the nucleus of the defect in the crystal. Indeed, the average position of the defect (i.e. configuration coordinate) is different in the excited state. The configuration coordinate is related to the average distance between the defect and the cage of the neighboring ions.[36] The difference between the minima of the ground states and the excited states is called Δq_{FC}.

If a photon of energy larger than the energy $E_1 - E_0$ (see figure 13) is absorbed, an electron is promoted to the electronic excited state and might reach one of the vibronic levels. Then, the electron can relax to the bottom of the excited state by creating phonons and finally return to the ground state by emitting a photon.

As the vibrational levels are the same in the excited band and ground state, the emission and absorption spectra are mirror images of each other, the mirror plan corresponding to the ZPL. The zero phonon line (ZPL) corresponds to the transition between the minimum of the electronic excited state to the ground state (i.e. $E_1 - E_0$): no phonons are involved. The resulting PL consists of a series of Lorentzian line-shapes, each one corresponding to one transition between a vibrational level in the excited state and one in the ground state of the defect. Because of the relaxation in the electronic excited state, the emission occurs at lower energies than the absorption. This redshift is called the Stokes Shift.

At low temperatures, the fine structure of the transitions between the phonon levels is visible. In the low-temperature approximation, emission transitions occur from the zero-phonon level of the excited state to the zero-phonon level of the ground state or to higher phonon levels of the ground state, as there is little thermal occupation of the other phonon modes. To find the relative intensity of the peak, one can apply the Franck–Condon principle and calculate the Franck-Condon overlap factor F_n^m. This factor contains the probability of transitions involving phonons which is determined by the overlap of the wavefunctions of the initial and final energy states: ψ_n and ψ_m. In addition to the Franck-Condon assumption, two other approximations are assumed. The first approximation is that each lattice vibrational mode is well described by a quantum harmonic oscillator model. The second approximation is that the interaction between the color center and the lattice is the same in both the ground and the excited state. Finally, the following expression can be found, where S is the Huang-Rhys dimensionless parameter, a well-defined function of the shift in configuration coordinate corresponding to the Stokes shift between the absorption and emission, and $L_m^{n-m}(S)$ are the General Laguerre polynomials. n is the quantum number of the vibrational final state, so the ground states for an emission process, and m of the vibrational initial state in the excited band.

$$F_n^m = |\int \psi_n^* \psi_m|^2 = e^{-S} S^{m-n} \frac{m!}{n!} (L_m^{n-m}(S))^2 e^{-m\frac{\hbar\omega_p}{k_B T}} \tag{41}$$

The last term, the Boltzmann term, takes into account the thermal occupation of the excited states in the initial state when the temperature is high enough. $\hbar\omega_p$ is the energy of the phonon involved in the transition.

2.4.4 PL of TiO_2 in literature

This section presents a literature review of the PL of TiO_2.

TiO_2, a transition metal oxides

Transition metal oxides (TMOs) are well-known to have interesting properties, such as a wide bandgap, a high dielectric constant, or ferromagnetism, due to their partially filled 3d-orbitals for the cation. The filling of these orbitals with electrons gives rise to a range of materials with properties from insulating to metallic. At the TMO range edges, TiO_2 with its empty $3d^0$ orbitals acts as a N-type semiconductor, while Cu_2O with its $3d^{10}$ electronic configuration behaves as a P-type semiconductor.[37]

To understand to what extent (defect and impurities free) TMOs have a specific behavior, one can take a look at their energy diagram in the ligand field theory. The ligand field theory is based on a molecular orbital approach. In this theory, the energy levels of the TMO are determined by linear combinations of atomic orbitals, predominantly of metal 3d-orbitals and oxygen 2p-orbitals. Therefore, the degeneracy of metal 3d-states is lifted resulting in a complex energy diagram.[38] The molecular orbital diagram of TiO_2 is shown in figure 14 a).

TiO_2 has an octahedral structure in the Bravais lattice cell where six oxygen atoms are bound to each titanium atom, forming $Ti^{+4}O_2$ complexes. The electronic structure of titanium is [Ar] $3d^2 4s^2$. Thus, even if the metal 3d orbitals are involved in the energy diagram, the Ti^{+4} cation has no valence electron to participate in the bonds. The hybridized orbitals of the complex are exclusively filled by electrons from oxygen atoms. For this reason, the occupied valence band is said to have an oxygen 2p-orbitals character, as these orbitals are mostly involved in the bond, while the unoccupied conduction band has mainly a Ti 3d-orbital character.[39, 40] Thus, if an electron is trapped in the crystal, it is most likely the Ti^{+4} cation that will trap it. This has been seen in calculations of the density of states projected for certain orbitals, as displayed in figure 14 b).

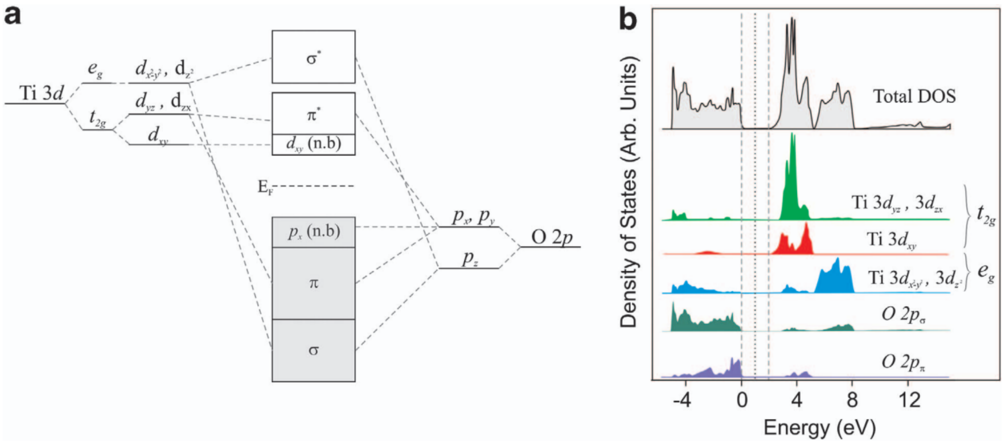

Figure 14: a) Energy diagram of the molecular orbitals of the $Ti^{+4}O_2$ complexes in TiO_2 crystals, the hybridization of 3d-orbitals of the titanium cation with 2p-orbitals of the oxygen atoms, b) Projection of the density of states (DOS) of TiO_2 for the different orbitals: 3d and 2p. Taken from Ref. [39], and previously adapted from a) Ref. [41] and b) Ref. [42].

As a result, TiO_2 has a large number of empty 3d-orbitals likely to accept free electrons or to bind to impurities. Also, the TiO_2 that is manufactured is subject to oxygen vacancies, leading to O_2 adsorption at its surface which can have a strong influence on the PL spectra.[43] Thus, the numerous energy levels resulting from combinations of oxygen and titanium orbitals complicate the behavior of TiO_2, especially when it comes to interactions with for example excitons or impurities. Even if TiO_2 is widely studied, the origins of its optical and electrical behaviors are still not fully understood.

PL of anatase in literature

In literature, only a few examples of PL on single crystals TiO_2 are available. Figures 15, 16, and 17 show examples of anatase and rutile PL that can be found in the literature. For anatase, a broad band below 3 eV with a maximal intensity between 2.0 eV and 2.5 eV is reported at low temperature by Sekiya et al. [44], Gallart et al. [45], Tang et al. [46] and Watanabe and Hayashi [47]. The four papers assign the band principally to STE (see section 2.4.2 for an explanation the STE). According to Toyozawa theory of self-localization, the longer inter-ionic distances Ti-Ti in anatase are in favor of STE formation. [48, 49, 50]

Anatase single crystal PL was also reported at RT, with a band slightly shifted towards higher energies. Tang et al. observed a shift of 0.2 eV between 300K and 5K, with a peak centered at 2.5 eV. An Urbach tail assigned to shallow states was also noticed by the group. Similar data were presented by Yamada and Kanemitsu.[51] However, they excluded the possibility of emissions from exciton states due to the high dielectric constant of the TiO_2 and the small exciton binding energy, and attributed the emission band to band-to-band recombination. An RT emission band centered at 2.5 eV is also measured in TiO_2 anatase thin film by Jin et al. [52] (on Si substrate) and by Pallotti et al. [49]. Both articles attribute the emission to STE and support Tang et al. interpretation of a tail due to shallow states, originating either from trap states or from surface states linked to oxygen vacancies.

This last interpretation should be nuanced, surface states and defect are mostly reported in works about TiO_2 nanoparticles, where the effect of the surface area is not negligible. For single crystals, as the incident light penetrates the bulk, the effect of the surface states on the photoluminescence seem likely to be lower. [45]

In an article, Choudhury and Choudhury investigated the effect of defects on the PL spectra.[53] For that, they created defective anatase samples with oxygen defects to induce absorption in the visible range. Two nanoparticle samples, referred to as TV200 and TA450, were prepared by Sol-Gel method and annealed in vacuum and air at 200° and 450° respectively. Through XRD, their predominant crystalline phase was verified to be anatase. Although, their different annealing conditions, the samples presented the same type of defects and thus were fitted in the same way. Four different types of defects were reported in the article: self-trapped excitons (STE) at 2.86 eV (anatase bulk), oxygen defects at 2.30 eV and 2.67 eV, and charge transfer from Ti^{3+} to TiO_6^{2-} at 2.52 eV. Finally, the peak at 3.19 eV was attributed to the phonon-assisted indirect transition from M to Γ in the first Brillouin zone of anatase TiO_2. Each contribution was fitted with a Gaussian distribution, whose area gives an idea of the proportion of the defect in the samples. This article was used to fit the anatase spectra in section 5.3.

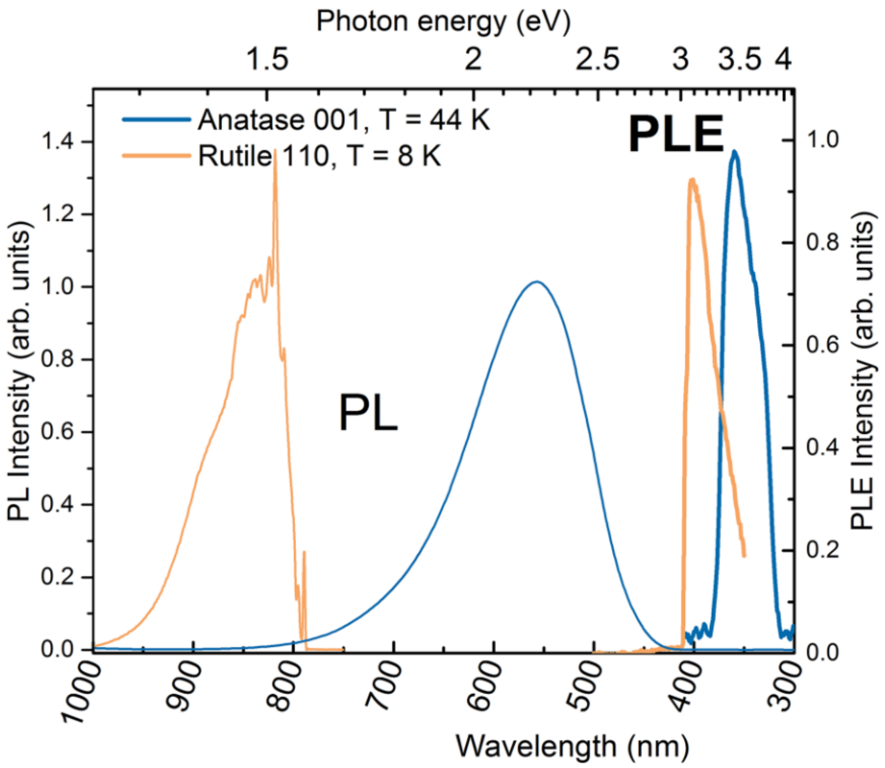

Figure 15: PL and PLE spectra of rutile and anatase single crystals at low temperature under 325 nm excitation from Gallart et al. Taken from Ref.[45].

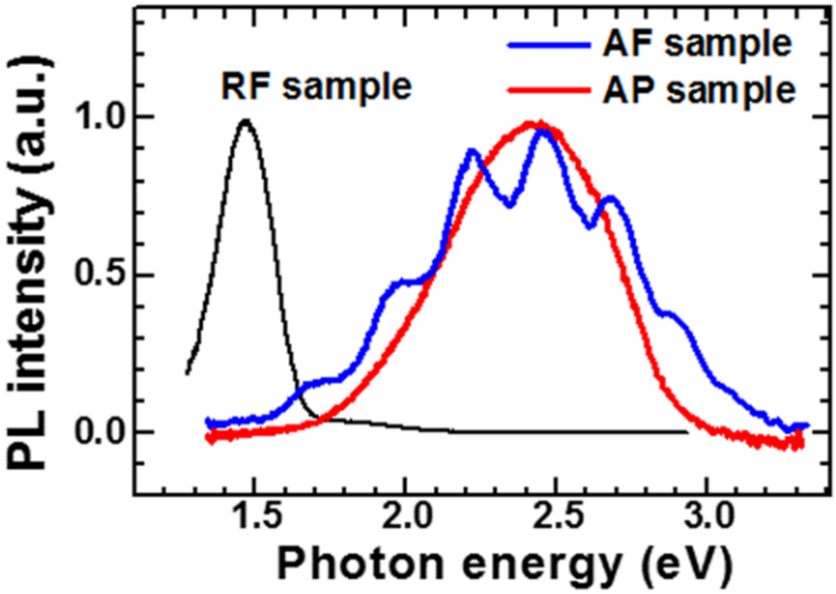

Figure 16: PL spectra of rutile thin film (RF) and anatase thin film (AF) and pellet (AP) at room temperature under 325 nm excitation from Pallotti et al. Adapted from Ref.[49].

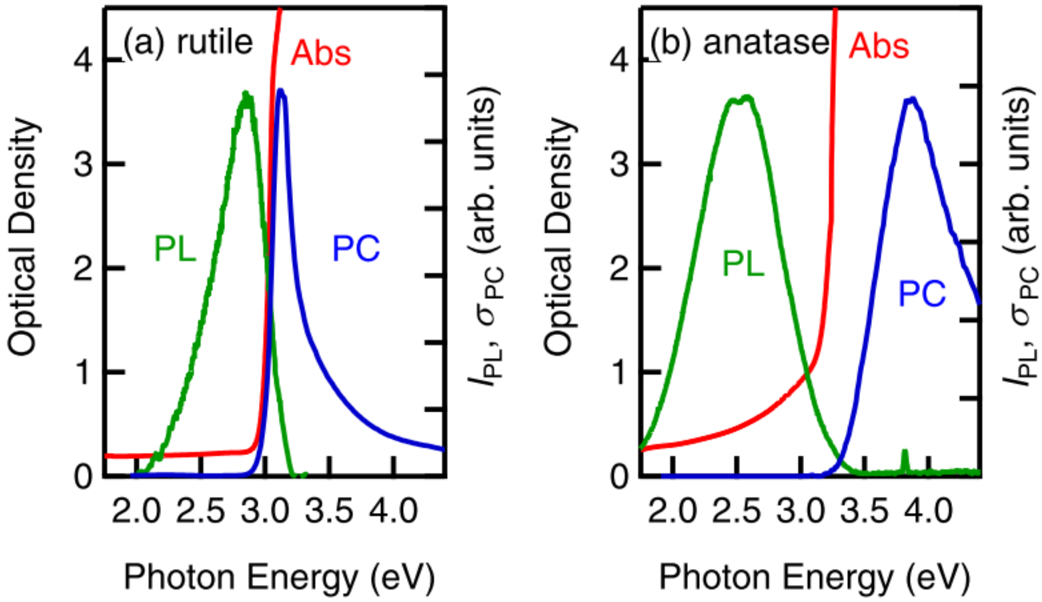

Figure 17: PL and PC (Photoconductivity) spectra of rutile (left) and anatase (right) single crystal (001)-oriented at room temperature under 3.5 eV (354 nm) excitation from Yamada and Kanemitsu. Taken from Ref. [51].

PL of rutile in literature

The literature reports for rutile either a sub-bandgap band similar to anatase PL, as illustrated in figures 15, 16, and 17, or a mid-bandgap band centered around 1.52 eV. The first band is split into two contributions: a band-to-band transition near 3.0 eV and a sub-bandgap contribution. The latter is often attributed to oxygen defects that create shallow states just below the conduction band. While the second band is related to deep levels inside the forbidden bandgap.

The PL of the rutile single crystals shows a weak sub-bandgap photoluminescence around [2.0, 3.2] eV. This band was detected only under strong pulse laser excitation for Yamada and Kanemitsu [51], and only after plasma treatment for Tariq et al. [54] (at RT). In the later article, the plasma treatment was believed to induce oxygen vacancies at the sample surface. Moreover, the PL in this energy region seems to be enhanced for nanocrystal rutile samples.[55, 56, 57] For example, Kernazhitsky et al. measured poly-dispersed nanostructured rutile at RT and attributed the sub-bandgap PL to excitonic peaks.[56] Takci attributed the PL of rutile nanoflowers to free exciton recombinations in the presence of oxygen vacancies. The PL enhancement could be explained by the higher surface-to-bulk ratio of nanocrystal samples, as they have a higher proportion of surface states and thus are more likely to present surface defects and impurities. Indeed, it has been demonstrated that TiO_2 can adsorbed species at its surface under certain conditions.[43]

The band centered at 1.52 eV (i.e. NIR band) is reported for single crystals [45, 49], thin films [52], and for annealed rutile powder [58, 59]. All papers agree that the band originates from a mid-bandgap state due to defects or impurities, however, the origin of the state differs from one article to another. On one hand, Pallotti et al. attribute the emission to electron-hole recombination, i.e. from an electron trapped in the deep midgap state with a valence hole.[49] While Jin et al. ascribe the PL to the complementary transition: the recombination of an electron in the conduction band with a hole trapped in the deep level.[**jin**] On the other hand Gallart et al., Montoncello et al. and Krivobok et al. associate the band with the presence of luminescent centers (i.e. color centers).[45, 58, 59]

For Gallart et al., the line-shape of the band originates from self-trapped exciton related to oxygen vacancies, while Montoncello et al. mentions the ionization of oxygen vacancies, and Krivobok et al. suggests intra-center transitions (i.e. d-d orbitals transitions) between vanadium impurities and titanium ions.[45, 58, 59] Figure 18 shows examples of the PL band at 1.52 eV attributed to color centers.

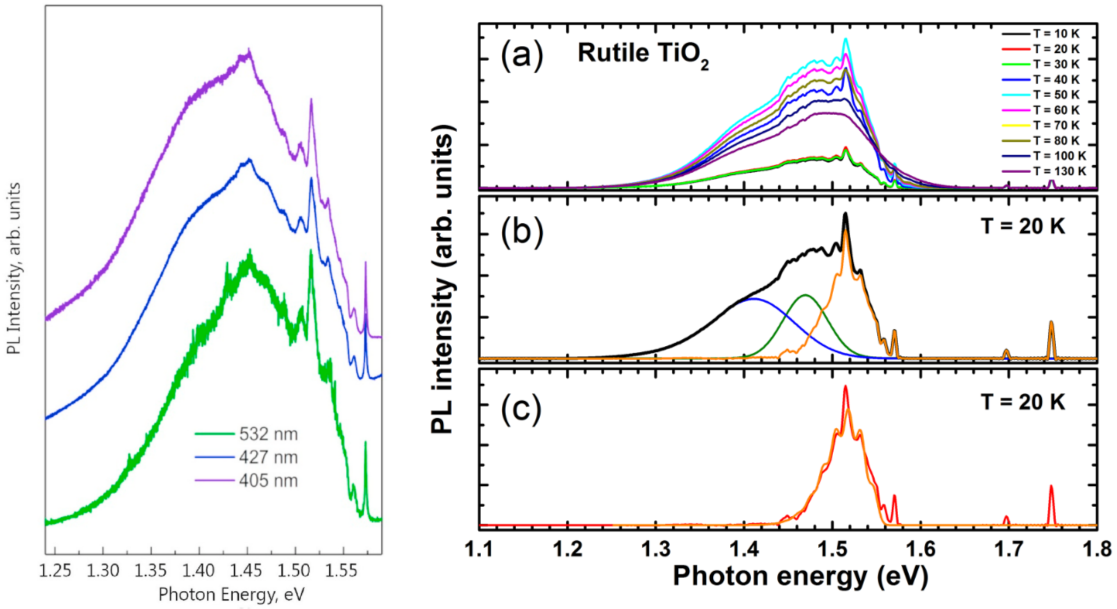

Figure 18: Near-IR PL spectra of rutile powder at 5K under three different excitations from Krivobok et al.(left), and of rutile single crystals under 325 nm excitation (right): a) at different temperatures, b) with the decomposition of the PL into bands at 20K, c) with a Franck-Condon simulation (dark orange) from Gallart et al. Taken from Ref. [59, 45].

2.4.5 PL of $SrTiO_3$ (STO) in literature

For completeness, a literature review of the PL of STO is presented here. The purpose of this review is to have an idea of what STO PL looks like in order to analyze later the PL of the undoped TiO_2 thin films grown STO substrate.

STO has an indirect bandgap at 3.25 eV, close to the anatase bandgap, as well as a direct bandgap at 3.75 eV. [60] Photoluminescence of STO occurs mainly in the visible region, depending on the measurement conditions either a green luminescence (GL) or a blue luminescence (BL) is reported, with sometimes a particularly intense UV near band edge (NBE) PL. The NBE is mostly attributed to band-to-band recombinations, and the GL and BL to defects, self-trapped holes (STH) or electrons (STE).

Yalishev et al. [61] and Yamada and Kanemitsu [62] measured a UV-NBE band in their Nb-doped STO samples, and attribute it to phonon-assisted indirect band-to-band recombination. In addition, Yalishev et al. recorded also a BL band between 2.1 eV and 3.0 eV, centered at 2.6 eV, which was associated with the electron doping in the bulk of the sample, whereas they related the NBE band to the presence of surface states.

Dadgostar et al. measured the PL of Nb-doped STO and undoped STO samples, as illlustrated in figure 19.[63] Their PL spectrum at 80K (λ_{exc} = 325 nm) shows a broad GL centered 2.4 eV, an NBE band at 3.25 eV as in [61], and a small a structured IR band (SIR) in the range [1.4, 1.6] eV.Zhang et al. reported that the dominant defects are oxygen vacancies (OV) near the surface, and then Ti interstitial defects in the bulk.[64] Based on this article, Dadgostar et al. interprets the GL band as being either from self-trapped holes (STH) by O^- of the oxygen vacancies or from STE originating from Ti interstitials.

Yamada and Kanemitsu reported the same GL band and the NBE emission at 8K in undoped STO single crystals annealed under oxygen flow to reduce the OV density, as illustrated in figure 20.[65] In addition they measured a BL at 300K centered at 2.8 eV. According to them, the GL is most likely due to impurities centers rather than STE, while the NBE corresponds as before to band-to-band electron-hole recombinations involving phonons.

Few articles mention the study of TiO$_2$ thin films on STO substrate. Li et al. measured TiO$_2$-SrTiO$_3$ thin film (1:1 proportion).[66] Kamei et al. studied anatase TiO$_2$ thin film on STO (001) single crystal.[67] In both cases, a broad blue-green band is reported, either centered at 2.57eV [66] or at 2.25eV [67].

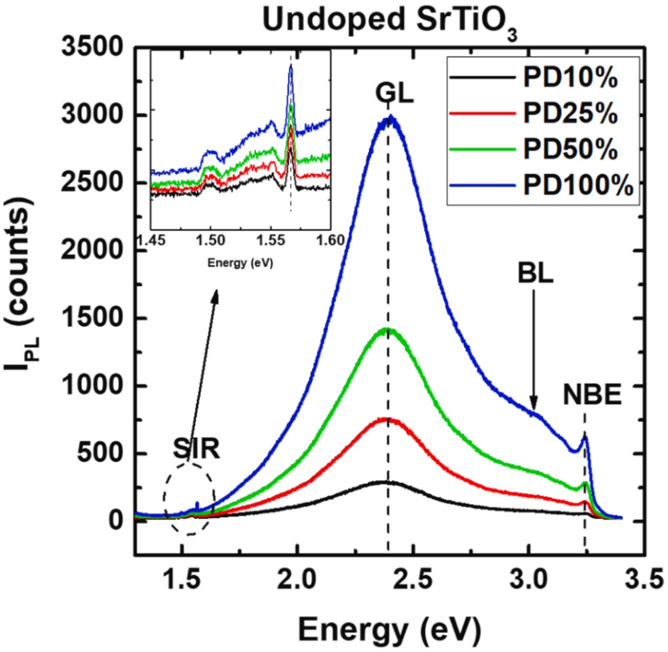

Figure 19: PL spectrum of STO from Dadgostar et al. Taken from Ref. [63].

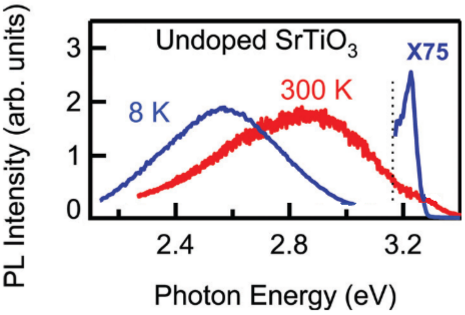

Figure 20: PL spectrum of STO at 8K and 300K from Yamada and Kanemitsu. Taken from Ref. [65].

3 Experimental Details

In this section, the TiO_2 samples characterized in this thesis by photoluminescence spectroscopy and spectroscopic ellipsometry in this thesis, as well as the photoluminescence setup and experiments are presented.

3.1 Samples

The final goal of the Solar Cell Physics group is to characterize (Cr,N)-co-doped TiO_2. Before the doped samples can be studied, it is first necessary to understand the origin of the properties and the behavior of the undoped matrix material. This is the reason why this thesis focuses firstly on TiO_2 single crystals, and secondly on the characterization of undoped thin films. The idea is to later be able to characterize the doped thin films and thus, to tune their intermediate band characteristics and to evaluate their performance.

Single crystal reference samples

The single crystals were purchased at MTI® corporation. TiO_2 anatase (110)-oriented single crystal is a natural crystal, one side polished of size 5mm x 5mm x 0.5mm and is very brittle. TiO_2 single crystals are expected to be transparent in the visible because of the large bandgap of TiO_2 (3.00 - 3.20 eV). However, in figure 21, the orange and black coloration of the sample is a visible sign of absorption in the visible region and of the natural origin of the sample. Defects or impurities, also called color centers, are responsible for the coloration of the sample. In an article from Yang et al., the visual aspect of anatase nanocrystal powder is related to the presence of oxygen vacancies.[68] This type of defect leads to a blue appearance, while oxygen vacancies filled with hydrogen atom turns the sample color into red.[69] In addition, anatase is reported to have two growth habits in a natural environment: the first one gives rise to an octahedral crystal shape with an indigo-blue-black color, and the second one to pyramidal faces with a honey-yellow-brown color. From its color and size aspect, the anatase (110) sample seems to originate from this second type.

The rutile samples are 10 mm x 10 mm x 0.5 mm one side polished single crystals oriented in the (110) and (001) direction, perfectly transparent (although slightly yellow), and grown by float zone method (i.e. crucible-free crystal growth).

The undoped TiO_2 thin films studied here are the ones of the so-called A and B series studied in the master thesis of Marcus Michaelsen, and deposited using pulsed laser deposition by PhD student Thomas Brakstad and Marina Jorge.

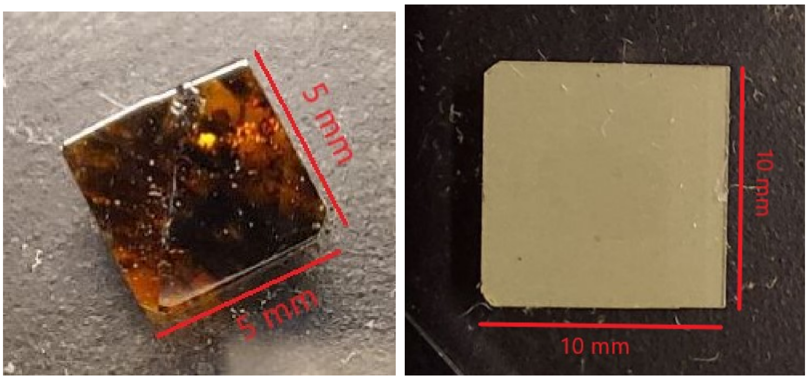

Figure 21: Photo of (110)-oriented anatase (left) and (110)-oriented rutile (right) single crystal samples.

Pulsed Laser Deposition (PLD)

TiO_2 thin films were prepared by pulsed laser deposition (PLD) in the group. Pulsed laser deposition is a physical vapor deposition technique, well-known to be suitable for thin-film growth. The technique was first invented by H·W Smith and A.F Turner in 1965, however, it is only thanks to Dijkkamp et al., in 1987 that the potential of the PLD technique was revealed, especially the production of high-quality thin film with very high purity.[70] A great variety of target materials is compatible with PLD; metallic material as well as semiconductors, ceramic layers, or oxides, thus allowing growth of films for numerous applications. The technique is based on laser-matter interaction. A high-energy laser beam hits a target. As the laser beam damages the surface structure of the target, breaking bounds, the target evaporates in the form of a plasma plume. The plasma then condenses on an adequate substrate placed in front of the target. For each laser pulse (femtosecond to nanosecond), a new thin layer is created on the substrate, where the atoms arrange on the substrate. The process takes place in a vacuum chamber to avoid any contamination from other species. The controlled environment of the chamber is primordial to ensure the purity as well as the desired design of the sample. Several chamber parameters can be adjusted: the temperature of the substrate, the laser fluence, the pressure in the chamber, and the gas flow. Ultra-light vacuum can be used to create high-purity thin films. Nevertheless, passive (Ar, N, etc...) or active gas are also interesting to build a specific material. For example, an oxygen atmosphere is usually used to create transition metal oxide thin films. In Figure 22, the TiO_2 target is vaporized by the laser in an O_2 atmosphere and forms a plume of Ti^+ and O^- ions and TiO_2 molecules. The presence O_2 atmosphere might help to fill the possible vacancies in the structure during the deposition.

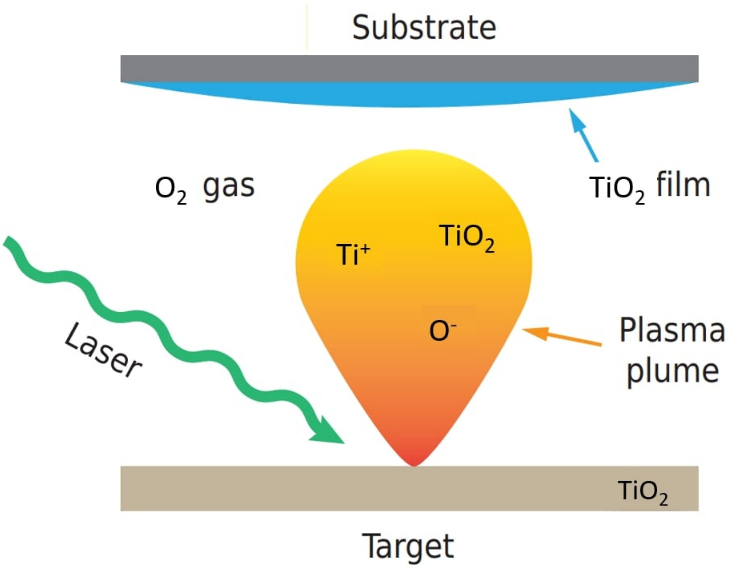

Figure 22: Principle of pulsed laser deposition of a TiO_2 thin film. Adapted from Marcus Michaelsen master's thesis.

As the plume is inhomogeneous due to its shape, the deposition is non-uniform on the substrate; more material is deposited at the center of the plume than at the edges. This is the main drawback of PLD when making flat thin films.

A and B series

The A and B series were made by previous PhD students in the group, Marina Rodrigues Jorge and Thomas Brakstad. These series consist of uniform undoped TiO_2 thin film samples prepared through PLD with varying parameters in order to change the film properties (pressure, O_2 and Ar flow, laser fluence). The table below presents the growth conditions of TiO_2 in the A and B series.

Table 1: Growth conditions of the A and B series samples studied in this thesis. Reproduced from Marcus Michaelsen master's thesis.

Sample label	O_2 (seem)	Ar (seem)	P_{dep} (mbar)	Laser Fluence (J/cm^2)	T_s (°C)	Thickness (nm)
A2	50	0	2.7×10^{-2}	2.0	700	229
B3	2	98	1.2×10^{-2}			667
B5	100	0	1.7×10^{-2}			687

Growing different materials on top of each other creates a boundary region where the two materials meet. If the lattice constants and crystal structures are different enough, the mismatching can cause strain, thus could lead to cracks or dislocations that propagate through the structure.

The A and B series were implanted on different substrates: silicon (Si), lanthanum aluminate (LAO), strontium titanate (STO), and sapphire (SPA). To establish the crystallinity of the A and B series, a previous master student, Marcus Michaelsen, determined the crystal phase of the thin films using XRD ($\theta - 2\theta$ diffractograms) and grazing incidence X-ray diffraction

(GIXRD). He found that the films on STO and LAO were more anatase-like, whereas the SAP samples were more rutile-like, which agrees with the article in the literature. The following table summarizes the results found by Marcus Michaelsen for the films on silicon, LAO, and STO substrates.

Table 2: Table of the crystal phase measured with XRD of A and B series samples studied in this thesis. Adapted by Joseba Ormaetxea from Marcus Michaelsen Thesis.

	Si (110)	LAO	STO	SAP
A2	Anatase; (001) and (112) preferred directions, and rutile with (100) preferred orientation.	Highly textured (001)-oriented anatase, with traits resembling that of epitaxial growth.	(001) textured anatase with some rutile grains.	Rutile (100) of considerably high crystalline quality.
B3	Rutile, with (100) preferred orientation.	(001)-oriented anatase, and a weak polycrystalline (100) rutile pattern.	(001) textured anatase with some rutile grains	Rutile (100) of considerably high crystalline quality.
B5	Anatase, with (004) and (112) preferred orientation. Also rutile, less dominant, with (100) preferred orientation.	Anatase (004) and (112), most dominant (004). Rutile (110) very weak.	(001) textured anatase.	Rutile (100).

For simplicity, thereafter the samples are denoted by their label (e.g. STO B5 sample). In this thesis, the study of the undoped thin film focuses mainly on the STO samples pictured in Figure 23. As the interpretation of the results appeared to be more complex than expected due to the broad PL band of the samples and the parasite PL of the substrate, the experiments stopped after having measured the undoped STO samples.

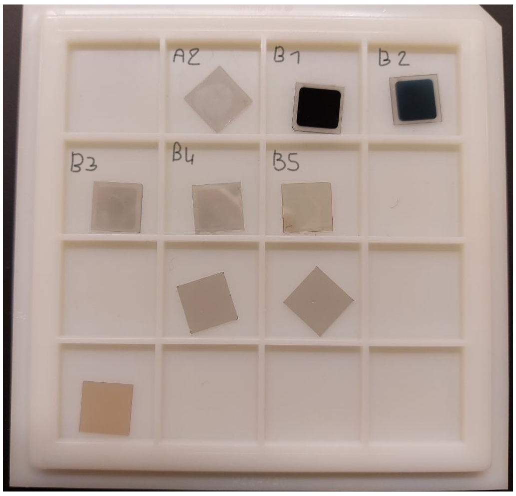

Figure 23: Photo of A and B series samples on STO substrate

3.2 Photoluminescence spectroscopy setup

The PL setup consists of a PL spectrometer provided by Horiba Jobin Yvon® , a turbomolecular pump (Lakeshore Janis model n°TP-75, or TS-85-D), and a cooling system composed of a cooling head (Sumitomo model n°HC-204SFF-N) (called later the cryostat) and a compressor (Sumitomo model n°HC-4A). Temperature control of the sample is monitored through a Lakeshore 331 temperature controller.

The PL setup is composed of an excitation source, two monochromators, and a photomultiplier detector (PMT R928), with working wavelengths at (200-900) nm, as illustrated in figure 24. Three excitation sources are available in the lab, a Xenon lamp (working range: (220-1000) nm). Inside the spectrometer, the beam passes through an excitation monochromator (with the gratings corresponding to the light source) to select the excitation wavelength. An adjustable slit selects the beam width which will illuminate the sample. A beam-splitter allows the measurement of the source intensity on a Si reference detector, as well as the intensity from the sample. Then, to study the emission spectra of the sample, an emission monochromator scans the wavelengths emitted beam with two additional gratings, chosen according to the detectors.

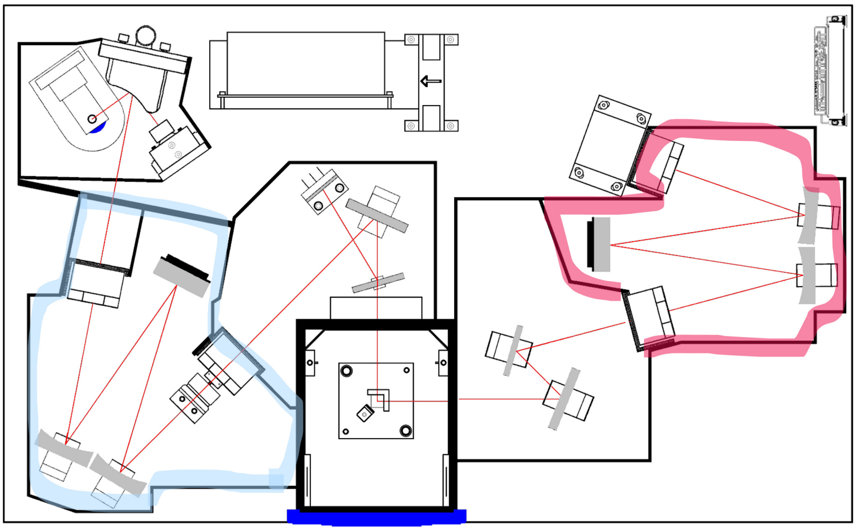

Figure 24: Schematic drawing of the PL spectrometer. The beam coming from the light source enters the excitation monochromator (blue), then a mirror splits the beam-splitter in two, a reference detector collects one part of the beam and the other is used to excite the sample. After the sample chamber, the emission monochromator (red) selected the detection wavelengths. Finally, the signal is recorded by the detector. Taken from Horiba's presentation of the instrument - 2011.

For PL measurements, usually, the excitation monochromator is fixed at λ_{ex} and the emission monochromator scans a range of λ_{em}. In the monochromators, a diffraction grating splits the beam in its composite wavelengths. Each grating is optimal for a specific wavelength, the blaze λ_b, but works well in a range around, which is defined by $[\frac{\lambda_b}{2}, 3\frac{\lambda_b}{2}]$. For example, using the Xenon lamp with the PMT, the appropriate gratings are 1200 groves/nm with $\lambda_b = 300$ nm for the excitation and 1200 groves/nm with $\lambda_b = 500$ nm for the emission. Figure 25 shows the working range of the monochromators in this configuration.

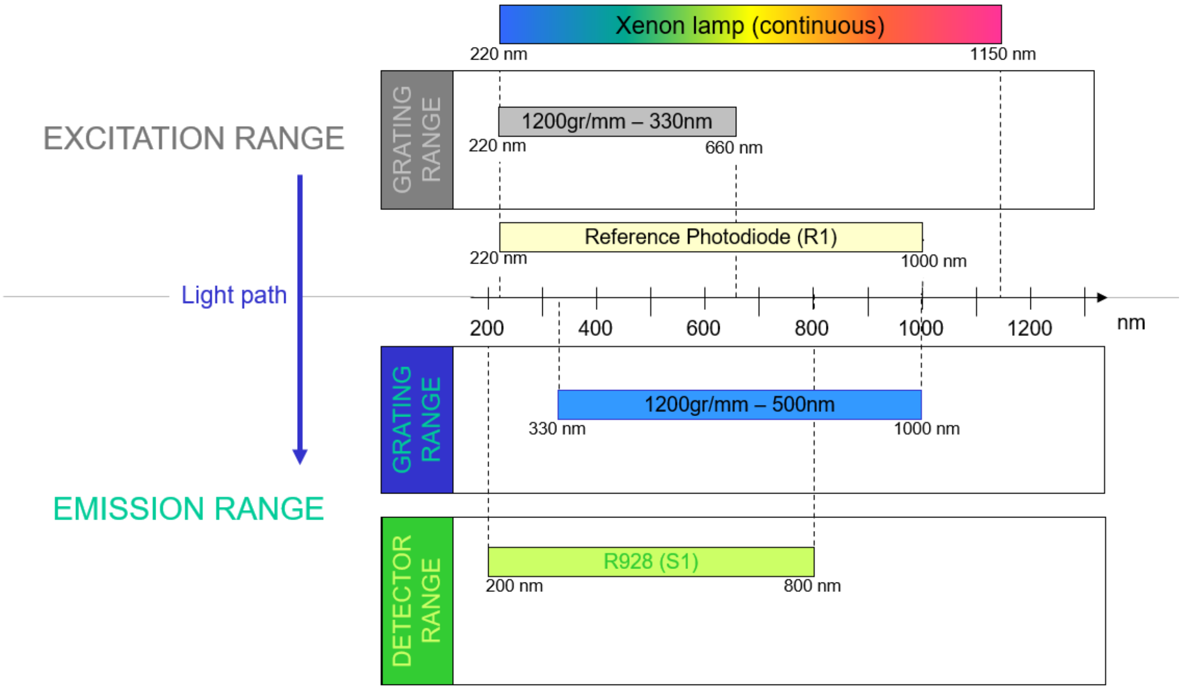

Figure 25: Schematic drawing representation of the working range of the different components of the spectrometer, the region where all the working ranges overlap is the operational range of the spectrometer. Taken from Horiba's presentation of the instrument - 2011.

3.3 Diffraction orders of the monochromators

Calculations from Fourier optics give the diffraction pattern of a light beam after a grating. The grating relation describes how each wavelength diffracts at different angles:

$$\lambda_{em} = m\lambda_{ex} = d[sin(\theta_i) \pm sin(\theta_m)]$$

where λ_{em} is the wavelength we look at after the diffraction, θ_i the incidence angle, θ_m the diffraction angle related to the diffraction order m, and d is the grating spacing. Indeed, the sinusoidal function being periodic the grating relation is satisfied for different couples $\{\theta_m, m\}$ for each wavelength. This phenomenon causes artifacts in the PL spectra. Contribution from the different orders appears on the spectra at the wavelengths λ_{em} but is actually the expression of $\frac{\lambda_{ex}}{m}$. Thus, for an excitation at $\lambda_{ex} = 300$ nm, a peak at $\lambda_{em} = 600$ nm (second order: m=2), at $\lambda_{em} = 900$ nm (third order: m=3), etc..., will appear with decreasing intensity. To avoid the second and above-order peaks, filters can be used. However, no suitable filters were found for the PL study in this thesis. Thus, the second-order peak of the emission monochromator is a recurrent artifact on the PL spectra. *Remark: In the literature, m=1 is the zeroth order, but in this thesis, we have shifted the naming by one digit.*

3.4 PL experiments

During this thesis, three types of measurements were performed. Typical PL emission spectra were mainly recorded. They work as follows: the sample is excited at a single wavelength selected by the excitation monochromator, while the emission monochromator scans a range of wavelengths. Photoluminescence excitation spectra (photoluminescence emission (PLE)) are also interesting to see which absorption wavelength contributes the most to the emission at a specific wavelength. This type of spectra consists of the inverse process of PL: while scanning the excitation wavelengths, the photoluminescence is detected at only one wavelength. The last type is a combination of both, forming a 3D map of the photoluminescence. Although the shape of the PL spectrum is less accessible with the 3D map, it gives a good idea of the PL intensity distribution and is useful to find the parameters optimizing the PL intensity. Seven or fewer main parameters for each spectrum can be adjusted: the emission and excitation ranges, the exit slit sizes of both monochromators, the increments, and the integration time.

In the first phase, the investigation of the influence of the parameters on the spectra and then their optimization were necessary to ensure the reliability of the data. The tests showed that an optimal pair of increment and slit had to be found. A too-large increment reduces drastically the accuracy of the result while a too little increases the noise, and a large slit averages the wavelengths as the slit works like a filter, that is a rectangular function with a not infinitesimal width (see the section D in the appendix for examples).

For all the samples, the measurements were performed in the same conditions to allow comparisons (with only some exceptions for the long wavelength range of the rutile references sample, which contains sharp peaks). Measurements were performed both at room temperature (RT) and 7K, using the Xe lamp as the source and the PMT detector. The excitation wavelength was set to $\lambda_{ex} = 300$ nm (4.13 eV) to excite above the bandgap of both rutile and anatase. The excitation and emission slits were chosen to be $d_{ex} = 5$ nm and $d_{em} = 2$ nm respectively, the second one to maximize the outgoing photon flux from the sample without losing too much of the spatial resolution. The integration time was set to $t_{int} = 3$ s. Finally, the emission range was taken the widest according to the working range of the detector, and the emission and excitation monochromators, usually $\lambda_{em} = (315 - 900)$ nm. To avoid the second-order peak at 600 nm, whose intensity was above the PMT damage threshold, the most recent spectra were recorded in two parts: $(315 - 590)$ nm and $(610 - 590)$ nm.

As a starting point, the single crystal anatase and rutile TiO_2 reference samples were studied in order to later identify anatase and rutile features in the A and B PL spectra.

The PL signal, called $S1$, detected by the PMT was recorded in counts per second, CPS (actually CPS/nm because of the aperture of the slits), or normalized by the intensity of the source $S1/R1$ [CPS/μm] in the function of the emission wavelength. However, for comparison purposes with other articles, the abscissa was converted to photon energy in eV. As photon energy is inversely proportional to wavelengths, to ensure that the integral of the curve stays consistent, an intensity conversion was also required: $I(E) = I(\lambda)\frac{\lambda^2}{hc}$ where c is the speed of light and h Plank constant. [71]

4 Data Analysis

In this section, the data analysis performed in Spectroscopic Ellipsometry and for the critical points is presented.

4.1 Spectroscopic Ellipsometry

This chapter is based on the book ***Spectroscopic Ellipsometry for Photovoltaics Volume 1*** *by Fujiwara and Collins and on the CompleteEase® manual.*

Ellipsometry is a powerful and complex technique as it requires a model-based analysis. On one hand, its strength lies in the fact that the inner characteristics of the sample are accessible, such as its crystallinity, its structure, and the properties of the different materials and layers that compose it. In particular, the dielectric functions can be extracted, which is not possible to measure directly with any optical instrument. On another side, the large variabilities of the analysis (parameters and different types of models) make the data processing complicated by the necessity to find the relevant parameters and the right model for this specific sample. It often requires to already know the sample before starting the analysis. Additionally, the fact that the characterization relies on optical models is a main drawback of ellipsometry, as models can introduce artifacts and always have deviations from reality. It is why, usually complementary methods are used in order to corroborate and confront the model. XRD is used to investigate the crystallinity, AFM for the roughness, and TEM or scanning electron microscopy (SEM) to explore the structure of the sample (eg. its anisotropy). Multiple sample analysis can also help improve the reliability of the model.

In the present thesis, the (ψ, Δ) data is analyzed through a software called CompleteEase®. The software permits to design of the structure of the sample by building all the layers that composite it and adding the known information for each, such as the material, the thickness, the anisotropy, n, and k if there are known, etc... For each layer, a suitable model for the dielectric functions is used to help fit ψ and Δ for the whole sample. Each model is selected depending on the properties of the layer, for example, if the material is transparent in the measured wavelengths range, then a Cauchy model will be more likely to be used, a contrario if it is absorbing, then several different oscillators models are possible (later introduced in the thesis), also depending on the type of material: insulator, metal, or semiconductor. In some models where the bandgap is a parameter, E_g can be extracted. Common parameters can also be fitted for all the layers, such as the roughness. Figure 26 summarizes the method of analysis in a simplified way.

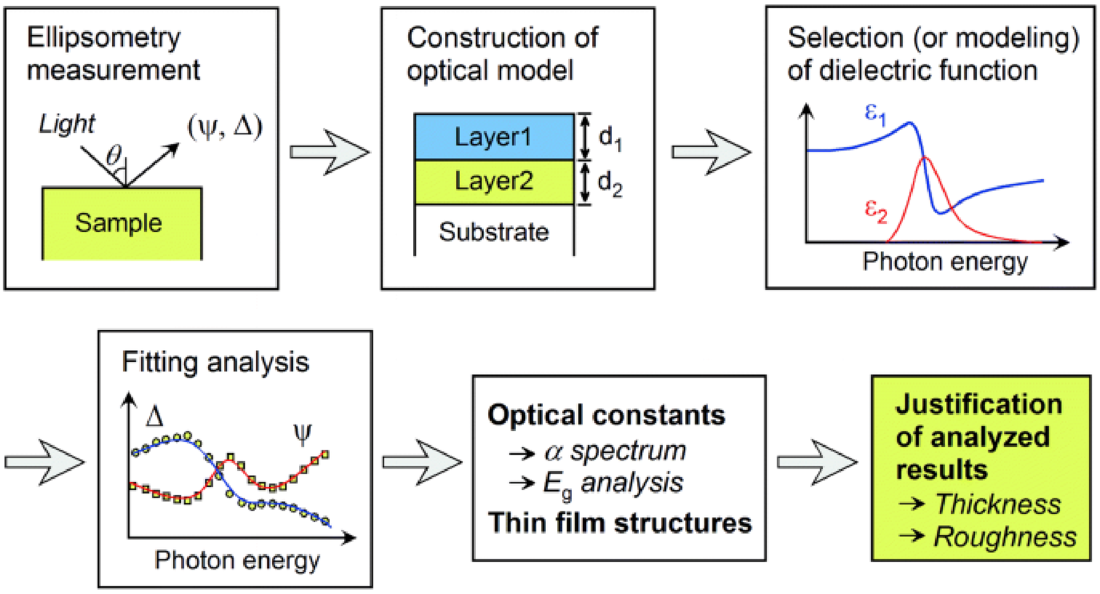

Figure 26: Schematic description of (ψ, Δ) data analysis process in ellipsometry. Taken from [21].

Once the model is built, ψ and Δ are fitted using regression analysis by allowing specific parameters of the model to vary. The improvement and the quality of the fit are evaluated through the mean square error (MSE). The MSE is proportional to the square of the model values minus the experimental ones, and is calculated as follows:

$$MSE = \sqrt{\frac{1}{2N-M}\sum_{i=1}^{N}[(\frac{\psi_i^{Mod}-\psi_i^{Exp}}{\sigma_{\psi,i}^{exp}})^2 + (\frac{\Delta_i^{Mod}-\Delta_i^{Exp}}{\sigma_{\Delta,i}^{exp}})^2]} \tag{42}$$

where N is the number of (ψ, Δ) couples, M is the number of variables (fit parameters) in the model, and σ is the standard deviation for each data point. An ideal MSE would be around 1. However, depending on the condition of the measurement and the sample, which cannot be ideal, is difficult to reach a perfect MSE with all the models, thus, in most of cases the experimenter must decide when he or she judges the MSE is sufficient, usually MSE between 5 and 1 are accepted. If the MSE is judged too high, either previous improving parameters can now be fixed and new ones fitted, or either another more appropriate model can be used. When the MSE is considered satisfying, then the final dielectric function model or optical constants can be extracted from the software and used for further analysis, such as critical point analysis or calculation of the absorption coefficient.

As with any model, it is important to ensure the physical reality of the model or at least the assumptions under which it can be applied. As the dielectric functions are complex, the Kramer-Kronig relations (KK) formalism is needed to maintain the consistency between the real and imaginary parts. In B-spline models, the dielectric functions can be calculated with the KK criteria or not. In oscillator-based models, where the plausibility relies on classical physics, the KK criteria are intrinsic to the model: the oscillator describes ε_2 and ε_1 is calculated from the KK relations.

There are a certain number of sample characteristics affecting the data and that must be taken into account in the model. Ellipsometry is highly sensitive to the thickness of the sample, with an accuracy of up to 0.1Å[72]. As a result, roughness on the sample becomes a critical problem. Usually, roughness is fitted in the software by adding an effective medium, made of 50% of the material surface layer and 50% of void or air. Roughness greater than or equal to the thickness sensitivity will largely affect Δ, and thus the dielectric functions. A study by James N. Hilfiker, Jianing Sun, and Nina Hong has highlighted that incorrectly fitted roughness alters the absorption coefficient near the bandgap Fujiwara and Collins, by overestimating it above E_g and adding an Urbach tail below E_g. Thus, the estimation of the bandgap deeply depends on the roughness.

The typical setup of a spectroscopic ellipsometer is composed of a light source, polarization generator, sample, polarization analyzer, and detector. For the VASE measurements analyzed in this thesis, the angle of incidence θ_{inc} varies between 55°and 75°with a 5°step. The spectral range measured covers the NIR to the UV: (2.00 - 6.00) eV. Additionally, the sample is rotated around the normal to its surface in the experimental frame. The crystal can therefore be probed along different axes. This is particularly interesting to find the ordinary and extraordinary axis of a material. In figure 27, the sample is depicted in the experimental frame with the Euler angles θ_{inc} and ϕ_{inc} (i.e. azimuth), which have a 360°rotation. By setting "assume all rotation angle" ON in the software, the model fits the data from all ϕ_{inc} instead of one incident angle (Figure 29).

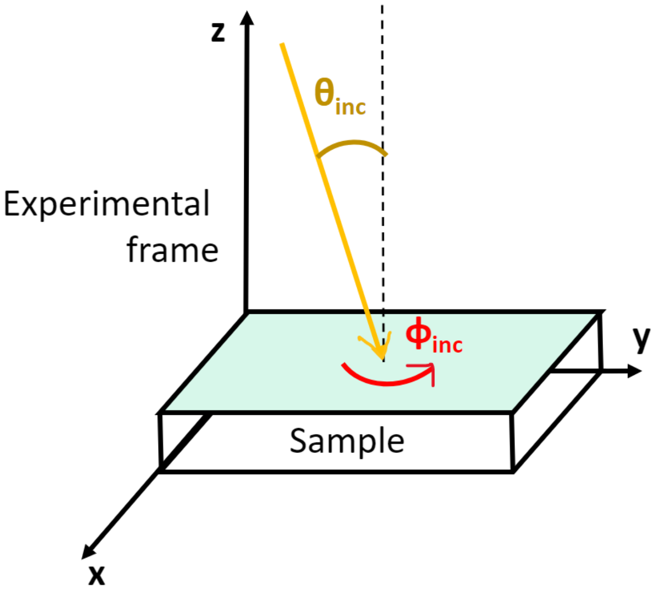

Figure 27: Schema of Euler angles in the experimental frame in Variable Angle Spectroscopic Ellipsometry.

Thanks to these multiple angles data, new and complementary information is available through the analysis, as the light will experience different optical paths, thus increasing the sensitivity in determining unknown parameters. This is particularly interesting to find the ordinary and extraordinary axis of a uniaxial material. However, this depends on the orientation (cut) of the crystal. Depending on the cut of the crystal, the atom arrangement at the surface, both axis, or just the ordinary axis can be investigated. In figure 28, if z//z', the sample surface plane is [001] and as the extraordinary axis (also called c-axis), is normal to the surface, only the ordinary axis is probed. In any other configuration, for example, z//y' or z//x', ordinary and extraordinary axis are both measured, [010] and [100] planes respectively. The orientation of the crystal in the experimental frame is provided by the Euler angles denoted as "Phi" ($\in [0, 2\pi]$) and "Theta" ($\in [0, \frac{\pi}{2}]$) in the software. In z//z' case, "Theta" will be set as 0°. If z is parallel to the (Ox'y')-plane, "Theta" is set to 90°. However, to account for non-perfect alignment, "Theta" is usually fitted in windows of ±5° around its nominal value. "Phi" is always fitted when rotation angles are available in the data set.

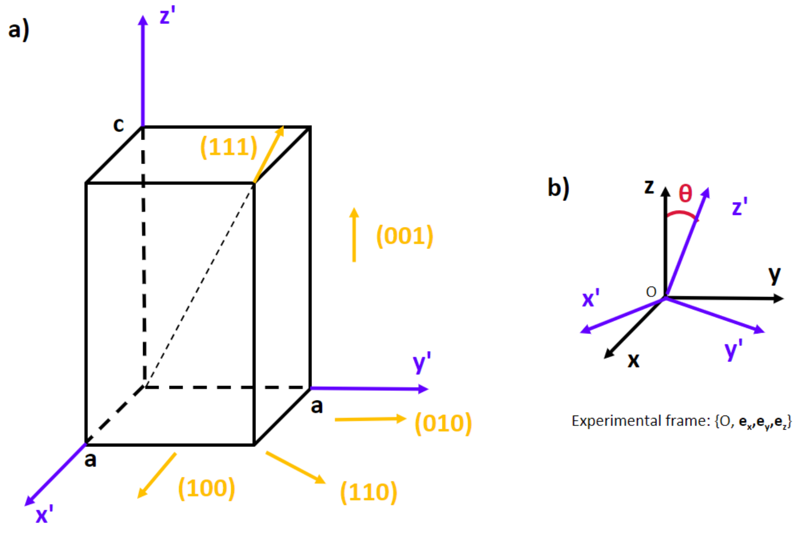

Figure 28: Schema of a) the different orientations of the crystal in the crystal frame {0,x',y',z'} and b) the crystal frame relative to the experimental one.

4.1.1 TiO_2 single crystals analysis procedure

As rutile and anatase TiO_2 are anisotropic uniaxial crystals, for each of their axes (ordinary and extraordinary) they have a set of dielectric functions ε_1 and ε_2. Therefore, to fully characterize them two samples are needed: sample A oriented such that the extraordinary axis is normal to the surface, so cut in the (001)-direction, in a way to get uniquely the ordinary axis optical functions, and sample B oriented in a way that both axes lie in the surface of the sample, for example, the (100), (010) or (110) directions. The analysis procedure applied here was the following:

- Create a B-spline model for the ordinary axis with sample A data;
- Convert to anisotropy the model and create a B-spline uniaxial model with sample B data;
- Parameterize layers of the ordinary axis and extraordinary axis separately and create a General Oscillator model (Gen-Osc) with Tauc-Lorentz functions.

B-spline model

In the first approach, a B-spline model is used to fit the data. A B-spline model consists of a series of control points (also called nodes) equally spaced in photon energy (eV) in order to fit the ψ and Δ data. The model is interpolated between each control points with a basis spline (i.e. a polynomial function). The polynomial functions are defined in a recursive manner by the B-spline formula from *Chenney and Kincaid "Numerical Mathematics and Computing", Third Edition, Brooks/Cole Publishing Company, 1994.* Each basis function is weighted by its amplitude, which can be a fitting parameter, and affects only the local slope near its node.[73] The summation of the polynomial functions gives the final B-spline model. A Kramers-Kronig consistent B-spline model also exists, where ε_1 is extracted from ε_2. However, the B-spline model does not ensure the physical meaning of the oscillators at each node, unlike the General-Oscillator (Gen-Osc) model which will be discussed later.
The settings in CompleteEase® allow one to choose a "Starting Material" from the literature or n and k as input to guide the model towards the expected optical functions. The option "Assume transparent region" allows forcing the splines to be zero below a certain photon energy by assuming a bandgap. It can be useful when the experimenter knows that the material is transparent in a specific energy range. However, since ellipsometry analysis is also a way to extract a bandgap from k, it is recommended to not impose a bandgap at its nominal value but 1 or 2 eV below to allow some flexibility to the fit. The option "Use default TieOff behavior" allows the model to acknowledge for absorbing regions outside the measured spectral range.

Figure 29 displays a typical B-spline uniaxial model. When switching to the uniaxial model, the data set must be changed to the sample B data (for example rutile (110) reference sample). Ex is assigned as the ordinary axis, and its values correspond to the previous model (the ordinary B-spline model first created), while Ez is for the extraordinary axis. At first, only the dielectric functions for Ez are fitted, and those for Ex are also fitted. When assuming the bandgap, to avoid the problem specified earlier, some roughness must be fitted at the same time. The fit weight designated from which type of data the model is calculated, here N,S,C designate the N,C,S coefficient from the isotropic Mueller matrix. The N,C,S fit weight is used for sample A as the ellipsometer sees only the ordinary axis whose data are supposed to be isotropic. However when the model is converted to anisotropy, the N,C,S fit weight can be kept at the beginning but then must be changed for the complete Mueller matrix.

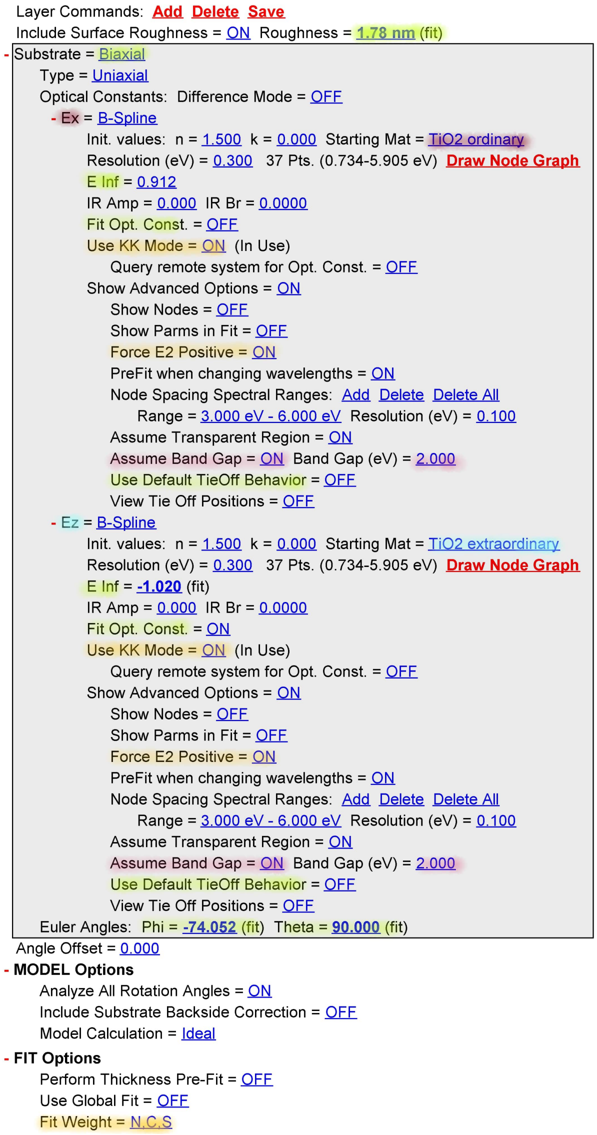

```
 Layer Commands:  Add  Delete  Save
 Include Surface Roughness = ON  Roughness = 1.78 nm (fit)
- Substrate = Biaxial
    Type = Uniaxial
    Optical Constants:  Difference Mode = OFF
      - Ex = B-Spline
          Init. values:  n = 1.500  k = 0.000  Starting Mat = TiO2 ordinary
          Resolution (eV) = 0.300   37 Pts. (0.734-5.905 eV)  Draw Node Graph
          E Inf = 0.912
          IR Amp = 0.000  IR Br = 0.0000
          Fit Opt. Const. = OFF
          Use KK Mode = ON  (In Use)
              Query remote system for Opt. Const. = OFF
          Show Advanced Options = ON
              Show Nodes = OFF
              Show Parms in Fit = OFF
              Force E2 Positive = ON
              PreFit when changing wavelengths = ON
              Node Spacing Spectral Ranges:  Add  Delete  Delete All
                  Range = 3.000 eV - 6.000 eV  Resolution (eV) = 0.100
              Assume Transparent Region = ON
              Assume Band Gap = ON  Band Gap (eV) = 2.000
              Use Default TieOff Behavior = OFF
              View Tie Off Positions = OFF
      - Ez = B-Spline
          Init. values:  n = 1.500  k = 0.000  Starting Mat = TiO2 extraordinary
          Resolution (eV) = 0.300   37 Pts. (0.734-5.905 eV)  Draw Node Graph
          E Inf = -1.020 (fit)
          IR Amp = 0.000  IR Br = 0.0000
          Fit Opt. Const. = ON
          Use KK Mode = ON  (In Use)
              Query remote system for Opt. Const. = OFF
          Show Advanced Options = ON
              Show Nodes = OFF
              Show Parms in Fit = OFF
              Force E2 Positive = ON
              PreFit when changing wavelengths = ON
              Node Spacing Spectral Ranges:  Add  Delete  Delete All
                  Range = 3.000 eV - 6.000 eV  Resolution (eV) = 0.100
              Assume Transparent Region = ON
              Assume Band Gap = ON  Band Gap (eV) = 2.000
              Use Default TieOff Behavior = OFF
              View Tie Off Positions = OFF
    Euler Angles:  Phi = -74.052 (fit)  Theta = 90.000 (fit)
 Angle Offset = 0.000
- MODEL Options
    Analyze All Rotation Angles = ON
    Include Substrate Backside Correction = OFF
    Model Calculation = Ideal
- FIT Options
    Perform Thickness Pre-Fit = OFF
    Use Global Fit = OFF
    Fit Weight = N,C,S
```

Figure 29: Typical B-spline uniaxial model from CompleteEase®, Ex corresponds to the ordinary axis (and to ordinary B-spline model firstly created) and Ez to the extraordinary axis. In green is highlighted what is usually fitted in the model, while elements highlighted in orange are for ensuring the physical plausibility (KK criteria and positive ε_2), the fit weight designated from which type of data the model is calculated, here N,S,C designate the N,C,S coefficient from the isotropic Mueller matrix. In pink is the assumed bandgap to avoid an Urbach tail below E_g.

Gen-Osc model

Once the B-spline model is satisfying, a general oscillator model (Gen-Osc) can be used to retrieve some physical meaning from the shape of the dielectric function, especially ε_2. Such models consist of a collection of oscillator functions. Depending on the material, metal, insulator, or semiconductor, specific oscillator functions are more appropriate. Figure 30 shows some of the models. For example, a Drude oscillator is suited to account for energy absorption (typically in the IR) without optical transition: the electrons are already in the conduction band of a metal before light absorption (i.e. free electrons). For a region where the sample is known to be transparent, a Cauchy or Sellmeier model is adapted to model the normal dispersion, where the optical index inversely proportional to wavelengths is a good approximation. However, in the absorbing region, a Lorentz, Tauc-Lorentz, or Cody-Lorentz oscillator is necessary to represent anomalous dispersion.

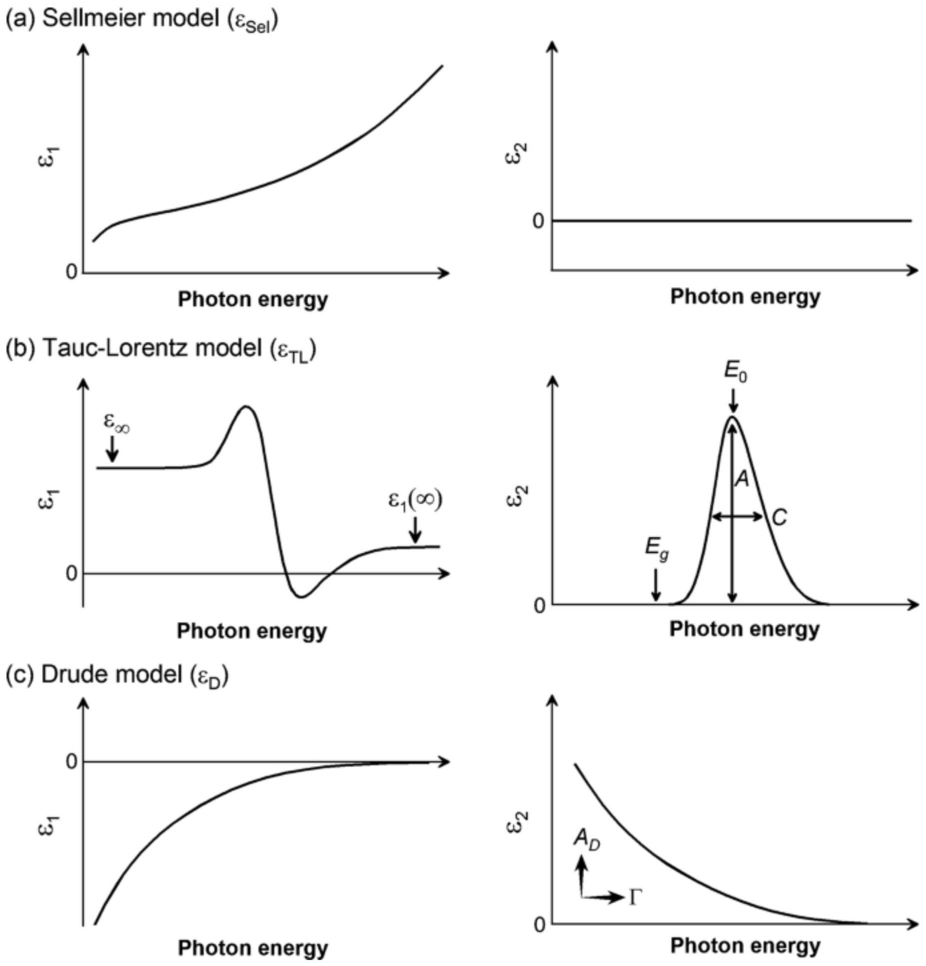

Figure 30: Example of the dielectric function for the following dispersion models: the Sellmeir model, the Tauc-Lorentz model and the Drude model. Taken from Ref.[21].

In practice, the ordinary and extraordinary dielectric functions are converted separately into a Gen-Osc, where their imaginary part ε_2 is first fitted, and then ε_1. Each absorption peak in ε_2 corresponds to an oscillator in the Gen-Osc model. For the samples studied here, Tauc-Lorentz oscillators are employed. They are well suited for semiconductors since their asymmetric shape fits properly the bandgap by setting the absorption to zero below E_g. If more than one oscillator are needed, their bandgaps are set to a common E_g as illustrated in figure 31. Then, ε_1 is fitted but only by adjusting parameters to account for absorption outside the measured spectral range. These parameter are: ε_∞ ("Einf"), $\varepsilon_1(\infty)$ and $\varepsilon_1(0)$ ("IR pole Amp."). ε_∞ is just a constant background for ε_1, while $\varepsilon_1(\infty)$ adds a tail when $E \to \infty$ whose amplitude is governed by the parameter "UV pole Amp." and energy by "UV pole En.". A non-zero "UV pole Amp." pulls ε_1 up. The closer is the "UV pole En." to the limit of the measured range, the greater is the tilt of the tail. $\varepsilon_1(0)$ for its part acts as a Drude term by pulling ε_1 down when $E \to 0$. Those parameters are important to maintain the KK consistency as the integrals involved in the relationship are over the whole spectrum.

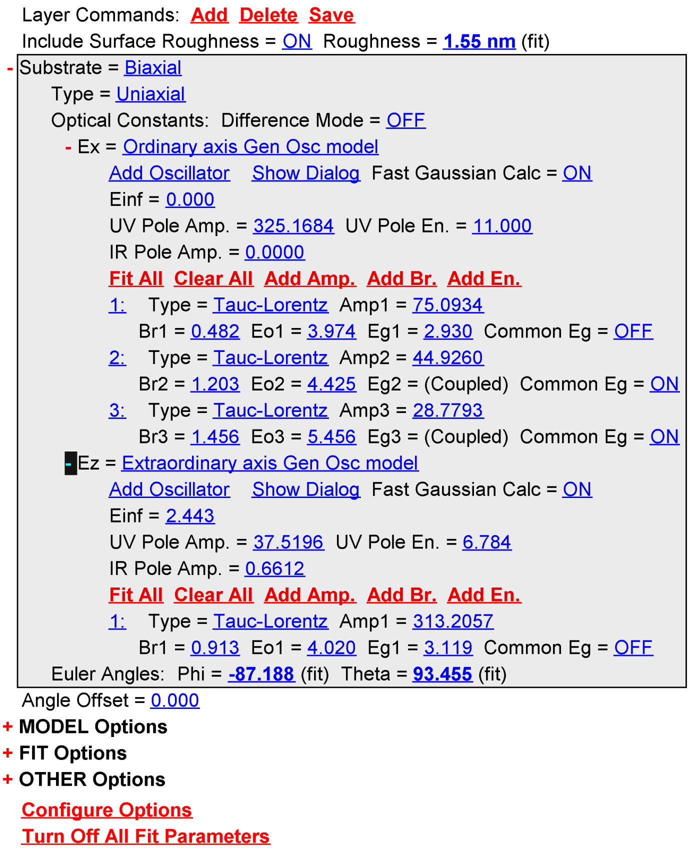

Layer Commands: Add Delete Save
Include Surface Roughness = ON Roughness = 1.55 nm (fit)
- Substrate = Biaxial
Type = Uniaxial
Optical Constants: Difference Mode = OFF
- Ex = Ordinary axis Gen Osc model
Add Oscillator Show Dialog Fast Gaussian Calc = ON
Einf = 0.000
UV Pole Amp. = 325.1684 UV Pole En. = 11.000
IR Pole Amp. = 0.0000
Fit All Clear All Add Amp. Add Br. Add En.
1: Type = Tauc-Lorentz Amp1 = 75.0934
Br1 = 0.482 Eo1 = 3.974 Eg1 = 2.930 Common Eg = OFF
2: Type = Tauc-Lorentz Amp2 = 44.9260
Br2 = 1.203 Eo2 = 4.425 Eg2 = (Coupled) Common Eg = ON
3: Type = Tauc-Lorentz Amp3 = 28.7793
Br3 = 1.456 Eo3 = 5.456 Eg3 = (Coupled) Common Eg = ON
- Ez = Extraordinary axis Gen Osc model
Add Oscillator Show Dialog Fast Gaussian Calc = ON
Einf = 2.443
UV Pole Amp. = 37.5196 UV Pole En. = 6.784
IR Pole Amp. = 0.6612
Fit All Clear All Add Amp. Add Br. Add En.
1: Type = Tauc-Lorentz Amp1 = 313.2057
Br1 = 0.913 Eo1 = 4.020 Eg1 = 3.119 Common Eg = OFF
Euler Angles: Phi = -87.188 (fit) Theta = 93.455 (fit)
Angle Offset = 0.000
+ MODEL Options
+ FIT Options
+ OTHER Options
Configure Options
Turn Off All Fit Parameters

Figure 31: Typical B-spline uniaxial model from CompleteEase®.

Common Gen-Osc dielectric functions are detailed in the next section: Lorentz, Tauc-Lorentz or Cody-Lorentz oscillators.

4.1.2 Oscillator models for the dielectric functions

Absorption is depicted by a resonance in ε_2. As in classical mechanics, oscillators are used to describe such response to a system, the word was borrowed and applied to absorption phenomena. In practice, an oscillator describes the shape of a resonance in ε_2 and ε_1 is deduced thanks to the Kramers-Kronig relations. Generally, optical transitions occur from UV to NIR, thus the following dispersion relations concerns this range. As said earlier, each material has its own appropriate dispersion law. The Tauc-Lorentz and Cody-Lorentz oscillators are primarily used for semiconductors, where they model well the region near E_g. The Gaussian oscillators are employed for organic material to describe molecular bonding. Critical Point Parabolic Band (CPPB) models are used for finding critical points (i.e. CPs) in semiconductors.

Lorentz Model

The Lorentz model draws an analogy between the dynamic of a mass on a spring in classical mechanics and the movements of an electron cloud around its nucleus due to the absorption of a photon. The spring corresponds to the electrostatic forces maintaining the electron cloud together with the nucleus. The absorption of photons induces an oscillation of the electron cloud from its equilibrium position. The emission of a photon can be seen as a dissipative force corresponding to friction in the mechanical model.
The general expression of the Lorentz dielectric function is the following:

$$\varepsilon(E) = \varepsilon_1(E) + i\varepsilon_2(E) = \varepsilon_1(\infty) + \frac{A\Gamma E_0}{E_0^2 - E^2 + i\Gamma E} \tag{43}$$

where A is the oscillation amplitude, Γ the broadening, and E_0 the central energy (i.e. the maximum of absorption). Figure 32 shows the shape of the oscillator.

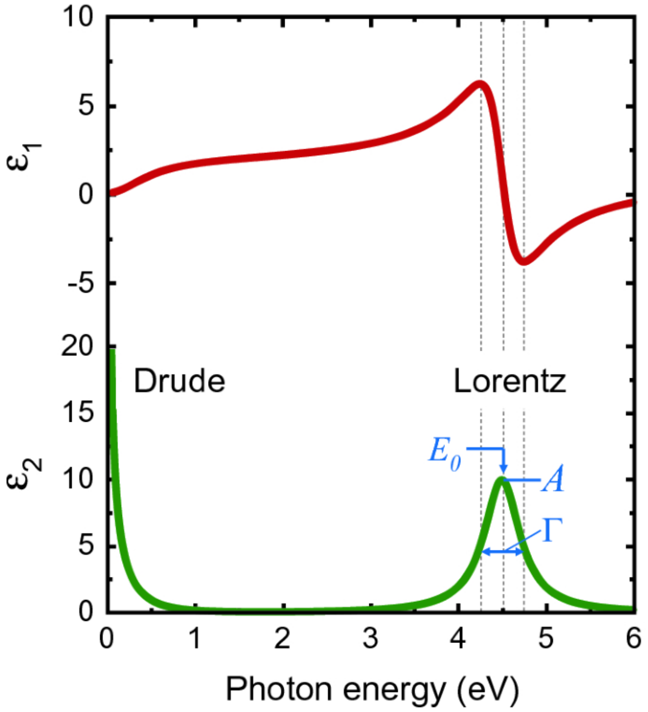

Figure 32: Graph of the dielectric functions where ε_2 is modeled by a Lorentz oscillator and a Drude model at low energies. Taken from Ref.[21].

The Lorentz model is not well suited for semiconductors at energies around the band gap, because of its symmetric line-shape. To remove the unphysical Urbach tail below E_g induced by the symmetry, two models were developed: the Tauc-Lorentz model by Jellison and Modine and the Cody-Lorentz model by Ferlauto et al. [74, 75]

Tauc-Lorentz Model

The Tauc-Lorentz model derives from the Lorentz model and was created to model the dispersion equation of a semiconductor near the bandgap. The imaginary part of the Lorentzian oscillator model is multiplied by a Tauc factor $(E-E_g)^2$ to break the symmetry of the Lorentzian shape, such that the absorption onset is sharper. Below E_g the Tauc-Lorentz is defined as zero as represented in figure 33. Above E_g, the model is defined as follows:

$$\varepsilon_2(E) = \frac{AC(E-E_g)^2}{[(E-E_0)^2 + C^2E^2]E} \tag{44}$$

where A is the strength of the absorption amplitude, C is the broadening, and E_0 is the energy at the resonance.

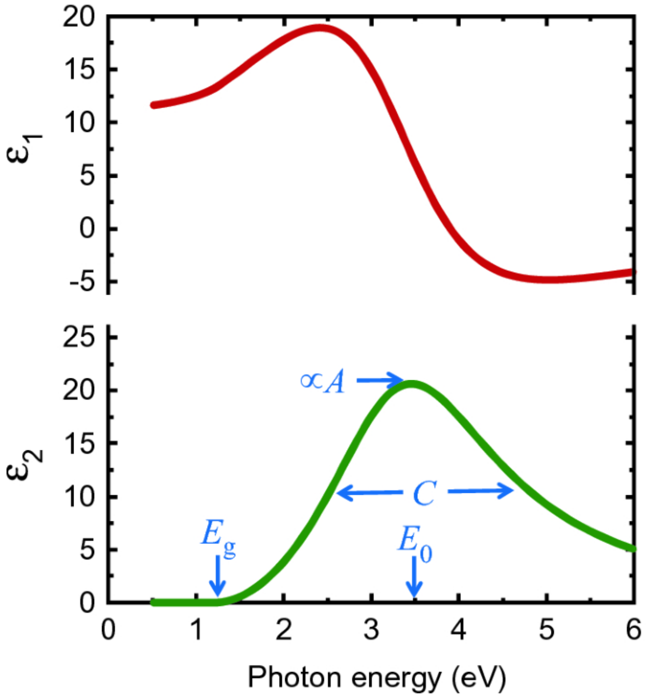

Figure 33: Graph of the dielectric functions where ε_2 is modeled by a Tauc-Lorentz oscillator. Taken from Ref.[21].

Cody-Lorentz model

Like the Tauc-Lorentz model, the goal of the Cody-Lorentz oscillator is to model the absorption of a semiconductor. Nevertheless, the trend of the absorption onset differs from the Tauc-Lorentz model: instead of being proportional to $\frac{(E-E_g)^2}{E^2}$, ε_2 is only proportional to $(E-E_g)^2$ as expressed in Eq.(46). Then, a small Urbach tail below E_g is included in this model:

$$\varepsilon_2(E) = \frac{E_1}{E}\exp(\frac{E-E_t}{E_u})\text{for}0 < E \leq E_t \tag{45}$$

$$\varepsilon_2(E) = \frac{(E-E_g)^2}{(E-E_g)^2 + E_p^2}\frac{AEE_0\Gamma}{(E^2-E_0^2)^2 + \Gamma^2E^2}\text{for}E > E_t \tag{46}$$

where A is the strength of the absorption amplitude, Γ the broadening, E_0 the resonant energy and E_u the Urbach energy. The behavior of the Cody-Lorentz model at the bandgap is compared to the Tauc-Lorentz behavior in figure 34. E_p is a parameter that can be adjusted by the experimenter to specify when the ε_2 switches from the Cody-Lorentz to the Lorentz model, which occurs at $E_g + E_p$. E_p tells when the Urbach tail ends and the band-to-band transition starts.

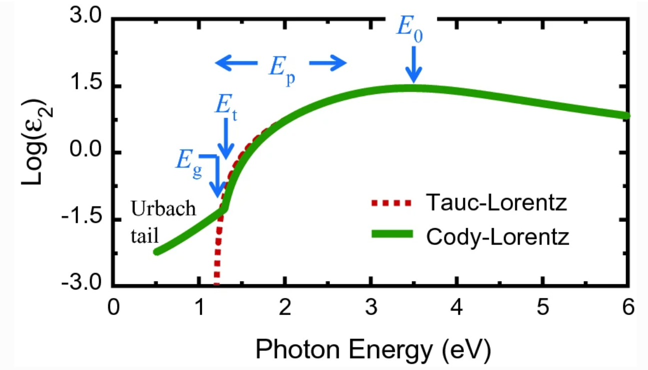

Figure 34: Comparison of the dielectric functions when ε_2 is modeled with the Cody-Lorentz model and the Tauc-Lorentz model. Taken from Ref.[21].

Critical Points Parabola Band models (CPPB)

The critical point parabola band model is a built-in model in CompleteEase®. It was created to fit derivative or modulation spectra and to locate critical points in the dielectric functions using quantum theory applied to inter-band transition. The dielectric functions from the B-spline model can be fitted using the expression in Eq.(38), which derives from the quantum calculations presented in section 2.3.1:

$$\varepsilon(\omega) = C - Ae^{i\phi}(\hbar\omega - E_g + i\gamma)^n \tag{47}$$

The exponent n describes the dimensionality of the critical point: 1D ($n = -\frac{1}{2}$), 2D ($n = 0$), 3D ($n = \frac{1}{2}$), or 0D for discrete excitons ($n = -1$). As this model can give a nonphysical shape, by allowing negative ε_2 or by adding an Urbach tail under the bandgap, it is only suitable for modeling the dielectric functions near the critical points or for fitting their derivative.

4.2 Critical points analysis

In this section, an attempt to clarify the interpretation of the critical points (CP) is first presented. Then, the fitting procedure of the dielectric functions with a CP line-shape is addressed.

4.2.1 Interpretation of the dimensionality of the CP

The interpretation of dimensionality of the CPs is unclear in the literature, and various analyses have been performed. In most of the papers, no direct interpretation is made of the dimensionality, and the dielectric functions are fitted with the best-suited line-shape for the data. Quite often, this results in using a excitonic lines-shape ($n = -1$). [26, 76, 21] The use of 2D CPs appears also regularly. [26, 76, 77] In some papers, the use of 2D CPs is correlated with polycrystalline samples. [78, 79] Some other papers mention fractional dimensionality ($0 <= n <= 3$) for anisotropic solids. However, the anisotropy they refer to seems to be related to the structure of the sample, such as chain-like structures (polymers), layered structures, or dot structures, and not to the optical anisotropy. [80, 81, 82]

Thus, the interpretation is complex. Fitting the dimensionality appears intrinsically related to fitting ϕ. According to Toyozawa et al. work, the optical spectra of a solid contains localized excitation (such as excitonic excitation) and band characteristics. If the band character dominates, the line-shape is given by the expression Eq.(38) in section 2.3.2 with $n = -1/2, 0, 1/2$ (1D,2D,3D), and a varying ϕ can account for the excitonic effects by allowing a mixture of CPs. In this case, the excitonic effect is weak. On the opposite, when localized excitations interacting with a band or a continuum of inter-band transitions predominate in the spectra, the expression Eq.(38) with $n = -1$ best fits the dielectric functions. In this case, the Lorentzian line shape is described accurately by a Fano-Breit-Wigner profile [84] and ϕ embodies the strength of the interaction. If $\phi = 0$, there is no coupling between the excitons and the continuum [76] In both cases, ϕ is a free parameter.

The description of the many-body effects by allowing ϕ to take non-integer multiples of $\frac{\pi}{2}$ (to account for a mix of CPs) has no theoretical basis. As a result, several attempts were made to find an analytical expression for the critical points introducing an excitonic effect when the band character is dominant. [85, 76] One of these attempts is to introduce a Koster-Slater contact interaction potential: $V(r) = -\delta(r)g$, $g > 0$, to screen the Coulomb interaction between the electron and hole in the exciton. The potential is non-zero only when the electron and hole are in the same unit cell. The Koster-Slater model is usually used to describe Frenkel excitons. However, in this case, the Koster-Slater model is used to approximate the effect of the Wannier-Mott exciton on the optical spectra. This leads to the modification of the one-electron dielectric function $\tilde{\varepsilon}$:

$$\varepsilon(\omega) = \frac{\tilde{\varepsilon}(\omega) - 1}{1 - g[\tilde{\varepsilon}(\omega) - 1]} + 1 \tag{48}$$

where g is linked to the depth of the potential well. When g tends towards zero, the dielectric function converges towards Eq.(38). Lautenschlager et al. tried to used the second derivative of Eq.(48) with $\phi = 0$ to fit g. Unfortunately, $\tilde{\varepsilon}$ cannot be determined in absolute from the experimental data, and their fit did not converge. They proceed by iterations and each time g tended towards a lower value. They conclude that Eq.(48) is not suitable when the one-electron picture presents a large phase shift ($\phi > 90°$).

Other methods exist to include the many-particle effect in the CP analysis. One of them is the effective mass approximation (EMA), in which the exciton Coulomb potential and its screening by the dielectric constant can be incorporated. However, this technique works only if one of the principal reduced masses is significantly bigger than the other two. A second approach is to characterize the electron-hole interaction by passing through the local-orbital treatment of the two-particle Green's function. Unfortunately, despite the fact that this method sounds promising, no analytical formula appropriate for the line-shape of the CPs was found. [76]

In a paper by Lautenschlager et al.[26], they noticed that the light III-V or II-VI compounds, as well as Si samples, were best fitted by excitonic line-shapes ($n = 1$), while 2D line shapes are best suited to heavier III-V or II-VI compounds and Ge samples. They observed that within a group of compounds, the higher the dielectric constant was (i.e. $\varepsilon_1(\infty)$), the lesser the line-shape had a localized character, because of the increasing screening of the Coulomb interaction in the exciton. From the following formula, the binding energy of the exciton is inversely proportional to the dielectric constant:

$$E_{ex} = \frac{2\mu}{\varepsilon_1(\infty)^2} \tag{49}$$

where μ is the effective mass. It has been measured that the exciton binding energy in rutile is about 4 meV and in anatase is about 180/275 meV. [86, 87] According to this binding energy, rutile would have a higher dielectric constant than anatase, and thus, a stronger localized character. In a previous paper, Lautenschlager et al. studied the effect of temperature on the critical point dimensionality. They remarked that below RT, the localized excitation interacting with a continuum was the dominant origin of the line-shape, they used a Fano profile. While above ambient temperature, the 2D Van-Hove singularities perturbed by the electron-hole attractive interaction took over the line-shape. They also demonstrate that the broadening of the line-shape is temperature dependant. At higher temperatures, the electron-phonon scattering events reduce the lifetime of the electronic states and increase the broadening.

The challenge here is to understand the significance of the dimensionality of the CPs to be able to fit it. The nature of the CPs is related to their positions and symmetry in the Brillouin zone and their corresponding properties. Usually, the center of the Brillouin zone is called Γ, and the other points depend on the geometry of the primitive cell of the material. These points are called the high symmetry points, and from their symmetry derives the electronic properties of the material. The directions between these points are denoted with Greek letters. The primitive cell of anatase is body-centered tetragonal (BCT), its irreducible high-symmetry points are Z-Γ-X-P-N-Γ. If its conventional tetragonal cell is considered, the high-symmetry points are Γ-R-Z-M-A-Z.[88]. For rutile, its primitive cell is the same as its conventional cell and is tetragonal (TET), its path is Γ-X-M-Γ-Z-R-A-Z—X-R—M-A (Figure 35). The band structure is built by plotting a section of the band in a specific direction of the Brillouin zone, allowing thus to plot a 4D diagram in 2D.

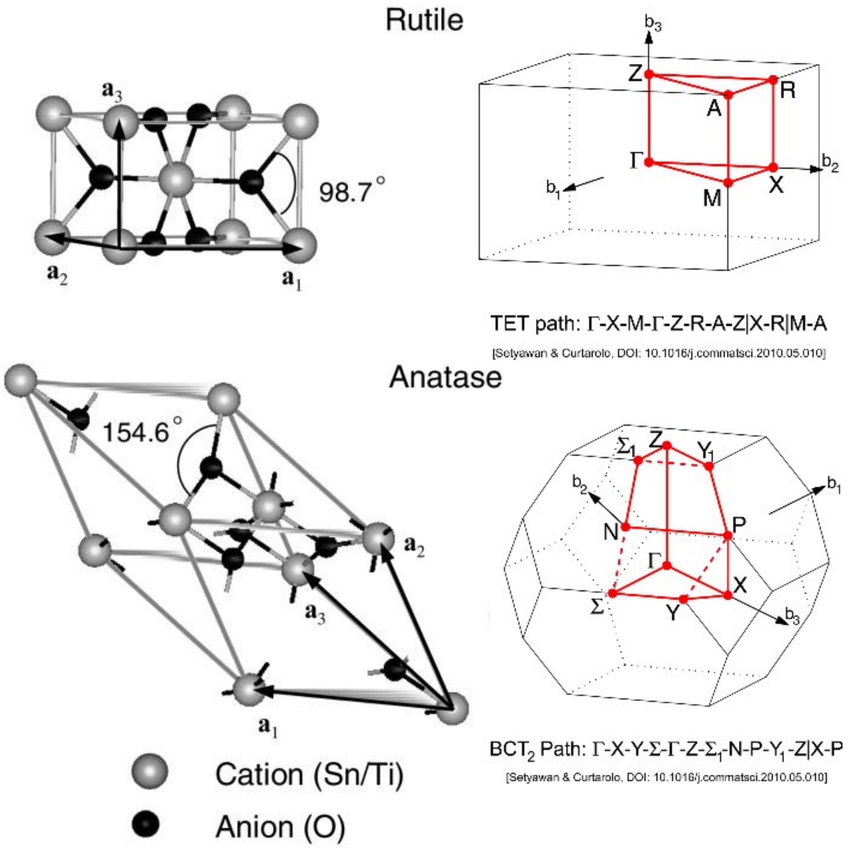

Figure 35: Primitive cells of rutile and anatase TiO_2 and their respective Brillouin zone: tetragonal, and body-centered tetragonal. Adapted from Ref.[89] and Ref.[90].

In the following, three different interpretations of the dimensionality are developed:

One interpretation of the dimensionality is related to the position of the high symmetry point corresponding to the CP. In this case, the 1D critical points could correspond to transition along one direction in the band structure, so to Latin letters. The 2D CPs could be associated with crosspoints of two directions in the band structure, so to Greek letters, except Γ. Finally, the 3D critical points would be the crosspoints of tree directions, such as Γ. However, this interpretation derives from the path chosen for the band structure representation, which is applied according to a consensus but in theory could be different. So, this interpretation does not seem really physical and plausible. For example, for rutile, all the high symmetry points are at the crossing tree directions, so they would all be 3D critical points, the points in between would be 1D CPs, and no 2D CPs would be involved (as illustrated in figure 35).

A second interpretation is related to the effective mass. The effective mass describes how the electron moves in the crystal, is positive for an electron and negative for a hole (i.e., the electron acts as a positive charge particle in response to an electric field). The curvature of the bands $\frac{d^2E_c}{dk^2}$ in (Γ, k_x, k_y, k_z) space is inversely proportional to the effective mass in this direction of the space. If the curve is almost flat, the effective mass is huge, and it is difficult for the electron to move from its site. On the opposite, if the curvature is important, the effective mass is small, and the electron can easily move.
In this case, the dimensionality is defined by the number of non-infinite effective mass, so of the non-flat band structure. A 0D CP would correspond to a localized excitation because

in three directions the effective mass is infinitely large such that the electron can not move from its position in any direction. A 1D CP would then be a point where two of the effective masses would be infinite, then the electron could move only in one direction in k-space. A 2D CP would correspond to the case with only one infinite effective mass, so thus with two allowed directions for the electron. Finally, the 3D critical point would be when in all directions the effective mass is non-infinite, thus, the electron can move all around. This interpretation derives from the paper of Loughin et al., and is supported by the number of type CP per dimensionality, which is descending with it. Originally, the type of CP is associated with a factor i^{r-d} in the JDOS (see Eq.(8) and (9) in [91]), where d is the dimensionality, r corresponds to the type and take values from $0, ..., d$ (not to $d-1$ as written in [91]). Later, the factor was replaced by e^{ϕ}, probably to have a parameter to vary continuously to account for a mix of CPs. Thus, for a 3D critical point, four different shapes are possible, for a 2D CP three shapes, and so on. Thus, the number of directions in which the conduction band energy is largely flat can be used to categorize the dimensionality of the critical point, which reduces the system dimensionality. Additionally, the type of critical point is indicated by the relative curvature of the conduction band energy surface in orthogonal directions (k_x, k_y, k_z).

This last interpretation seems to be the most relevant hypothesis and logic from a physical point of view and was adopted in the following analysis.

4.2.2 Fit of Critical Point line-shape

The critical point analysis is performed with a Matlab code written by Benjamin Roaldsson Hope, a previous master's student of the Solar Cell Physics group. The code is mainly divided into parts: the calculation of the second derivative of $\varepsilon = \varepsilon_1 + i\varepsilon_2$ and the fit of the derivative with the CP line-shapes (i.e. Eq.(53)). First, the data are interpolated over 1000 points equally spaced and smoothed with a Gaussian filter. Then, the second derivative is calculated according to the following definition:

$$\frac{d\varepsilon}{dE} = \frac{[\varepsilon(E+h) - \varepsilon(E)] - [\varepsilon(E) - \varepsilon(E-h)]}{h^2} \tag{50}$$

where h is infinitesimally small. In practice, h was taken to be the distance between two points after the interpolation. Finally, the second derivative is fitted with the CP line-shapes. The number of oscillations in the second derivative will give an estimate of the minimum number of CP involved in absorption spectra. For N CPs, each one is fitted with Eq.(38). The result of the fit corresponds to the sum of each the line-shape for all CPs, as follow:

$$\varepsilon_{fit}(E) = \sum_{i=1}^{N} \varepsilon_i(E, \vec{p_i}) \tag{51}$$

where the vector $\vec{p_i}$ contains the parameters of the fit for one CP:

$$\vec{p_i} = (A_i, \Gamma_i, E_{0,i}, \phi_i n_i) \tag{52}$$

and with:

$$\varepsilon_i(E, \vec{p_i}) = \begin{cases} C - A_i e^{j\phi_i}(E - E_{0,i} + i\Gamma_i)^n & \text{if } n \neq 0 \\ C - A_i e^{j\phi_i} \ln(E - E_{0,i} + i\Gamma_i) & \text{if } n = 0 \end{cases} \tag{53}$$

where j is the complex number.

Before fitting the CPs, one must initialize them. This consists in fixing the dimensionality of the CP by fixing n to one of these values: $-1, -\frac{1}{2}, 0, \frac{1}{2}$, and setting an initial value as well as a lower and upper bound to the other parameters. The bounds used for the initialization in the following analysis are:

Table 3: Table summarizing the upper and lower bounds for certain parameters of the fit.

Parameter	**Bounds**
A	[0,10] or [0,15]
ϕ	$[0,360]^\circ$
Γ	[0.01,0.5] or [0.01,1]

The bounds for $E_{0,i}$ were chosen in most of the cases in a range of ±100 meV around $E_{0,i}$, while $E_{0,i}$ were initialized with the positions of the local minimum in the second derivative curve.

5 Results and Discussion

This section contains first the ellipsometry analysis of anatase and rutile single crystals, then an initial critical point line-shape analysis for the ordinary axis of rutile, and finally the PL spectroscopy analysis of the singles crystals and of three undoped TiO_2 thin films grown on STO.

5.1 Ellipsometry analysis results

In this section, the dielectric functions of rutile and anatase are presented. Two types of optical models were built for each sample, an anisotropic B-spline model and then a general oscillator (Gen-Osc) model. Finally, the bandgap is determined through different techniques and compared. From the Gen-Osc models, the bandgaps of the ordinary and extraordinary axis are determined to be 2.944 eV and 3.130 eV respectively for rutile, and 3.246 eV and 3.630 eV for anatase.

5.1.1 Rutile dielectric functions

First, the anisotropic B-spline model is presented, and then the general oscillator model.

Anisotropic B-spline model

First, a B-spline model was built with the data of rutile (001) sample to model the ordinary dielectric function of rutile. Rutile (001) is oriented in a way that the extraordinary axis is normal to the sample surface. Thus, mainly the ordinary axis of the sample is probed during the VASE measurements, allowing the extraction of the ordinary axis optical properties separately from that of the extraordinary axis. The model is presented in section A.1 in the appendix. Then, this model is converted into an anisotropic B-spline model to fit jointly the ordinary and extraordinary dielectric functions. The anisotropic B-spline model is based on rutile (110) data. For this sample, both axes lie in the plane of the surface. The data are measured at 65° incident angle, while the sample is rotated from 0° to 360°. This model is decomposed into two B-spline models, each for one optical axis. The dielectric functions from Tiwald and Schubert were used as starting material.[92]

To take into account the off-diagonal elements of the anisotropic tensor in the analysis, the model is calculated from the full Mueller matrix data, and not only the N,C,S elements. Thus, the MSE reduced from 5.48 to 3.85. Figure 36 shows the ordinary and extraordinary dielectric function of rutile. For both axes, the absorption starts around 3.0 eV, the bandgap of rutile. The imaginary part of the extraordinary dielectric functions, containing the absorption behavior of rutile, shows one broad and intense peak. In the imaginary part of the ordinary dielectric functions, three peaks are distinguishable and participate in the absorption, which is less intense than for the extraordinary axis.

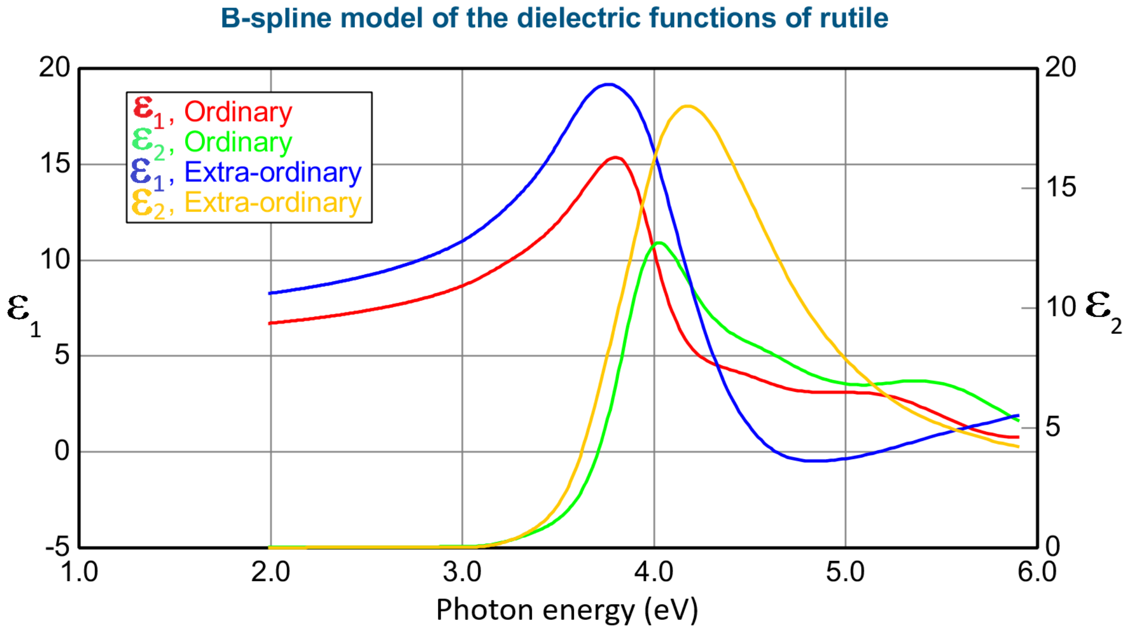

Figure 36: Graph of the B-spline model of the dielectric functions of rutile (MSE = 3.85).

The B-spline model calculated with the N,C,S elements, the B-spline model calculated with the full Muller matrix, and the Schubert dielectric functions are compared in figure 37. The three models have almost identical results for the ordinary axis. For the extraordinary axis, deviations are observed: the B-spline model (N,C,S) seems to overestimate the amplitude of the absorption, while the Schubert model seems to underestimate it a little. The ordinary and extraordinary ε_2 appear to have a similar absorption onset around 3.00 eV, coherent with the bandgap of rutile. As the ordinary axis can be measured almost separately from the extraordinary, by choosing an appropriate crystal orientation (e.g. rutile (001)), it seems coherent that its dielectric functions are more accurately modeled.

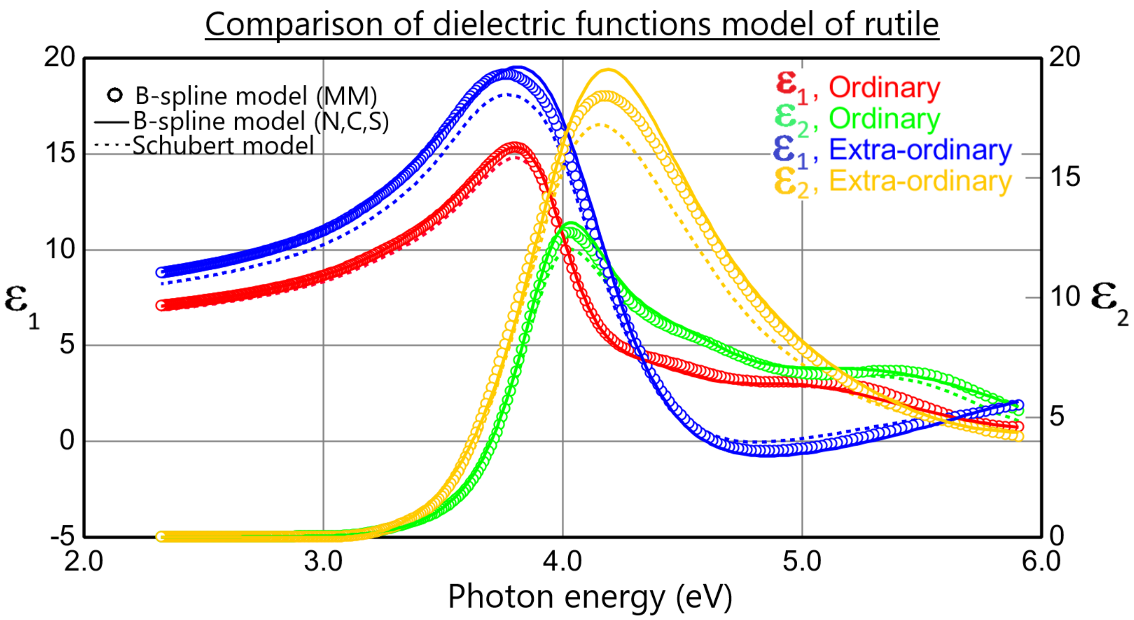

Figure 37: Comparison of dielectric functions models of rutile. The solid line corresponds to the B-spline model calculated with the N,C,S elements (MSE = 5.48), the circle line to the B-spline model calculated with the full Mueller matrix (MM) (MSE = 3.85), and the dashed line to Schubert model.[92]

The VASE technique allows measurements of ψ and Δ at different azimuth angles. Consequently, it is possible by aligning the wave vector of the incoming electromagnetic field with the extraordinary axis to maximize the interaction with the electric dipoles and record mainly the extraordinary optical properties. When the position of the extraordinary axis is unknown, the pseudo dielectric functions, which are functions of the azimuth angle, can be compared to the B-spline model of each axis to identify the ordinary and extraordinary axis orientations in the crystal. In section A.2 in the appendix, the ordinary and extraordinary orientation in the crystal are determined as a function of the azimuth angles.

Gen-Osc model

The purpose of the B-spline model is only to retrieve the overall shape of the dielectric functions from the data by using parabolic functions. However, this model has no physical origin and can not be interpreted in terms of oscillators. Thus, the B-spline model (MSE = 3.85) was converted into a general oscillator model to give a physical meaning to the dielectric function shape. In the classical picture, the absorption of an electromagnetic wave by a material induces an oscillating movement of its electric dipoles, whose frequency depends on the wavelengths of the incoming wave. The center frequency of the oscillators corresponds to the resonance frequency, at which the absorption is maximum.

Each absorption peak is modeled by a Tauc-Lorentz function. This function allows to model the behavior of the semiconductor below the bandgap. The number of oscillators required is based on the shape of the ε_2 function. The Gen-Osc model has an MSE of 3.8, similar to the anisotropic B-spline model with the Mueller matrix.

Figure 38 shows the general oscillator model for each axis. The ordinary axis is well-fitted with three Tauc-Lorentz oscillators, and their bandgaps are coupled. For the extraordinary axis, the intense absorption peak is well-fitted with only one Tauc-Lorentz oscillator.

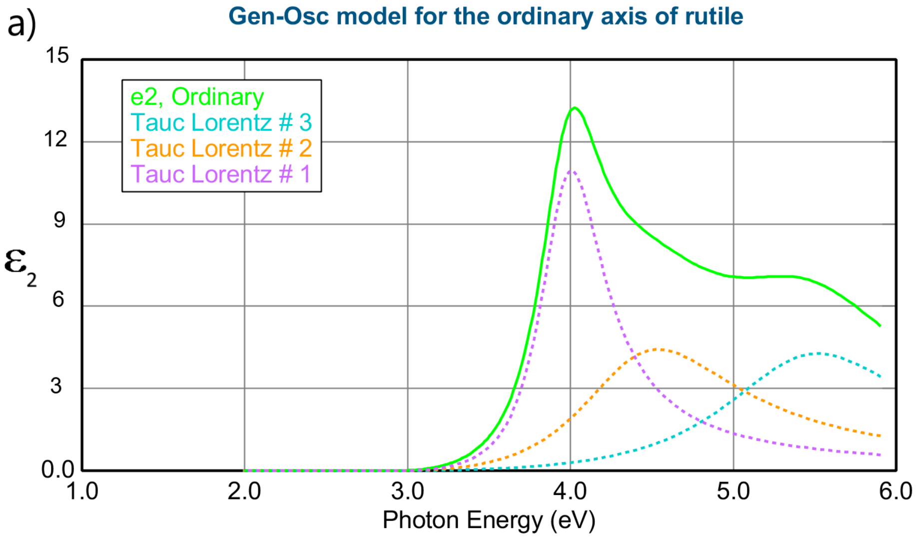

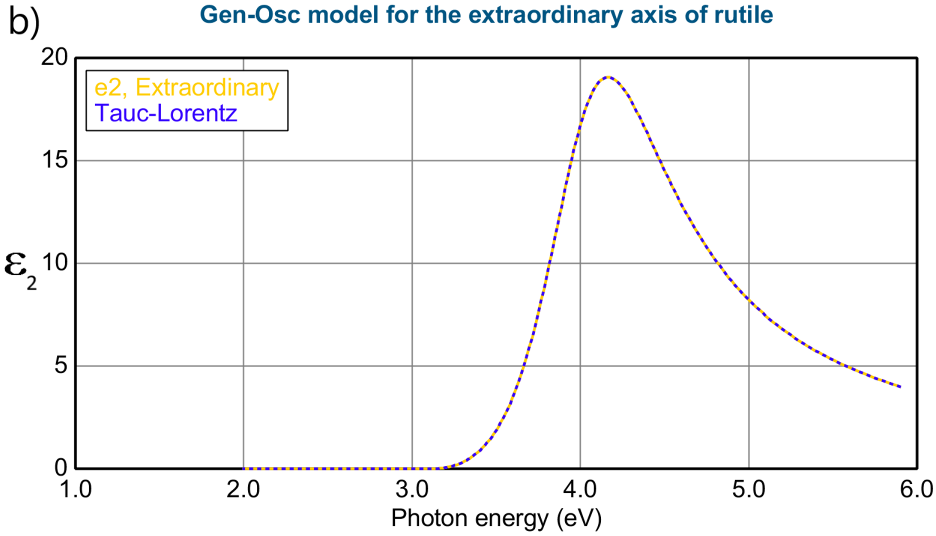

Figure 38: Graph of the General-Oscillator model (ε_2) for a) rutile ordinary axis and b) rutile extraordinary axis using Tauc-Lorentz oscillators (MSE = 3.8).

Table 4 presents the parameters of the Tauc-Lorentz for the Gen-Osc model for the ordinary and extraordinary axis of rutile.

Table 4: Parameters of the Gen-Osc model of rutile for the extraordinary and ordinary axis.

Type/Name	**Amplitude**	**Broadening**	E_o **(eV)**	E_g **(eV)**
		Ordinary axis		
Tauc-Lorentz #1	88.47	0.50	3.97	2.98
Tauc-Lorentz #2	32.48	0.97	4.47	coupled
Tauc-Lorentz #3	34.59	1.54	5.45	coupled
		Extraordinary axis		
Tauc-Lorentz	319.33	0.90	4.02	3.14

The three oscillators for the ordinary axis show that at least three optical transitions are involved in the absorption of rutile in this spectral range. The large broadening of the second and third Tauc-Lorentz oscillators, of 0.97 and 1.54 respectively, suggests that probably more optical transitions are contributing to the absorption. The unique Tauc-Lorentz of the extraordinary axis is a sign of intense absorption, where one transition is likely predominating. However, its large broadening suggests, as for the ordinary axis, that other transitions less intense are involved in the absorption process. More oscillators could have been used to fit the data, but without more information about the energy of the optical transitions, it can not be done in a relevant way. Later, the parameters of the Gen-Osc model can be used for the critical point analysis to initialize the parameters of the double derivative of ε_2.

The models give a bandgap of 2.98 eV for the ordinary axis and of 3.24 eV for the extraordinary axis. The ordinary bandgap coincides with the bandgap of rutile, 3.00 eV. Thus, during experimentation, such as PL, the measured bandgap is likely to be the ordinary bandgap.

Bandgap determination

Usually, direct bandgap materials have a sharper transition from the transparent region to the absorbing region, making it easier to determine the bandgap. For an indirect band, as the optical transition needs to be phonon-assisted, a smoother transition is expected. The dielectric function of rutile shows a sharp transition. Even if the nature of rutile bandgap is still discussed, this observation reinforces the idea of a direct bandgap.

In the following, a comparative study of the determination of the optical bandgap of rutile is presented. Two categories of methods are used, the first one based on linear fits of the absorption coefficient or of the extinction coefficient (Tauc plot), and the second one based on the dispersion relation used to fit the imaginary part of the dielectric function (ε_2) (i.e. the Tauc-Lorentz model). In addition, the values are compared to visual estimation of E_g directly from ε_2 as the curve presents a sharp elbow, and is discussed regarding the accuracy limit of the ellipsometry measurement (i.e. $k < 0.001$ or $\alpha < 3 \times 10^2 cm^{-1}$ at 500 nm).[21]

The Tauc plot is calculated from the absorption coefficient. The absorption coefficient for the extraordinary and ordinary axis of rutile are presented in figure 39.

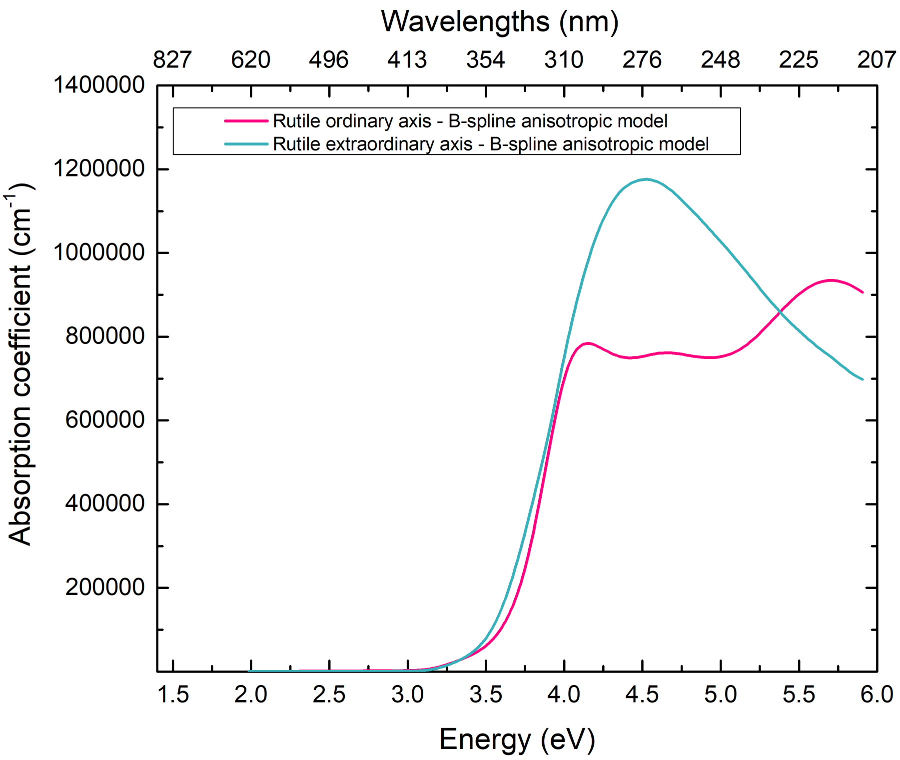

Figure 39: Absorption coefficient of rutile extracted from the B-spline model (MSE = 3.85).

The Tauc plot consist of fitting the graph of $(\alpha E)^{1/\gamma}$ using the following linear regression:

$$(\alpha E)^{1/\gamma} = A(E - E_g) \tag{54}$$

where A is a constant. Depending on the type of bandgap, the exponent γ changes from $\frac{1}{2}$ for a direct bandgap to 2 for an indirect bandgap.[93]

The following figure 40 shows different linear regressions for the determination of the bandgap of rutile from the dielectric functions of the anisotropic B-spline model. The uncertainty is calculated by taking three times the standard deviation for the values of the slope and the intersect. For the extinction coefficient, the linear regression is calculated for a range of values between 20% and 50% of the absorption maximum as in the paper by Di et al. [94] For the Tauc plot, two tangents are measured as the curves present two sections with different slopes.

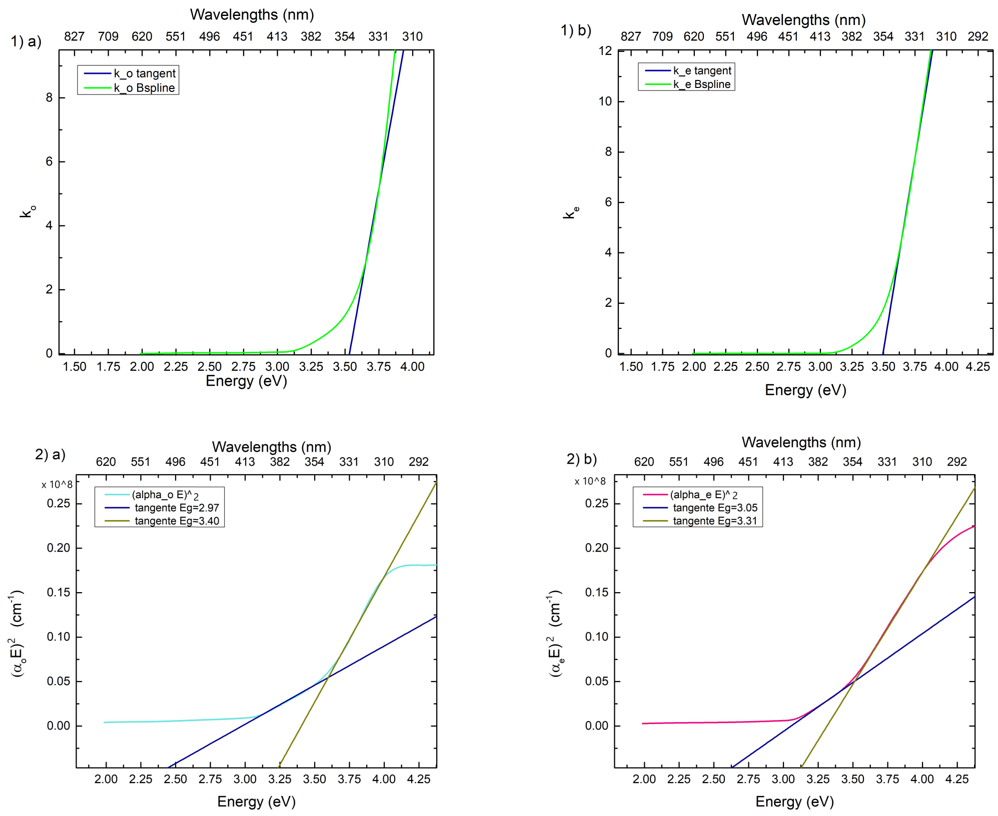

Figure 40: Determination of the bandgap through different methods: 1) via linearly fit of k, 2) via Tauc plot. a) and b) show respectively the ordinary and extraordinary axis.

However, the use of the Tauc plot method must be nuanced. Firstly, it was originally used for amorphous semiconductors, which have a smoother/lower bandgap transition than crystalline semiconductors.[93] Amorphous semiconductors present localized states near the band edges due to a lack of long-range order.[95] Secondly, the method is based on the assumption that the density of states of the conduction band and valence band behave as E^2 above the bandgap, and that $\hbar\omega\sqrt{\varepsilon_2} \sim E^2$[96]. The Eq.(54) was inspired by the work of Jan Tauc on amorphous germanium, to be extended and adapted to different materials and types of transition by selecting γ accordingly.

A second method is to use the accuracy limit of the SE measurement. Indeed, the ellipsometer is not sensitive to absorption below $3\times10^2 cm^{-1}$ (sometimes $5\times10^2 cm^{-1}$ or $6\times10^2 cm^{-1}$ values are also mentioned in the literature).[21] Figure 41 shows the absorption coefficient calculated with the dielectric functions from the anisotropic model (MSE = 3.85) and isotropic B-spline model (MSE = 1.10) for rutile (110) and (001) respectively.

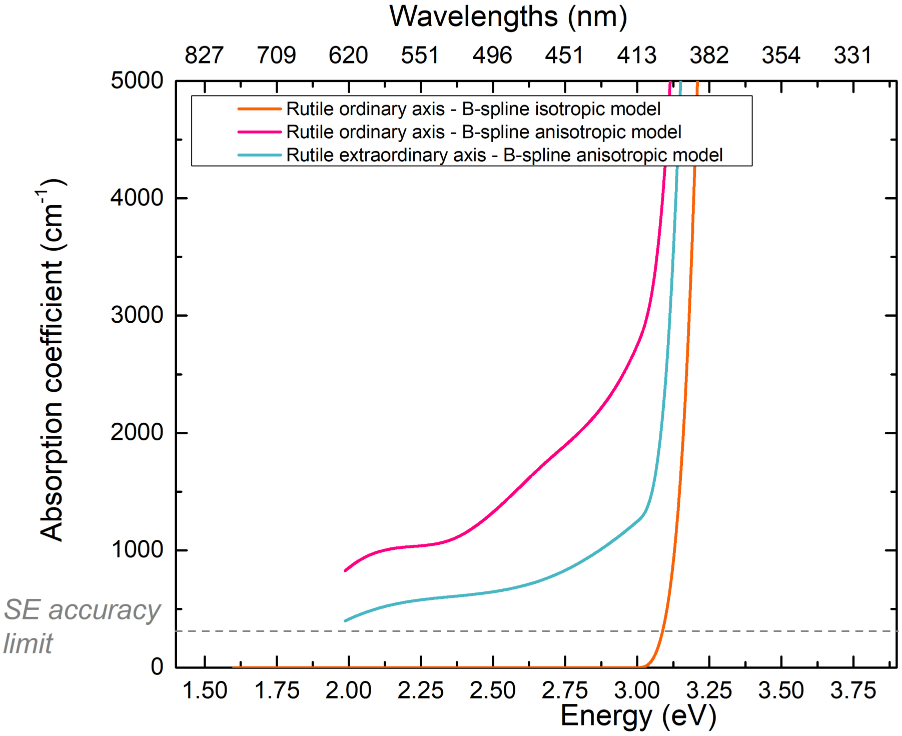

Figure 41: Graph of the absorption coefficient calculated from the anisotropic (MSE = 3.85) and isotropic B-spline model (MSE = 1.10) for rutile (110) and (001) respectively. The gray line shows the accuracy limit of the ellipsometer.

The transparent region of rutile is well modeled with the isotropic B-spline model from rutile (001) data, while, the anisotropic B-spline model represents poorly the transparent region of the semiconductor. Even if the absorption shows a sharp increase around the bandgap, the model fails to fit the data and seems to add an Urbach tail. As in rutile (110), both axes are measured and impossible to isolate completely. The fit induces a non-zero absorption below 3.00 eV. As a last estimation, the sharp transition at the absorption onset permits to notice the bandgap by a visual approach using the slope break.

The bandgap values obtained from the different methods are resumed in the following table:

Table 5: Comparison table of the bandgap of rutile determined from the anisotropic B-spline model (MSE = 3.85) and the isotropic B-spline model (MSE = 1.10) using the following methods: linear regression of k, Tauc plot, extraction of E_g from dielectric functions model with Tauc-Lorentz dispersion low, accuracy limit of the absorption coefficient, and visual estimation (i.e. slope break of α).

	Anisotropic B-spline model		**Isotropic B-spline model**
Method	**Ordinary axis**	**Extraordinary axis**	**Ordinary axis**
Linear regression of k	3.53 ± 0.50 eV	3.49 ± 0.19 eV	
Tauc plot (tangent 1)	2.97 ± 0.07 eV	3.05 ± 0.18 eV	
Tauc plot (tangent 2)	3.40 ± 0.15 eV	3.31 ± 0.03 eV	
Tauc-Lorentz model	2.944 ± 0.005 eV	3.130 ± 0.005 eV	3.046 ± 0.004 eV
Accuracy limit $\alpha < 3 \times 10^2 cm^{-1}$	*not possible*	*not possible*	3.08 ± 0.05 eV
α slope break	3.02 ± 0.05 eV	3.03 ± 0.05 eV	3.01 ± 0.05 eV

The linear regression k and the Tauc plot second tangent give higher estimations of the bandgap, while the first tangent and the bandgap from the Tauc-Lorenz model are closer to the experimental bandgap. For the method with the SE accuracy limit, no value can be determined for the anisotropic B-spline model, as the absorption coefficient presents an Urbach tail that exceeds the accuracy limit. Nevertheless, the isotropic B-spline model allows to extract a value for the bandgap at the point where the curve meets the accuracy limit (i.e. $\alpha = 3 \times 10^2 cm^{-1}$). Finally, the visual estimation using the slope break agrees with the globally admitted bandgap of rutile (3.00 eV). Both the Tauc-Lorentz method and the visual estimation give slightly higher bandgaps for the extraordinary axis of rutile.

The first two methods use linear regressions and thus depend highly on the energy range selected for the analysis. As depicted in figure 40 and table 5, two sets of data give hardly different values for the bandgap depending on the part of the curve chosen to calculate the tangents. Thus, although the Tauc plot is widely used in literature to determine the bandgap it is not a rigorous method and it is not possible to rely safely on the values it gives.

An exact determination of the bandgap is impossible by using the Tauc plot technique. In some cases, the accuracy limit of the absorption coefficient (respectively the extinction coefficient k) can be useful to estimate E_g, however, this estimation depends on the goodness of the model and on the measurements. In this present case, even if the MSE of the anisotropic B-spline model is quite low, the model is not perfect below the bandgap, and the absorption coefficient stays above the accuracy limit. There is no unanimous method to determine the bandgap from SE data. Thus, in the present SE analysis, the Tauc-Lorentz bandgap is used as an estimation of the bandgap.

5.1.2 Anatase dielectric functions models

Anisotropic uniaxial B-spline model

As for rutile samples, a B-spline model was built with the data of anatase (001) sample to model the ordinary dielectric function of rutile. The model is presented in section B.1 in the appendix. Then, the B-spline model for the ordinary axis is converted into an anisotropic uniaxial model in order to fit as well the extraordinary axis. This model is based on the anatase (110) sample which has both axes in its surface plane.

The dielectric functions of anatase (110) modeled by the anisotropic uniaxial model are depicted in figure 42, the model presents an MSE of 5.97.

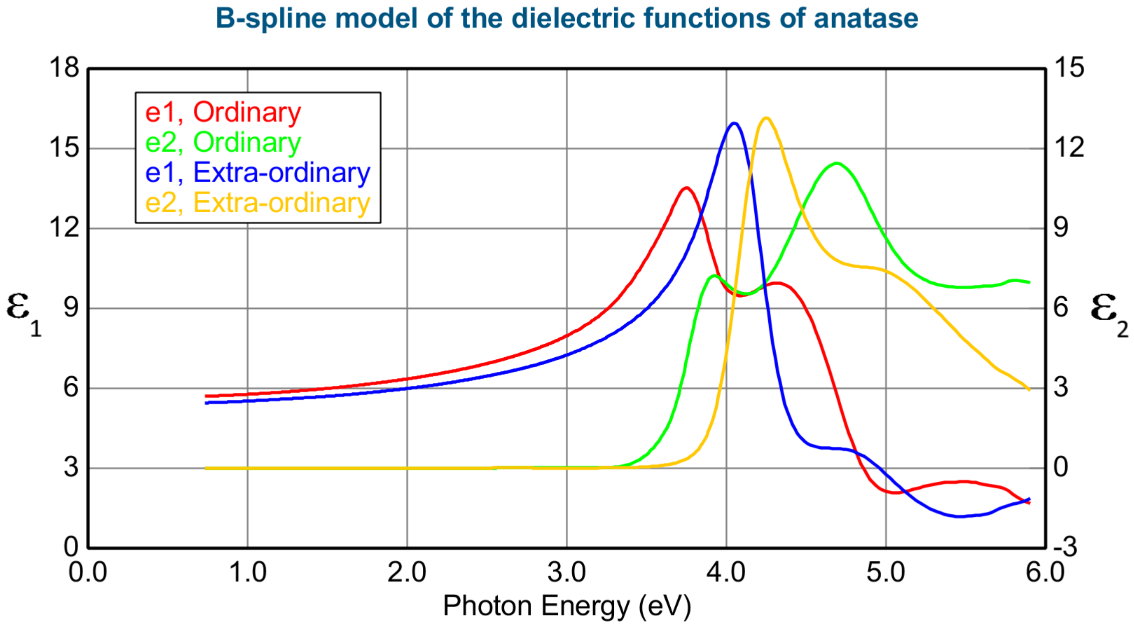

Figure 42: Dielectric function of anatase (110) fitted with an anisotropic uniaxial B-spline model (MSE = 5.97).

The sample presents a transparent region from 1.00 eV to ∼ 3.20 eV, and an absorbing region above 3.20 eV. The ordinary axis shows principally two contributions to the absorption. The first contribution is centered at ∼ 3.92 eV, and the second peak is at ∼ 4.69 eV. As for rutile, the extraordinary axis of anatase has the highest absorption than the ordinary one. The main peak is located at ∼ 4.25 eV, and a second peak is visible ∼ 4.90 eV. The broadening of the peaks suggests an absorption including multiple critical points. The absorption onset of the extraordinary axis appears to be ∼ 0.30 eV above the ordinary axis one. This difference can be explained by the difference in lattice constant between the axes, the extraordinary lattice constant c is about 40% of the ordinary lattice constant a ($c = 3.784$ Åand $a = 9.515$ Å[13]). Moreover, rutile shows a smaller difference in energy between the absorption onset of its ordinary and extraordinary axis, and has closer ordinary and extraordinary lattice constants; c = 64% a ($c = 2.9587$ Åand $a = 4.5936$ Å[13]). Thus, the higher asymmetry of the first Brillouin zone (i.e. the unit cell) in anatase compared to rutile corroborates the observation of a larger bandgap energy difference between the ordinary and extraordinary axis for anatase.

Section B.2 in the appendix presents the determination of the orientation of the extraordinary and ordinary axis of the anatase as a function of the azimuth angles.

Gen-Osc models for anatase

The dielectric functions extracted from the anisotropic B-spline model and from the isotropic B-spline model (see section B.1 in the appendix) were converted into two general oscillator models for anatase.

Figures 43 and 44 show the Gen-Osc model for the ordinary and extraordinary dielectric function of anatase. In Figure 43, the Gen-Osc converted from the anisotropic B-spline model and from the isotropic B-spline model are plotted for comparison purposes. The thin line corresponds to the anisotropic Gen-Osc model, while the dashed lines were extracted from the isotropic Gen-Osc model. Table 6 and 8 resumes the parameters of the Tauc-Lorentz oscillators used in the models.

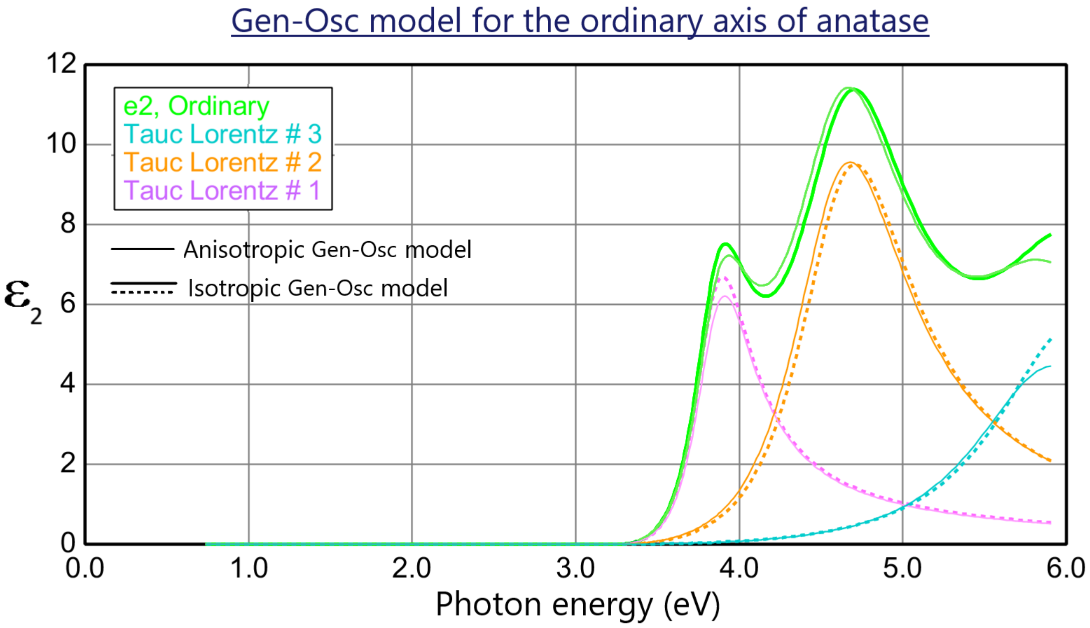

Figure 43: Comparison of the Gen-Osc models calculated from the isotropic B-spline model and the anisotropic uniaxial model of the dielectric functions for anatase ordinary axis of anatase. The thin line shows the Tauc-Lorentz oscillators of the anisotropic Gen-Osc, while the dashed line corresponds to the isotropic Gen-Osc model. The green curves are the sum of the oscillators in each model and represent the imaginary part of the dielectric function.

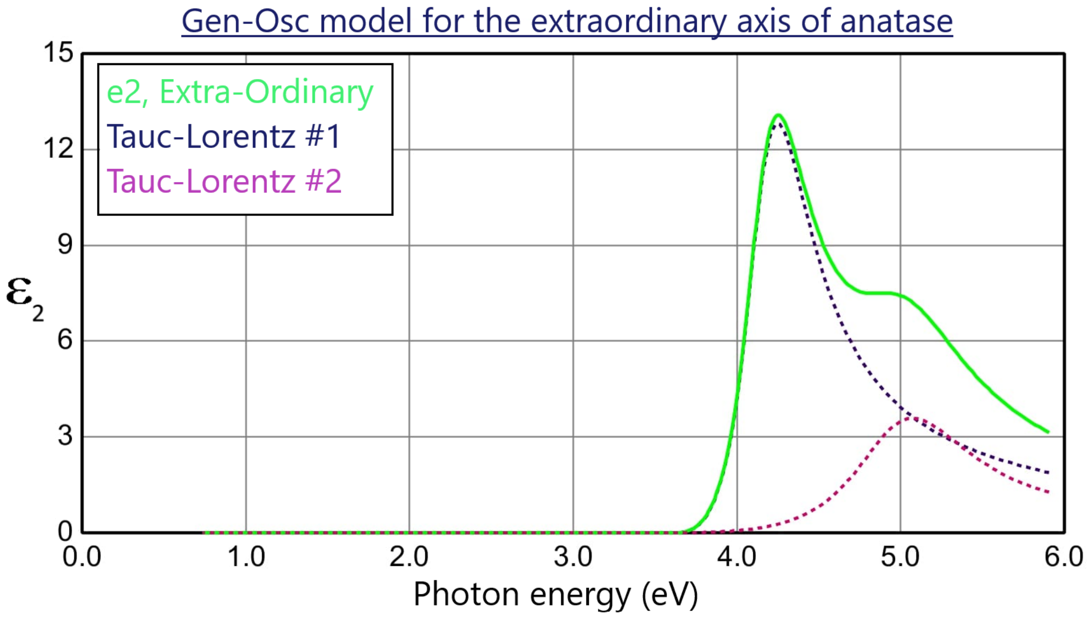

Figure 44: Gen-Osc model of the dielectric functions of the extraordinary axis of anatase.

Table 6: Table of the parameters of the Tauc-Lorentz oscillators for the ordinary axis of anatase, extracted from the isotropic (MSE = 2.23) and anisotropic Gen-Osc model (MSE = 5.91).

Type/Name	**Amplitude**	**Broadening**	E_o **(eV)**	E_g **(eV)**	**UV pole (Amp. – En. (eV))**	ε_∞
			Ordinary axis – Isotropic Gen-Osc model			
Tauc-Lorentz #1	114.628	0.423	3.841	3.259		
Tauc-Lorentz #2	89.858	0.860	4.637	coupled	15.260 – 6.708	1.870
Tauc-Lorentz #3	33.4119	1.273	6.043	coupled		
			Ordinary axis – Anisotropic Gen-Osc model			
Tauc-Lorentz #1	102.729	0.440	3.852	3.246		
Tauc-Lorentz #2	92.243	0.869	4.601	coupled	120.796 – 9.041	0.880
Tauc-Lorentz #3	27.243	1.233	5.886	coupled		

Table 7: Table of the Tauc-Lorentz oscillators for the extraordinary axis of anatase extracted from the anisotropic Gen-Osc model (MSE = 5.91).

Type/Name	**Amplitude**	**Broadening**	E_o **(eV)**	E_g **(eV)**	**UV pole (Amp. – En. (eV))**	ε_∞
			Extraordinary axis - Anisotropic Gen-Osc model			
Tauc-Lorentz #1	336.800	0.485	4.162	3.630	167.706 – 9.031	0.880
Tauc-Lorentz #2	41.230	0.886	4.990	coupled		

In figure 43, the absorption along the ordinary axis is modeled with three Tauc-Lorentz oscillators. Small deviations are visible between the isotropic Gen-Osc model and the anisotropic Gen-Osc model, especially for the energy position of the Tauc-Lorentz #2 (orange). In table 6, the parameters of the Tauc-Lorentz function are listed. The Tauc-Lorentz #1 exhibits a shift of 0.01 eV between the isotropic and anisotropic models, while the Tauc-Lorentz #2 shows a shift of $\sim$ 0.04 eV and the Tauc-Lorentz #3 a shift of 0.16 eV.
The bandgap varies also a little, from 3.246 eV for the anisotropic Gen-Osc to 3.259 eV for the isotropic Gen-Osc model. Both fitted bandgap are slightly above the experimental bandgap of anatase.

The extraordinary axis Gen-Osc model is composed of two Tauc-Lorentz functions, the first one at 4.162 eV and the second one at 4.990 eV. The extraordinary bandgap is determined to be 3.630 eV, which is considerably higher than the experimental bandgap of anatase, 3.20 eV. Thus, as for rutile, the indirect bandgap of anatase bandgap is the one measured experimentally.

Determination of the bandgap

Different methods were tested to determine the bandgap of rutile, and have shown that only a few methods give reliable values. Thus, for the bandgap analysis of anatase only the Tauc-Lorentz model, the accuracy limit of the absorption coefficient and the visual estimation are compared. Despite the fact that anatase has been determined to have an indirect bandgap, the absorption curves of the ordinary and extraordinary axis show a sharp transition allowing to estimate the bandgap directly from the model (as illustrated in figure 45).

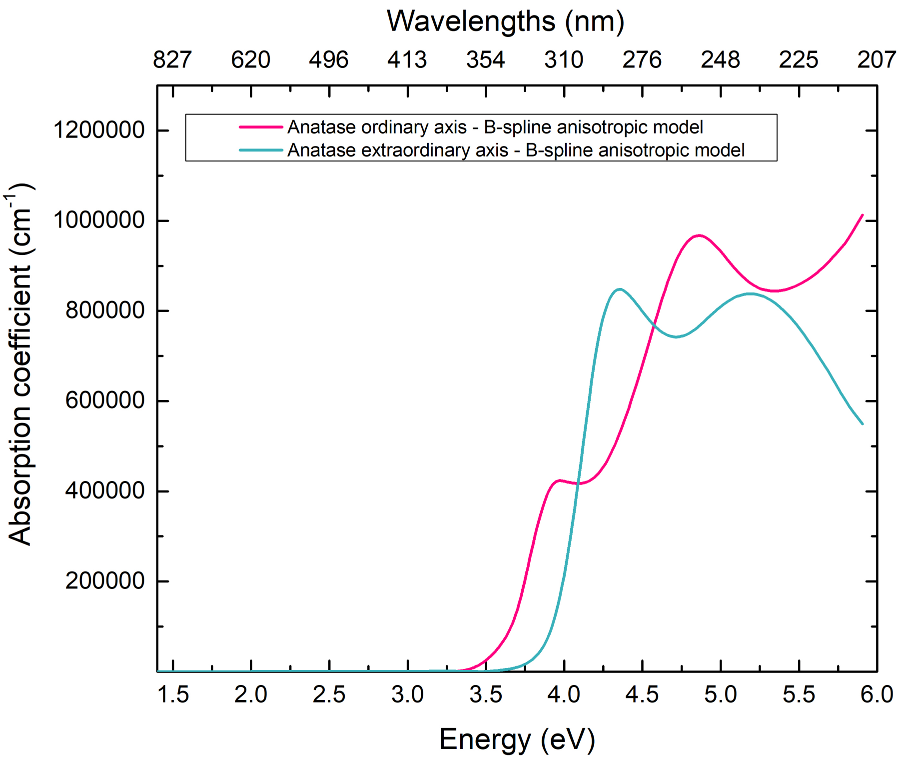

Figure 45: Absorption coefficient of anatase extracted from the B-spline model (MSE = 5.97).

Figure 46 shows the absorption coefficient from the anisotropic B*-spline model and the isotropic B-spline near the bandgap for comparison purposes. Like previously in the analysis of the bandgap of rutile, only the isotropic model for the ordinary axis models well the bandgap and respects the semiconductor behavior. Because of the presence of both axis in anatase (110), which complicates the analysis, the anisotropic B-spline model adds an absorption tail below the expected bandgap.

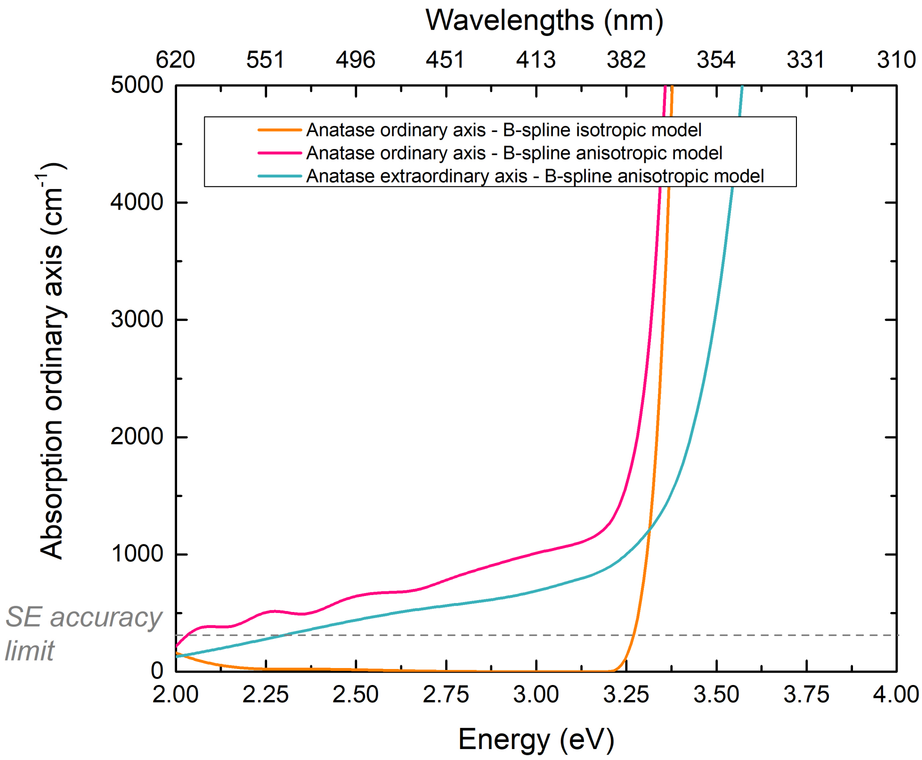

Figure 46: Absorption coefficient of anatase near the bandgap, comparison between the isotropic B-spline model and the anisotropic B-spline model.

Table 8: Table of the Tauc-Lorentz oscillators for the ordinary axis of anatase extracted from the isotropic Gen-Osc model (MSE = 2.23).

Type/Name	**Amplitude**	**Broadening**	E_o **(eV)**	E_g **(eV)**	**UV pole (Amp. – En. (eV))**	ε_∞
Ordinary axis – Isotropic Gen-Osc model						
Tauc-Lorentz #1	114.628	0.423	3.841	3.259	15.260 – 6.708	1.870
Tauc-Lorentz #2	89.858	0.860	4.637	coupled		
Tauc-Lorentz #3	33.4119	1.273	6.043	coupled		

Table 9 permits a comparison of the Tauc-Lorentz bandgap with the one determined via the accuracy limit of the absorption coefficient and with a visual estimation (i.e. slope break) for anatase. For the ordinary axis, the anisotropic B-spline model gives coherent values with both methods and the value from the literature. The isotropic B-spline model presents also values in accordance with the literature, although slightly higher for the Tauc-Lorentz and the accuracy limit methods. For the extraordinary axis, the value differs more between the different methods. Being subjective, the visual estimation is not a rigorous way to determine the bandgap. Thus, the Tauc-Lorentz seems a more relevant and reliable method for both axes. Like rutile, the extraordinary axis of anatase processes a larger bangap than its ordinary axis, which is thus the limiting bandgap.

Table 9: Comparison table of the bandgap of anatase determined from the anisotropic B-spline model (MSE = 5.97) and the isotropic B-spline model (MSE = 2.23) using the Tauc-Lorentz dispersion low from the Gen-Osc model, the accuracy limit of the absorption coefficient, and a visual estimation (i.e. slope break of α).

	Anisotropic B-spline model		**Isotropic B-spline model**
Method	**Ordinary axis**	**Extraordinary axis**	**Ordinary axis**
Tauc-Lorentz model	3.246 ± 0.005 eV	3.630 ± 0.005 eV	3.259 ± 0.005 eV
Accuracy limit $\alpha < 3 \times 10^2 cm^{-1}$	*not possible*	*not possible*	3.27 ± 0.05 eV
α slope break	3.20 ± 0.05 eV	3.30 ± 0.05 eV	3.19 ± 0.05 eV

Conclusion

Rutile and anatase dielectric functions present a larger absorption for the extraordinary axis, in addition to a higher bandgap: 3.630 eV versus 3.246 eV for anatase and 3.130 eV versus 2.944 eV for rutile (determined via the Tauc-Lorentz Gen-Osc model). In both cases, the ordinary bandgap corresponds to the literature values and is the limiting one. The close bandgap values for the ordinary and extraordinary axis of rutile could be due respectively to the direct and indirect transition. DFT calculations have shown that rutile possesses an indirect transition near its direct transition. [16] This could be verified by connecting the dielectric functions to the band structure of rutile if the critical points analysis is successful. An interpretation of the anisotropy from the shape of the absorption curves of the ordinary and extraordinary axes is difficult, however, the more pronounced amplitude difference in the case of rutile may suggest a stronger anisotropy than anatase.

5.2 Critical Points analysis – Initial study

In this section, an analysis of the critical points (CP) is performed on the dielectric function modeled with the B-spline model and on the theoretical dielectric functions calculated by DFT by Rasmus Hoholm during his master thesis. The ultimate purpose of such an analysis is to label the critical points in the band structure, which corresponds to the allowed optical transitions. To find the critical points in the band structure of TiO_2, the second derivatives of the dielectric functions are fitted with a CP line-shape:

$$\varepsilon(\omega) = C - Ae^{i\phi}(\hbar\omega - E_0 + i\gamma)^n \tag{55}$$

where $n = d/2 - 1$, ϕ is a multiple of π and accounts for the different kinds of CP giving its symmetry [25], A the amplitude, E_0 the energy of the transition at the CP, γ the lifetime broadening and C a constant background. Thus, for each feature in the second derivative, one or more critical points may be involved. As in every study involving data analysis with modeling and fitting, often several solutions are possible and the most technical point of the analysis is to select the most relevant one and find the correct assumptions. In the literature, the interpretation of the dimensionality of the CP ($n = d/2 - 1$) is subject to different interpretations, without having a clear meaning.

This chapter focuses on the ordinary axis of rutile. The first section contains a comparison of the theoretical and experimental dielectric functions. In the second section, the interpretation of the dimensionality and type of critical point is summarized for the reader. In the third section, an attempt to fit the critical points of the ordinary dielectric functions of rutile from the B-spline model and from the theoretical (DFT) dielectric functions is presented. The underestimated bandgap from the DFT calculations seems to be corrected with a blueshift of 1.17 eV. The DFT dielectric functions were best fitted with seven excitonic CPs located respectively at 3.98 eV,4.15 eV, 4.44 eV, 4.79 eV, 5.10 eV, 5.44 eV, and 5.90 eV. The SE dielectric functions were best fitted with four excitonic CPs located at 3.89 eV, 4.01 eV, 4.42 eV, and 5.57 eV.

5.2.1 Comparison of the theoretical and experimental dielectric functions

One of the challenges of this analysis is to find agreements between the theoretical dielectric functions and those based on the experimental model. DFT calculations are well known to underestimate the bandgap (i.e. find bandgap values lower than the experimental bandgap). This deviation is believed to result from the assumptions made in the calculation and the calculation itself. However, it has not been established yet in the literature if the DFT gives a wrong bandgap or not. For TiO_2, the DFT calculations of Rasmus Hoholm conduct to a bandgap of 1.81 eV for rutile and of 2.07 eV for anatase.

The first challenge is therefore to correct the DFT bandgap in order to find matches between theoretical and experimental data. To do so, the most common solution is to use the ”scissor operator” and to move the theoretical dielectric function to higher energies.[97] The main disadvantage of this method is that it introduces an uncertainty in the calculation of the energy positions of the optical transitions, because the shift cannot be performed in a foolproof way. The choice of the energy shift will have a direct impact on the position of the critical points, and thus of the optical transitions in the band structure. In addition to the shift, narrowing/shrinking or extending the theoretical dielectric functions could also facilitate the comparison, while adding additional uncertainty to the energy determination of the CP. For this reason, these additional tools were not used in this thesis. The shift also depends on the method used to determine the bandgap, which is different in the DFT calculation and in the Tauc-Lorentz model. In the model, the bandgap is one of the fitted parameters. While in the DFT calculation, its value depends on the approximations employed and its definition. However, the bandgap is originally defined as the difference of the ground states energy of a N-particles system with systems of (N-1)-particles and (N+1)-particles:$E_g = (E_{N+1} - E_N) - (E_N - E_{N-1})$. [98]

The DFT dielectric function were shifted to higher energies by the following shifts in order to determine the optimum shift:

- 1.02 eV to match the bandgap of rutile, i.e. 3.00 eV;
- 0.964 eV to match the ordinary axis Tauc-Lorentz bandgap of rutile, i.e. 2.964 eV;
- 1.17 eV to to match the first minimum of $\frac{d^2\varepsilon_{2,o}}{dE^2}$;
- 1.19 eV to to align the first peak of $\varepsilon_{2,o}$.

Figures 47, 48, 49, 50 show the comparison of the dielectric functions for the four shifts.

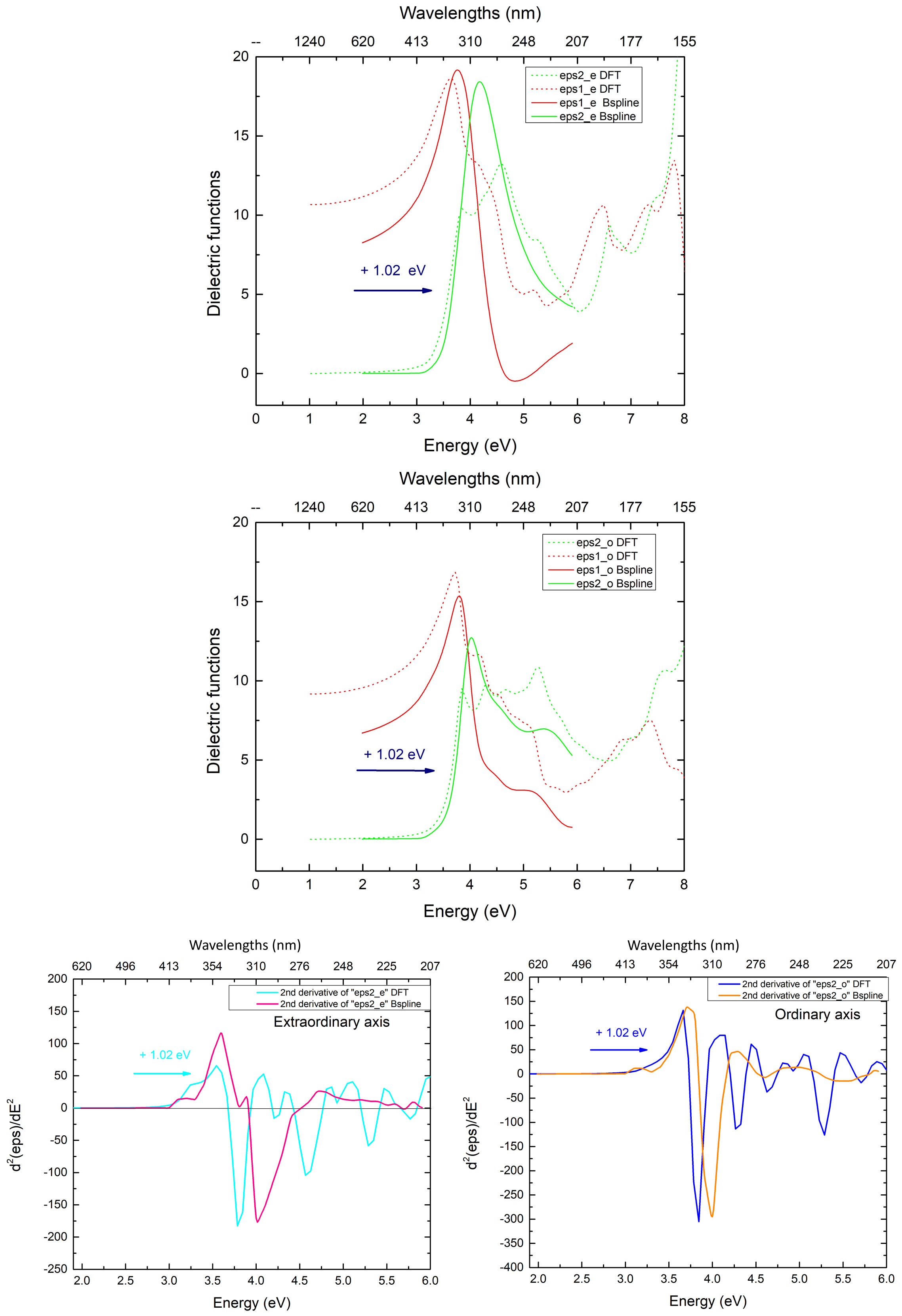

Figure 47: Comparison of the DFT dielectric functions shifted of 1.02 eV with the B-spline model (top graphs) and of their second derivative (lower graphs) for the ordinary and extraordinary axis.

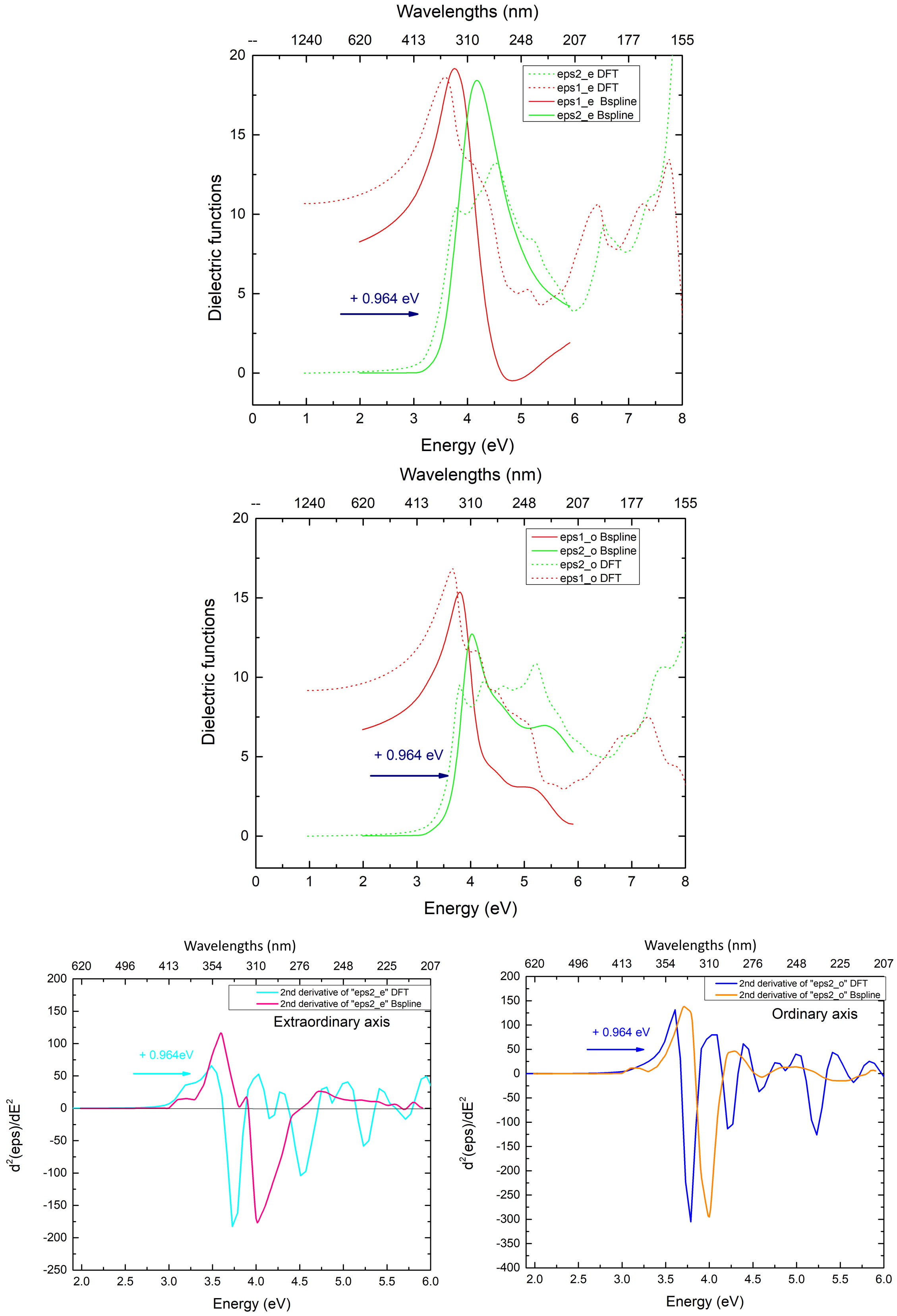

Figure 48: Comparison of the DFT dielectric functions shifted of 0.964 eV with the B-spline model (top graphs) and of their second derivative (lower graphs) for the ordinary and extraordinary axis.

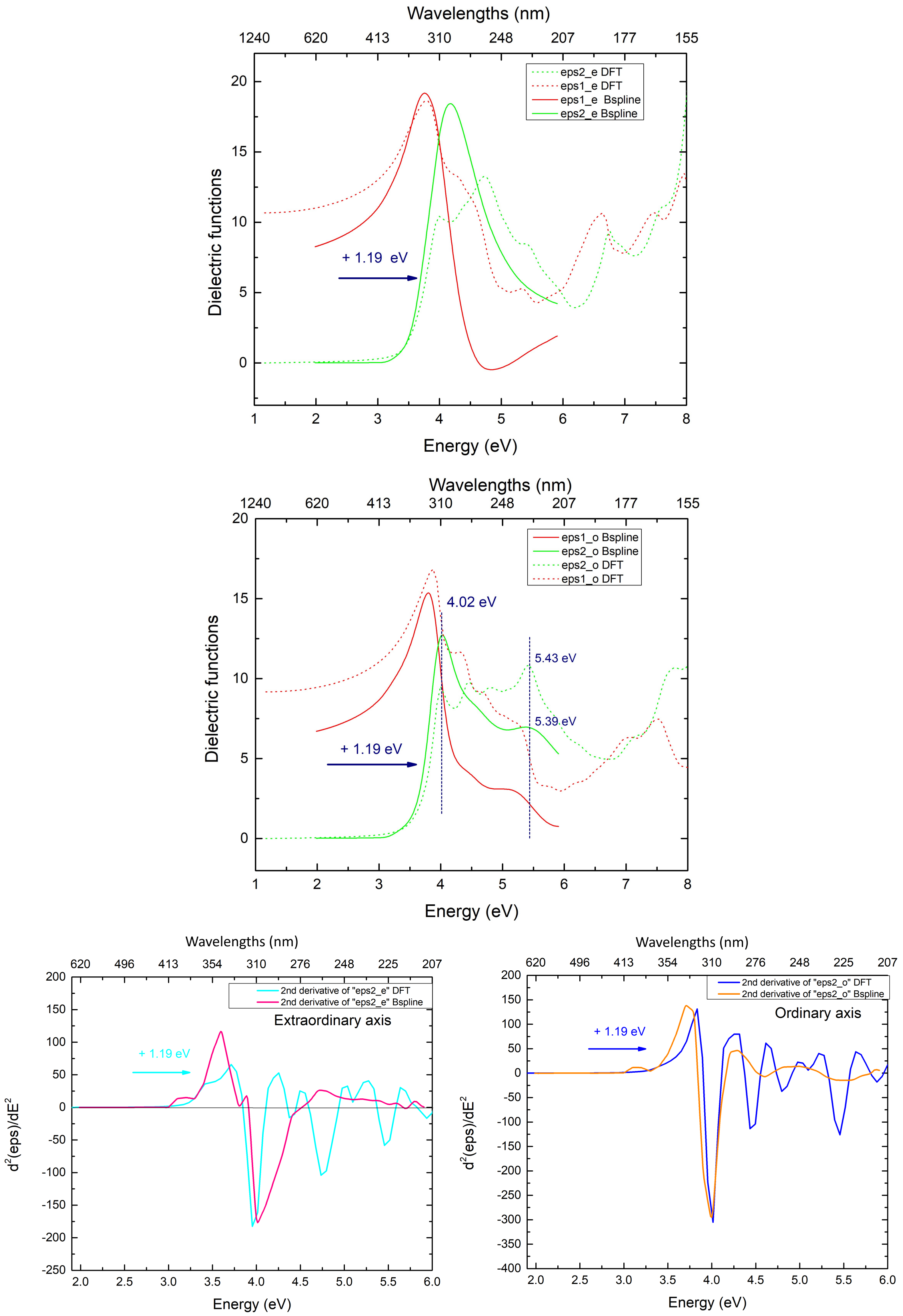

Figure 49: Comparison of the DFT dielectric functions shifted of 1.19 eV with the B-spline model (top graphs) and of their second derivative (lower graphs) for the ordinary and extraordinary axis.

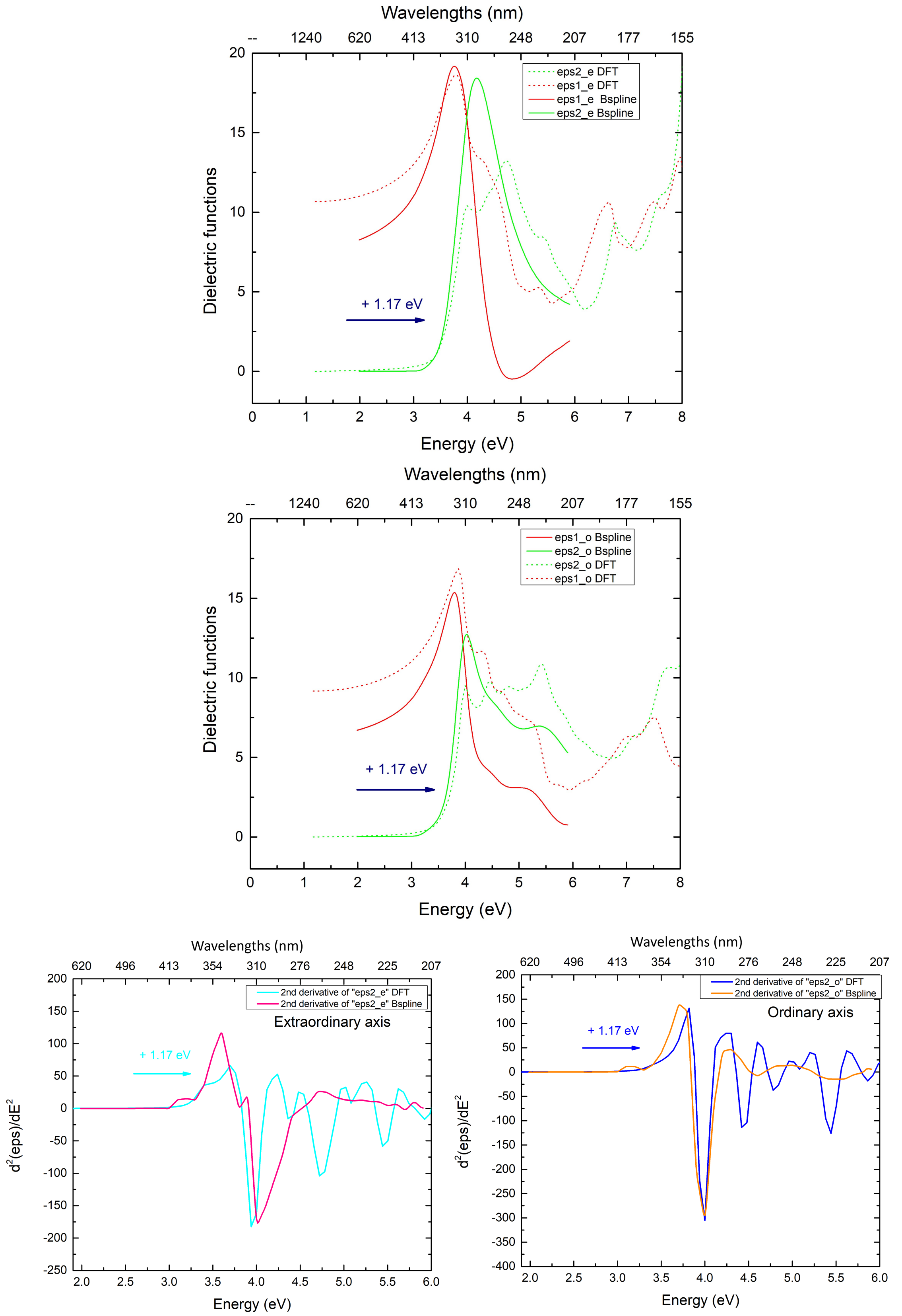

Figure 50: Comparison of the DFT dielectric functions shifted of 1.17 eV with the B-spline model (top graphs) and of their second derivative (lower graphs) for the ordinary and extraordinary axis.

When the theoretical functions are shifted by 1.02 eV to match the bandgap of rutile, they overlap pretty well with the B-spline model for both axis, as illustrated in figure 47. Let us consider the ordinary axis. The two first absorption peaks of the DFT calculations merged together to form a high peak in the B-spline model. While the third DFT peak seems to correspond to the shoulder of the B-spline. Finally, the last B-spline peak is more or less aligned with the fourth DFT peak. When one looks at the second derivative, the curves do not seem to overlap well anymore. The first oscillation, the most resonant, appears to be shifted to higher energies in the B-spline. Nevertheless, the results are coherent with the previous observation. A closer look at the second derivative shows that actually the b-spline oscillation is wider and incorporates the two oscillations corresponding to the two first DFT peaks. The six main oscillations (resonance shape) in the second derivative of the DFT data suggest that at least six critical points are involved, which means that six transitions are possibly associated with the absorption in the (3.00-6.00) eV range. For the extraordinary axis, it seems that the two first DFT peaks merged also to form only one intense peak in the B-spline model. About the second derivative, similar features are noticed than for the ordinary axis, six CPs also seem to be involved.
When the theoretical curves are shifted by 0.964 eV to match the bandgap extracted from the Tauc-Lorentz Gen-Osc model, as illustrated in figure 48, similar interpretations and connections can be done between the curves, but the shift seems less optimal.
As the DFT dielectric functions are rather broad in the range of (3.00-6.00) eV and count more CPs than the B-spline, the attempts to overlap the dielectric functions can be achieved with many different shifts. Conversely, since the second derivatives strengthen the sharpest features of the dielectric function, it is less easy to overlap them.

Afterward, shifts based on visual observations are tested to find optimal correlations. These methods produced successful results although the shifts are less easy to justify. One strategy is to choose the shift in order to align a maximum between the dielectric functions, which corresponds to a zero of the second derivative. Thus, the correspondence between at least one CP of the theoretical and B-spline curve is ensured. Shifting the DFT curve of 1.19 eV allows the overlap of the first absorption peak, as illustrated in figure 49. A second strategy is to directly choose the shift in order to overlap two features of the second derivative. This is the case for the 1.17 eV shift, whose purpose is to overlap the first minimum of $\frac{d^2\varepsilon_{2,o}}{dE^2}$, as illustrated in figure 50. The shifts of 1.19 eV and 1.17 eV give a good correlation between the dielectric function curves and the second derivatives. Considering the ordinary axis, for both shifts, the first B-spline and DFT peak can be assimilated to each other, but with the latter less intense for an unknown reason. Then, the second and third DFT peaks form the shoulder in the B-spline, and the fourth peaks are aligned. About the second derivatives, the first oscillation overlaps well, especially since they have the same amplitude, which would be helpful for the CP analysis. Since these offsets are chosen in terms of the ordinary axis, the correlation of the extraordinary axis is a little less optimal.

When attention is brought to the bandgap position, in the case of the 1.02 eV shift, the absorption onset is higher for the B-spline. This is at the opposite of what would be expected. In practice, the experimental data, more likely to include the effect of defects or impurities, should have logically a lower bandgap. To correct this, one solution would have been to shrink the DFT curve so that the broadening of the B-spline first peak covers the DFT peaks.
In the case of the 1.19 eV and 1.17 eV shifts, the B-spline presents a sharper absorption than the DFT curve which could suggest that its bandgap is above. However, it is clearly visible that the absorption in the experimental data starts at lower energies, which is more logical

and expected.

For the purpose of this analysis, that is to find correspondences of CPs between the B-spline model and the DFT dielectric functions, their second derivatives must match each-other to some extent. Shifting the DFT curve to the bandgap of rutile provides a low correlation between the curves, which is not really optimal for performing the critical points analysis. For this reason and the reason exposed previously regarding the bandgap, the 1.19 eV or 1.17 eV shifts are preferred in the further analysis, instead of the 1.02 shift which in the first instance seemed the most legitimate. Furthermore, the two absorption ranges, discussed in the next paragraph, of the DFT dielectric functions coincide better with Schubert dielectric functions (which were measured up to 8.00 eV) for the 1.19 eV and 1.17 eV shifts than for the 1.02 eV shift.

In the following, the 1.17 shift was selected with an uncertainty on the energies values is ±0.02 eV

The theoretical dielectric functions were calculated up to 30.00 eV. However, the major part of the absorption ranges between 2.00 eV and 10.00 eV (if the functions are considered before the "scissor operator"), and between 3.00 eV and 11.00 eV if considered after. The absorption of rutile can be divided into two parts: (3.50-6.50) eV region and above 6.5 eV. The DOS was also calculated by Rasmus and highlighted the same regions. The dielectric functions modelled with the B-spline model correspond to the first region. Because of the absence of measurements after 6.00 eV, the existence of a second region cannot be certified. However, the shape of the experimental dielectric functions, its decreasing trend, suggests the end of a first absorbing region. In a paper by Jiang et al., see figure 14 b) in section 2.4.4, the density of states of the different orbitals of TiO_2 were calculated. It was demonstrated that the DOS below the bandgap is mainly due to oxygen 2p-orbitals, while the 3d-orbitals of the titanium are mainly involved above the bandgap. In particular, the first region (3.50-6.50 eV) appear to be associated with $3d_{yz}$, $3d_{zx}$ and $3d_{yy}$ Ti orbitals, which all have a t_{2g} symmetry, whereas the second region involves $3d_{y^2-x^2}$ and $3d_{z^2}$ Ti orbitals, which have an e_g symmetry. The correlations between the density of states and the imaginary part of the dielectric functions demonstrates that the absorption peaks in the first region observed in the B-spline model and in the DFT calculations are due to transitions of electrons from the valence band, so in the 2p-orbitals of the oxygen, to $3d_{yz}$, $3d_{zx}$ and $3d_{yy}$ Ti orbitals. While the absorption peaks above 6.50 eV in the DFT calculation correspond to transitions from oxygen 2p-orbitals to $3d_{y^2-x^2}$ and $3d_{z^2}$ Ti orbitals.

5.2.2 Interpretation of the critical points

According to the theory, for a 3D critical point ϕ should take one of the following values: $0, \pi, \frac{\pi}{2}$ or $\frac{3\pi}{2}$. Only four types of CP are possible: a minimum (M_0), a maximum (M_3), and two saddle points (M_1,M_2). The critical points correspond to the poles of $\frac{1}{\nabla_k(E_c(k)-E_v(k))}$.

The type of CP is defined by the shape of the conduction bands in the reciprocal space. M_0 occurs when the conduction band is a minimum for the three directions in k-space (k_x, k_y, k_z), where k is the momentum of the electron in the crystal, M_3 when it is a maximum. The saddle points M_1 or M_2 take place when the conduction band presents a minimum or a maximum for two directions and the opposite type of extremum for the last direction.

Nevertheless, when the critical point analysis is performed and when it comes to fitting the parameters in Eq.55, forcing ϕ to be an integer multiple of π does not allow the fit to converge properly. As a matter of fact, its values listed above correspond to transitions between uncorrelated one-electron bands. This picture derives from the assumptions taken for computing the Hamiltonian and does not consider, for example, interactions between electrons and holes such as excitons. However, it is possible to take into account the many-body effects afterward by allowing ϕ to vary and take non-integer multiples of $\frac{\pi}{2}$. [21, 26]

The critical point line-shape in section 2.3.1 was calculated in the band model approximation where the system is reduced to one-electron in this crystal potential. Interactions between localized functions, such as Frenkel excitons, and delocalized wavefunctions (i.e. the band continuum) are not a part of this model. However, in practice, both types of wave-functions, localized and delocalized, participate in the energy levels of the crystal and affect the optical absorption spectra. Depending on the type of material, the localized effects are more or less significant.

In semiconductors with small bandgap and large dielectric constant (i.e. high polarizability ability), band-to-band transitions predominate in the CP line-shape (i.e. $n = -\frac{1}{2}, 0$ or $\frac{1}{2}$: 1D, 2D or 3D CP).[83] Their high polarizability ability leads to the screening of the Coulomb interaction of the excitons, if any, which results in large radii and weakly bound excitons. These excitons follow the Mott-Wannier model. Their energy levels can be assimilated to the hydrogen atom, and are given by a modified Rydberg equation. In this case, the critical points correspond to the Van Hove singularities, and the line-shape analysis can be treated as mentioned in section 2.3.2. Then, the critical points are said to have a band character according to Ref.[83]. Then, if the effect of the Wannier excitons is important, they can induce metamorphism of Van Hove singularities, which results in allowing a mixture of CPs, so ϕ to vary.

At the opposite, in semiconductors with large bandgap and small dielectric constant, Frenkel excitons take over the absorption spectrum and the CP can be fitted with a 1D line-shape (i.e. n = 0 and $\phi = 0$). [83] The Coulomb interaction between the electron and hole is strong, thus forming small and tightly bound excitons. Usually the electron and hole are located on the same atom but can hop to neighboring atoms, similarly to the propagation of a wave. The critical points are said to have a localized excitation character according to Ref.[83]. In this case, if the exciton energy states interact with the bands, once again this can be described by a metamorphism of Van Hove singularities. The line-shape now results from mixtures of excitonic CP with band-to-band CP, which is simply done by allowing ϕ to vary.

5.2.3 CP line-shape analysis

Now the experimental data correspond to the B-spline or DFT dielectric functions and the fitted data correspond to the dielectric functions fitted with the CP line-shapes. The analysis focuses on the ordinary axis of rutile.

In this part, different configurations of critical point line-shapes are tested and compared. The three variables that most influence the overall shape of the dielectric functions are the dimensionality embodied and associated with the parameter n, the type of CP ruled by ϕ and the energy of the transition E_0 at the CP. Depending on the initialization of these parameters, the amplitude A and the broadening Γ adjust themselves to fit the experimental curve. The parameters after the fit vary a lot from one initialization to another, for example, if ϕ is initialized to 180°instead of 0°will influence the final ϕ. However, the following comparison of different CP line-shapes shows that the energy position of the CP in the band-structure is nearly constant from one fit to another for the DFT dielectric functions. After the analysis, the limitations of the fit will be discussed.

Here, six fits are compared, denoted with alphabetical letters and the critical points with numbers. The first four fits are performed on the DFT dielectric functions shifted by 1.17 eV to match the B-spline dielectric functions, while the last two correspond to the B-spline model (MSE = 3.8). Excitonic CPs (i.e. n = -1) are mostly used for all the fits, except for CP1 and CP5 which are respectively 2D in fit b) (i.e n = 0) and 1D in fit a) (i.e n = -0.5). According to the theory, if the CPs are purely excitonic, ϕ must be zero. For this reason, all the excitonic CPs were initialized with $\phi = 0°$, but, ϕ was set unconstrained (i.e. no bounds: [0, 360] °) to authorize possible interactions between the band continuum and localized excitations, such exciton excitations.

The CP line-shape described as in Eq.(55) is valid only in an interval around E_0, but not for energies far from it. However, in the code the CPs are not restricted around their E_0 values. Consequently, it appears that some line shapes can affect the amplitude and broadening of the other CPs, as well as the overall shape of the functions. This is the case of the 1D, 2D, and 3D line-shapes whose dispersion is wider than for an excitonic CP (i.e. 0D). For this reason, in most papers and also in this study, excitonic line-shapes are the ones that best match the dielectric functions, even if from the theory a combination of CPs with different dimensionality seems the most likely. Moreover, without further analysis of the structure of the bands, it is impossible to say which CP has which dimensionality. Then the initialization of the dimensionality in the code can only be done by guessing. In future work, an analysis of the band structure in 4D (k_x, k_y, k_z, E) could allow the estimation of the CP positions by searching parallel tangents between the CB and the VB, and the estimation of the dimensionality by analyzing the curvature of the CB in the three reciprocal space directions. Then, these estimations could be used to initialize the CP parameters in the code.

The objective of fit c) and d) is to determine whether the fit may be made better with the incorporation of 1D and 2D CPs despite the tails of these CPs, particularly the resnorm (i.e., the residual squared norm).

The critical points are located at maxima in ε_2 which correspond to local minima in the second derivative. A visual analysis of the double derivative of the DFT dielectric functions shows that at least six critical points are involved in the absorption spectra, located respectively at the energies E_0: 3.99 eV, 4.41 eV, 4.77 eV, 5.07 eV, 5.43 eV, and 5.86 eV as illustrated in figure 51. Thus, all critical points were initialized with six CPS, corresponding to these six energy positions. For fit a) an additional CP was added at 4.17 eV (i.e. CP7) to match a specific feature of the second derivative. The initialization parameters for each fit are available in Section C.3 in the appendix. For the fits of the B-spline model, fit e) is initialized with the same positions as the DFT data, while fit d) is initialized with the following positions: 3.30 eV, 3.99 eV, 4.59 eV, and 5.31 eV, corresponding to the four local minima in figure 51.

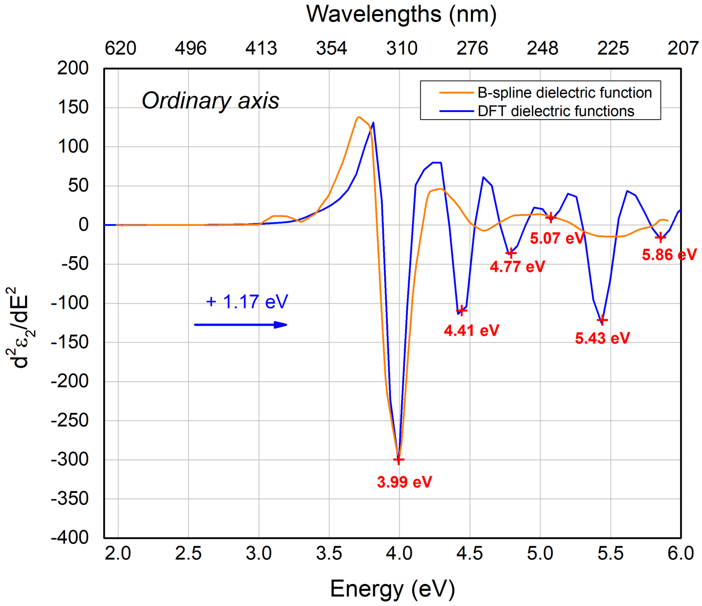

Figure 51: Comparison of the second derivative of ε_2 from the DFT dielectric functions shifted by 1.17 eV, and from the anisotropic B-spline model for rutile ordinary axis. The red crosses indicate the six possible CPs.

In the selection of the best fit, a particular attention was brought to:

- A squared norm of the residual as low as possible;
- ε_2 positive and a minimal offset between ε_2^{exp} and ε_2^{fit};
- No or as few as possible parameters close to the bounds after the fit.

The analysis starts with a comparison of the different fits in terms of the parameters: n, ϕ, and A, and then continues with a closer look at each fit. As already mentioned, the energies of each CPs are pretty stable from one fit to another for the DFT dielectric functions, as illustrated in figure 52. The DFT second derivative is indeed composed of well defined oscillations facilitating the analysis. For the B-spline model, as different positions were used for the initialization and a different number of CPs, E_0 differs between the fit. However, for fit e) which has the same initialization as the previous fits, the positions of the CPs are slightly lower but follow the same trend as fit a) to d). The energy of CP1 is comprised of [3.89, 3.98] eV.

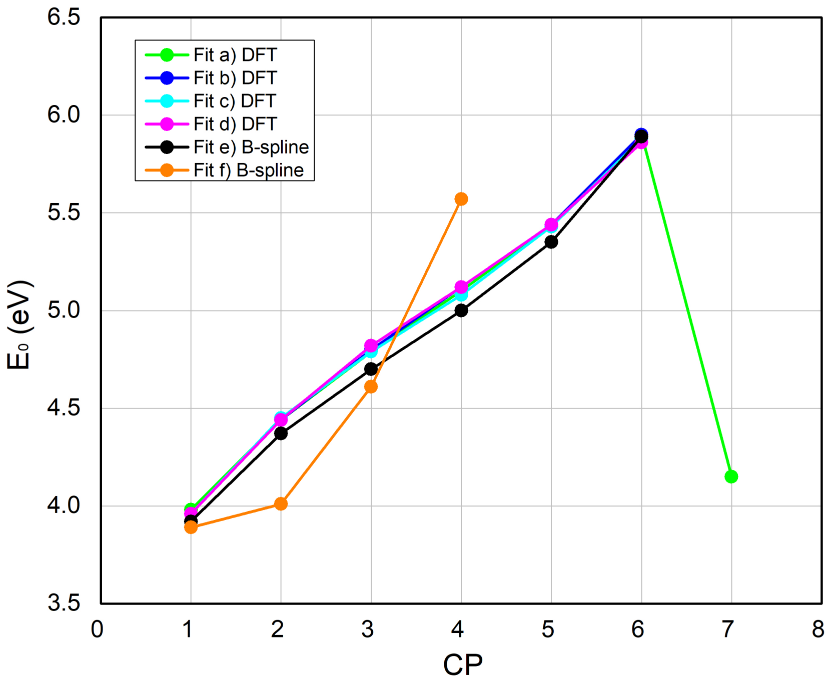

Figure 52: Comparison of the energy positions E_0 at each CPs for different fits. Fits a) to d) are performed on the DFT dielectric functions, while fits e) and f) are on the anisotropic B-spline dielectric functions for the ordinary axis of rutile (MSE = 3.8). All the CPs are excitonic (i.e. n = -1), except for CP1 and CP5 which are respectively 2D in fit c) and 1D in fit d). CP7 corresponds to the additional CP at 4.19 eV, which is why it is apart.

For A and ϕ, the values are more dispersed. It is evident from figure 53 that the amplitude depends on the dimensionality of the CPs: A is below 2.5 for most of the excitonic CPs (fit e) is an exception) and jumps between 3.5 and 4.6 for the 1D and 2D CPs. So most of the CPs have approximately the same weight in the fitted dielectric functions, except in fit e) where CP5 takes the lead over the others, especially CP6.

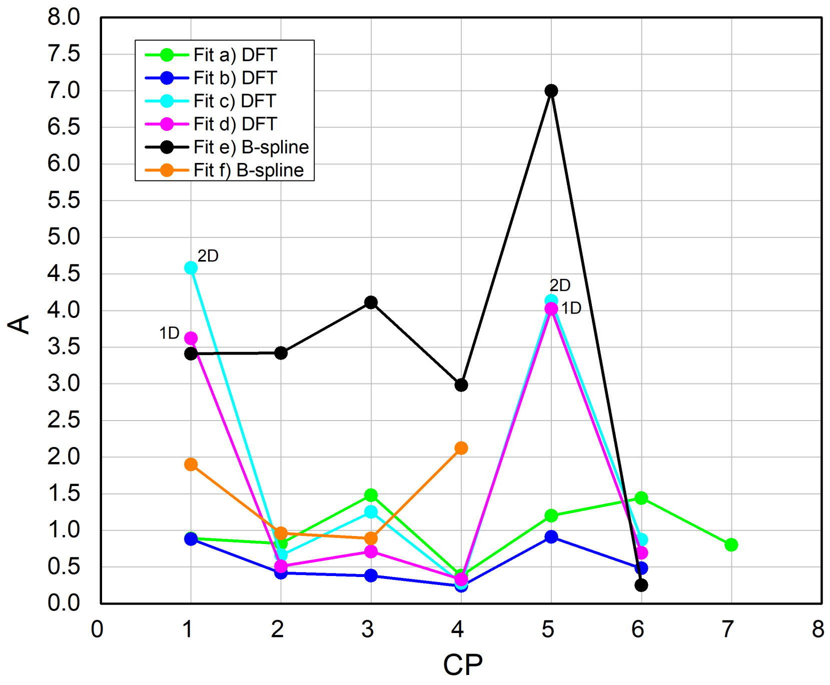

Figure 53: Comparison of the energy positions A at each CPs for different fits. Fits a) to d) are performed on the DFT dielectric functions, while fits e) and f) are on the anisotropic B-spline dielectric functions for the ordinary axis of rutile (MSE = 3.8). All the CPs are excitonic (i.e. n = -1), except for CP1 and CP5 which are respectively 2D in fit c) and 1D in fit d).

For ϕ, a majority of the values are dispersed around zero and 360 °), except fit e), as illustrated in figure 54, so relatively close to the pure excitonic case. For the 0D CPs, ϕ is close to 90°, while for the 2D CPs, ϕ is rather large, but not close to any nominal value of ϕ (i.e. integer multiple of $\frac{\pi}{2}$). The fit f) of the B-spline model follows quite well the fit b) of the DFT.

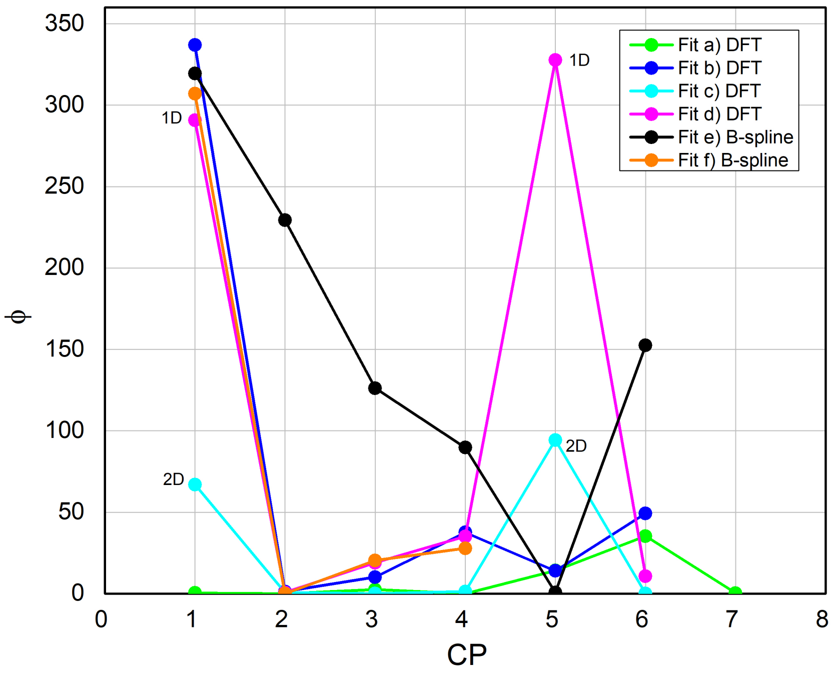

Figure 54: Comparison of the energy positions ϕ at each CPs for different fits. Fits a) to d) are performed on the DFT dielectric functions, while fits e) and f) are on the anisotropic B-spline dielectric functions for the ordinary axis of rutile (MSE = 3.8). All the CPs are excitonic (i.e. n = -1), except for CP1 and CP5 which are respectively 2D in fit c) and 1D in fit d).

For conciseness, only the fits a) and f), the fits that seemed the best for respectively the DFT dielectric functions and the B-spline dielectric function, are presented here. The detailed analysis of fits b), c), d) and e) can be found in the section C in the appendix.

- Fit a)

In this fit, ϕ is initialized to 0, and an additional CP was set at 4.17 eV. The fit has the lowest squared norm of the residuals, 1.39×10^4. In figure 55, each oscillation is fitted by one critical point, which is the purpose of the second derivative: to isolate the CPs to fit them separately. The deviations from the experimental curves are almost negligible.

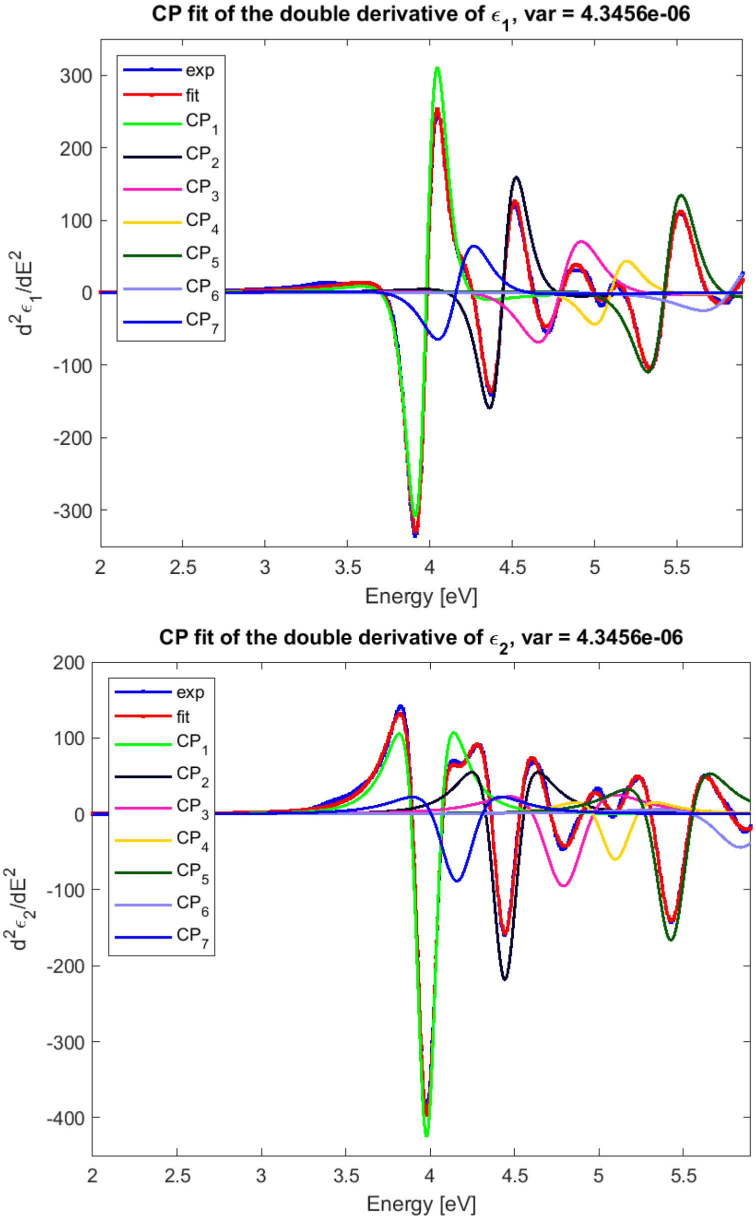

Figure 55: Experimental and fitted double derivative of ε_1 and ε_2 in fit a).

On figure 56, ε_1 and ε_2 are plotted. Only CPs in the [3.00, 6.00] eV range are used in the fit. An offset is noticed between the experimental and the theoretical curves in ε_1, but their shapes are similar. This constant difference results from the fitting procedure. As the fit is performed on the second derivative of the dielectric functions, the constant background C is not directly included in the fit, and so must be adjusted after. The sum of the CPs reproduces quite accurately the shape of the dielectric function in ε_2, however, it seems that the weights of the individual critical points do not match the experimental curve. For instance, CP5 and CP6 should have greater amplitudes. However, if that were the case, the tails of the CPs would cause the sum of the CPs to rise at lower energies as well, deviating from the experimental line. Last but not least, $\varepsilon_{2,fit}$ does not converge to zero below the bandgap, 3.00 eV, as quickly as it is predicted because of the tails. Nevertheless, the energy positions E_0 of the fit as well as the shape of the critical point around them seem correct. Because the critical point line-shapes are valid only around E_0, then if the dielectric functions do not overlap completely but the second derivative is well fitted, it doesn't mean that the fit is necessarily bad.

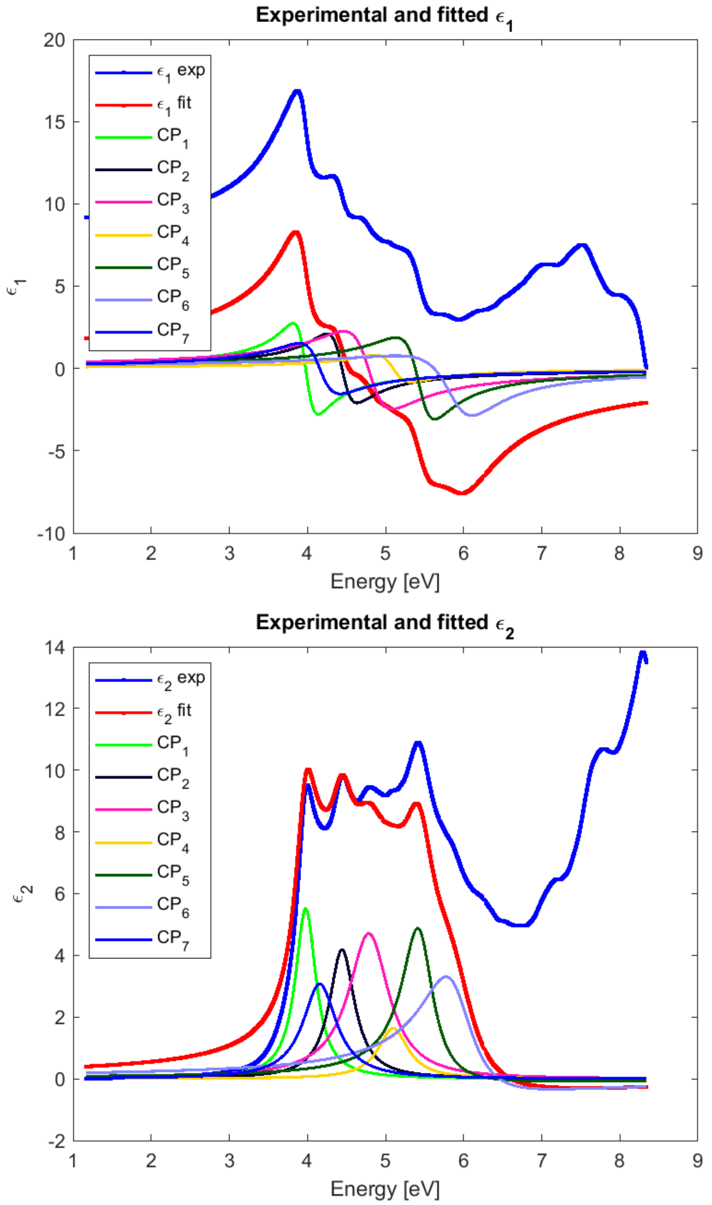

Figure 56: Experimental and fitted ε_1 (up) and ε_2 (bottom) for fit a).

The parameters of fit a) are presented in table 10. The energy positions of the CPS coincide with the values noticed in the visual approach in figure51. ϕ is rather small for all the critical points, suggesting that most of them correspond to pure excitonic CPs. Except for CP5 and CP6, which ϕ value rather away from integers multiples of $\frac{\pi}{2}$ suggests that they derive from the interaction of the exciton with the crystal lattice.

Table 10: Final parameters of the critical point line-shapes for fit a).

Name	A	Γ	E_0 **(eV)**	ϕ **(°)**	**n**	**CP type**
CP1	0.89	0.16	3.98	0.42	-1	0D
CP2	0.82	0.19	4.44	0.01	-1	0D
CP3	1.48	0.31	4.79	2.46	-1	0D
CP4	0.38	0.23	5.10	0.00	-1	0D
CP5	1.20	0.24	5.44	14.17	-1	0D
CP6	1.44	0.39	5.90	35.26	-1	0D
CP7	0.80	0.26	4.15	0.29	-1	0D

Table 19 in the appendix summarizes the initial parameters for fit a).

- Fit e)

Figure 57 shows the fitted and experimental second derivative of the dielectric functions. The fit seems correct: the fitted and experimental curves overlap. The squared norm of the residue is 2 times higher than fit a), which has the lowest value.

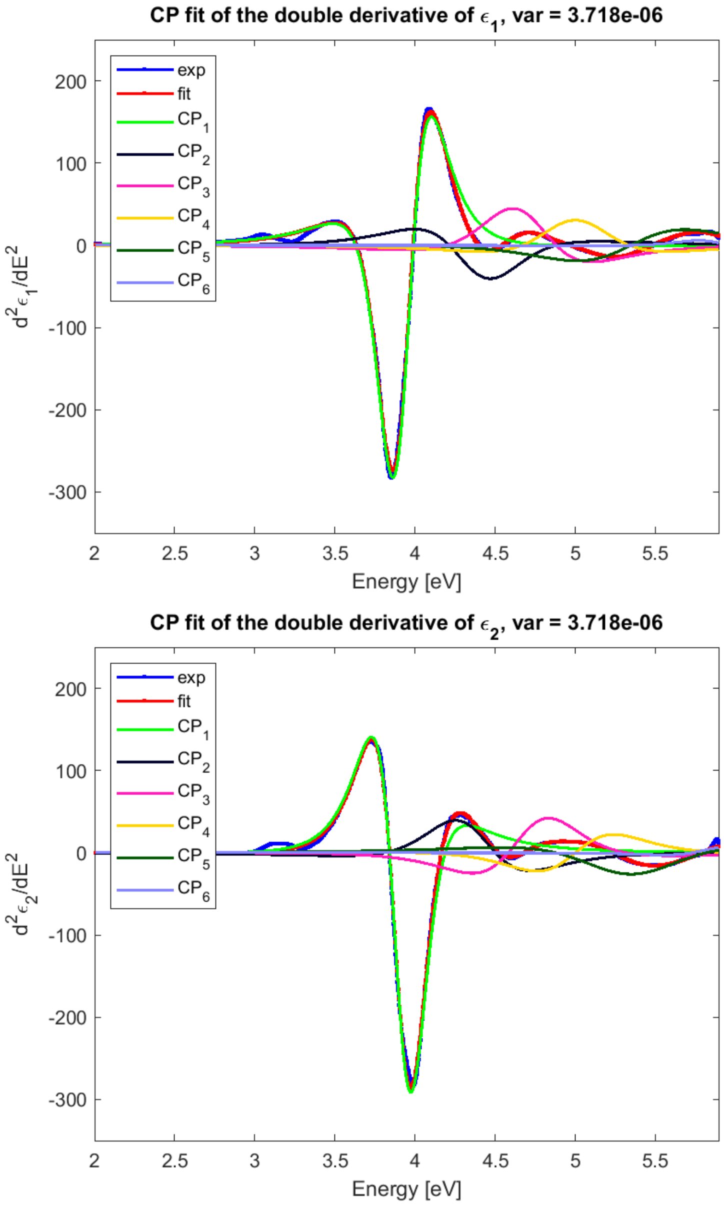

Figure 57: Experimental and fitted double derivative of ε_1 and ε_2 in fit e).

In figure 58, the dielectric functions are plotted. As before, the experimental and fitted ε_1 are shifted by a constant. For ε_2, the fitted curve, the sum of all the CPs, almost converges to zero below 3.00 eV, the bandgap. At higher energies, the curves do not overlap anymore. Due to the tails and width of CP3 and CP4, CP5 has to compensate by a large amplitude and broadening as illustrated in table 11.

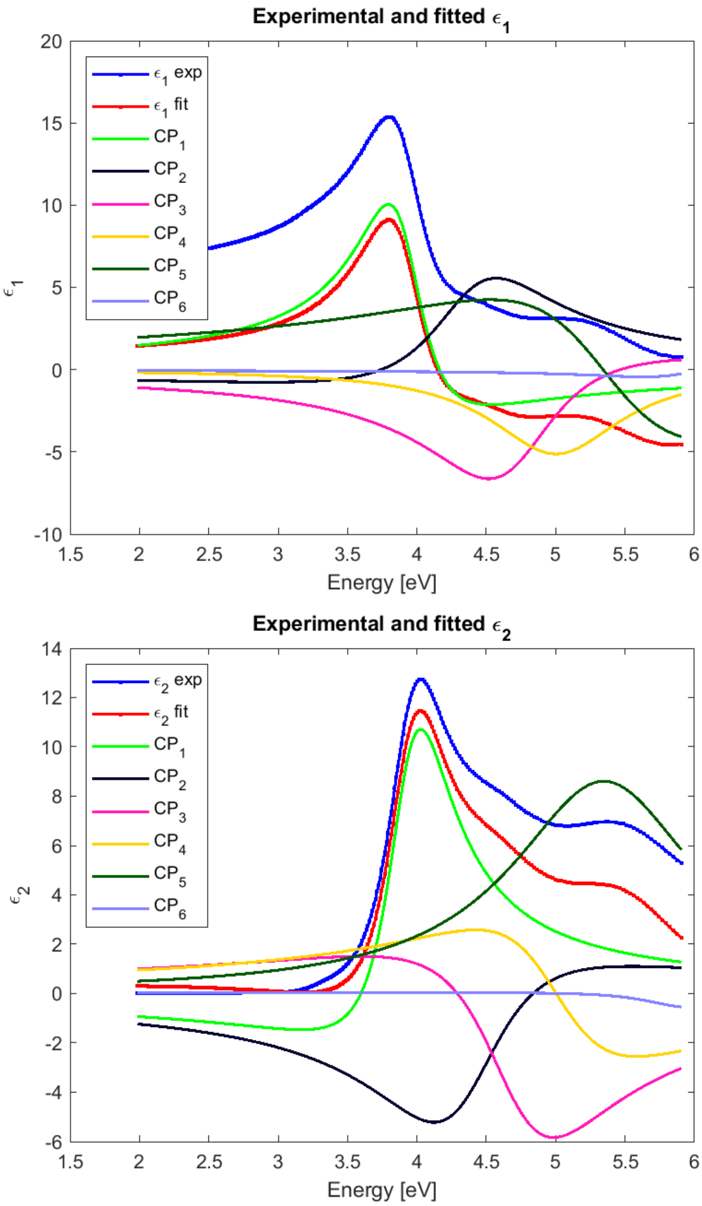

Figure 58: Experimental and fitted ε_1 (left) and ε_2 (right) for fit e).

Table 11 shows the final parameters of fit e). The phase ϕ are dispersed, only CP5 has a ϕ close to zero and could be considered as a pure excitonic CP. For all the other CPs, their ϕ values suggest a mix of CPs resulting from the interaction of the excitonic excitation with the band continuum.

Table 11: Final parameters of the critical point line-shapes for fit e).

Name	A	Γ	E_0 **(eV)**	ϕ **(°)**	**n**	**CP type**
CP1	3.41	0.28	3.92	319.42	-1	0D
CP2	3.42	0.54	4.37	229.38	-1	0D
CP3	4.11	0.56	4.70	126.12	-1	0D
CP4	2.98	0.58	5.00	89.66	-1	0D
CP5	7.00	0.81	5.35	0.71	-1	0D
CP6	0.25	0.42	5.89	152.42	-1	0D

Table 23 in the appendix summarizes the initial parameters for fit e).

- Fit f)

In figure 59, the second derivative of the dielectric functions is plotted. The fitted and experimental curves almost overlap perfectly. The squared norm of the residue is slightly lower than for fit e), so slightly better, and only 1.5 times higher than fit a).

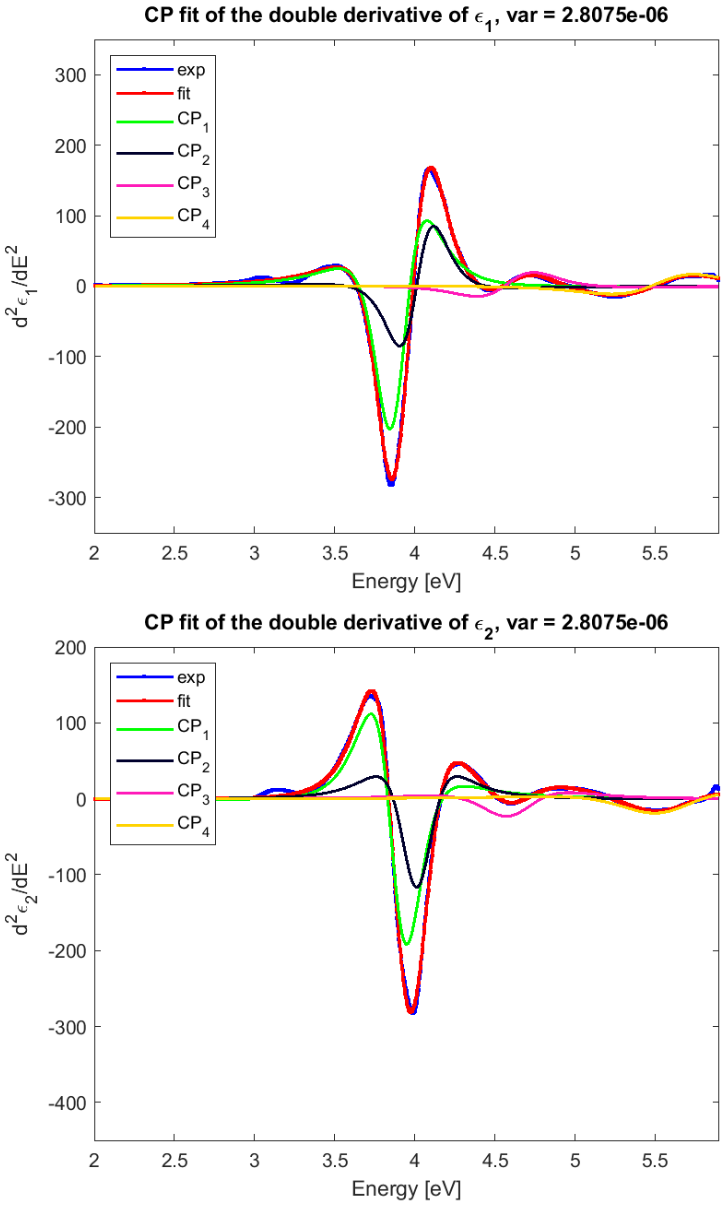

Figure 59: Experimental and fitted double derivative of ε_1 and ε_2 in fit f).

Figure 60 shows the dielectric function calculated from the fit, the fitted curves have similar features in fit e). But, this time it is CP1 that cancels with its tail a little the contribution of CP4.

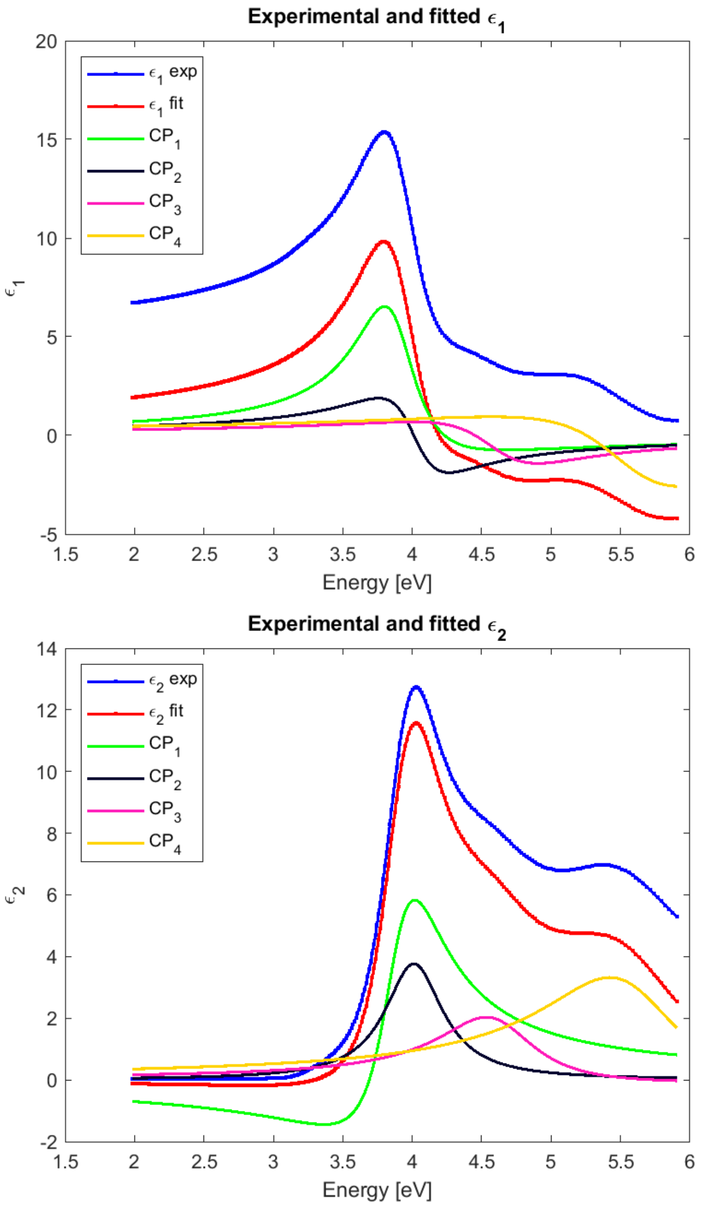

Figure 60: Experimental and fitted ε_1 (left) and ε_2 (right) for fit f).

Table 12 shows the final parameters of fit f). According to its ϕ, CP4 located at 4.61 eV is a purely excitonic CP, while the others result from a mix.

Table 12: Final parameters of the critical point line-shapes for fit f).

Name	A	Γ	E_0 **(eV)**	ϕ **(°)**	**n**	**CP type**
CP1	1.9	0.26	3.89	307.08	-1	0D
CP2	0.96	0.25	4.01	0.00	-1	0D
CP3	0.89	0.42	4.61	20.34	-1	0D
CP4	2.12	0.60	5.57	27.78	-1	0D

Table 24 in the appendix summarizes the initial parameters for fit f).

5.2.4 Conclusion

All the fits presented here manage to model globally the optical properties of the ordinary rutile axis, but the plausibility of each is questionable. Moreover, the code used is also subject to improvement, the limitations are described in the section C.2 in the appendix. In this context, it is difficult to designate one fit to be completely right, which is why the most correct fits were presented here.

Despite their differences, the fits of the DFT dielectric functions seem to agree on the energy of the transitions. So even though the dimensionality (n) and type (ϕ) of the critical point cannot be determined with certainty, the fits provide a first indication of the transitions involved in the absorption spectrum of the rutile. Comparing these energies with possible transitions in the rutile band structure, the critical points can maybe be associated with a high symmetry point in the first Brillouin zone. Nevertheless, based on their lower squared norm of the residue, fit a) seems to be the most relevant (followed by fit d)) for the analysis of the DFT data. The DFT dielectric functions were best fitted with seven excitonic CPs located respectively at 3.98 eV,4.15 eV, 4.44 eV, 4.79 eV, 5.10 eV, 5.44 eV, and 5.90 eV.

Fit e) shows that the B-spline dielectric functions can be fitted with almost the same number of critical points as for the DFT fit a), but with different line-shapes (i.s the phase ϕ are not the same in these fits). Nevertheless, fit f) with its four CPs appears to fit better the B-spline dielectric functions. Indeed, the B-spline model is smoother and wider than the DFT dielectric functions, thus, fewer CP line-shapes are necessary to reproduce its shape, leading to a fit with a better squared norm of the residue. The B-spline dielectric functions were best fitted with four excitonic CPs located at 3.89 eV, 4.01 eV, 4.42 eV and 5.57 eV.

On one hand, according to fit a) most of the CPs are purely excitonic, that is originating from absorption between the exciton energy levels in the crystal. These localized excitations are related to Frenkel excitons. On the other end, fits d), e), and f), present phases ϕ that do not coincide with an integer multiple of $\frac{\pi}{2}$. Thus according to the theory, the line-shape can be described by a mix of CPs. The absorption results from the coupling between the excitonic levels and the band continuum of the crystal lattice.

In general, the dielectric constant is inversely proportional to the square of the band gap energy.[99] Thus, TiO_2 as a large bandgap semiconductor would have a small dielectric constant. Then, according to Toyozawa et al., its optical spectra would be expected to show a localized excitation character (i.e. transition resulting mainly from excitons locally excited). In this case, fit a) seems to be the most relevant to describe the optical properties of the ordinary axis of rutile. On the other hand, TiO_2 has a high dielectric constant, which means that it mostly favors the formation of Wannier-Mott exciton, and thus its optical spectra would have predominantly a band character. From this perspective, the fit d), e) and f) would describe better the properties of rutile.

5.3 PL Results

In this section, the PL spectra of anatase (110), rutile (001) and rutile (110) single crystals and of the undoped TiO_2 thin films on STO substrate (named A2, B3 and B5) are presented and discussed. If the excitation wavelengths is not specified in the spectrum, $\lambda = 300$ nm was used.

5.3.1 Anatase (110)

Figure 61 shows the PL spectrum of anatase (110) reference sample at RT and 7K. A unique PL band in the emission range (2.20 - 3.90) eV is visible both at room and low temperatures. Both peaks have Gaussian shapes. The room temperature (RT) spectrum shows a wide band centered 2.82 eV with a full width half maximum (FWHM) of 1.05 eV. The 7K spectrum presents a large band centered to 2.78 eV and the FWHM increases to 1.11 eV. The strong peak at 2.07 eV is an artifact of the monochromator, the second-order peak of the source. The increasing tail at low energy is an amplification of the constant noise level due to the energy conversion. Indeed, the energy conversion transforms every constant function into a parabolic function, as the formula is proportional to λ^2.

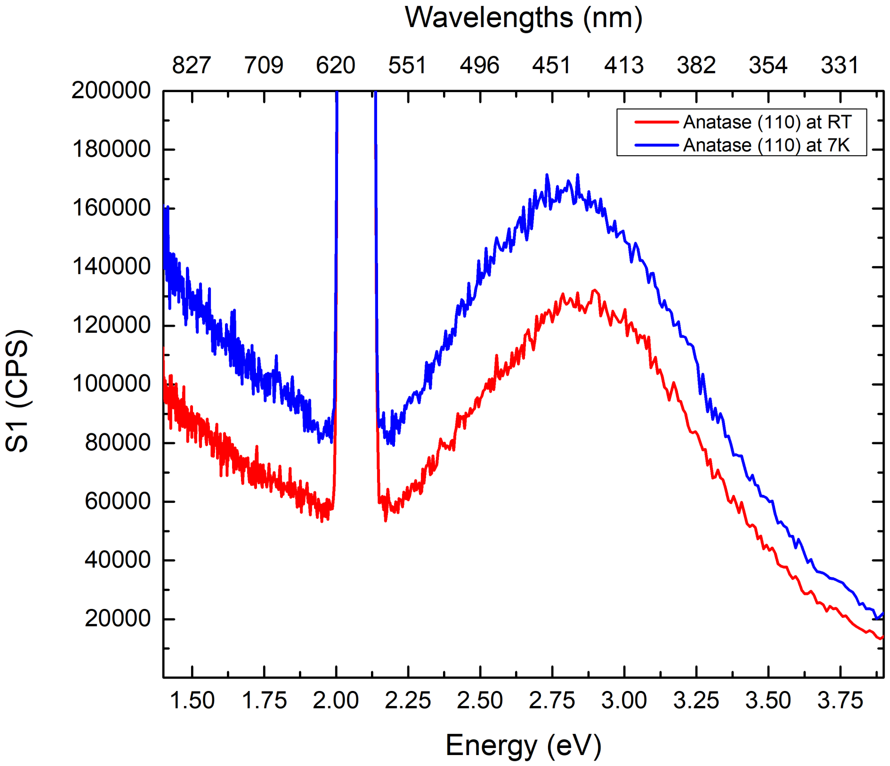

Figure 61: PL spectrum of anatase (110) recorded at RT and 7K, showing emission in the visible range.

Figure 62 shows the evolution of the PL intensity while varying the excitation wavelength. As the excitation wavelength increases, the band shifts towards lower energies, and the intensity of the band decreases. The PL spectrum at $\lambda = 300$ nm was recorded earlier in the day and does not follow the trend of the spectra at higher excitation wavelengths. Some light processes affect the luminescence of the $\lambda = 320$ nm and $\lambda = 340$ nm spectra at 3.16 eV and 3.35 eV.

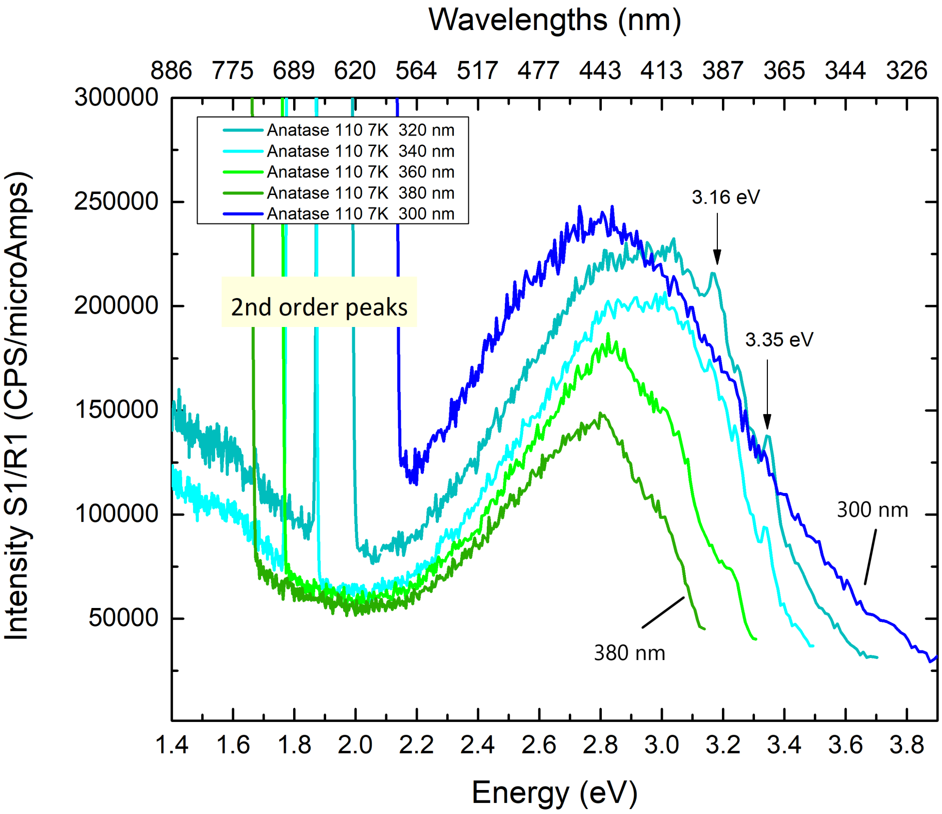

Figure 62: Anatase (110) PL intensity normalized by the reference detector intensity at varying excitation wavelengths: 300 nm (4.13 eV), 320 nm (3.88 eV), 340 nm (3.65 eV), 360 nm (3.44 eV) and 380 nm (3.26 eV).

A curve fitting of the spectrum is performed in order to determine the possible origins of the broadening and of the sub-bandgap emission. As the band does not show any obvious peak which would have given an idea of how to deconvolute the spectrum, the strategy is to achieve a comparative study. The PL band is fitted accordingly to the PL analysis in the article Ref.[53], described in section 2.4.4. Four different types of defects are reported in the article: self-trapped excitons (STE) at 2.86 eV (anatase bulk), oxygen defects at 2.30 eV and 2.67 eV, and charge transfer from Ti^{3+} to TiO_6^{2-} at 2.52 eV. Finally, the peak at 3.19 eV is attributed to the phonon-assisted indirect transition from M to Γ in the first Brillouin zone of anatase $\mathrm{TiO_2}$. Each contribution is fitted with a Gaussian distribution, whose area gives an idea of the proportion of the defect type in the samples.

Figure 63 shows the results of the fit for the measurement at RT. The positions of the peaks are fitted with five Gaussian functions and fixed at the positions used in Ref.[53]. The details of the fit parameters are in table 13. Figure 64 presents the results of the fit for the measurement at 7K. The parameters of the fit are shown in table 14.

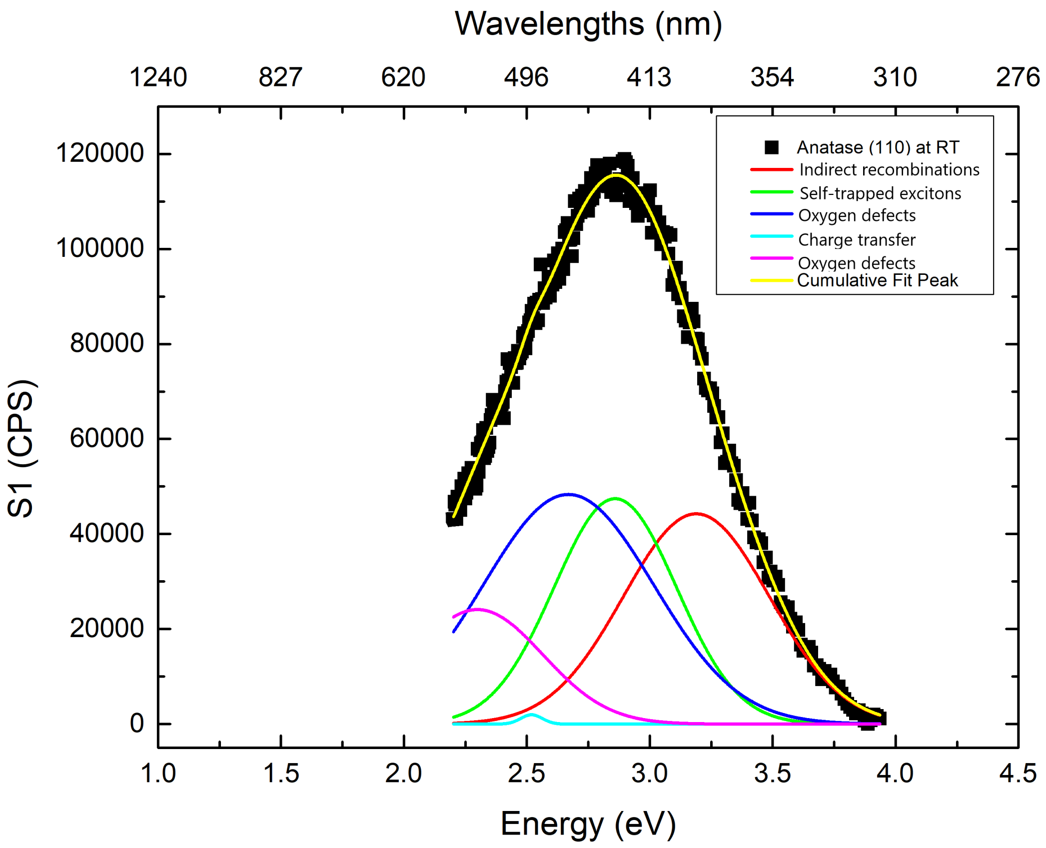

Figure 63: Curve fitting of anatase (110) PL spectrum at RT using the same Gaussian positions as in Ref.[53]. The red curve is attributed to indirect transitions, the green curve to STE, the dark blue and pink to oxygen defects, and the light blue to the charger transfer related emission.

Table 13: Fitting parameters for RT anatase (110) PL spectra curve fitting.

Origin of the emission	E_{peak} (eV)	Peak Area	FWHM	Intensity (CPS)
Indirect recombination	3.19	$(32.9 \pm 6.6) \times 10^3$	0.70 ± 0.14	$(44.2 \pm 8.8) \times 10^3$
Self-trapped excitons	2.86	$(29.6 \pm 5.9) \times 10^3$	0.59 ± 0.12	$(47.4 \pm 9.5) \times 10^3$
Oxygen defects (F or F^{2+})	2.67	$(42.0 \pm 8.4) \times 10^3$	0.82 ± 0.16	$(48.3 \pm 9.6) \times 10^3$
Charge transfer	2.51	216 ± 43	0.10 ± 0.02	$(2.0 \pm 0.4) \times 10^3$
Oxygen defects (F^+)	2.30	$(16.1 \pm 3.2) \times 10^3$	0.26 ± 0.05	$(24.1 \pm 4.8) \times 10^3$

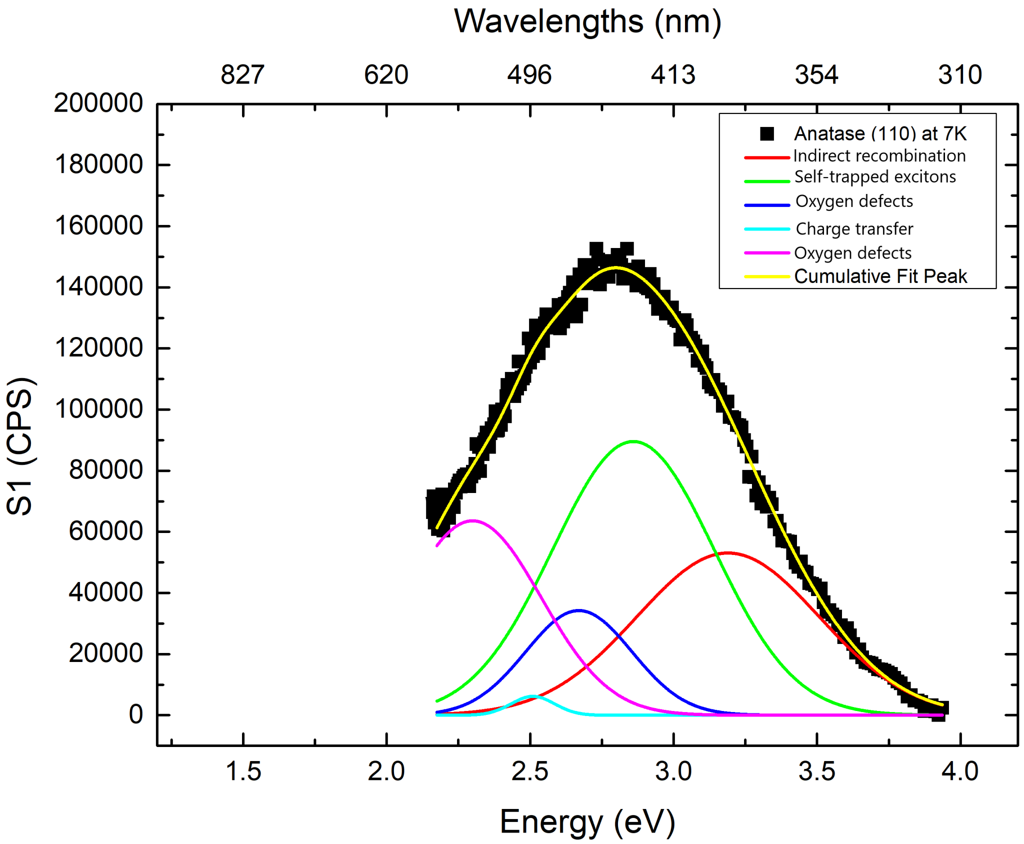

Figure 64: Curve fitting of anatase (110) PL spectrum at 7K using the same Gaussian positions as in Ref.[53]. The red curve is attributed to indirect transitions, the green curve to STE, the dark blue and pink to oxygen defects, and the light blue to the charger transfer related emission.

Table 14: Fitting parameters for 7K anatase (110) PL spectra curve fitting.

Origin of the emission	$E_{peak}(eV)$	Peak Area	FWHM	Intensity (CPS)
Indirect recombination	3.19	$(42.3 \pm 4.2) \times 10^3$	0.75 ± 0.07	$(53.0 \pm 5.3) \times 10^3$
Self-trapped excitons	2.86	$(63.0 \pm 6.3) \times 10^3$	0.66 ± 0.07	$(89.6 \pm 9.0) \times 10^3$
Oxygen defects (F or F^{2+})	2.67	$(15.9 \pm 1.6) \times 10^3$	0.44 ± 0.04	$(34.2 \pm 3.4) \times 10^3$
Charge transfer	2.51	$(1.2 \pm 0.1) \times 10^3$	0.19 ± 0.02	$(6.2 \pm 0.6) \times 10^3$
Oxygen defects (F^+)	2.30	$(38.0 \pm 3.8) \times 10^3$	0.56 ± 0.06	$(63.6 \pm 6.6) \times 10^3$

The curve fitting gives an idea of the proportion of different defects in the material and of the main contribution of the PL. However, as the band is large and smooth this analysis is only indicative. Based on it, for the RT spectrum, the indirect bandgap recombinations at 3.19 eV, the STE emission at 2.86 eV, and the oxygen defects emission at 2.67 eV are the main contributions to anatase (110) PL, as illustrated in figure 63. Then comes the contribution of the oxygen defects at 2.30 eV, while the charge transfer from Ti^{3+} to TiO_6^{2-} contribution at 2.52 eV is very little. At 7K, the main contribution seems to be attributed to STE at 2.86 eV, then to oxygen defects at 2.30 eV, and to indirect recombination at 3.16 eV, as illustrated in figure 64. Oxygen defects at 2.67 eV have a smaller contribution. Finally, as previously the charge transfer contribution is very little at 2.52 eV.

Discussion

The PL spectra show clearly that energy states below the bandgap (i.e. below 3.20 eV) are involved in the recombination processes, either from defects or impurities that induce states below the CB or above the VB. An optical broadening of a band is a sign of the non-perfect uniformity of the sample. Indeed, the PL spectra are very sensitive to the environment where is taken the measurement, but also the history and purity of the sample. Thus, PL spectroscopy often gives a lower bandgap (i.e. emission onset) than other bandgap determination techniques. If the measurement conditions and the sample were ideal, a PL band starting at the bandgap would be expected. A similar emission band is reported in the literature both at RT and 7K, as described in section 2.4.4. The band is mainly attributed to STE and oxygen defects emissions. The curve fitting agrees with the literature, at RT the emissions related to the indirect band-t-band transition, to the STE and to the oxygen, defect have similar contributions. This result corroborates the fact that TiO_2 is known to have oxygen defects and that its anatase polymorph favors the formation of STE. At 7K, the STE contribution stands out more. The excitonic emission in anatase is expected to be more important than in rutile, as the exciton binding energy in anatase is larger. [86]

At low temperatures, the non-radiative recombination is reduced because fewer phonons are available and because the thermal energy in the material is too small compared to the activation barriers of certain processes. This explains why the intensity of the band increases at 7K compared to RT, as illustrated in figure 61. At the same time, from the curve fitting it appears that the emission from STE increases at 7K (green curve in figure 63 and 64), and the maximum of the emission undergoes a little red-sift.

Figure 62 shows the evolution of the PL intensity while varying the excitation wavelength. As the excitation wavelength increases, the band shifts towards lower energies, highlighting the contribution of lower energy states inside the conduction band and of sub-bandgap states. These states and thus this emission are likely due STE and oxygen vacancies according to the curve fitting. In particular, the PL spectrum at $\lambda_{exc} = 380$ nm ($E_{exc} = 3.26$ eV) shows no bandgap emission at all (i.e. nothing above 3.2 eV). Measuring the PL spectrum at lower excitation energy gives an insight into the proportion of the defects and impurities in the sample.

Conclusion

In conclusion, as the width of the band is large and the sample is natural, and so its purity and history are unknown, the possible origins of the sub-bandgap PL are difficult to determine accurately. However, from the curve fitting of the data and the literature review, STE emissions seem to contribute the most to the sub-bandgap PL at 7K. Indeed, the STE formation is favored by the octahedral geometry of the TiO_6 complex which is the build unit of the crystal. This emission occurs mainly just below the bandgap. For emissions even deeper in the bandgap, oxygen defects and impurities in the bulk appear to be the plausible origin of the PL, due to the natural crystal nature of the anatase (110) sample.

The curve fitting was a useful tool to investigate the origin of the PL, which moreover agrees with the literature. However, this curving fitting must be taken with some criticism, because of the wide PL band of anatase, no specific features could be fitted. Moreover, the position of the Gaussian was fixed to the values of Ref.[53], which influences hardly the results. The fitted Gaussians are not necessarily completely representative of the recombination process happening and are just indicative.

5.3.2 Rutile (001) and (110)

Figures 68 and 67 show the PL spectra of rutile (001) and (110) samples at 7K and RT in the short wavelength range, (310-620) nm. Figures 66 and 65 show the PL spectra of rutile (001) and (110) samples at 7K and RT in the long wavelength range, (730-890) nm.

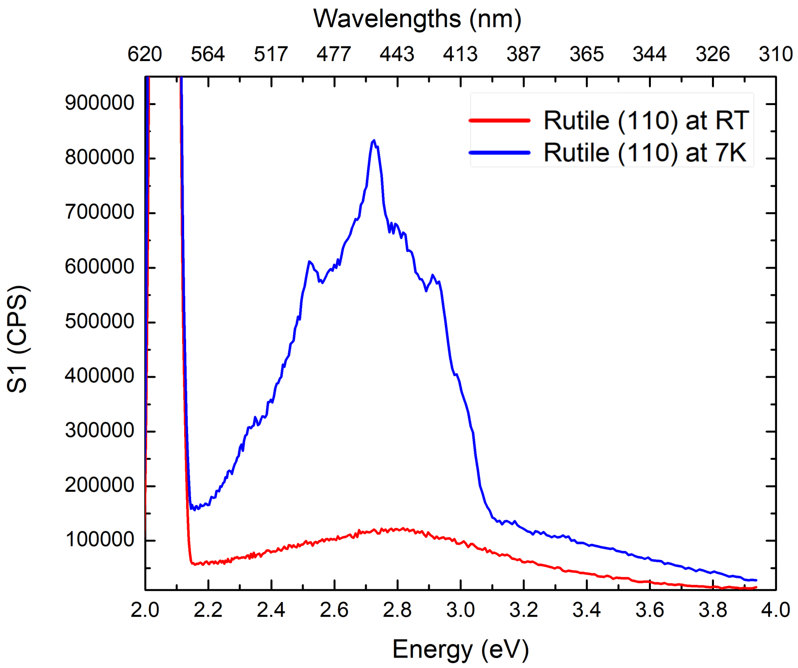

Figure 65: PL spectrum of rutile (110) sample at RT and 7K in the short wavelength range in the long wavelength range; NIR band.

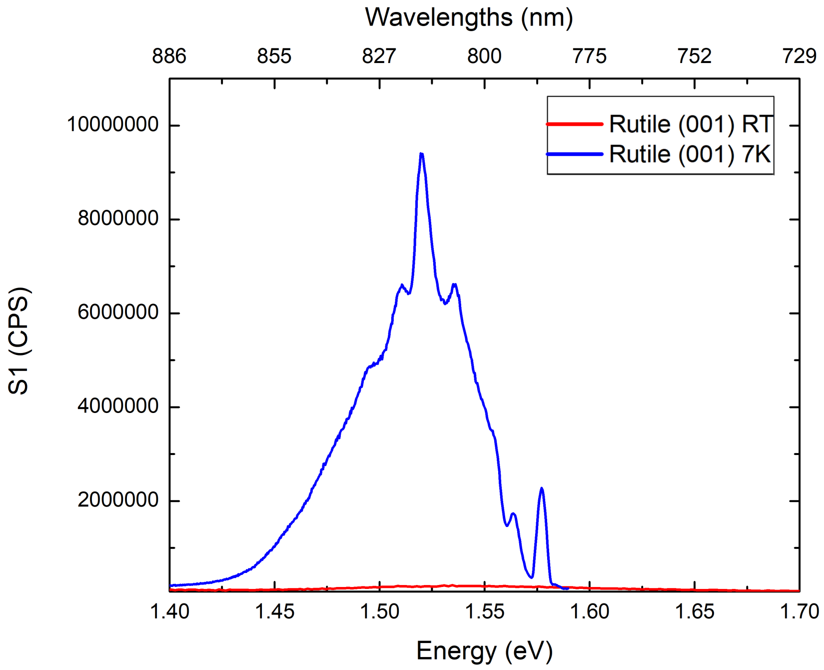

Figure 66: PL spectrum of rutile (001) sample at RT and 7K in the long wavelength range; NIR band.

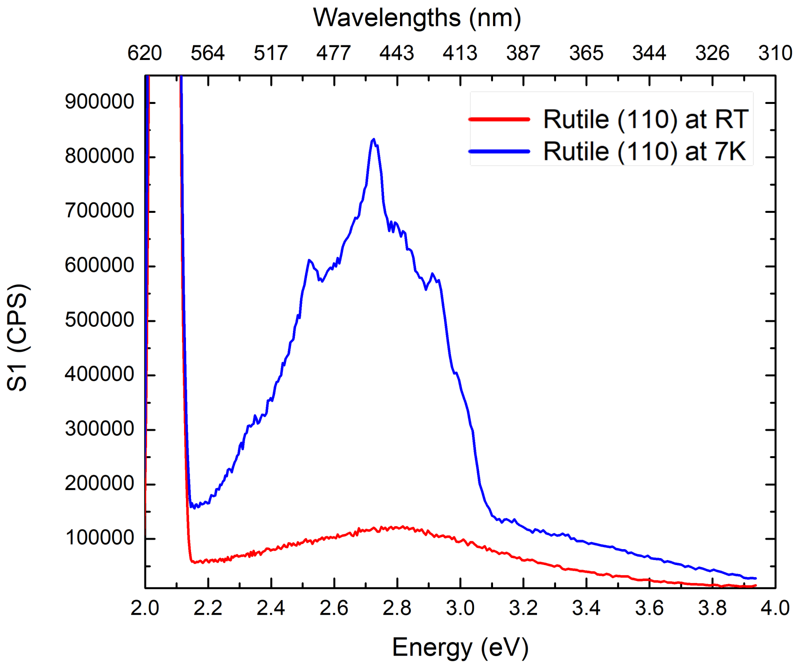

Figure 67: PL spectrum of rutile (110) sample at RT and 7K in the short wavelength range; VIS-UV band (left) and in the long wavelength range; NIR band (right). The high peak on the left is the second-order peak of the source, an artifact.

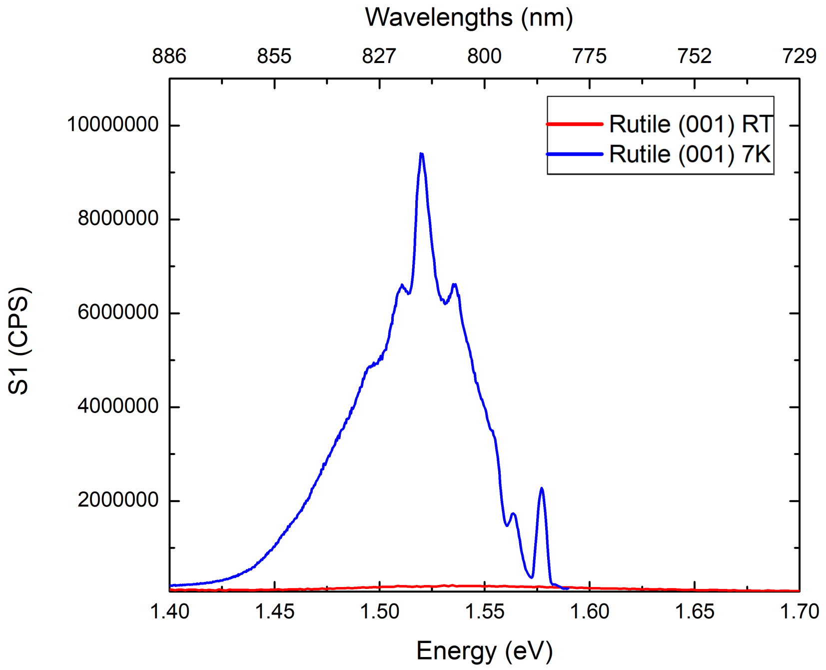

Figure 68: PL spectrum of rutile (001) sample at RT and 7K in the short wavelength range; VIS-UV band. The high peak on the left is the second-order peak of the source, an artifact.

The samples have similar photoluminescence spectra, showing two distinct contributions: a band in the VIS-UV, (2.20 - 4.00) eV, as for the anatase samples; asymmetric with respect to the bandgap (3.00 eV) and a second band close to the NIR region, centered at 1.52 eV. The NIR band shows a sharp fine structure, with five clear peaks located at 1.510 eV, 1.520 eV, 1.535 eV, 1.562 eV, and 1.557 eV. The VIS-UV band contains also three fairly clear peaks even if they are noisy, located at 2.520 eV, 2.729 eV, and 2.922 eV.

Figures 69 and 70 show the evolution of the UV-VIS (short wavelength) band as a function of the excitation wavelength for the rutile (110) and (001) samples, at 7K. Figures 71 and 72 show the evolution of the NIR (long wavelength) band as a function of the excitation wavelength for the rutile (110) and (001) samples, at 7K. The spectra in figure 67, 65, 68, and 66 were measured with an excitation at λ_{exc} = 300 nm (4.13 eV), which corresponds to about 1.13 eV above the bandgap. In the following figures, the excitation energy has been lowered by 20 nm steps, in order to probe the PL closer to the bandgap. From these figures, one can find the excitation wavelength that maximizes the emission, and thus how to optimize the parameters of the acquisition. This map gives also information about the origin of the photoluminescence.

The intensity of the PL of the UV-VIS band (short wavelength) decreases globally with increasing the excitation wavelengths for both single crystals, while for the NIR band (long wavelength) it is the opposite trend. In figure 69, the rutile (001) PL spectrum has two prominent peaks at 2.8 eV and 3.0 eV, especially visible at λ_{exc} = 360 nm, these two peaks are barely visible in the rutile (110) spectrum in figure 70.

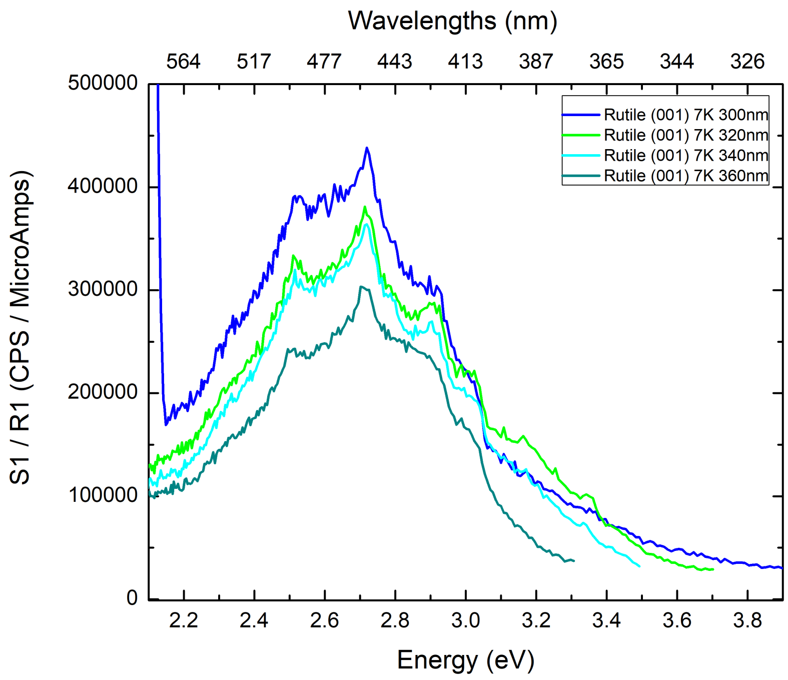

Figure 69: PL spectrum of rutile (001) sample at 7K for different excitation wavelengths in the short wavelength range; VIS-UV band. The high peak on the left is the second-order peak of the source, an artifact.

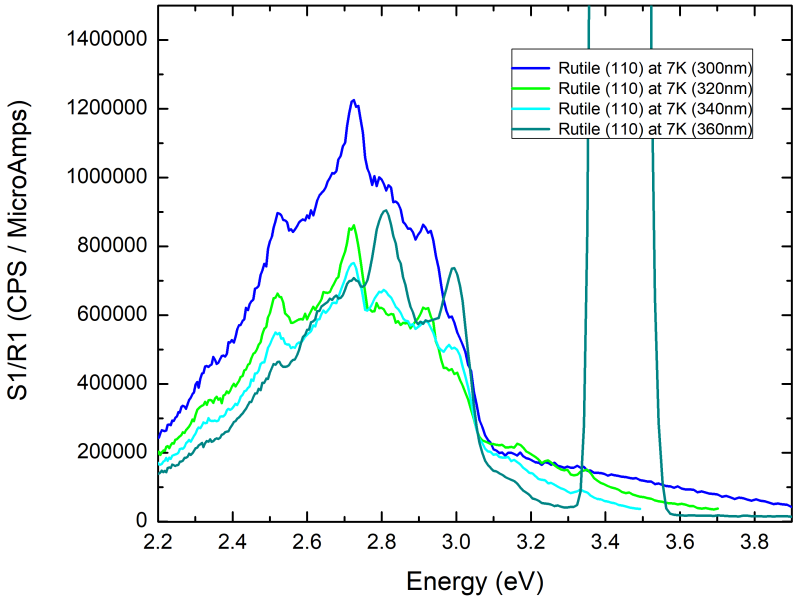

Figure 70: PL spectrum of rutile (110) sample at 7K for different excitation wavelengths in the short wavelength range; VIS-UV band. The large and highly intense peak at 3.44 eV is the first order of the source.

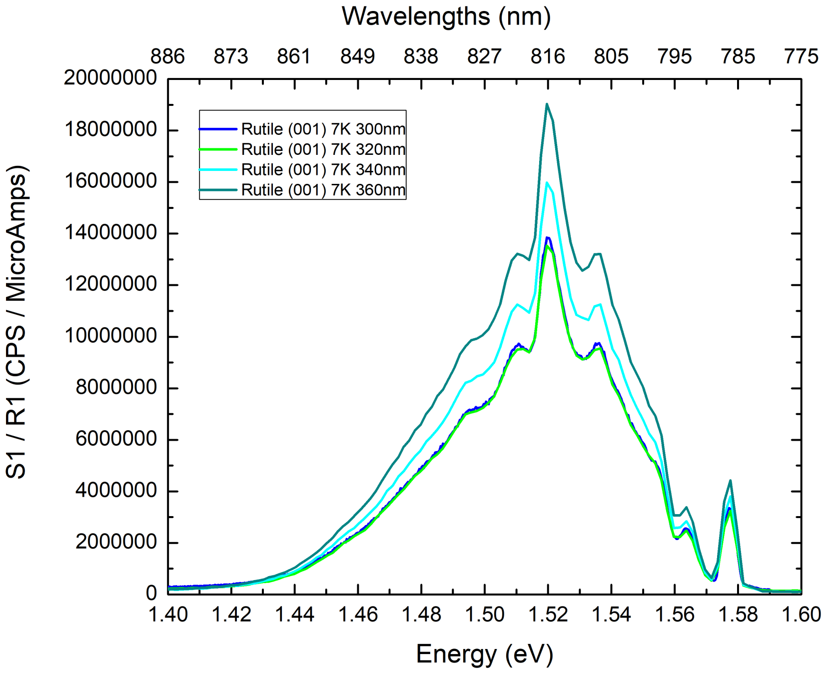

Figure 71: PL spectrum of rutile (001) sample at 7K for different excitation wavelengths in the long wavelength range; NIR band (right).

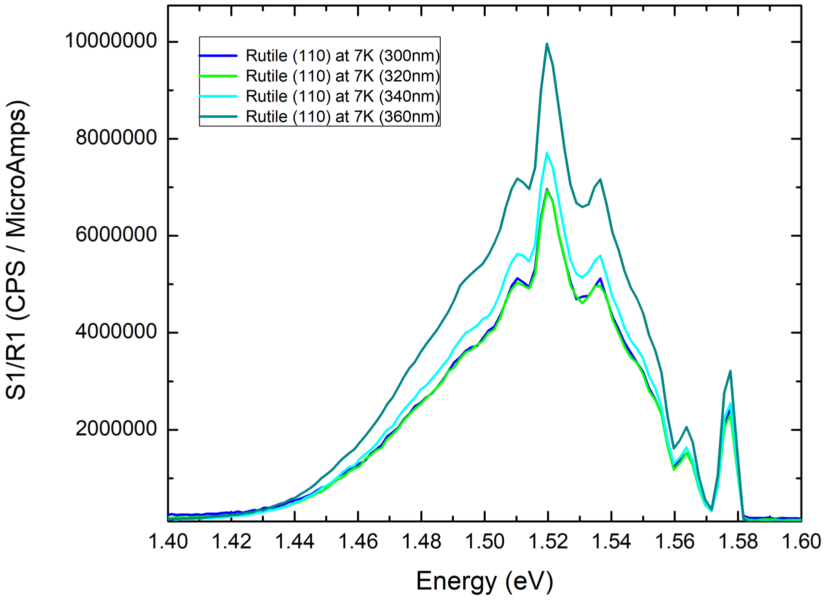

Figure 72: PL spectrum of rutile (110) sample at 7K for different excitation wavelengths in the long wavelength range; NIR band.

Discussion

First, the fact that rutile (001) and (110) samples have the same PL bands suggests that the crystal orientation does not play an important role in photoluminescence in these experiments. The UV-VIS band corresponds most likely to band-to-band radiative recombinations and to recombination from defect states inside the bandgap, which was also found in the literature in section 2.4.4. In the literature, this sub-bandgap PL of the UV-NIR band was attributed to radiative recombination through oxygen defects or excitons, similar to anatase. The NIR band corresponds to emission from states inside the bandgap.

The UV-VIS and NIR bands behave in opposite ways when increasing the excitation wavelengths; the VIS-UV band decreases in intensity while the NIR band increases, as illustrated in figures 69, 70, 71 and 72. On one hand, as the wavelength increases, the photons penetrate more into the bulk which reduces the effect of surface defects. This is the application of Beer-Lambert law for a set of wavelengths close to the bandgap, where the absorption coefficient is an increasing function of the excitation energy. From section 5.1.1 in the SE analysis, the absorption coefficient is about 14 times higher at $\lambda_{exc} = 300$ nm, than at $\lambda_{exc} = 380$ nm. On the other hand, if the PL intensity increases when varying the excitation wavelengths, this means that more radiative recombination centers are generated or fewer non-radiative recombination centers. From these two aspects, the UV-VIS PL seems to originate more from the surface layers of the sample, as the intensity decreases with the excitation wavelength, while the NIR band seems to originate more from the bulk as its intensity increases with the excitation wavelength.

Therefore, as the composition of the bulk is most likely similar between the rutile (110) and (001) sample, it is coherent that the line-shape of the NIR PL band looks identical for rutile (110) and (001), as illustrated in figures 66 and 65. This PL were attributed later to possible color centers. On the other side, the fact that the relative intensity of inner peaks in the VIS-UV band changes between the samples is coherent with a PL originating from the surface layers. The surface layers are more subject to defects. Thus, the differences between the spectra in figure 68 and 67 could be explained by the different quality (purity, history,...) of the surface of the samples. Similarly, the presence in the rutile (110) spectra at $\lambda_{exc} = 360$ nm (figure 69) of two peaks almost invisible for the rutile (001) sample can be also explained by different surface defects in rutile (001) and (110).

The NIR band centered at 1.52 eV was associated to associate this NIR band to the presence of color centers by Gallart et al.[45], Montoncello et al. [58] and Krivobok et al.[59]. For Gallart et al. claimed that the line-shape of the band originates from self-trapped exciton related to oxygen vacancies, while Montoncello et al. mentions the ionization of oxygen vacancies, and Krivobok et al. suggests intra-center transitions (i.e. d-d orbitals transitions) between vanadium impurities and titanium ions.[45, 58, 59] It should be noted that powder samples favor contaminations from external chemicals, and could explain the presence of vanadium impurities in that study, while in Gallart et al. paper the presence of vanadium is highly unlikely. Thus, here the interpretation of Gallart et al. is preferred, as their samples are single crystals like rutile (001) and (110) samples. Moreover, their spectra are very similar to the NIR spectra measured in this thesis for rutile (001) and (110), as illustrated in figure 73.

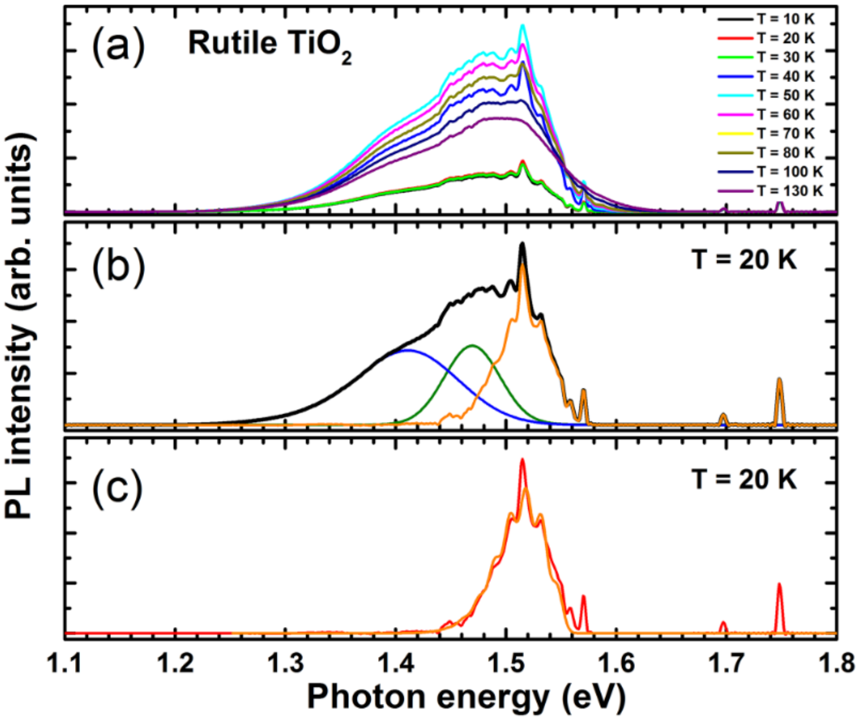

Figure 73: (a) PL spectrum of the rutile sample R100 for different temperatures. (b) Analysis of the PL emission into two broad components and a set of narrow lines at higher energies. (c) Simulation of the structured high-energy part of the PL emission by a Franck-Condon emission spectrum. Taken from Ref. [45].

Therefore, it seems likely that the NIR rutile band results from a Franck-Condon emission from color centers. First, the band is located around 1,52 eV, which is consistent with the observation that the color centers introduce energy levels into the bandgap. In this case, the color centers appear to be located in the middle of the rutile bandgap. Secondly, the shape of the PL is also a sign of electronic transitions involving phonons. The peak at 1.57 eV has the characteristics of the zero-phonon line (ZPL), as it is located at the edge of the band that corresponds to the most energetic emission. In addition, the series of peaks around the maximum at 1.52 eV represents well the phonon lines of the side-band.

Conclusion

In conclusion, the rutile samples show two distinct bands. The VIS-UV band is attributed to band-to-band direct transitions, as well as possibly states close to the surface as the UV light penetrates less in the bulk, such as oxygen defect or excitons states. The NIR band, for its part, is attributed to the PL of color centers in the bulk, which introduces levels deep in the bandgap. The small differences in the spectra of rutile (110) and (001) samples seem more attributed to their different purity and history, than their different crystal orientations.

Figure 74 shows a schematic drawing of the optical transitions involved in the PL of rutile. The light blue arrow corresponds to band-to-band recombination. As the UV-VIS band is broad, the defect states responsible for the sub-bandgap part can be considered as a continuous band. From this "continuum", recombination can occur either from the excitonic states, close to the CB and originating from Ti defects, to the VB (cyan arrow), or from the oxygen defects, forming states close to the VB, to the CB (green arrow). Finally, the color center emits in the IR, and can occur either from the CB to the color defect state or from the color defect state to the VB. These color center states are believed to originate from F center (i.e. oxygen vacancy filled with one or two electrons which affects their surrounding) which behave as single atoms and are spread over the sample.

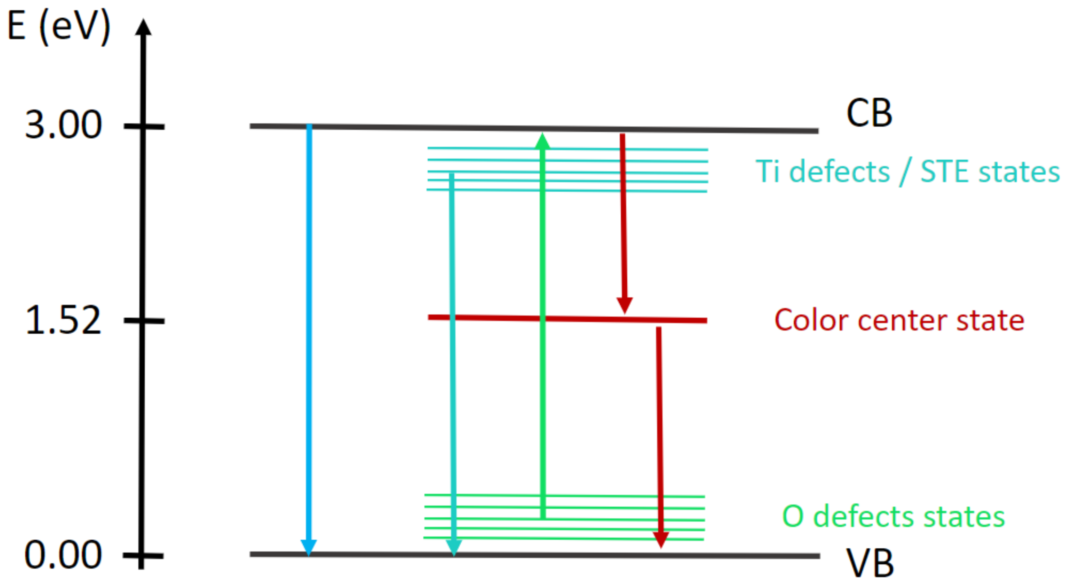

Figure 74: Schematic drawing of the optical transition involved in the PL of rutile.

5.3.3 TiO_2 thin films on STO substrate (undoped A & B series)

This section presents the PL of three TiO_2 thin films from the A and B series, grown on $SrTiO_3$ (STO) substrates. In the literature, it has been shown that using an STO substrate favors the crystalline form of anatase, due to their similar lattice constants. The crystallinity of the thin films was verified through XRD measurements by a former student of the group and is coherent with the theory. A2, B3, and B5 are polycrystalline, mostly textured anatase but A2 and B3 have in addition some rutile grains. Thus, the spectrum of A2, B3, and B5 is expected to show similarities with the PL of the anatase single crystal measured previously. The thin film A2 has a thinner thickness (i.e. 229 nm), than A3 (i.e. 667 nm) and A5 (i.e. 687 nm). Moreover, B3 is deposited with less oxygen present in the growth chamber.

In the following, it will be seen that the thin films have a PL band in the same energy range as anatase. Unfortunately, the substrate, STO, has a bandgap of 3.25 eV, just slightly above anatase (3.20 eV). Thus, the PL of the substrate is likely to interfere with the PL of the TiO_2 thin film. This consideration is especially important since TiO_2 is known to have a weak PL, which is why samples were measured at low temperatures. The PL spectra of STO are presented first, and then the PL spectra of the A2, B3, and B5 TiO_2 thin films.

The spectra of STO and the anatase (110) are plotted in figure 75. The STO substrate shows a broad blue-green PL band in the (2.0-4.0) eV range, only slightly shifted from the anatase band. As for anatase (110), the main contribution to the intensity comes from sub-bandgap states.

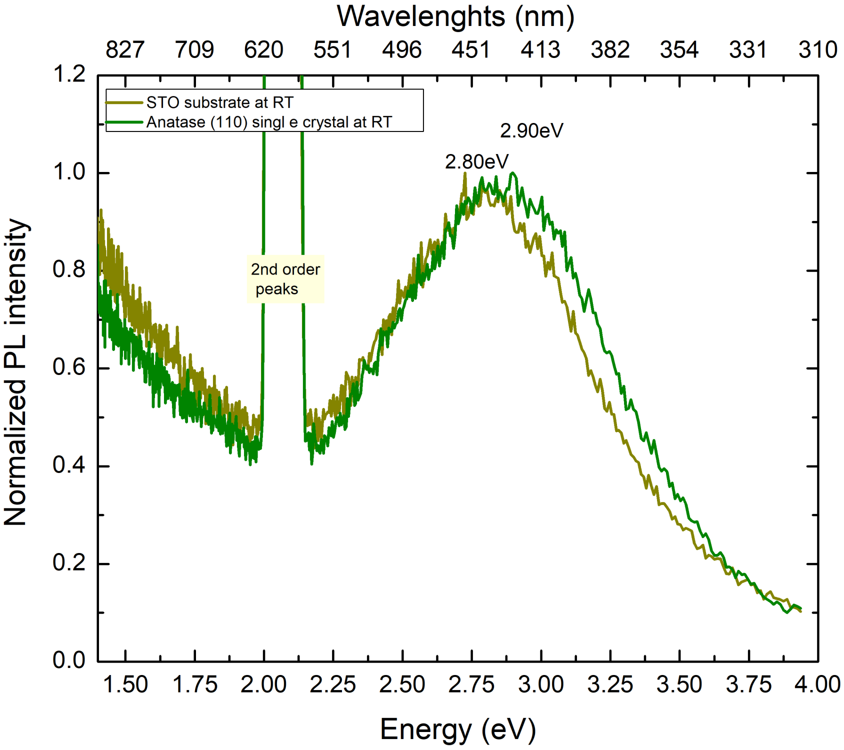

Figure 75: PL spectrum of the STO substrate and the anatase (110) single crystal, at room temperature.

Figure 76 shows the PL at 7K of STO together with the anatase (110) PL. As previously, they both show a broad blue-green band. Their maxima are separated as before by about 0.10 eV.

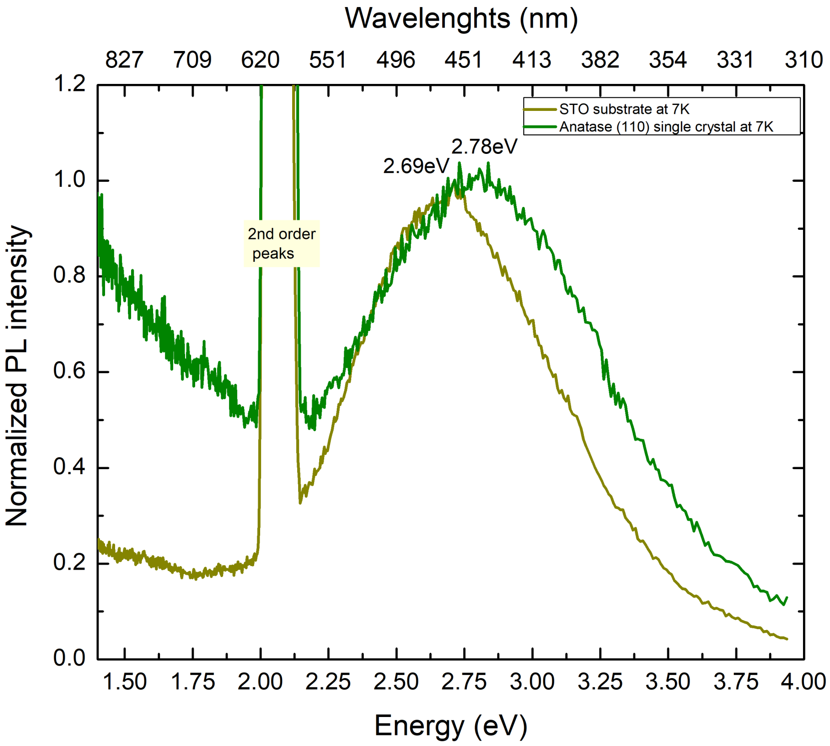

Figure 76: PL spectrum of STO substrate and anatase (110) single crystal at 7K.

Figure 77 shows the evolution of the PL spectrum of STO with different excitation wavelengths. The intensity of the band increases with decreasing the photon energy of the excitation, while the peak maximum shifts towards the UV.

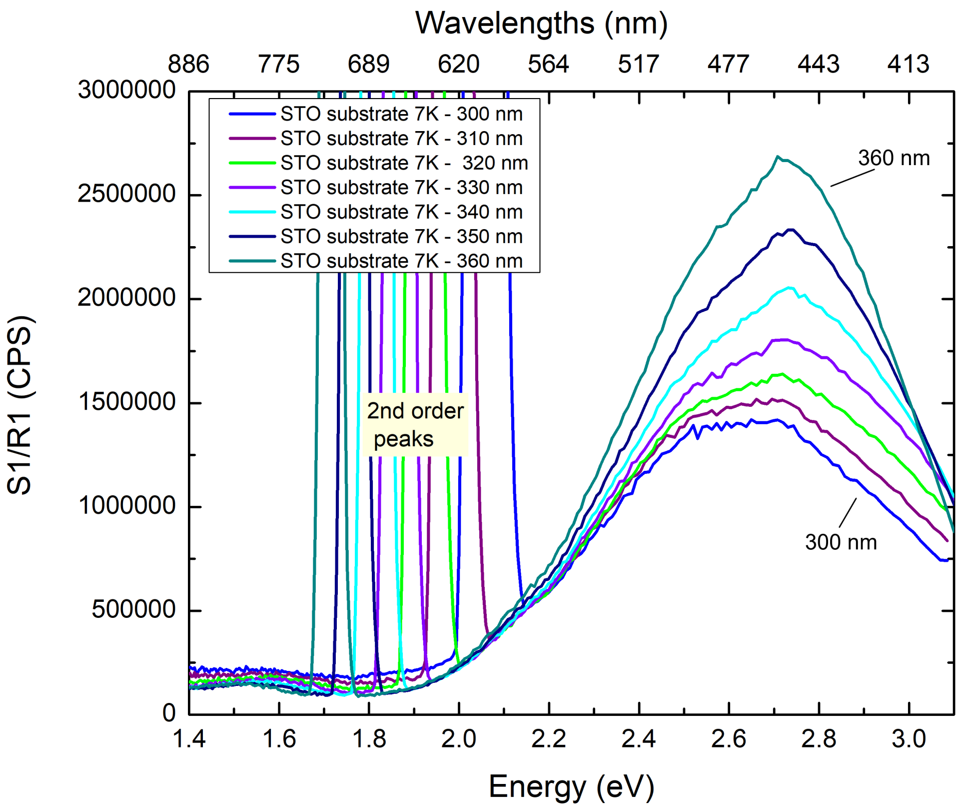

Figure 77: Evolution of PL spectrum of STO substrate at 7K with varying excitation wavelengths.

The PL of A2, B3, and B5 TiO_2 thin films is presented in the following.

At room temperature, the spectra of the A2, B3, and B5 TiO_2 thin films have a band in the visible region: (2.0 - 4.0) eV as illustrated in figure 78. The samples, A2 and B5, show the same green band centered at 2.81 eV, similar to the PL band of anatase, while B3 shows an intense PL, slightly shifted to higher energies.

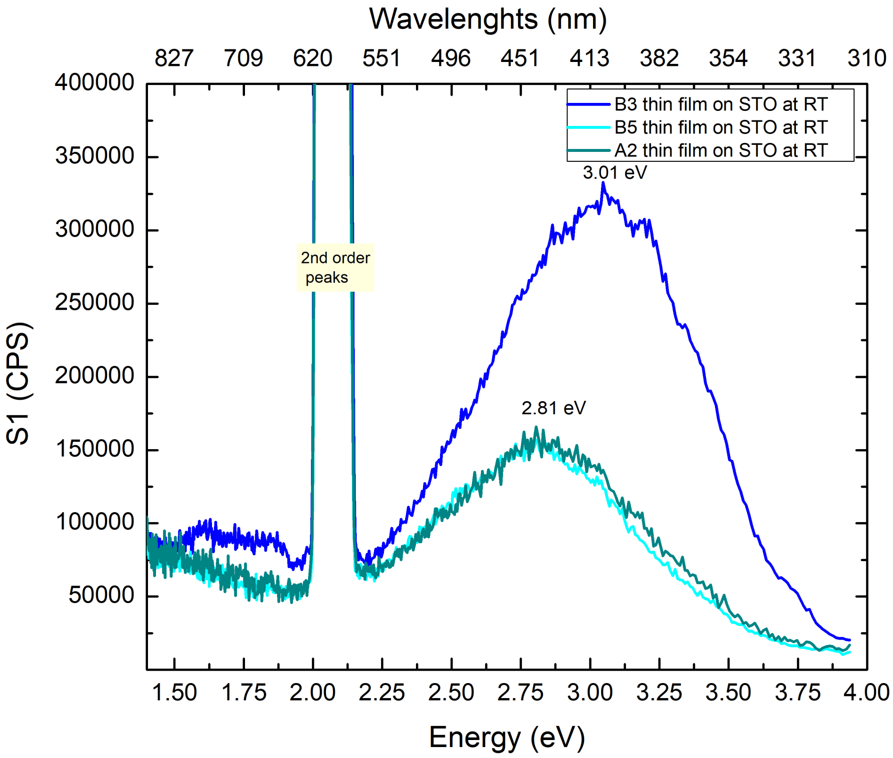

Figure 78: PL spectrum of undoped A2, B3 and B5 thin films on STO substrate at room temperature.

At 7K, the PL of A2, B3, and B5 TiO_2 thin films undergoes a redshift, as illustrated in figure 79, with the following new peak positions respectively at 2.42 eV, 2.38 eV, and 2.47 eV. Moreover, A2 and B5 PL present a shoulder at 2.18 eV. A2 seems to include in addition two extra shoulders at 2.7 eV and 2.9 eV. The intensity increase also greatly: the peaks are narrower and stronger than for STO and the anatase (110).

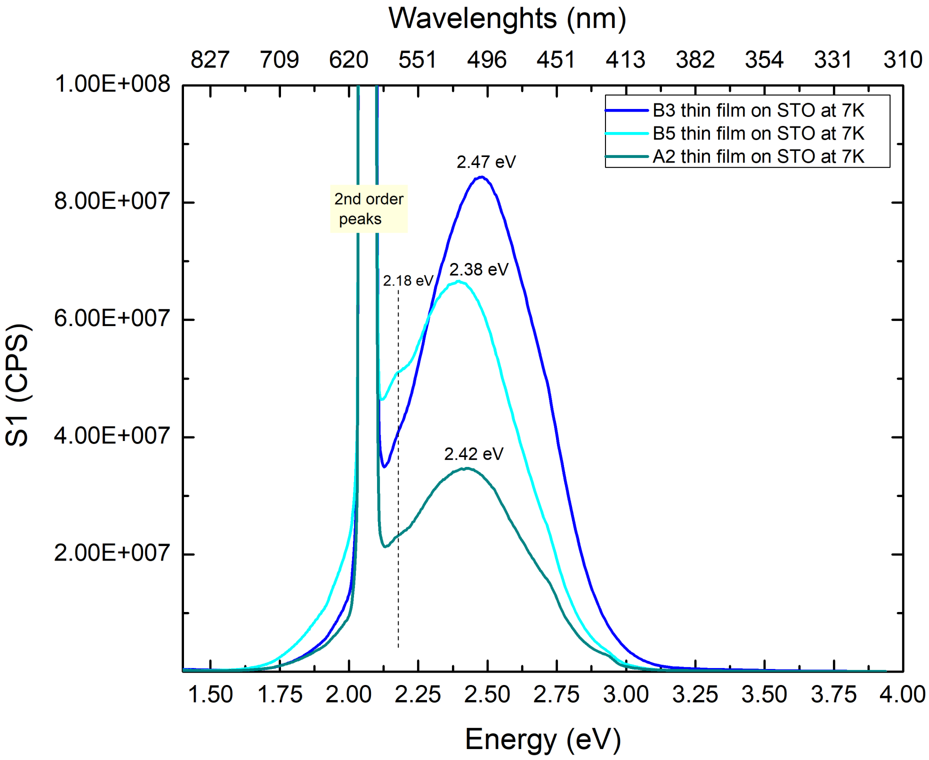

Figure 79: PL spectrum of undoped A2, B3 and B5 thin films on STO substrate at 7K.

Figures 80, 81, and 82 show the evolution of the PL with increasing excitation wavelengths (i.e. decreasing excitation energies). The globally same behavior is noticed for all the samples: an increase in intensity with increasing λ_{exc}. Two exceptions of this trend are noticed: the $\lambda_{exc} = 300$ nm spectrum in figure 81 and the $\lambda_{exc} = 380$ nm spectrum in figure 82. However, no shift of the maximum is observed, unlike what was observed in the STO PL in figure 77 or in anatase (110) in figure 62.

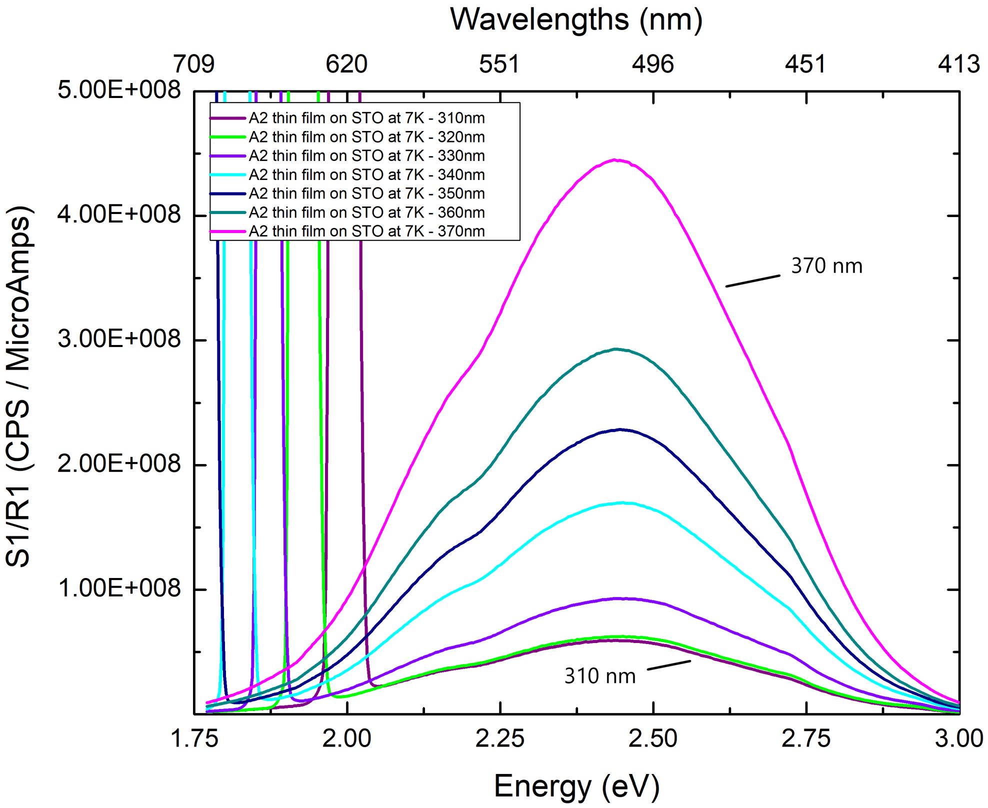

Figure 80: Evolution of PL spectrum of A2 TiO_2 thin film grown on STO substrate at 7K with varying excitation wavelengths.

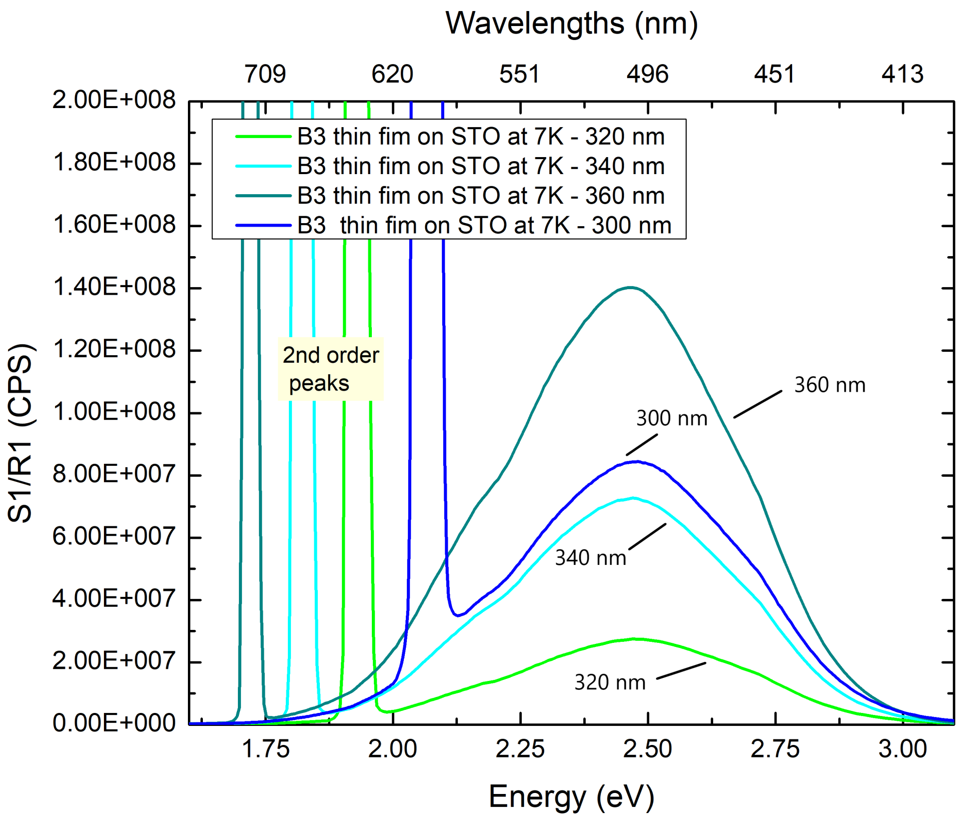

Figure 81: Evolution of PL spectrum of B3 TiO_2 thin film grown on STO substrate at 7K with varying excitation wavelengths.

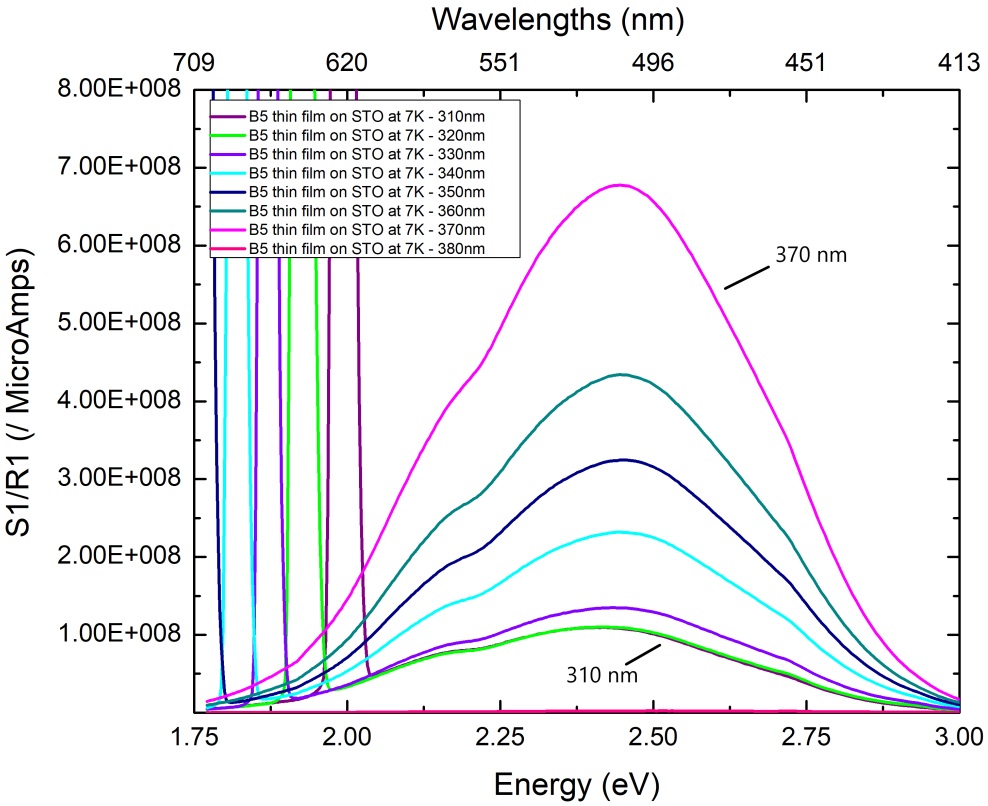

Figure 82: Evolution of PL spectrum of B5 TiO_2 thin film grown on STO substrate at 7K with varying excitation wavelengths.

Discussion

As expected, the PL of STO and anatase overlaps due to their close bandgap, 3.25 eV and 3.20 eV. In figures 75 and 76, the similarity is such that it will make it difficult to extract the contribution of the TiO_2 thin films from their PL spectrum, which are expected to resemble the one of anatase. Due to the reduction of non-radiative recombination at low temperatures as explained in the anatase discussion, the STO band undergoes a redshift of 0.10 eV at 7K. Unexpectedly, the anatase sample seems to emit more near its bandgap than STO does: even if the bandgap of STO is higher than the anatase one, its PL maximum is located at lower energies than anatase. This may be due to a lower crystalline quality of the STO substrate.

An analysis of figure 77 shows that the contribution from the band-to-band emission of STO at 7K seems to increase as the excitation energy is lowered. This could be due to the fact that the conduction electrons are less likely to take other recombination paths than the band-to-band emission when they are excited to states near the bottom of the conduction band. From these states, the band-to-band might be favored.

The PL of STO, unlike what was found from the literature in section 2.4.4 seems to originate mostly from sub-bandgap emission related to self-trapped holes (STH) by O^- of the oxygen vacancies or from STE originating from Ti interstitials according to Dadgostar et al.[63] The band-to-band emission seems really weak in the sample measured here.

Now the PL spectra of the A2, B3, and B5 TiO_2 thin films will be discussed. The spectra of A2, B3, and B5 do not show the characteristics of the band-to-band transition neither of STO or anatase, maybe except for B3 at RT. At 7K, the PL of all the samples shifts towards the NIR. This redshift shows the predominance of radiative recombination through states inside the bandgap at 7K, from STE or oxygen defects. If the PL of the STO substrate is predominant, the sub-bandgap part could originate from self-trapped holes (STH) by O^- of the oxygen vacancies or from STE originating from Ti interstitial.

In figures 80, 81, and 82, the PL spectra of the TiO_2 thin films show globally an increase of the intensity of the band with increasing λ_{exc}. This PL enhancement suggests that absorption of photon energies closer to the bandgap of anatase leads to an overall increase of the emissions from or to oxygen defects states. The PL spectrum at $\lambda_{exc} = 300$ in figure 81 and PL spectrum at $\lambda_{exc} = 380$ nm in figure 77 are two exceptions of this trend, that are attributed to the detector (e.g. saturation). It has been observed that sometimes the intensity increases or decreases abruptly from one measurement to another without any apparent reason.

If the PL is mostly from the thin film, the curve fitting of anatase can be used to interpret the PL. Unfortunately, by a lack of time, a curve fitting of the thin films was not performed. From the curve fitting of the anatase (110), performed according to Ref.[53], the two main contributions to the PL at 7K are oxygen defects emission at 2.30 eV and STE emission at 2.86 eV. In addition, contributions at 2.52 eV and 2.67 eV were attributed respectively to emissions related to charge transfers from Ti^{3+} to TiO_6^{2-} and oxygen defects emissions. Thus, the PL of A2, B3, and B3 could be due to a majority of emissions from oxygen defect states. The PL would result in the sum of two Gaussian functions centered at 2.30 eV and 2.67 eV. This is emphasized by the shoulders in A2 and B5 PL, both around 2.30 eV and 2.67 eV. However, due to the shape of the should, a contribution from the charge transfer is also plausible, especially for B3 which does not show any shoulder. If it is the case, this is a specific characteristic of TiO_2 thin films. This contribution was almost negligible in the anatase (110) spectrum.

The huge intensity of the peaks at 7K for the three thin films could suggest at first glance that only the STO substrate is emitting, however, some indications suggest the opposite. First, the respective intensity of the thin film peaks is coherent with the respective thickness of the films (229 nm, 667 nm, and 687 nm for respectively A2, B3, and B5). The PL of A2 is less intense than B5, which in return is less intense than B3. Indeed, a thinner film is expected to emit less, as fewer recombination centers are available. Secondly, introducing the absorption coefficient of anatase calculated in section 5.1.2 in the Beer-Lambert law shows that at $\lambda_{exc} = 300$ nm most photons are absorbed within the first 50 nm of the films, so in the layers close to the surface. Finally, the thin films are polycrystalline meaning that they are composed of grains. At each grain boundary, more defects are forming during the deposition of the thin films. This could possibly explain why almost no band-to-band PL is observed in the thin films. This is also coherent with the analysis performed above from the curve fitting data of anatase: oxygen defects are the most contributing to the PL. Moreover, B3 was deposited with less oxygen present in the growth chamber, which means that B3 contains more oxygen vacancies than B5 and A2. Thus, the strongest PL of B3 at 7K seems directly linked to its higher proportion of oxygen vacancies. From the reason exposed above, the PL of A2, B3, and B5 seems likely to not originate from the thin films rather than the STO substrates.

Conclusion

From the spectra, it is impossible to separate the PL on the STO substrate from the PL of the TiO_2 thin films, that are supposed to have mostly an anatase character. However, several features indicate that the PL could come from the thin films. If the PL of the film is actually detected, then the PL at 7K is mostly a sign of states in the bandgap from oxygen defects with maybe a contribution of emission induced by charge transfers from Ti^{3+} to TiO_6^{2-}.

6 Conclusion

TiO_2 anatase and rutile single crystals were characterized optically, through spectroscopic ellipsometry. This analysis was followed by an initial critical point line-shape analysis of the dielectric functions of rutile ordinary axis, and the DFT calculations of Rasmus Hoholm were compared to the anisotropic B-spline model of rutile. Finally, the single crystals: anatase (110), rutile (110) and (001), as well as three undoped TiO_2 thin films on STO substrate (A2, B3, and B5) were characterized with photoluminescence spectroscopy.

An optical B-spline model was first built for the ordinary axis of the two TiO_2 polymorphs studied here, with the data of the rutile (001) and anatase (001) samples. Then, an anisotropic uniaxial B-spline model was built for both the ordinary and extraordinary dielectric function with the data from the anatase (110) and rutile (110) single crystals. Finally, the anisotropic B-spline models was converted into a general-oscillator model and the absorption peaks were fitted with Tauc-Lorentz oscillators. From this model, the extraordinary dielectric function of rutile was fitted with a single Tauc-Lorentz centered at 4.02 eV, and a bandgap of 3.14 eV was founded. The ordinary dielectric functions were fitted with three Tauc-Lorentz, at 3.97 eV, 4.47 eV, and 5.45 eV, and gave a bandgap of 2.98 eV. Thus, the experimental bandgap, 3.00 eV, was found to originate from the ordinary axis. The ordinary dielectric function of anatase was fitted with three Tauc-Lorentz as for rutile, centered respectively at 3.85 eV, 4.60 eV, and 5.88 eV, and gave a bandgap of 3.25 eV for the anisotropic B-spline model. For the extraordinary axis, two Tauc-Lorentz were sufficient, at 4.16 eV and 4.99 eV, and gave a bandgap of 3.63 eV. Similarly to rutile, the experimental band gap of anatase corresponds to the ordinary bandgap. Anatase seems to present a larger anisotropy than rutile.

The initial critical point study focused on the ordinary axis of rutile. The dielectric functions were fitted with CP line-shapes. First, the interpretation of the dimensionality and of the type of the CP were investigated through a literature review. The absorption spectra can have either a band character, meaning that most of the transitions are from band-to-band for narrow bandgap semiconductors with high dielectric constant, or a localized excitation character (i.e. due to Frenkel excitons) for large bandgap semiconductors with low dielectric constant. For TiO_2, a large bandgap semiconductor with high dielectric constants, it was unclear which character will be the most pronounced. The interpretation of Loughin et al. seems the most relevant for the dimensionality. The dimensionality is associated to the curvature of the conduction band, and so the the effect mass and the motions of a conduction electron in k-space, a 0D CP corresponding to an infinite effective mass in all directions and a 3D CP of a small effective mass in all the directions.

Excitonic CPs were used mostly to fit the dielectric functions and mix of CPs to account for many-body effect were allowed by setting the phase ϕ as a free parameter. The analysis showed that at least six CPs were involved in the DFT dielectric functions of the ordinary axis of rutile, but that seven CPs are giving a better fit. Three of the critical points correspond to the three positions of the Tauc-Lorentz oscillators. The experimental B-spline dielectric functions were well fitted with four critical points. However, a six CPs fit gave also a fit. The energy positions of the transitions were systematically a little lower than for the DFT, but the trend was generally consistent. The excitonic CPs are believed to give the best fit because of their narrower line-shape, while 1D, 2D and 3D are more likely to affect the CPs around.

From the almost zero phases ϕ for the seven CPs of the DFT and from the ϕ taking non-integer multiples of $\frac{\pi}{2}$ values for four CPs of the B-spline model, it seems that TiO_2 could have predominantly a localized excitation character, and that its optical properties are governed mostly by excitonic transitions.

The analysis of the PL spectra turned out to be complex, as it appears not only band-to-band emissions were involved in the radiative recombination processes. The spectra of the anatase (110) single crystal shows a PL band centered around 2.82 eV at RT and 2.78 eV at 7K. The band can be decomposed in a band-to-band contribution centered around 3.20 eV, the bandgap of anatase, and a sub-bandgap contribution. The sub-bandgap contribution was attributed in the thesis mainly to two origins as was done in literature. The first one for the region just below 3.0 eV, is associated with the recombination of self-trapped excitons. The octahedral structure of the TiO_6 in the lattice is believed to favor the formation of excitons. The second origin concerns states even deeper in the bandgap and is suspected to be from oxygen defects. The latter is in accordance with the brown-orange color and the natural crystal nature of the anatase (110) sample.

The 7K and RT spectra of rutile (110) and (001) single crystals show two bands, one similar to anatase PL: a broad band with a majority of sub-bandgap contributions, a second one centered at 1.52 eV and constituted of well-resolved peaks. The first band at (2.0-3.5) eV can probably be attributed to band-to-band emission around 3.00 eV, the bandgap of rutile, and to self-trapped excitons and possibly oxygen defect states for the lower energy region of the spectra. The band centered at 1.52 eV, due to its well-resolved structure, was attributed to color center emission probably involving oxygen vacancies. The peaks result from the couplings of the electronic states of the defect with the phonon modes of the crystal. The peak at 1.57 eV has the characteristics of the zero-phonon line.

The 7K PL of the undoped TiO_2 thin films on STO show a strong PL with a single band centered at 2.38 eV for A2, 2.42 eV for B5, and 2.47 eV for B3. The growth of the thin film on the STO substrate is believed to favor the anatase crystal structure, thus a similar PL was expected. However, the STO substrate was found to have almost identical spectra to anatase, due to its close band gap, 3.25 eV. From this observation, it was difficult to distinguish the contribution of the substrate from that of the thin films. However, several features in the PL of A2, B3, and B5 at 7K suggest that the PL could originate from the thin film. Then, the main contribution would be from oxygen defects states.

In conclusion, from the PL and SE analysis, the optical properties of TiO_2 seem dominated by excitons. The PL results complement nicely the SE analysis, by showing the importance of the sub-bandgap state, whereas in SE only the above bandgap states were present in the spectra.

Suggestion of future work

For a future PL analysis, the first thing that would seem interesting to try is to measure the other undoped TiO_2 thin films of the A and B series, but on different substrates. However, from their bandgaps they are very likely to emit also at the energy range we are interested in. So, the only thing that might be interesting could be to measure the doped TiO_2 thin films on STO substrate to see if they present a different PL.

An interesting analysis could be performed if the setup was modified to introduce a confocal microscope together with the laser source. A confocal microscope allows the collection of the photoluminescence at well resolved points of the sample on the surface (with a laser source, the spot size can be of few manometers), but also inside the sample by adapting the depth of field of the system with a piezoelectric stage. By scanning either the depth or the surface, one can then get a map of the photoluminescence. This would be interesting to see how the color centers in rutile single crystals are distributed for example, as well as if the surface PL is different than from the bulk. Finally, it could be possible to record the PL of the thin film without measuring the PL of the substrate. However, this idea for the future remains hypothetical as it would be coasting and not straight forward to add a confocal microscope to the actual PL setup.

Concerning the critical points analysis, first the CP analysis Matlab code would need to be improved to fix the convergence problem. Secondly, it would be interesting to implement the possibility to restrict the critical point to an energy range around the energy of the transitions E_0. Thus, the dielectric functions could maybe be fitted with higher dimensionality CPs than excitonic CPs. One of the current problems is also the initialization of the parameters. The dimensionality seems connected to the electron effective masses in the conduction band in the three k directions. So, once the critical points are found in the band structure, an analysis of the effective masses at this point could allow to estimate the dimensionality of the critical point. Thus, the estimate value could be used to initialize n and ϕ in the code.

References

[1] Felix Pretis and Max Roser. ‘Carbon dioxide emission-intensity in climate projections: Comparing the observational record to socio-economic scenarios’. In: *Energy* 135 (2017), pp. 718–725.

[2] Elmar Kriegler et al. ‘Fossil-fueled development (SSP5): An energy and resource intensive scenario for the 21st century’. In: *Global Environmental Change* 42 (2017), pp. 297–315.

[3] H. O. Rama et al. ‘Climate Change 2022: Impacts, Adaptation and Vulnerability Working Group II Contribution to the Sixth Assessment Report of the Intergovernmental Panel on Climate Change’. In: (2022).

[4] Nico Bauer et al. ‘Shared Socio-Economic Pathways of the Energy Sector – Quantifying the Narratives’. In: *Global Environmental Change* 42 (2017), pp. 316–330.

[5] Tanveer Ahmad and Dongdong Zhang. ‘A critical review of comparative global historical energy consumption and future demand: The story told so far’. In: *Energy Reports* 6 (2020), pp. 1973–1991.

[6] Marc Perez and Richard Perez. ‘Update 2022 – A fundamental look at supply side energy reserves for the planet’. In: *Solar Energy Advances* 2 (2022), p. 100014.

[7] NREL. ‘Best research-cell efficiency chart’. In: ().

[8] William Shockley and Hans J. Queisser. ‘Detailed Balance Limit of Efficiency of p-n Junction Solar Cells’. In: *Journal of Applied Physics* 32.3 (1961), pp. 510–519.

[9] Gerardo L. Araújo and Antonio Martí. ‘Absolute limiting efficiencies for photovoltaic energy conversion’. In: *Solar Energy Materials and Solar Cells* 33.2 (1994), pp. 213–240.

[10] Antonio Luque and Antonio Martí. ‘Increasing the Efficiency of Ideal Solar Cells by Photon Induced Transitions at Intermediate Levels’. In: *Physical Review Letters* 78.26 (1997), pp. 5014–5017.

[11] E. Antolín, A. Martí and A. Luque. ‘1.29 - Intermediate Band Solar Cells’. In: *Comprehensive Renewable Energy* (2012), pp. 619–639.

[12] Wenguang Zhu et al. ‘Band Gap Narrowing of Titanium Oxide Semiconductors by Noncompensated Anion-Cation Codoping for Enhanced Visible-Light Photoactivity’. In: *Physical Review Letters* 103.22 (2009), p. 226401.

[13] Shang-Di Mo and W. Y. Ching. ‘Electronic and optical properties of three phases of titanium dioxide: Rutile, anatase, and brookite’. In: *Physical Review B* 51.19 (1995), pp. 13023–13032.

[14] Pol Torres and Riccardo Rurali. ‘Thermal Conductivity of Rutile and Anatase TiO2 from First-Principles’. In: *The Journal of Physical Chemistry C* 123.51 (2019), pp. 30851–30855.

[15] Jinfeng Zhang et al. ‘New understanding of the difference of photocatalytic activity among anatase, rutile and brookite TiO2’. In: *Physical Chemistry Chemical Physics* 16.38 (2014), pp. 20382–20386.

[16] Tong Zhu and Shang-Peng Gao. ‘The Stability, Electronic Structure, and Optical Property of TiO2 Polymorphs’. In: *The Journal of Physical Chemistry C* 118.21 (2014), pp. 11385–11396.

[17] Tim Luttrell et al. ‘Why is Anatase a Better Photocatalyst Than Rutile? - Model Studies on Epitaxial TiO2 Films’. In: *Scientific reports* 4 (2014), p. 4043.

[18] Fengcheng Wu et al. ‘Quantum efficiency of intermediate-band solar cells based on non-compensated n-p codoped TiO2’. In: *The Journal of Chemical Physics* 137.10 (2012), p. 104702.

[19] Thorlabs. ‘How is a Poincare Sphere useful for representing polarization states?’ In: (2020).

[20] Munise Cobet. ‘Ellipsometric study of ZnO from multimode formation of Exciton-Polaritons to the Core-level regime’. PhD thesis. 2010.

[21] Hiroyuki Fujiwara and Robert Collins. *Spectroscopic Ellipsometry for Photovoltaics Volume 1: Fundamental Principles and Solar Cell Characterization: Volume 1: Fundamental Principles and Solar Cell Characterization.* 2018.

[22] J.A. Woollam. ‘Interaction of light and material’. In: ().

[23] N. J. Podraza and G. E. Jellison. ‘Ellipsometry’. In: *Encyclopedia of Spectroscopy and Spectrometry (Third Edition)* (2017), pp. 482–489.

[24] F Bassani, Giuseppe Pastori Parravicini and R A Ballinger. ‘Electronic States and optical transiiton in solids’. In: *Franklin Book Co.* (1993).

[25] D. E. Aspnes. ‘Chapter 5 - The Accurate Determination of Optical Properties by Ellipsometry’. In: (1997), pp. 89–112.

[26] P. Lautenschlager et al. ‘Temperature dependence of the dielectric function and interband critical points in silicon’. In: *Physical Review B* 36.9 (1987), pp. 4821–4830.

[27] D. E. Aspnes. ‘Third-derivative modulation spectroscopy with low-field electroreflectance’. In: *Surface Science* 37 (1973), pp. 418–442.

[28] D. E. Aspnes. ‘The analysis of optical spectra by fourier methods’. In: *Surface Science* 135.1 (1983), pp. 284–306.

[29] D. Dorfs et al. ‘1.02 - Quantum Dots: Synthesis and Characterization’. In: *Comprehensive Nanoscience and Nanotechnology (Second Edition)* (2011), pp. 17–60.

[30] Juan Jiménez and Jens W. Tomm. ‘Spectroscopic Analysis of Optoelectronic Semiconductors’. In: (2016).

[31] Wei Lu and Ying Fu. ‘Photoluminescence’. In: *Spectroscopy of Semiconductors: Numerical Analysis Bridging Quantum Mechanics and Experiments* (2018), pp. 107–158.

[32] Ivan Pelant and Jan Valenta. ‘161Luminescence of excitons’. In: *Luminescence Spectroscopy of Semiconductors* (2012), p. 0.

[33] R. T. Williams and K. S. Song. ‘The self-trapped exciton’. In: *Journal of Physics and Chemistry of Solids* 51.7 (1990), pp. 679–716.

[34] H. Ikoma. ‘Semiconductors, Impurity and Defect States in’. In: *Encyclopedia of Condensed Matter Physics* (2005), pp. 330–334.

[35] Wikipedia. ‘Frank-Condon principle’. In: ().

[36] Mathijs de Jong et al. ‘Resolving the ambiguity in the relation between Stokes shift and Huang–Rhys parameter’. In: *Physical Chemistry Chemical Physics* 17.26 (2015), pp. 16959–16969.

[37] S. R. Meher. ‘6 - Transition metal oxide-based materials for visible-light-photocatalysis’. In: *Nanostructured Materials for Visible Light Photocatalysis* (2022), pp. 153–183.

[38] A. J. Moulson. ‘Transition Metal Oxides’. In: *Concise Encyclopedia of Advanced Ceramic Materials* (1991), pp. 497–499.

[39] Mark Greiner and Zheng-Hong Lu. ‘Thin-film metal oxides in organic semiconductor devices: Their electronic structures, work functions and interfaces’. In: *NPG Asia Materials* 5 (2013).

[40] Masahiro Miyauchi et al. ‘Photoinduced Surface Reactions on TiO2 and SrTiO3 Films: Photocatalytic Oxidation and Photoinduced Hydrophilicity’. In: *Chemistry of Materials* 12.1 (2000), pp. 3–5.

[41] R. Asahi et al. ‘Electronic and optical properties of anatase TiO_2’. In: *Physical Review B* 61.11 (2000), pp. 7459–7465.

[42] B. Jiang et al. ‘Charge density and chemical bonding in rutile, TiO2’. In: *Acta Crystallographica Section A: Foundations of Crystallography* 59.4 (2003), pp. 341–350.

[43] Ye-Fei Li et al. ‘Adsorption and Reactions of O2 on Anatase TiO2’. In: *Accounts of Chemical Research* 47.11 (2014), pp. 3361–3368.

[44] T. Sekiya et al. ‘Relaxation process in anatase TiO2 single crystals with different colors’. In: *Journal of Luminescence* 108.1 (2004), pp. 69–73.

[45] Mathieu Gallart et al. ‘Temperature dependent photoluminescence of anatase and rutile TiO2 single crystals: Polaron and self-trapped exciton formation’. In: *Journal of Applied Physics* 124.13 (2018).

[46] H. Tang et al. ‘Photoluminescence in TiO2 anatase single crystals’. In: *Solid State Communications* 87.9 (1993), pp. 847–850.

[47] M. Watanabe and T. Hayashi. ‘Time-resolved study of self-trapped exciton luminescence in anatase TiO2 under two-photon excitation’. In: *Journal of Luminescence* 112.1 (2005), pp. 88–91.

[48] Yutaka Toyozawa. ‘Elementary processes in luminescence’. In: *Journal of Luminescence* 12-13 (1976), pp. 13–21.

[49] Deborah K. Pallotti et al. ‘Photoluminescence Mechanisms in Anatase and Rutile TiO2’. In: *The Journal of Physical Chemistry C* 121.16 (2017), pp. 9011–9021.

[50] Yutaka Toyozawa. ‘Dynamics of excitons in deformable lattice’. In: *Journal of Luminescence* 24-25 (1981), pp. 23–30.

[51] Yasuhiro Yamada and Yoshihiko Kanemitsu. ‘Determination of electron and hole lifetimes of rutile and anatase TiO 2 single crystals’. In: *Applied Physics Letters* 101.13 (2012).

[52] Chunyan Jin et al. ‘Structure and photoluminescence of the TiO2 films grown by atomic layer deposition using tetrakis-dimethylamino titanium and ozone’. In: *Nanoscale Research Letters* 10.1 (2015), p. 95.

[53] Biswajit Choudhury and Amarjyoti Choudhury. ‘Oxygen defect dependent variation of band gap, Urbach energy and luminescence property of anatase, anatase–rutile mixed phase and of rutile phases of TiO2 nanoparticles’. In: *Physica E: Low-dimensional Systems and Nanostructures* 56 (2014), pp. 364–371.

[54] Fawad Tariq et al. ‘Room temperature photoluminescence in plasma treated rutile TiO2 (110) single crystals’. In: *Vacuum* 171 (2020), p. 108999.

[55] V. Melnyk et al. ‘Low-temperature luminescence of different TiO2 modifications’. In: *Journal of Molecular Structure* 744-747 (2005), pp. 573–576.

[56] L. Kernazhitsky et al. ‘Room temperature photoluminescence of anatase and rutile TiO2 powders’. In: *Journal of Luminescence* 146 (2014), pp. 199–204.

[57] Deniz Kadir Takci. ‘Synthesis, characterization and dielectric properties of rutile TiO2 nanoflowers’. In: *Journal of Crystal Growth* 578 (2022), p. 126442.

[58] F. Montoncello et al. ‘Near-infrared photoluminescence in titania: Evidence for phonon-replica effect’. In: *Journal of Applied Physics* 94.3 (2003), pp. 1501–1505.

[59] V. S. Krivobok et al. ‘Sharp luminescence system in titanium dioxide with zero-phonon transition at 1.573 eV’. In: *Journal of Luminescence* 252 (2022), p. 119352.

[60] K. van Benthem, C. Elsässer and R. H. French. ‘Bulk electronic structure of SrTiO3: Experiment and theory’. In: *Journal of Applied Physics* 90.12 (2001), pp. 6156–6164.

[61] Vadim Sh Yalishev et al. ‘Critical points in photoluminescence spectra and their relation with phase transition in Nb-doped SrTiO3’. In: *Applied Physics A* 126.7 (2020), p. 483.

[62] Yasuhiro Yamada and Yoshihiko Kanemitsu. ‘Band-to-band photoluminescence in $SrTiO_3$’. In: *Physical Review B* 82.12 (2010), p. 121103.

[63] Shabnam Dadgostar et al. ‘Luminescence in undoped and Nb-doped SrTiO3 crystals: Bulk and surface emission’. In: *Materials Science and Engineering: B* 283 (2022), p. 115830.

[64] Jun Zhang et al. ‘Depth-resolved cathodoluminescence spectroscopy study of defects in SrTiO3’. In: *Journal of Vacuum Science Technology B: Microelectronics and Nanometer Structures Processing, Measurement, and Phenomena* 26.4 (2008), pp. 1466–1471.

[65] Yasuhiro Yamada and Yoshihiko Kanemitsu. ‘Blue light emission from strongly photoexcited and electron-doped SrTiO3’. In: *Journal of Applied Physics* 109.10 (2011), p. 102410.

[66] Jun Li et al. ‘Enhancement of the photoelectric properties of composite oxide TiO2-SrTiO3 thin films’. In: *Advanced Composites and Hybrid Materials* 5.2 (2022), pp. 1557–1565.

[67] Masayuki Kamei et al. ‘Comparative Study of TiO2 Anatase Epitaxial Thin Films Grown by Magnetron Sputtering and Metalorganic Chemical Vapor Deposition’. In: *Japanese Journal of Applied Physics* 42.11R (2003), p. 7025.

[68] Yongqiang Yang et al. ‘An Unusual Strong Visible-Light Absorption Band in Red Anatase TiO2 Photocatalyst Induced by Atomic Hydrogen-Occupied Oxygen Vacancies’. In: *Advanced Materials* 30.6 (2018), p. 1704479.

[69] Siyoung Na, Sohyeon Seo and Hyoyoung Lee. ‘Recent Developments of Advanced Ti3+-Self-Doped TiO2 for Efficient Visible-Light-Driven Photocatalysis’. In: *Catalysts* 10 (2020), p. 679.

[70] D. Dijkkamp et al. ‘Preparation of Y-Ba-Cu oxide superconductor thin films using pulsed laser evaporation from high Tc bulk material’. In: *Applied Physics Letters* 51.8 (1987), pp. 619–621.

[71] Jonathan Mooney and Patanjali Kambhampati. ‘Get the Basics Right: Jacobian Conversion of Wavelength and Energy Scales for Quantitative Analysis of Emission Spectra’. In: *The Journal of Physical Chemistry Letters* 4.19 (2013), pp. 3316–3318.

[72] James N. Hilfiker, Harland G. Tompkins and Matthew R. Linford. ‘Spectroscopic Ellipsometry: Practical Application to Thin Film Characterization’. In: (2016).

[73] Blaine Johs and Jeffrey S. Hale. ‘Dielectric function representation by B-splines’. In: *physica status solidi (a)* 205.4 (2008), pp. 715–719.

[74] G. E. Jellison and F. A. Modine. ‘Parameterization of the optical functions of amorphous materials in the interband region’. In: *Applied Physics Letters* 69.3 (1996), pp. 371–373.

[75] A. S. Ferlauto et al. ‘Analytical model for the optical functions of amorphous semiconductors from the near-infrared to ultraviolet: Applications in thin film photovoltaics’. In: *Journal of Applied Physics* 92.5 (2002), pp. 2424–2436.

[76] P. Lautenschlager et al. ‘Interband critical points of GaAs and their temperature dependence’. In: *Physical Review B* 35.17 (1987), pp. 9174–9189.

[77] Toshiyuki Kawabata et al. ‘Dielectric function spectra and inter-band optical transitions in TlGaS2’. In: *Thin Solid Films* 571 (2014), pp. 589–592.

[78] M. I. Alonso et al. ‘Optical functions of chalcopyrite CuGaxIn1-xSe2 alloys’. In: *Applied Physics A* 74.5 (2002), pp. 659–664.

[79] P. D. Paulson, R. W. Birkmire and W. N. Shafarman. ‘Optical characterization of CuIn1xGaxSe2 alloy thin films by spectroscopic ellipsometry’. In: *Journal of Applied Physics* 94.2 (2003), pp. 879–888.

[80] Xing-Fei He. ‘Fractional dimensionality and fractional derivative spectra of interband optical transitions’. In: *Physical Review B* 42.18 (1990), pp. 11751–11756.

[81] X. F. He. ‘Anisotropy and isotropy: A model of fraction-dimensional space’. In: *Solid State Communications* 75.2 (1990), pp. 111–114.

[82] Xing-Fei He. ‘Interband critical-point line shapes in confined semiconductor structures with arbitrary dimensionality:inhomogeneous broadening’. In: *Journal of the Optical Society of America B* 14.1 (1997), pp. 17–20.

[83] Yutaka Toyozawa et al. ‘Coexistence of Local and Band Characters in the Absorption Spectra of Solids I. Formulation’. In: *Journal of the Physical Society of Japan* 22.6 (1967), pp. 1337–1349.

[84] U. Fano. ‘Effects of Configuration Interaction on Intensities and Phase Shifts’. In: *Physical Review* 124.6 (1961), pp. 1866–1878.

[85] J. E. Rowe and D. E. Aspnes. ‘Approximate Treatment of Exciton Effects in Electric Field Modulation Via the Slater-Koster Interaction’. In: *Physical Review Letters* 25.3 (1970), pp. 162–165.

[86] Letizia Chiodo et al. ‘Self-energy and excitonic effects in the electronic and optical properties of TiO_2 crystalline phases’. In: *Physical Review B* 82.4 (2010), p. 045207.

[87] Brendan Enright, Gareth Redmond and Donald Fitzmaurice. ‘Spectroscopic determination of flatband potentials for polycrystalline TiO2 electrodes in mixed solvent systems’. In: *The Journal of Physical Chemistry* 98.24 (1994), pp. 6195–6200.

[88] A. Suresh and N. Soundararajan. ‘The conventional cell and the primitive cell electronic structure of anatase titanium dioxide crystal’. In: *Materials Research Express* 4.3 (2017), p. 036301.

[89] Maofeng Dou and Clas Persson. ‘Comparative study of rutile and anatase SnO2 and TiO2: Band-edge structures, dielectric functions, and polaron effects’. In: *Journal of Applied Physics* 113.8 (2013), p. 083703.

[90] Wikipedia. ‘Brillouin Zone’. In: ().

[91] S. Loughin et al. ‘Critical point analysis of the interband transition strength of electrons’. In: *Journal of Physics D: Applied Physics* 29.7 (1996), p. 1740.

[92] Tom Tiwald and Mathias Schubert. ‘Measurement of rutile TiO2 dielectric tensor from 0.148 to 33 um using generalized ellipsometry’. In: *Proceedings of SPIE - The International Society for Optical Engineering* 4103 (2000).

[93] Patrycja Makuła, Michał Pacia and Wojciech Macyk. ‘How To Correctly Determine the Band Gap Energy of Modified Semiconductor Photocatalysts Based on UV–Vis Spectra’. In: *The Journal of Physical Chemistry Letters* 9.23 (2018), pp. 6814–6817.

[94] Ming Di et al. ‘Comparison of methods to determine bandgaps of ultrathin HfO2 films using spectroscopic ellipsometry’. In: *Journal of Vacuum Science Technology A* 29.4 (2011), p. 041001.

[95] Richard H. Bube. ‘Electrons in Solids’. In: *Encyclopedia of Physical Science and Technology (Third Edition)* (2003), pp. 307–329.

[96] J. Tauc. ‘Optical properties and electronic structure of amorphous Ge and Si’. In: *Materials Research Bulletin* 3.1 (1968), pp. 37–46.

[97] Faruque M. Hossain et al. ‘Optical properties of anatase and rutile titanium dioxide: Ab initio calculations for pure and anion-doped material’. In: *Journal of Physics and Chemistry of Solids* 69.7 (2008), pp. 1820–1828.

[98] L. J. Sham and M. Schlüter. ‘Density-Functional Theory of the Energy Gap’. In: *Physical Review Letters* 51.20 (1983), pp. 1888–1891.

[99] N. M. Ravindra, Preethi Ganapathy and Jinsoo Choi. ‘Energy gap–refractive index relations in semiconductors – An overview’. In: *Infrared Physics Technology* 50.1 (2007), pp. 21–29.

[100] J. N. Hilfiker and J. A. Woollam. ‘INSTRUMENTATION — Ellipsometry’. In: *Encyclopedia of Modern Optics* (2005), pp. 297–307.

Appendix

A Ellipsometry analysis – Rutile

A.1 B-spline model for theordinary axis of rutile

The ordinary B-spline model for rutile is built from rutile (001) single crystal data (data file: ”tio2_rutile_001_55-70-5_20s_MM.SE”). Rutile (001) is oriented in a way that the extraordinary axis is normal to the sample surface. Thus, mainly the ordinary axis of the sample is probed during the VASE measurements, allowing the extraction of the ordinary axis optical properties separately from that of the extraordinary axis.

An isotropic B-spline model is built to fit the data. Figure 83 extracted from CompleteEase® contains the parameters of the fit. The real part of the dielectric function is calculated from the imaginary part through the Kramer-Kronig formula, ε_2 is enforced positive to avoid non-physical negative absorption. The B-spline resolution is set to 0.30 eV in the range of the tail of ε_2, i.e. [0.70, 3.00] eV, and to 0.05 eV in the range of the absorption peaks, i.e.[3.00, 5.90] eV. The sample shows almost no depolarization, as illustrated in figure 84, a sign that thickness non-uniformity and instrument bandwidth are negligible for the sample. Thus, the ideal model calculation is used. Because the incoming electromagnetic field interacts mainly with the electric dipoles parallel to the sample surface, which in this case correspond only to the ordinary axis, the dielectric functions are extracted from the isotropic form of the Mueller matrix by setting the fit weight to N,C,S. As a reference, the ordinary dielectric functions from Schubert et al.[92] are used as the starting material for the B-spline model.

The imaginary part ε_2, which contains the absorption properties of the material, is expected to vanish below the experimental bandgap of rutile of 3.0 eV. In order to determine the experimental bandgap from VASE data, the bandgap in the model is assumed below the expected bandgap. Moreover, the bandgap for the ordinary and extraordinary axis might be different and could vary from the tabulated value. Simultaneously, the roughness is fitted to prevent incorrect absorption coefficient near the bandgap as suggested in their paper in Ref.[72].

The Tie-Off function is used to account for absorption outside the measured spectral range, in order to give the correct trend at the edge of the experimental data. The resulting absorption can then be compared to Schubert et al. data.[92]

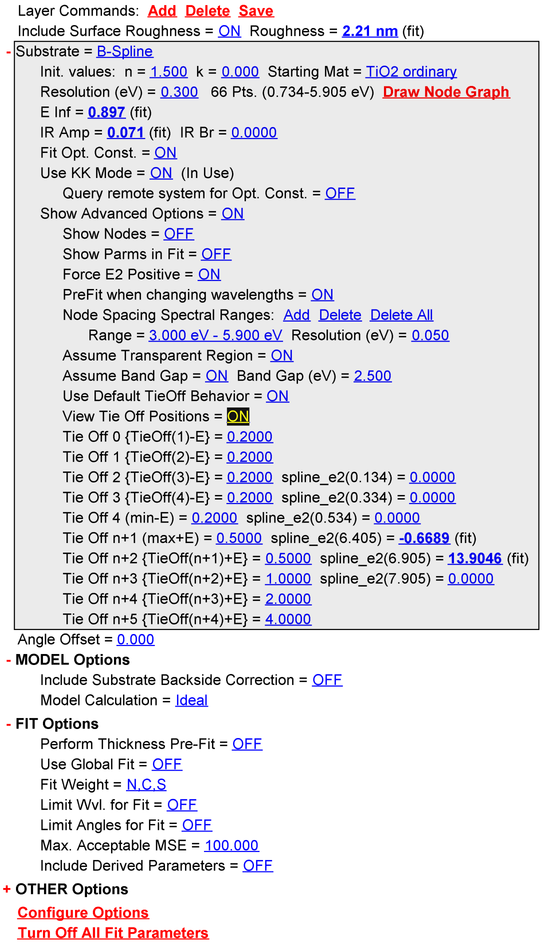

```
  Layer Commands:  Add  Delete  Save
  Include Surface Roughness = ON  Roughness = 2.21 nm (fit)
- Substrate = B-Spline
     Init. values:  n = 1.500  k = 0.000  Starting Mat = TiO2 ordinary
     Resolution (eV) = 0.300   66 Pts. (0.734-5.905 eV)  Draw Node Graph
     E Inf = 0.897 (fit)
     IR Amp = 0.071 (fit)  IR Br = 0.0000
     Fit Opt. Const. = ON
     Use KK Mode = ON  (In Use)
        Query remote system for Opt. Const. = OFF
     Show Advanced Options = ON
        Show Nodes = OFF
        Show Parms in Fit = OFF
        Force E2 Positive = ON
        PreFit when changing wavelengths = ON
        Node Spacing Spectral Ranges:  Add  Delete  Delete All
           Range = 3.000 eV - 5.900 eV  Resolution (eV) = 0.050
        Assume Transparent Region = ON
        Assume Band Gap = ON  Band Gap (eV) = 2.500
        Use Default TieOff Behavior = ON
        View Tie Off Positions = ON
        Tie Off 0 {TieOff(1)-E} = 0.2000
        Tie Off 1 {TieOff(2)-E} = 0.2000
        Tie Off 2 {TieOff(3)-E} = 0.2000  spline_e2(0.134) = 0.0000
        Tie Off 3 {TieOff(4)-E} = 0.2000  spline_e2(0.334) = 0.0000
        Tie Off 4 (min-E) = 0.2000  spline_e2(0.534) = 0.0000
        Tie Off n+1 (max+E) = 0.5000  spline_e2(6.405) = -0.6689 (fit)
        Tie Off n+2 {TieOff(n+1)+E} = 0.5000  spline_e2(6.905) = 13.9046 (fit)
        Tie Off n+3 {TieOff(n+2)+E} = 1.0000  spline_e2(7.905) = 0.0000
        Tie Off n+4 {TieOff(n+3)+E} = 2.0000
        Tie Off n+5 {TieOff(n+4)+E} = 4.0000
  Angle Offset = 0.000
- MODEL Options
     Include Substrate Backside Correction = OFF
     Model Calculation = Ideal
- FIT Options
     Perform Thickness Pre-Fit = OFF
     Use Global Fit = OFF
     Fit Weight = N.C.S
     Limit Wvl. for Fit = OFF
     Limit Angles for Fit = OFF
     Max. Acceptable MSE = 100.000
     Include Derived Parameters = OFF
+ OTHER Options
  Configure Options
  Turn Off All Fit Parameters
```

Figure 83: Parameters of the B-spline model for rutile (001).

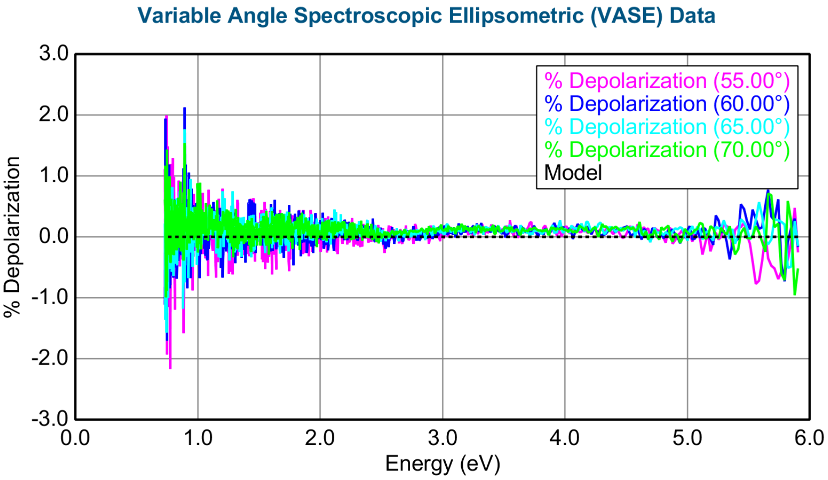

Figure 84: Depolarization data of Rutile (001) at various incidence angles, the dotted line shows the results of the B-spline model.

The figures 85 and 86 show the ψ and Δ data measured on rutile (001) single crystal with VASE by Thomas Brakstad, a previous PhD student of the Solar Cell Physics group. The dotted line shows the results of the B-spline model, which follows well the experimental data. The fit presents an MSE of 1.10 which confirms the goodness of the model, as an MSE of 1 corresponds to the ideal case. The curves can be divided into two regions: the transparent region (i.e. normal dispersion) and the absorbing region (i.e. anomalous dispersion). In the first region under 3.00 eV, Δ is roughly constant, and is equal to 180° for $\theta_i = 55.00°, 60.00°, 65.00°$, here ρ only depends on ψ. In the second region, after 3.00 eV, the ψ curves show oscillations as an effect of the absorption. For $\theta_i = 70.00°$, Δ switches from 0° to 180° in the transparent region, while it has a similar behavior to the other incidence angles in the absorbing region.

As it was shown in Section 2.2.3 in equation 21, in the simple case where the optical properties can be directly extracted from the $\rho = \tan(\psi)e^{i\Delta}$, an analytic expression connects the dielectric functions to the angles of incidence.
When multiple angles of incidence are measured, the location of the minimum of ψ can give an insight into the Brewster angle θ_B of the material, if Δ equals 90° or 270°. The Brewster angle corresponds to the incident angle where the p-polarization is totally transmitted through the material. In the present case, ψ shows a minimum of at 2.81 eV while Δ equals 90° for an incidence of 70°. Thus, the Brewster angle of anatase can be estimated at around 70°. Denser incident angle data are needed to determine more precisely the Brewster angle. However, this observation is consistent with the expected range of θ_B for a semiconductor. Usually, the Brewster angle ranges from 55° for a low-index dielectric material to 75° or 80° for a semiconductor or a metal.[100]

No interference modulates the curve in the transparent region because the sample is one side polished. This is why only SE measurements in reflection were performed on the sample. A two sides polished sample is necessary to measurements SE data in transmission, allowing for example to extract the thickness of a layer from the interference fringes.

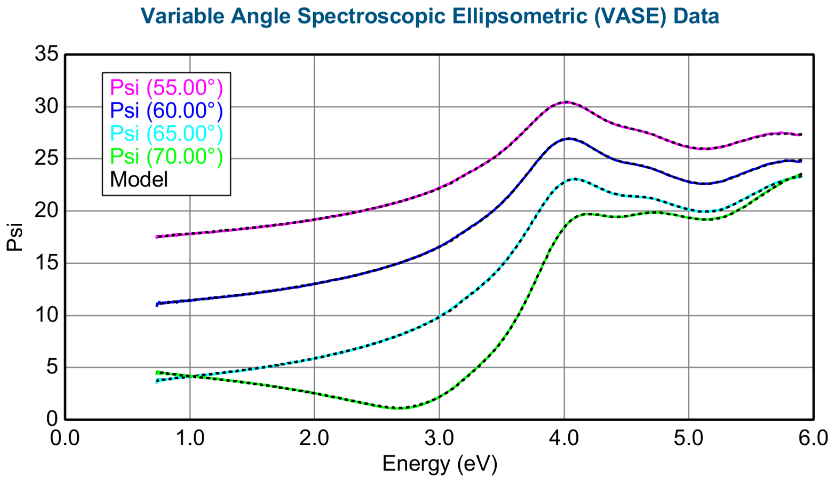

Figure 85: Rutile (001) ψ data for various incidence angles, the dotted line shows the results of the B-spline model.

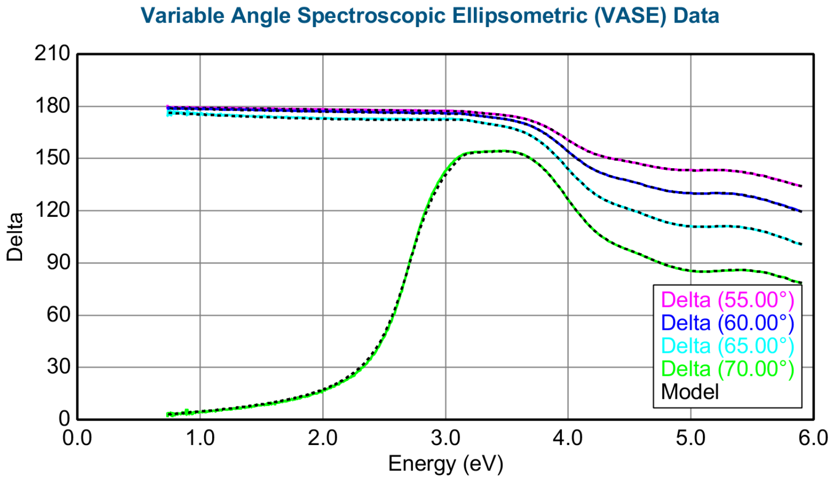

Figure 86: Rutile (001) Δ data for various incidence angles, the dotted line shows the results of the B-spline model.

The dielectric functions calculated by the model are presented in figure 87 (dashed line), the red and green curves depict the dielectric functions from Tiwald and Schubert.[92] The analysis of ε_2 gives an insight of the absorption of the rutile. As expected the sample presents absorption only above 3.00 eV. Three oscillators seem to participate in the absorption, respectively located at $\sim$ 3.98 eV, $\sim$ 4.60 eV, and $\sim$ 5.44 eV, suggesting at least the presence of three critical points. The outer range oscillation at $\sim$ 7.14 eV is shifted by 1.40 eV compared to Tiwald and Schubert data, but the Tie-Off function purpose is to shape the dielectric functions at the edges rather than giving with accuracy the positions of the absorption peaks outside the range. Differences between the B-spline model and the Schubert model are noticed at the spectral range edge. The peak at $\sim$ 5.44 eV is sharper in the B-spline model. The shape of the Schubert data suggests that the peaks at $\sim$ 4.60 eV and $\sim$ 5.44 eV have a larger broadening and possibly merged together. The differences do not appear to be linked to the quality of the fit, but rather to the condition of the experiment (type of measurement, accuracy of the angle of incidence, broadening of the monochromator lines, etc...) and to the quality of the sample which differs from one to another.

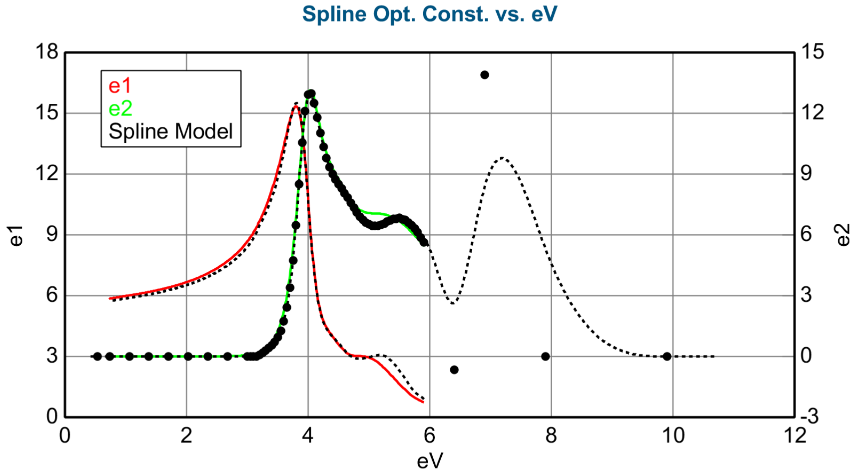

Figure 87: Rutile (001) dielectric function from the B-spline model (MSE = 1.10) for the dashed line, and respectively the imaginary and real part of dielectric functions from Schubert et al.[92] in green and red. The dots represent the nodes of the B-spline.

For further comparison, figure 88 shows in addition to the B-spline model the pseudo dielectric function and Schubert model. The pseudo dielectric functions give a quantitative estimate of the real dielectric function, which explains that the amplitude of the curve differs from the B-spline model. However, the resemblance between the curves suggests that the sample is close to the ideal case described in Section 2.2.3 in Eq.21. Moreover, this is consistent with the small fitted roughness, only 2.21 nm.

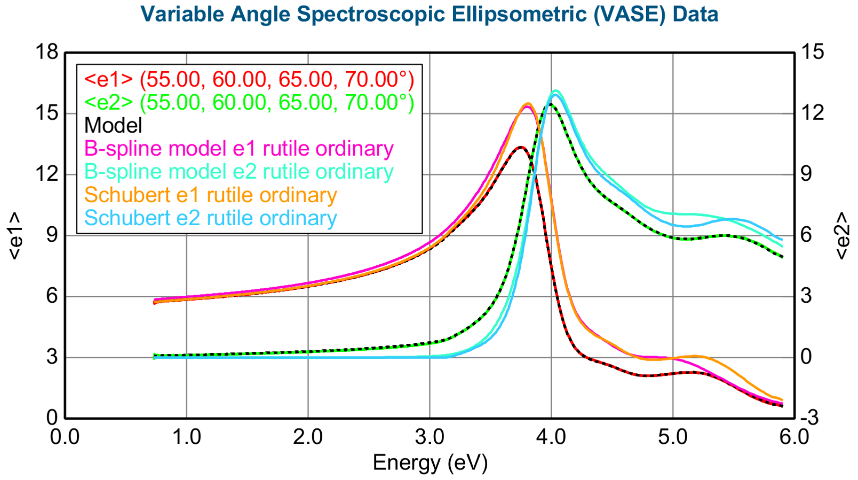

Figure 88: Comparison of the dielectric function from the B-spline model for rutile (001), the pseudo dielectric function extracted for the experimental ψ and Δ, and the dielectric functions modeled by Schubert et al.[92].

A.2 Determination of the ordinary and extraordinary orientation

When the sample is measured at several angles of rotation, the shapes of the pseudo-dielectric functions can give the orientation of the ordinary and extraordinary axis regarding the orientation of the crystal in the measurement frame. At azimuth angles where the incident light wave vector aligns with one of the axes of the sample, thus the dielectric function of this axis predominates in the data. This can be observed with the rutile (110) sample.

At 75.00°, the pseudo dielectric functions look greatly like the modeled dielectric functions for the ordinary axis. While at 165°, the pseudo dielectric function shapes reassemble effectively the extraordinary axis dielectric functions (as illustrated in figures **??**, **??**, and 89). These orientations are perfectly orthogonal like the ordinary and extraordinary axis are. As the data are measured every 5°, the incertitude of the determination is ±5°. At the same time, the elements of the Mueller matrix belonging to the off-diagonal blocks are small ($\ll 1$), noisy, and not well fitted at these angles, where the Mueller matrix is supposed to be almost isotropic, because mainly one axis contributes to the dielectric functions. These elements are not completely zero, because even when the sample the ordinary axis is perpendicular to the sample surface, a small interaction between the light beam and the extra-ordinary axis electric dipoles remains. This only exception is when the light beam arrives at normal incidence with the sample surface but then there is no reflection so no ellipsometry data.

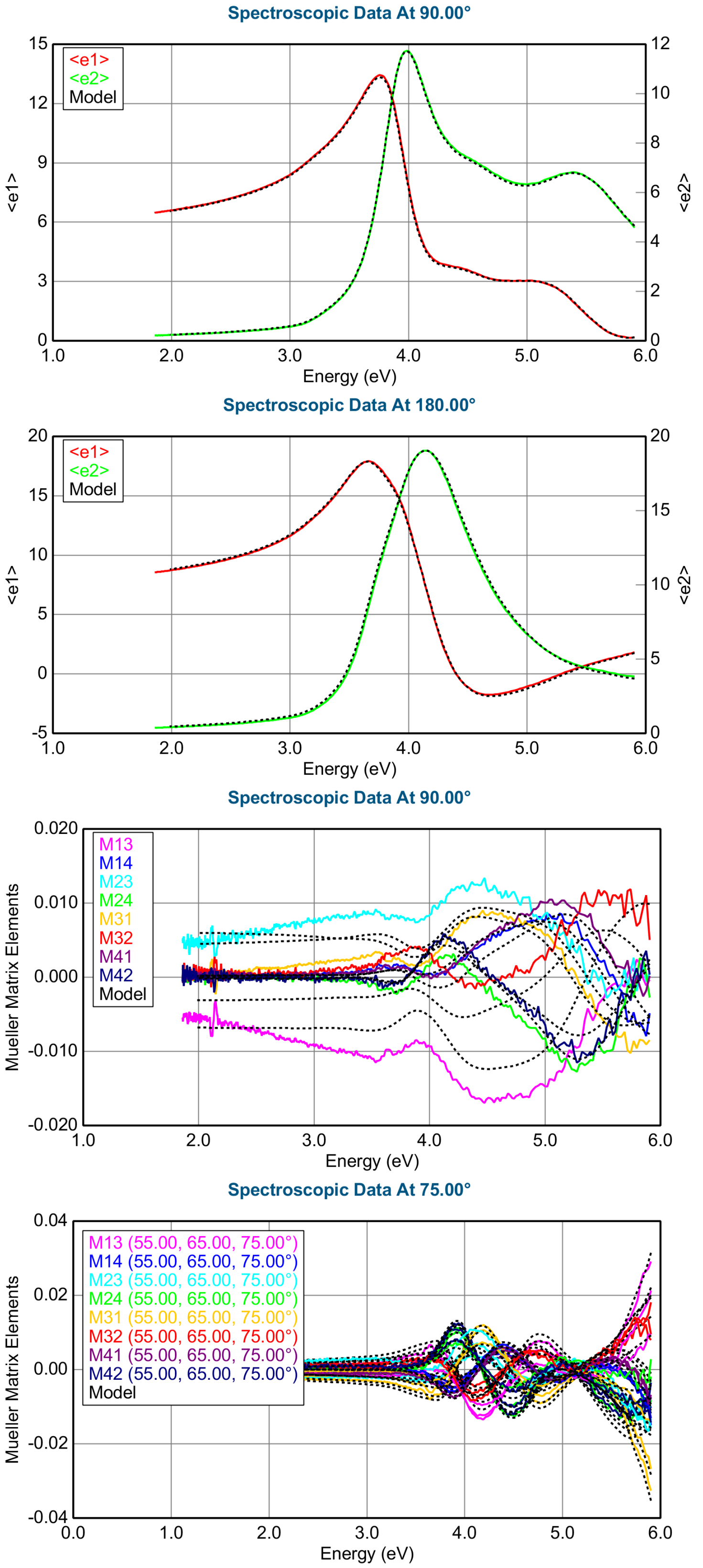

Figure 89: Pseudo dielectric function and off-diagonal blocks elements of the Mueller Matrix at different azimuth angles, allowing the determination of orientation in rutile (110) single crystal of the ordinary and extraordinary axis: 90° corresponds to the ordinary axis while 180.00° correspond to the extraordinary axis.

B Ellipsometry analysis – Anatase

B.1 B-Spline model for the ordinary axis of anatase

The dielectric functions of the ordinary axis are calculated from the anatase reference sample oriented in the (001) direction (data file: "anatase_ref001_fp_55-75-5_20sec_MM"). In this case, the extraordinary axis is perpendicular to the sample surface and the incoming light beam cannot interact with it, allowing the isolation of the ordinary optical properties.

The model follows the same procedure as presented for the ordinary axis of rutile. The bandgap of anatase is expected at 3.20 eV, thus in order to let this parameter free but to include in the model that the sample is a semiconductor, a bandgap is assumed at 2.00 eV. In return, the model fitted 1.51 ± 0.052 nm roughness. If not fitted, the roughness can add an absorption tail at the bandgap. As the purpose of the analysis is to retrieve the bulk optical properties of TiO_2, the surface effect on the dielectric functions is not studied here.

The anatase ordinary axis B-spline model possesses a good MSE of 2.23. No obvious deviation from the ψ and Δ is noticed in figure 90. The sample presents a transparent region from 1.00 eV to $\sim$ 3.20 eV, and an absorbing region above 3.20 eV, identifiable with the ψ and Δ oscillations. These are not signs of interference but of the variation in phase and amplitude of the polarization during reflection. Before 3.20 eV, the polarization of light does not change during the reflection because there is no absorption, for each angle of incidence, the s and p polarization remain in phase (i.e. an integer multiple of π).

Each incidence angle corresponds to a different pathway in the material, and the interaction/projection (scalar product) between the wave vector of the incoming light and the polarization vector of the material varies with θ_i, thus probing each time a part of the dielectric functions of the sample. By gathering all the information from all the θ_i, one can get a good estimation of the optical properties of the sample.
In the two lower Δ curves ($\theta_i = 70.00°$ and $75.00°$ respectively) a phase change occurs around the bandgap of $\sim \pi$ for the 70.00° curve, which is just a result of the measurement due to the periodicity of Δ, and of 90° for 75.00° curve which corresponds to a phase opposition between the s and p polarization.

As for the rutile ordinary axis, ψ displays a minimum of around 2.81 eV while Δ equals 90° for an incident angle of 70°. Thus, supporting a Brewster angle around 70°for both anatase and rutile. Their Brewster angles are not necessarily the same, however, it seems coherent that the values do not differ much, as for a semiconductor, θ_B should lies around 75°. [100] The lower value could be the effect of the large bandgap of TiO_2, which is sometimes referred to as a dielectric material with high dielectric constants, because of its bandgap above 3.00 eV.

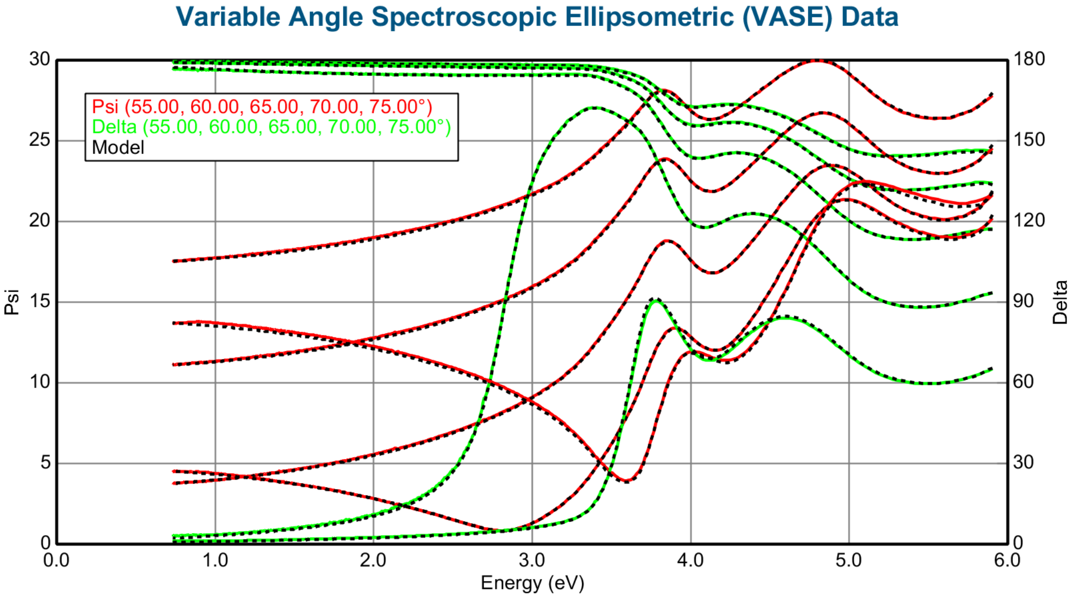

Figure 90: Anatase (001) reference sample ψ and Δ curves (MSE = 2.23).

The resulting dielectric function for the ordinary axis is presented in figure 91. A transparent region below 3.20 eV and an absorbing region above is indeed remarkable. The imaginary part ε_2 includes two obvious critical points at 3.90 eV and 4.72 eV approximately, and probably one outside the spectral range between 6.00 eV and 7.00 eV. The corresponding resonances of ε_1 are particularly visible and sharp.

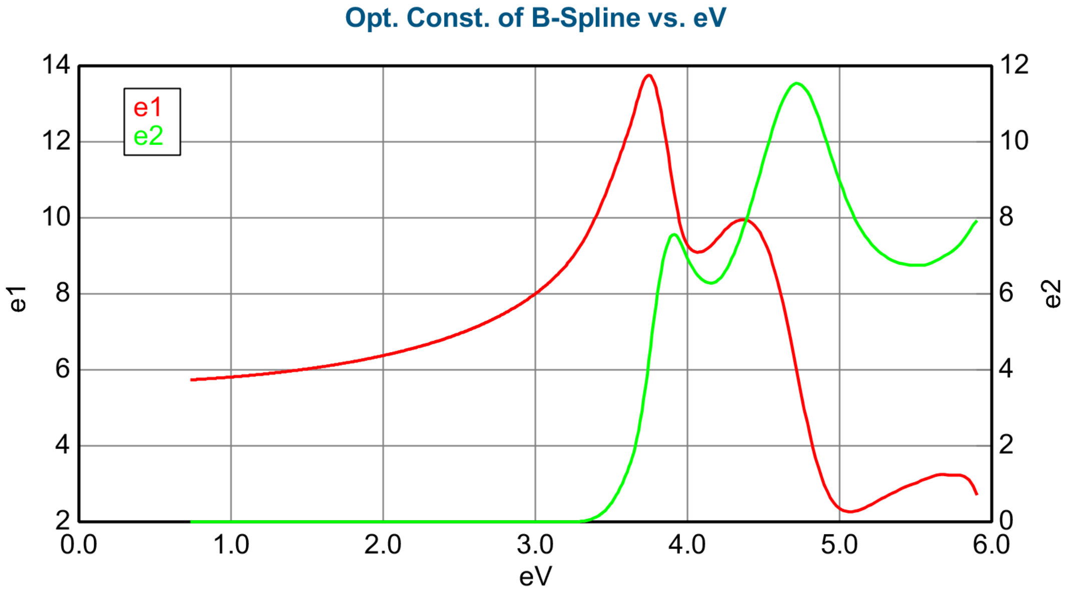

Figure 91: Dielectric function of the ordinary axis, B-spline model from anatase (001) data (MSE=2.23).

B.2 Determination of the ordinary and extraordinary orientation

Similarly to the study performed for the rutile (110) sample, the orientation of the ordinary and extraordinary axis of anatase can be determined by comparing the pseudo dielectric functions at different rotation angles to the modeled dielectric functions from the anisotropic B-spline model. At 75.00°, the pseudo dielectric function reassembles greatly to the modeled dielectric functions for the ordinary axis. While at 165°, the pseudo dielectric function shape reassembles effectively the extraordinary axis dielectric functions (as illustrated in figure 42 and 92). At the same time, one can notice that for these angles the elements of the Mueller matrix belonging to the off-diagonal blocks are small ($\ll 1$), noisy, and less well-fitted. This observation can be explained by the fact that at those angles the Mueller matrix should be almost isotropic and these elements should tend towards zero.

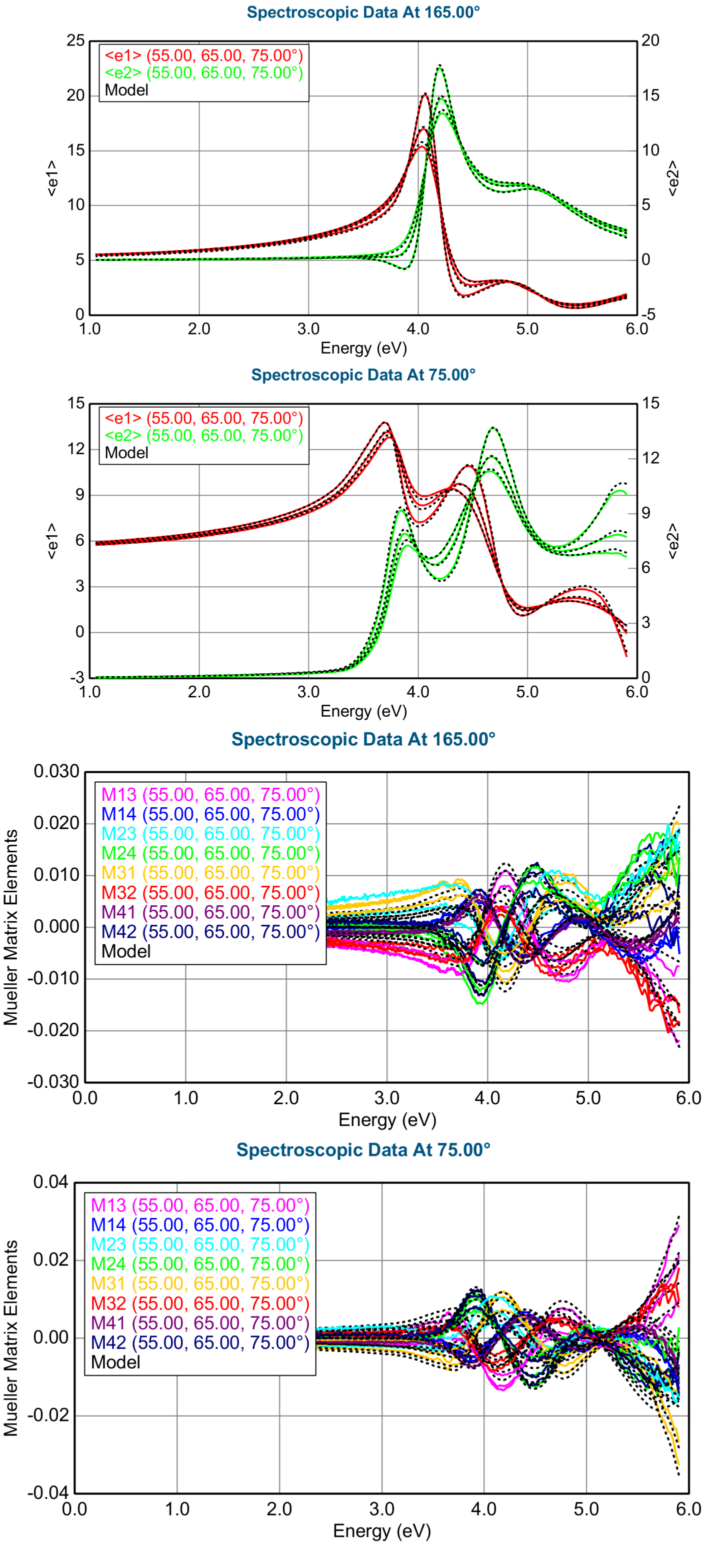

Figure 92: Pseudo dielectric function and off-diagonal blocks elements of the Mueller Matrix at different azimuth angles, allowing the determination of orientation in anatase (110) single crystal of the ordinary and extraordinary axis: 75.00° corresponds to the ordinary axis while 165.00° correspond to the extraordinary axis.

C Critical point analysis

C.1 Additional fits of the DFT dielectric functions

Here, is detailed the analysis of the CPs for fit b), c), and d).

- Fit b)

Fit b) is similar to fit a) with the exception that the CPs 4.17 eV is removed. Table 20 summarizes the initial parameters for fit b). As a result, the residual squared norm is slightly higher than in fit a): 4.52×10^4 and the fitted second derivative is smoother between CP1 and CP2. Nevertheless, all the other features in the second derivative are well-fitted, as illustrated in figure 93.

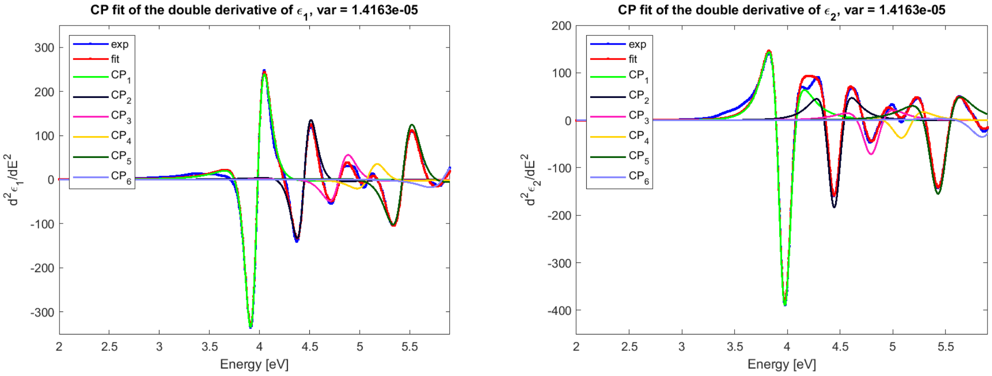

Figure 93: Experimental and fitted double derivative of ε_1 and ε_2 in fit b).

Similarly to fit a), the $\varepsilon_{1,exp}$ and $\varepsilon_{1,fit}$ only defers by a constant, as illustrated in figure 94. For ε_2, as mentioned before only the position of the CPs, and their shape around E_0 are relevant to be evaluated. In this case, all the fitted CPs seem to correspond to the experimental curve. Moreover, CP1 and CP5 appear to contribute the most to the shape of ε_2. The sub-bandgap part of the spectrum reassembles more what is expected than in fit a), due to the lower amplitude of all the CPs in this fit.

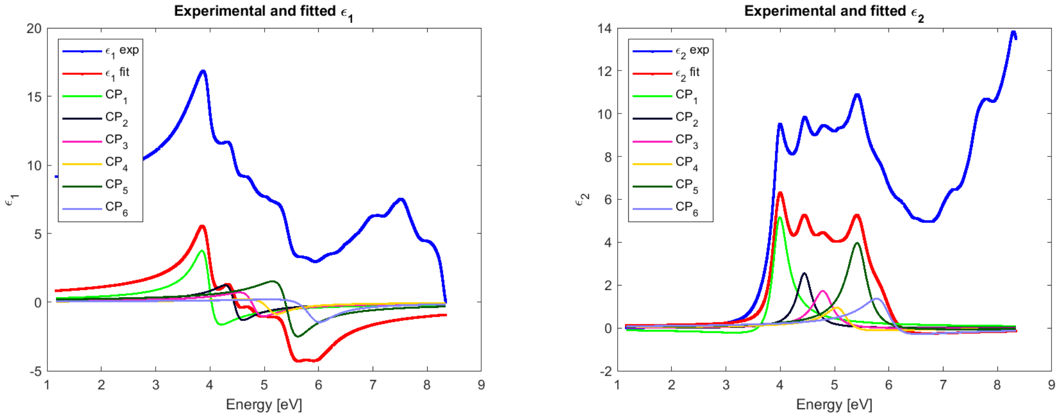

Figure 94: Experimental and fitted ε_1 (left) and ε_2 (right) for fit b).

Table 15 shows the final parameters of fit b). Unlike fit a), the phase ϕ varies a lot from one CP to the others. Only CP1 is close to zero and could result from purely excitonic absorption. For the other CPs, the value of ϕ suggests a mix of higher dimensionality critical points with excitonic CPs. So according to fit b), the many-body effect seems to be strong for the absorption along the ordinary of rutile.

Table 15: Final parameters of the critical point line-shapes for fit b).

Name	A	Γ	E_0 **(eV)**	ϕ **(°)**	**n**	**CP type**
CP1	0.88	0.16	3.96	336.92	-1	0D
CP2	0.42	0.17	4.44	1.32	-1	0D
CP3	0.38	0.22	4.80	10.12	-1	0D
CP4	0.24	0.23	5.12	37.60	-1	0D
CP5	0.91	0.22	5.44	13.96	-1	0D
CP6	0.48	0.29	5.90	49.25	-1	0D

- Fit c)

Converting CP1 and CP5 to 2D CPs could help to fill the amplitude gap between the experimental and fitted ε_2 curves. Table 21 summarizes the initial parameters for fit c). This fit has a resnorm value of 7.88×10^4, so around 5.5 times higher than fit a). As a consequence, the fitted derivative deviates from the experimental one, especially in amplitude, as illustrated in figure 95. In figure 95, the large amplitudes and tails of the CP1 and CP5 affect greatly the sum of the critical points.

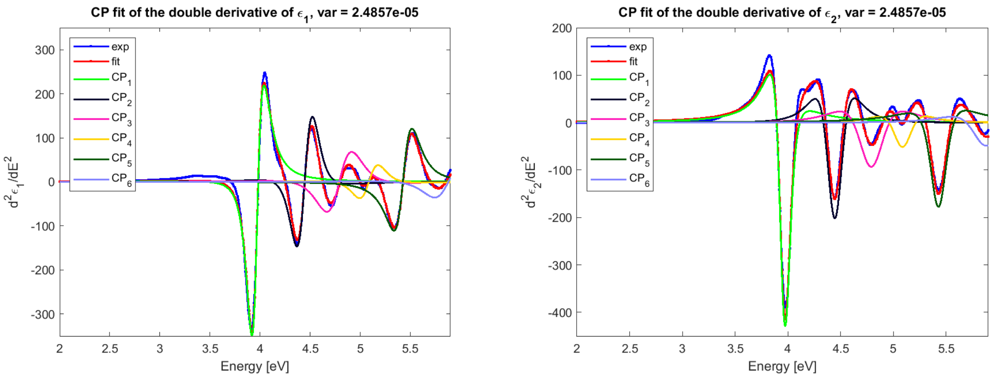

Figure 95: Experimental and fitted double derivative of ε_1 and ε_2 in fit c).

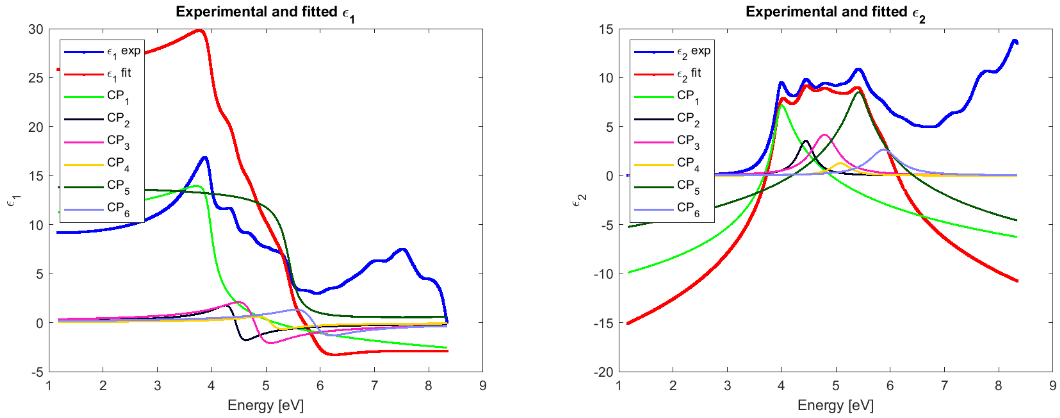

Figure 96: Experimental and fitted ε_1 (left) and ε_2 (right) for fit c).

Table 16 shows the final parameters of fit c). As in fit a), most of the CPs seem to be purely excitonic as they have near 0 ϕ values, except for CP1 and CP5. CP5 is close to 90°, so likely to be a saddle point in the band structure according to Loughin et al. [91] CP1 seems for its part to result from a mix of CPs, and thus from the interaction of the band continuum with the localized excitations.

Table 16: Final parameters of the critical point line-shapes for fit c).

Name	A	Γ	E_0 **(eV)**	ϕ **(°)**	**n**	**CP type**
CP1	4.58	0.10	3.96	66.92	0	2D
CP2	0.66	0.19	4.45	0.68	-1	0D
CP3	1.25	0.30	4.79	0.00	-1	0D
CP4	0.28	0.22	5.08	1.31	-1	0D
CP5	4.13	0.15	5.43	94.26	0	2D
CP6	0.87	0.33	5.88	0.00	-1	0D

- Fit d)

Table 22 summarizes the initial parameters for fit d). In fit d), CP1 and CP5 are converted into 1D critical points. The 1D CP has a slightly narrower shape than the 2D CP, leading to a lower resnorm than fit c) and b): 2.81×10^4. As previously, the fitting of the second derivative agrees well with the experimental data as illustrated in figure 97. The main deviation is around 4.17 eV. In the corresponding dielectric functions in figure 98, as before an offset is observed in ε_1. This could be corrected by adding a constant C. For ε_2, the 1D critical points allow retrieving almost the DFT dielectric functions, its narrow shape fits well CP1 and CP5, even if its long tail act as a constant offset over all the energy range, preventing the dielectric function to converge to zero below the bandgap.

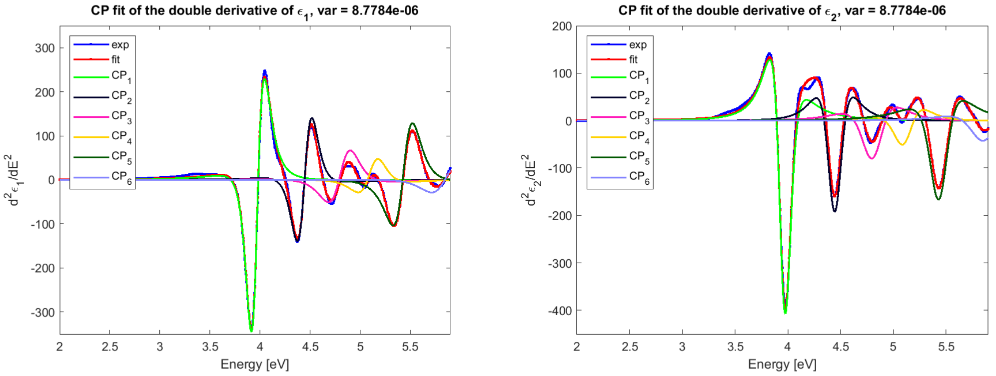

Figure 97: Experimental and fitted double derivative of ε_1 and ε_2 in fit d).

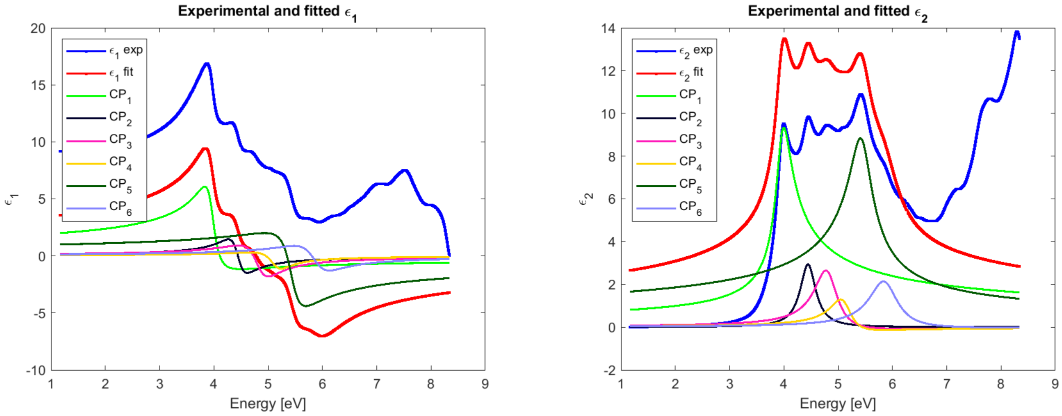

Figure 98: Experimental and fitted ε_1 (left) and ε_2 (right) for fit d).

Table 17 shows the final parameters of fit d). This time CP1 and CP5 were initialized to 180°. Only CP2 appears to be a purely excitonic peak according to its almost zero ϕ. CP6 maybe also be an excitonic peak as $\phi = 10.73°$. For all the other CPs, ϕ is a non-integer multiple of $\frac{\pi}{2}$, thus the CPs seem to result from the interaction either of localized excitation with the band continuum for CP3, CP4, and CP6, or the reverse, leading to a mix of 1D CPs with excitonic CPs for CP1 and CP5.

Table 17: Final parameters of the critical point line-shapes for fit d).

Name	A	Γ	E_0 **(eV)**	ϕ **(°)**	**n**	**CP type**
CP1	3.62	0.13	3.96	290.73	-0.5	1D
CP2	0.51	0.17	4.44	0.73	-1	0D
CP3	0.71	0.25	4.82	18.98	-1	0D
CP4	0.33	0.23	5.12	35.09	-1	0D
CP5	4.02	0.20	5.44	327.62	-0.5	1D
CP6	0.69	0.32	5.86	10.73	-1	0D

C.2 Limitations of the fits

The main limitation of the CP model for the dielectric function is the number of parameters. For each CP, four parameters describe the line-shape, and for three of them, a lower and an upper bound are selected. Thus, to perform the fit one need a powerful algorithm able to deal with multiple parameters. In this case, the nonlinear least-squares solver (i.e. *lsqcurvefit* function in Matlab) was not able to reach the global minimum as all the previous fits stopped because the maximum function evaluation was reached. As a result, the squared 2-norm of the residual is abnormally high as illustrated in table 18, a sign that the fits did not converge. Nevertheless, if the relative quality of the fit is considered, fit a) is the most correct of the DFT fits, and fit f) of the B-spline fits. Fit d) has a resnorm 2 times higher than fit a), fit b) 3.2 higher, and c) 5.6 times higher.

Table 18: Squared norm of the residuals (resnorm) of the different fits.

Fit	a)	b)	c)	d)	e)	f)
Resnorm	1.3959×10^4	4.5239×10^4	7.8834×10^4	2.8128×10^4	2.8522×10^4	2.1543×10^4

Another limitation of the fit is the tails of the CPs that affect the overall shape of the dielectric functions, especially 1D, 2D, and 3D as observed in fit c) and d). For future analysis, the energy range should be restricted to the energy around each CP, so on this range only one CP contributes to dielectric functions. This could be performed similarly to how the Tauc-Lorentz model suppresses the Lorentzian tail below the bandgap. A consequence of this limitation is that principally excitonic CPs among the others model accurately the dielectric functions, due to their narrower shape, then comes the 1D CPs, as seen in fit d), and after 2D CPs and 3D CPS. This limitation impacts directly the quality of the fit. Despite the convergence problem of the fit, the excitonic and 1D CPs give a lower square norm of residual as they approach closer the experimental data.

C.3 Initialisation parameters of the CP analysis

Table 19: Initial parameters of the critical points for fit a), the bounds are in parenthesis.

Name	A_{ini}	Γ_{ini}	$E_{0,ini}$ **(eV)**	ϕ_{ini} (°)	**n**	**CP type**
CP1	0.8 [0,10]	0.3 [0.01, 1]	3.99 [3.94,4.04]	0 [0,360]	-1	0D
CP2	0.4 [0,10]	0.3 [0.01, 0.5]	4.41 [4.36,4.46]	0 [0,360]	-1	0D
CP3	0.2 [0,10]	0.3 [0.01, 0.5]	4.77 [4.72,4.82]	0 [0,360]	-1	0D
CP4	0.1 [0,10]	0.3 [0.01, 0.3]	5.07 [5.02,5.12]	0 [0,360]	-1	0D
CP5	0.4 [0,10]	0.3 [0.01, 0.5]	5.43 [5.38,5.48]	0 [0,360]	-1	0D
CP6	0.1 [0,10]	0.3 [0.01, 0.5]	5.86 [5.81,5.91]	0 [0,360]	-1	0D
CP7	0.1 [0,10]	0.3 [0.01, 1]	4.17 [4.12,4.22]	0 [0,360]	-1	0D

Table 20: Initial parameters of the critical points for fit b), the bounds are in parenthesis.

Name	A_{ini}	Γ_{ini}	$E_{0,ini}$ **(eV)**	ϕ_{ini} (°)	**n**	**CP type**
CP1	0.8 [0,10]	0.16 [0.01, 1]	3.99 [3.94,4.04]	180 [0,360]	-1	0D
CP2	0.51 [0,10]	0.17 [0.01, 0.5]	4.41 [4.36,4.46]	0 [0,360]	-1	0D
CP3	0.70 [0,10]	0.2 [0.01, 0.5]	4.77 [4.72,4.82]	0 [0,360]	-1	0D
CP4	0.32 [0,10]	0.23 [0.01, 0.3]	5.07 [5.02,5.12]	0 [0,360]	-1	0D
CP5	1.24 [0,10]	0.24 [0.01, 0.5]	5.43 [5.38,5.48]	180 [0,360]	-1	0D
CP6	0.68 [0,10]	0.31 [0.01, 0.5]	5.86 [5.81,5.91]	0 [0,360]	-1	0D

Table 21: Initial parameters of the critical points for fit c), the bounds are in parenthesis.

Name	A_{ini}	Γ_{ini}	$E_{0,ini}$ **(eV)**	ϕ_{ini} (°)	**n**	**CP type**
CP1	0.8 [0,10]	0.16 [0.01, 1]	3.99 [3.94,4.04]	0 [0,360]	0	2D
CP2	0.8 [0,10]	0.19 [0.01, 0.5]	4.41 [4.36,4.46]	0 [0,360]	-1	0D
CP3	1.44 [0,10]	0.3 [0.01, 0.5]	4.77 [4.72,4.82]	0 [0,360]	-1	0D
CP4	0.66 [0,10]	0.27 [0.01, 0.3]	5.07 [5.02,5.12]	0 [0,360]	-1	0D
CP5	1.24 [0,10]	0.24 [0.01, 0.5]	5.43 [5.38,5.48]	0 [0,360]	0	2D
CP6	1.37 [0,10]	0.37 [0.01, 0.5]	5.86 [5.81,5.91]	0 [0,360]	-1	0D

Table 22: Initial parameters of the critical points for fit d), the bounds are in parenthesis.

Name	A_{ini}	Γ_{ini}	$E_{0,ini}$ **(eV)**	ϕ_{ini} (°)	**n**	**CP type**
CP1	0.8 [0,10]	0.16 [0.01, 1]	3.99 [3.94,4.04]	180 [0,360]	-0.5	1D
CP2	0.8 [0,10]	0.19 [0.01, 0.5]	4.41 [4.36,4.46]	0 [0,360]	-1	0D
CP3	1.44 [0,10]	0.3 [0.01, 0.5]	4.77 [4.72,4.82]	0 [0,360]	-1	0D
CP4	0.66 [0,10]	0.27 [0.01, 0.3]	5.07 [5.02,5.12]	0 [0,360]	-1	0D
CP5	1.24 [0,10]	0.24 [0.01, 0.5]	5.43 [5.38,5.48]	180 [0,360]	-0.5	1D
CP6	1.37 [0,10]	0.37 [0.01, 0.5]	5.86 [5.81,5.91]	0 [0,360]	-1	0D

Table 23: Initial parameters of the critical points for fit e), the bounds are in parenthesis.

Name	A_{ini}	Γ_{ini}	$E_{0,ini}$ **(eV)**	ϕ_{ini} (°)	**n**	**CP type**
CP1	7 [0,15]	0.3 [0.01, 1]	3.99 [3.9,4.05]	180 [0,360]	-1	0D
CP2	4 [0,15]	0.3 [0.01, 1]	4.41 [4.35,4.46]	180 [0,360]	-1	0D
CP3	2 [0,15]	0.3 [0.01, 1]	4.77 [4.7,4.85]	180 [0,360]	-1	0D
CP4	2 [0,15]	0.3 [0.01, 1]	5.07 [5.0,5.15]	180 [0,360]	-1	0D
CP5	2 [0,15]	0.3 [0.01, 1]	5.43 [5.35,5.55]	180 [0,360]	-1	0D
CP6	2 [0,15]	0.3 [0.01, 1]	5.86 [5.8,5.95]	180 [0,360]	-1	0D

Table 24: Initial parameters of the critical points for fit f), the bounds are in parenthesis.

Name	A_{ini}	Γ_{ini}	$E_{0,ini}$ **(eV)**	ϕ_{ini} **(°)**	**n**	**CP type**
CP1	0.2 [0,10]	0.3 [0.01, 1]	3.30 [3.2,4.09]	0 [0,360]	-1	0D
CP2	0.8 [0,10]	0.3 [0.01, 1]	3.99 [3.89,4.09]	0 [0,360]	-1	0D
CP3	0.4 [0,10]	0.3 [0.01, 1]	4.59 [4.4,4.85]	0 [0,360]	-1	0D
CP4	0.2 [0,10]	0.3 [0.01, 1]	5.31 [5.21,6]	0 [0,360]	-1	0D

D PL analysis

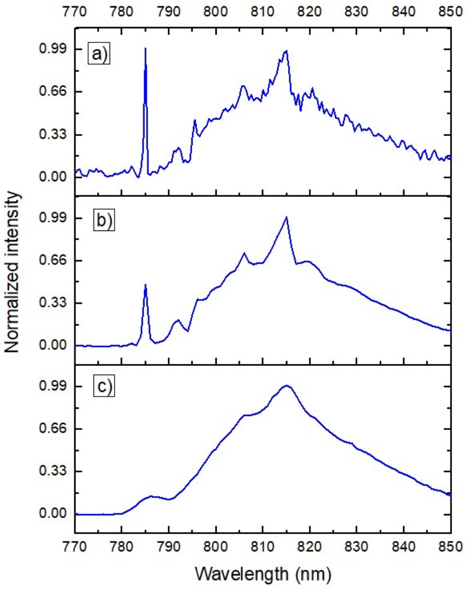

Figure 99: Comparison of the long wavelengths range PL spectra of rutile for experiments a), b) which has wider excitation slit, and c) which has wider emission slits.

Table 25: Parameters of the PL spectra of rutile for experiments a), b) which has wider excitation slit, and c) which has wider emission slits.

Integration time: 2 s	a)	b) wider excitation slit	c) wider emission slit
Excitation λ [slit] in nm	300 [1]	300 [5]	300 [1]
Emission λ (Inc.) [slit] in nm	315-900 (1) [1]	315-900 (1) [1]	315-900 (1) [5]

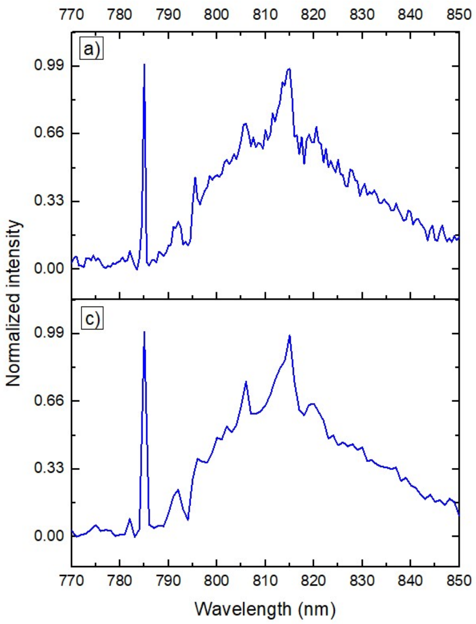

Figure 100: Comparison of the long wavelengths range PL spectra of rutile for experiments a) and c). a) has smaller increments and a shorter acquisition time than c).

Table 26: Parameters of the long wavelengths range PL spectra of rutile for experiments a) and c).

	a) smaller increment ($t_{int} = 1s$)	b) ($t_{int} = 2s$)
Excitation λ [slit] in nm	300 [10]	300 [10]
Emission λ (Inc.) [slit] in nm	315-900 (0.5) [0.2]	315-900 (1) [0.2]

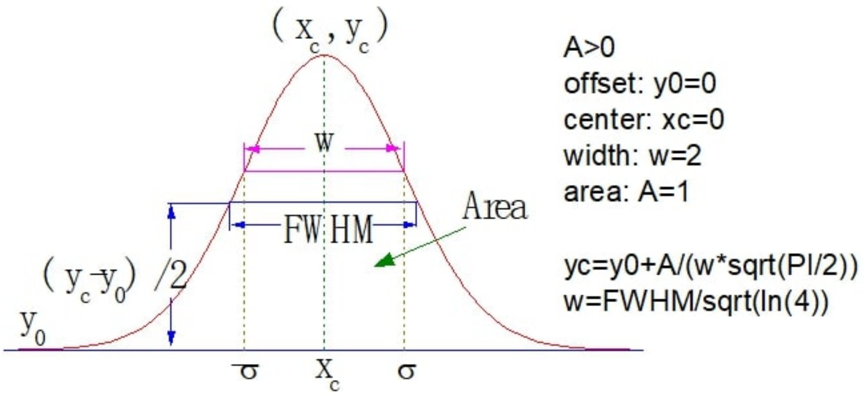

Figure 101: Description of the Gaussian functions used to fit the PL of anatase in Origin® software

.

NTNU

Norwegian University of
Science and Technology